



LUND UNIVERSITY

Diffraction in high-energy collisions

Rasmussen, Christine

2019

Document Version:

Publisher's PDF, also known as Version of record

[Link to publication](#)

Citation for published version (APA):

Rasmussen, C. (2019). *Diffraction in high-energy collisions*. [Doctoral Thesis (compilation), Theoretical Particle Physics - Undergoing reorganization]. Lund University, Faculty of Science.

Total number of authors:

1

General rights

Unless other specific re-use rights are stated the following general rights apply:

Copyright and moral rights for the publications made accessible in the public portal are retained by the authors and/or other copyright owners and it is a condition of accessing publications that users recognise and abide by the legal requirements associated with these rights.

- Users may download and print one copy of any publication from the public portal for the purpose of private study or research.
- You may not further distribute the material or use it for any profit-making activity or commercial gain
- You may freely distribute the URL identifying the publication in the public portal

Read more about Creative commons licenses: <https://creativecommons.org/licenses/>

Take down policy

If you believe that this document breaches copyright please contact us providing details, and we will remove access to the work immediately and investigate your claim.

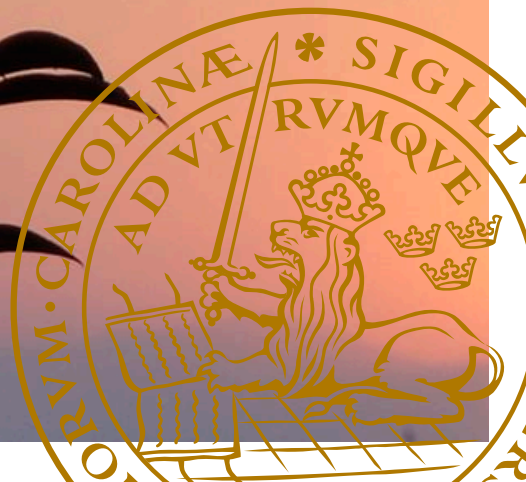
LUND UNIVERSITY

PO Box 117
221 00 Lund
+46 46-222 00 00



Diffraction in high-energy collisions

CHRISTINE OVERGAARD RASMUSSEN
FACULTY OF SCIENCE | LUND UNIVERSITY





Diffraction in high-energy collisions

Diffraction in high-energy collisions

by Christine Overgaard Rasmussen



LUND
UNIVERSITY

Thesis for the degree of Doctor of Philosophy
Thesis advisor: Prof. Torbjörn Sjöstrand
Faculty opponent: Prof. Leszek Motyka

To be presented, with the permission of the Faculty of Science of Lund University, for public criticism
in Lundmarkssalen at the Department of Astronomy and Theoretical Physics
on Friday, the 27th of September 2019 at 10:00.

Organization LUND UNIVERSITY Department of Astronomy and Theoretical Physics Sölvegatan 14A SE-223 62 Lund Sweden		Document name DOCTORAL DISSERTATION	
		Date of disputation 2019-09-27	
Author(s) Christine Overgaard Rasmussen		Sponsoring organization	
Title and subtitle Diffraction in high-energy collisions			
Abstract <p>This thesis concerns itself with low-momentum-transfer processes in high-energy particle collisions. These processes cannot be described in the framework of the fundamental theory of quantum chromodynamics (QCD), but rely on a pre-QCD approach, the Regge theory. Several models containing various degrees of complexity have been proposed within this framework, some of which have been developed and studied in this thesis. All models have been implemented in a numerical simulation (a Monte Carlo event generator), which allows for precise predictions of several types of particle collisions at various energies.</p> <p>Paper I: A model for hard diffractive events in pp collisions is proposed. It is based on evaluating a probability for diffraction, but employs an additional dynamical choice of survival of the proposed diffractive events. This dynamical description is the first of its kind and offers an explanation of earlier discrepancies between data and theory.</p> <p>Paper II: Existing models are reviewed and new ones developed for all components of the pp cross section; the total, elastic and diffractive cross sections. The models are implemented in the event generator PYTHIA 8, thus offering improved predictions for these collisions at LHC energies.</p> <p>Paper III: In this work the model for hard diffraction is extended to photoproduction. The dynamical survival effect is by construction only present in a subset of these collisions and thus puts forward an explanation of the discrepancies between data and theory of hard diffractive dijet events in the photoproduction regime.</p> <p>Paper IV: Here a new model for initial state evolution is implemented and studied in PYTHIA 8. This model opens up for asymmetrical matter distributions within the colliding particles, and consequences because of these asymmetries are studied within ep, pp, pA and AA collisions. Predictions for the color fluctuations in the cross sections in eA collisions are presented as a first step towards a complete description of electron-ion collisions.</p>			
Key words QCD, Soft QCD, Phenomenology, Diffraction, Multiparton Interactions, Dipole model, Initial state evolution, BFKL evolution.			
Classification system and/or index terms (if any)			
Supplementary bibliographical information		Language English	
ISSN and key title		ISBN 978-91-7895-215-1 (print) 978-91-7895-216-8 (pdf)	
Recipient's notes		Number of pages 263	Price
		Security classification	

I, the undersigned, being the copyright owner of the abstract of the above-mentioned dissertation, hereby grant to all reference sources the permission to publish and disseminate the abstract of the above-mentioned dissertation.

Signature _____

Date 2019-09-02

Diffraction in high-energy collisions

by Christine Overgaard Rasmussen



LUND
UNIVERSITY

A doctoral thesis at a university in Sweden takes either the form of a single, cohesive research study (monograph) or a summary of research papers (compilation thesis), which the doctoral student has written alone or together with one or several other author(s).

In the latter case the thesis consists of two parts. An introductory text puts the research work into context and summarizes the main points of the papers. Then, the research publications themselves are reproduced, together with a description of the individual contributions of the authors. The research papers may either have been already published or are manuscripts at various stages (in press, submitted, or in draft).

Cover illustration front: Sunrise in Nepal, spring 2010.

© Christine Overgaard Rasmussen 2019

Faculty of Science, Department of Astronomy and Theoretical Physics

ISBN: 978-91-7895-215-1 (print)

ISBN: 978-91-7895-216-8 (pdf)

Printed in Sweden by Media-Tryck, Lund University, Lund 2017



This thesis is based upon the following publications:

- I Christine O. Rasmussen and Torbjörn Sjöstrand,
Hard diffraction with dynamic gap survival,
JHEP **1602** (2016) 142
doi:10.1007/JHEP02(2016)142
e-Print: arXiv:1512.05525 [hep-ph]
MCnet-15-36, LU TP 15-56.

- II Christine O. Rasmussen and Torbjörn Sjöstrand
Models for total, elastic and diffractive cross sections,
Eur. Phys. J. C **78** (2018) no.6, 461
doi:10.1140/epjc/s10052-018-5940-8
e-Print: arXiv:1804.10373 [hep-ph]
MCnet-18-08, LU TP 18-06.

- III Ilkka Helenius and Christine O. Rasmussen
Hard diffraction in photoproduction with Pythia 8,
Eur. Phys. J. C **79** (2019) no.5, 413
doi:10.1140/epjc/s10052-019-6914-1
e-Print: arXiv:1901.05261 [hep-ph]
MCnet-19-01, LU TP 19-06.

- IV Christian Bierlich and Christine O. Rasmussen
Dipole evolution: perspectives for collectivity and γ^*A collisions,
Submitted to JHEP
e-Print: arXiv:1907.12871 [hep-ph],
MCnet-19-17, LU TP 19-32.

POPULÆR SAMMENFATNING PÅ DANSK

I årtusinder har mennesket beskæftiget sig med fysik. Fysikken er den gren af videnskaben, der beskriver hvordan verden ser ud, hvad den består af og hvordan vi skal forstå den. En af de grundlæggende grene af fysikken er partikelfysikken. Partikelfysik omhandler de mindste dele af alting, det som kaldes elementarpartikler. Elementarpartikler defineres som partikler, der ikke kan brydes i mindre elementer, i modsætning til fx. atomer, der kan deles i protoner, neutroner og elektroner. Elementarpartiklerne inddeles i to klasser kaldet kvarker og leptoner, og vekselvirker med andre partikler ved hjælp af bosoner – en tredje type elementarpartikler, der bærer tre ud af fire kendte naturkræfter: den stærke og den svage kernekraft samt elektromagnetismen. Endnu har vi ikke fundet bosonen, der antages at være bærer af tyngdekraften, hvorimod Higgs bosonen, der giver masse til de andre elementarpartikler, for nyligt er blevet fundet.

For detaljeret at beskrive hvordan disse forskellige vekselvirkninger foregår, har man brug for en matematisk teori, der forklarer hvilke regler, de forskellige elementarpartikler er underlagt. En væsentlig teori for denne afhandling er kvante-kromodynamik (på engelsk *quantum chromodynamics* (QCD)), der fortæller hvordan partikler, der er ladet under den stærke kernekraft, vekselvirker med hinanden. Ligesom elektrisk ladning (indirekte) er kvantetallet for elektromagnetismen, findes kvantetallet *farve* (color) i QCD, ikke at forveksle med de farver, vi kender fra hverdagen. De eneste elementarpartikler, der er ladet under den stærke kernekraft, er kvarkerne og gluonerne, hvoraf de sidste er bærere af den stærke kernekraft.

I modsætning til elektromagnetismen, hvor frie elektrisk ladede partikler er tilladt, er det ikke er muligt at observere frie farve-ladede partikler. Kun under helt specielle omstændigheder, for eksempel ved enormt høje energier, kan vi tale om frie kvarker og gluoner, der kan vekselvirke. Under helt normale omstændigheder er kvarkerne bundet sammen af den stærke kernekraft på en sådan måde, så de observeres som farve-neutrale (eller farveløse). Eksempler herpå er protoner og neutroner.

Ved høje energier, hvor kvarkerne og gluonerne kan anses for frie, kan man benytte perturbativ QCD (pQCD) til at udregne sandsynligheden for forskellige processer. Forsimplet går pQCD ud på at man approksimerer den fulde teori med en, der kan udregnes ved en given præcision. Men hvad gør man, hvis energierne eller energioverførslen mellem partiklerne ikke er høje nok til at kvarkerne og gluonerne kan anses som frie partikler? I disse tilfælde kan man ikke benytte sig af pQCD, og man er derfor nødsaget til at bruge fænomenologiske modeller. Tag som eksempel en elastisk proton-proton kollision. Her forestiller vi os en kollision som på et pool-bord. To kugler kolliderer med hinanden og er intakte bagefter. Men hvordan skal vi beskrive denne process? Vi har jo lært at protoner ikke er kugler – de er opbygget af kvarker og gluoner. Hvordan kan det være, at de stadig er bundet sammen på (næsten) præ-

cis sammen måde efter kollisionen? Og hvilken type af partikler er ansvarlige for at udveksle energi mellem protonerne, uden at de går i stykker?

Processer, der ikke kan beskrives med pQCD, kaldes ofte bløde kollisioner (på engelsk *soft processes*). Historisk er de blevet beskrevet som en udveksling af en anden type af sammensatte objekter. En teori, der beskriver disse udvekslinger, kaldes Regge teorien. Denne teori er grundlaget for de fleste artikler i denne afhandling. Bl.a. undersøges de ovennævnte elastiske processer, samt en anden type – de diffraktive processer. I diffraktive processer, brydes en (eller begge) af protonerne i en elastisk proces op, men på en helt særlig måde: i sådanne processer er der store områder af faserummet, hvori der ikke er partikelproduktion. Man vil derfor eksperimentielt kunne lede efter sådanne 'huller' i ens detektor. I disse diffraktive kollisioner sker det særlige, at vi benytter os af Regge-teorien til at forklare hvor ofte sådanne kollisioner sker, mens måden, hvorpå de diffraktive systemer opfører sig, ofte kan beskrives med pQCD.

Det særlige miljø, som disse typer af kollisioner danner, er yderst unikt netop på grund af dette sammenspil mellem perturbative og ikke-perturbative beskrivelser. Arbejdet i denne afhandling er et forsøg på at give ekstra opmærksomhed til dette regime: der er her udviklet nye modeller og værktøj, der giver ny indsigt i de diffraktive hændelser og kan benyttes til videre studier.

Contents

Introduction	I
1 The theoretical foundations	3
2 Monte Carlo event generators	6
3 Multiparton interactions	11
4 Detecting events	15
5 Models for soft collisions	18
6 Outlook	42
7 Publications	49
8 Acknowledgments	51
I Hard Diffraction with Dynamic Gap Survival	53
1 Introduction	54
2 The model	56
3 Validation	64
4 Comparisons with data	79
5 Summary and outlook	87
6 Acknowledgments	89
II Models of Total, Elastic and Diffractive Cross Sections	95
1 Introduction	96
2 The current status of PYTHIA 8	99
3 Total and elastic cross sections	105
4 Single diffractive cross sections	110
5 Double diffractive cross sections	117
6 Central diffractive cross sections	122
7 Results	124
8 Conclusions	134
9 Acknowledgments	136
III Hard Diffraction in Photoproduction	143
1 Introduction	144
2 Event generation with PYTHIA 8	146
3 The photoproduction framework	148

4	Hard diffraction in PYTHIA 8	153
5	Diffractive dijets in the photoproduction range	157
6	Photoproduction in ultra-peripheral collisions	170
7	Conclusions	174
8	Acknowledgments	176
IV	Dipole evolution: perspectives for collectivity and γ^*A collisions	183
1	Introduction	184
2	Proton substructure evolution	186
3	From substructure to observables	192
4	Monte Carlo implementation	195
5	Results I – comparing cross sections	205
6	Results II – eccentricities in small and large systems	211
7	Results III – dynamic color fluctuations in Glauber calculations	216
8	Conclusion and outlook	221
9	Acknowledgments	223
10	Appendix: The dipole model	224
11	Appendix: The ANGANTYR model for heavy ion collisions	230
12	Appendix: Additional eccentricity figures	233

Introduction

This thesis consists of two parts. The main body, part two, consists of four journal articles, referred to as Papers I–IV. All deal with model-building and phenomena related to quantum chromo-dynamics (QCD), and represent the majority of work I have pursued during my Ph.D. The purpose of the first part, this introduction, is to present the reader with the theoretical background for understanding the articles in part two. The goal is not to teach the reader the actual methods of calculation — for this a textbook is more appropriate — instead I intend to present the concepts and ingredients that go into such calculations, and how these are utilized, extended and understood in Papers I–IV. This introduction is thus an appetizer: it will give a short overview of QCD and introduce why it is common to speak of two regimes (“soft” and “hard”) here. Methods for calculating scattering processes in both regimes are presented, and the classification of soft processes in theoretical and experimental communities is discussed. As the articles are developed within the framework of Monte Carlo event generators, the constituents of such event generators are also presented. If the reader becomes inspired by this introduction, an outlook is given to how the work presented in part two can be improved and continued.

QCD is the theory of colored particles (quarks and gluons, collectively called partons) and their interactions, giving rise to the strong force. When discussing QCD (as well as other theories), often many different scales are used: short and long distance scales as well as small and large momentum transfer scales. Here we recall that these are related through the uncertainty principle, $\Delta x \Delta p \geq \hbar/2$, such that large momentum transfers are equivalent to short distances and vice versa. Large distance scales in QCD correspond to roughly 1 fm (10^{-15} m), where the quarks and gluons are bound (confined) inside color-neutral objects (hadrons) such as protons and neutrons. These large distances are equivalent to processes with momentum transfers of approximately $(\hbar c)/1\text{fm} \sim 0.2$ GeV, with $\hbar c \sim 0.2$ GeV·fm a unit conversion factor. Short distances in QCD, however, means that the individual partons of the hadrons can be probed. This occurs roughly at or below 0.1 fm,

corresponding to momentum transfers in the GeV range. Thus in collisions with large momentum transfers it is possible to consider the quarks and gluons as free particles and from these study e.g. the heavier elementary particles.

The interesting measurable quantities (observables) also depend on the scales of the process considered. Observables related to processes with large momentum transfers are thus based on the partonic degrees of freedom, say an interaction probability (cross section) determined from a partonic scattering process, e.g. where two quarks scatter by the transfer of a single gluon. As the small momentum transfer processes cannot resolve the partonic degrees of freedom, the relevant degrees of freedom are instead the hadronic ones, and observables could then e.g. be the hadronic scattering cross sections. In such processes, however, the strong force is too large to invoke the standard perturbative method of calculating cross sections in QCD (cf. section 1), and thus other approaches or phenomenological models have to be used. The regimes where perturbation theory breaks down are often called nonperturbative or soft regimes, and from the uncertainty principle consist of QCD on both large distance scales and at small momentum transfers. Soft QCD is thus an umbrella-term spanning many different topics including (but not limited to): hadronic scattering processes, hadronization models, low energy processes, QCD at small momentum fractions (x) and so on.

Part two explores the regime of soft QCD. The primary focus of this thesis is diffraction, a subset of the hadronic scattering processes, explored in Papers I–III. In diffractive processes, no color is exchanged between the two colliding beams. This does not imply that *nothing* is exchanged, because often the diffractively excited beam particles are widely different from the incoming ones. Some even show evidence of hard scales by e.g. the formation of heavy elementary particles or highly energetic sprays of particles (jets). The interplay between soft and hard scales in these diffractive processes is unique, and allows us to study the connection between these two regimes in great detail. In this thesis diffraction is studied in both proton-(anti)proton ($pp, p\bar{p}$) collisions, in electron-proton (ep) collisions and in ultra-peripheral proton-ion (pA) collisions. In the latter two collision types diffraction occurs because of the non-zero probability for a photon to fluctuate into a hadronic state.

Paper IV explores QCD at small x , where a perturbative approach can be utilized. The small- x evolution model is used to predict the matter distribution of the hadrons just before a collision, and its implications are studied in ep, pp, pA and ion-ion (AA) collisions. The first steps towards creating fully exclusive final states for electron-ion (eA) collisions are also taken, by studying the color fluctuations of the hadronic cross sections in photon-proton (γ^*p) and the effects of these on photon-ion (γ^*A) collisions.

Throughout this introduction, unless otherwise stated, the focus is on pp collisions. Natural units ($\hbar = c = 1$) are used throughout, such that masses, energies and momenta are expressed in units of giga-electron-volt (GeV), length either expressed in GeV^{-1} or in

femtometer/fermi (fm) and finally cross sections are given in units of area, millibarn (mb) with 1 fm^2 corresponding to 10 mb.

1 The theoretical foundations

Historically, the development in theoretical particle physics has been driven by the need and aim to describe unexplained phenomena observed in experiments. The most convincing theories or models, however, have also been able to make predictions later confirmed by experiment. The theoretical and experimental community thus exhibit a symbiosis, and both play a crucial role in pushing the limits of our knowledge. In theoretical particle physics, two of the most spectacular theories of the last century, quantum mechanics and special relativity, are combined into quantum field theory (QFT). Here, particles are seen as excitations of an underlying field, and the description of how these fields interact is given by mathematical objects called Lagrangians. A Lagrangian describes the difference between the kinetic and potential energy of a (set of) field(s) and can be used to find the equations of motion and other useful quantities. The ingredients of a QFT Lagrangian includes matter content (elementary particles), force carriers (gauge bosons), the strength with which these interact (the coupling), along with the symmetries of the theory, that are related to the conserved quantities.

As of today we have managed to create a QFT describing the interactions between all known particles along with an explanation of the origins of three of the four fundamental forces, gravity excluded.¹ This model is known as the Standard Model (SM) of particle physics, and is given as a sum of the Lagrangians of each of the three included interactions: the QCD Lagrangian and the electroweak (EW) Lagrangian, that combines the weak interactions with the electromagnetic. The quantum numbers of interest in the EW theory are electric charge and weak isospin. In QCD the quantum number is color charge — not to be confused with ordinary colors — of which there are three: red, green and blue. Here, the analogy with ordinary colors become visible, as red, green and blue can be combined to form white, while the quantum numbers red, green and blue can form color-neutral objects (baryons). Similar to the electric charge, we can also combine a color and an anticolor to form color-neutral objects (mesons).

The elementary particles are the half-integer spin fermions and integer spin bosons. The latter include the gauge bosons and the Higgs boson, giving rise to the masses of the elementary particles. The fermions are divided into two groups, quarks and leptons, where the former of the two are the only ones affected by the strong force carried by the gluon. Electrically charged fermions are affected by the electromagnetic force carried by the pho-

¹Gravity is excluded because of the difficulties with including it in a renormalizable QFT: a QFT where divergencies can be absorbed into physical quantities.

ton, while all fermions are affected by the weak force carried by the W^\pm and Z^0 bosons. It is common to group the fermions into three generations based on their masses, each generation containing four particles: a pair of quarks and a pair of leptons.

The electroweak Lagrangian describes the interactions between the gauge and Higgs bosons and the fermions. The QCD Lagrangian is shown in box 1. Contrary to the photon in QED, the QCD Lagrangian allows for self-interactions of the gluon, cf. the last term of eq. (1). One could thus imagine forming a bound state of gluons, similar to the hadrons being bound states of quarks. Some glueball candidates have been proposed, see e.g. [1], but at present it is not possible to claim hard evidence of such states due to mixing between the glueballs and quark states.

Box 1: The QCD Lagrangian

The QCD Lagrangian is given as:

$$\mathcal{L}_{\text{QCD}} = \bar{\psi}_i (i(\gamma^\mu D_\mu)_{ij} - m\delta_{ij})\psi_j - \frac{1}{4} G_{\mu\nu}^a G_a^{\mu\nu}, \quad (1)$$

$$D_\mu = \partial_\mu - i\frac{g\lambda_a}{2}A_\mu^a, \quad (2)$$

$$G_{\mu\nu}^a = \partial_\mu A_\nu^a - \partial_\nu A_\mu^a + g f^{abc} A_\mu^b A_\nu^c, \quad (3)$$

where ψ denotes the quark fields, γ^μ the Dirac gamma matrices, D_μ is the covariant derivative of QCD, λ_a the Gell-Mann matrices, A_μ^a the gluon fields and $G_{\mu\nu}^a$ the gluon field strength tensor. g

is the QCD coupling, related to the strong coupling through $\alpha_S = g^2/4\pi$. Renormalization of the QCD Lagrangian forces the strong coupling to be energy-dependent. It can in principle be calculated to any order in perturbation theory. At first order the strong coupling is,

$$\alpha_S(Q^2) = \frac{4\pi}{\beta_0 \log(Q^2/\Lambda^2)}, \quad (4)$$

with $\beta_0 = 11 - \frac{2}{3}n_f$. Q a momentum scale, n_f the number of active quark flavours present at this momentum scale and Λ a cutoff scale.

Once the SM Lagrangian has been written down, it is time to make predictions with it. Despite the seemingly mathematical simplicity of the SM Lagrangian, this turns out to be almost impossible. This means that approximations often have to be used in order to make predictions. One approximation could be to discretize the continuous space-time variables, which reduces the difficulties in evaluating the integrals that arise in the calculations, a method used in Lattice QCD. Another approximation is to use perturbation theory. In perturbation theory the full solution to a problem is approximated by a power series in some small parameter. In a QFT this small parameter is the coupling of the theory. The precision of the approximation of course increases with the number of orders kept in the series, such that a leading order (LO) prediction is less precise than a next-to-leading order (NLO) prediction and so on. Note, however, that this perturbative approach *only* works if the coupling of the theory is small. If the coupling is small, the higher orders of the perturbative expansion are smaller than the lower orders. If the couplings are of order unity or above, the higher orders are larger than the lower orders, and our perturbative expansion breaks down.

In the theory of leptons and photons, quantum electrodynamics (QED), the coupling of interest is the fine-structure constant, $\alpha = \frac{e^2}{4\pi} \simeq \frac{1}{137}$. The smallness of the fine-structure

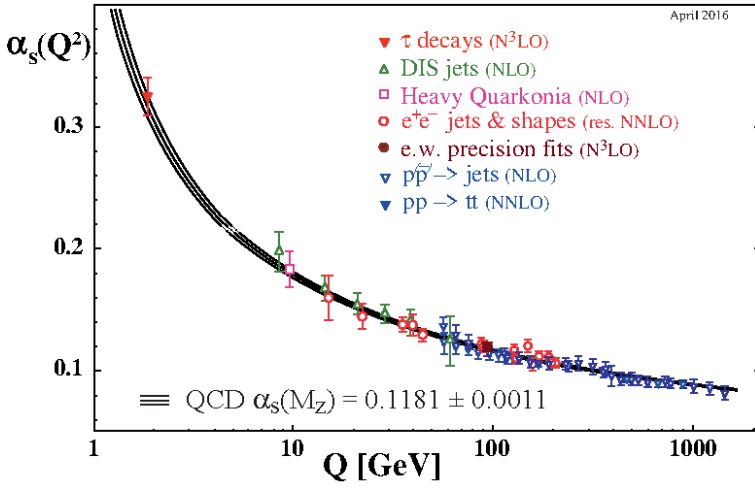


Figure 1: The running of the strong coupling as a function of Q [2]. Data points show the large variety of experiments, that are able to measure the strong coupling constant, with parantheses indicating the perturbative order at which the calculation is performed.

constant thus allows for a perturbative description throughout. For small momentum transfers, the value of the strong coupling, α_s , is of order unity. Thus at a first glance, perturbation theory is not applicable in QCD. But it turns out that renormalization of QCD introduces an energy-dependence to the coupling,² a feature often called a running coupling. In QCD, it turns out that the coupling vanishes asymptotically as the energy scale of the process increases. This form of energy dependence is called asymptotic freedom, and allows for a perturbative description of QCD when the relevant energy scale of the process is high. A comparison between theoretical prediction for α_s and experimental measurements is given in figure 1.

Equation (4) in box 1 show the theoretical prediction for the strong coupling. It is evident that if $Q \gg \Lambda$ the coupling becomes weak and the quarks and gluons can be considered as free particles. Similarly we see that as $Q \rightarrow \Lambda$ the coupling blows up. Thus at low energy scales, $Q \sim \Lambda$, the quarks and gluons are confined inside the aforementioned hadrons. This feature has yet to be proven from what is called first principles, i.e. from the underlying QFT, but as all evidence points towards this (no free quarks and gluons are observed at everyday energies), several models have proposed explanations for confinement. The most convincing models explain confinement by examining the potential of QCD. Where QED

²Renormalization of *any* QFT introduces energy-dependent couplings, but this can be ignored if the coupling of the QFT is small even at low momentum transfers.

predicts a potential falling off at large distances, $V_{\text{QED}}(r) \sim 1/r$, Lattice QCD predicts that the QCD potential has an additional linear term, $V_{\text{QCD}}(r) \sim 1/r + \kappa r$, with κ often called the string tension. At large distances the linear term dominates, and the former can be ignored. The full color field between a color and an anticolor can then be approximated by a one-dimensional string stretched between the two color charges, hence the name for κ . The linear term results in a constant force at large separation, $F = \kappa$, thus pulling the two charges infinitely far apart requires an infinite amount of energy and is simply not achievable. The energy stored between the separating charges will, at some point, be large enough that it is energetically favorable to create a new color-anticolor pair, splitting the original force-field into two. Thus instead of two free charges one obtains two neutral composite objects with the color-anticolor pairs confined, but not in their original configuration. Repeated breaks of the field or string may occur, such that a single string could produce several mesons in this way.

Due to the breakdown of perturbative QCD at low energy scales, phenomenological models are required to describe many aspects of QCD. Some of these models can be calculated analytically, but many require numerical simulations. Because the quantum world is inherently probabilistic, the methods of probability theory are often employed in such numerical simulations. Hence the term “Monte Carlo” is often used in the name of such numerical simulations.

2 Monte Carlo event generators

All results in this thesis have been developed within a Monte Carlo event generator. This is a tool that takes a theory or model and generates a complete event from which observables can be defined and predicted. An event here means a complete simulation of what theorists believe occurred in a single collision. This includes the chain of processes that transform two incoming particles into a (normally) larger set of outgoing particles. Often some observables can be predicted from theory without generating events, e.g. a scattering angle in an elastic pp collision. Others cannot be found without having the entire event available, especially if one wants to compare to actual experimental data where detector resolution effects have to be taken into account. The predictions from Monte Carlo event generators can thus be compared to experimental data, allowing theorists to revisit their models to make improvements. As most nonperturbative and phenomenological models contain parameters that one cannot predict the value of, the experimental data is also used to tune the Monte Carlo event generators, a process where the value of a given parameter is chosen such that there is best agreement between simulation and data.

In this section, the main components of a general purpose event generator will be described: the hard scattering process and the extraction of the partons from the beams, the showering

process and the hadronization process. The treatment of additional scatterings between the incoming beams, the multiparton interactions (MPIs), are postponed to section 3. Many other components go into the generation of a full event, e.g. the treatment of beam remnants, decays of unstable particles and so on, but as these parts are not crucial for this thesis, they will not be described here.

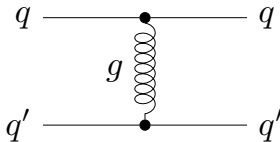


Figure 2: The LO diagram for $qq' \rightarrow qq'$.

In the regime where the colored particles can be considered free, we can employ the standard methods of calculating differential cross sections. To exemplify this we consider a simple hard scattering process: two quarks exchanging a gluon, $qq' \rightarrow qq'$, where $q \neq q'$ for simplicity, see figure 2. This is the QCD analogue of the QED process of two leptons exchanging a photon, e.g. $e\mu \rightarrow e\mu$. The two processes actually only differ by couplings and by prefactors of order unity. The process is described by a leading order partonic differential cross section,

$$\frac{d\sigma(qq' \rightarrow qq')}{d\hat{t}} = \frac{4\pi\alpha_s^2(Q^2)}{9\hat{s}^2} \frac{\hat{s}^2 + \hat{u}^2}{\hat{t}^2}, \quad (5)$$

where we have introduced the Mandelstam variables.³ Had we been studying the QED process $e\mu \rightarrow e\mu$, this differential cross section would have been the final story. But as we have just learned, quarks are confined within hadrons. Assuming both quarks have been extracted from protons, we have to be able to describe the probability of extracting such quarks from the proton. This probability is called a parton distribution function (PDF), cf. box 2.

Convolution of the partonic cross section with the PDFs of the protons gets us some way towards the actual measurable quantity. Having assigned a fractional momentum to each of the incoming quarks, we arrive at the cross section differential in Mandelstam variable \hat{t} and energy fractions x_1, x_2 ,

$$\frac{d^3\sigma(pp \rightarrow qq')}{dx_1 dx_2 d\hat{t}} = f_q(x_1, Q^2) f_{q'}(x_2, Q^2) \frac{d\sigma(qq' \rightarrow qq')}{d\hat{t}}. \quad (6)$$

The energy of the outgoing partons from the hard scattering is still large enough that they can be considered free particles. But such highly energetic particles have the tendency to

³The Mandelstam variables are defined from the momenta of the particles in a scattering process, $a(p_1) + b(p_2) \rightarrow c(p_3) + d(p_4)$, such that $\hat{s} = (p_1 + p_2)^2 = (p_3 + p_4)^2$, $\hat{t} = (p_3 - p_1)^2 = (p_4 - p_2)^2$ and $\hat{u} = (p_4 - p_1)^2 = (p_3 - p_2)^2$.

radiate off some of their energy, similar to an electron radiating photons when accelerated. This subsequent radiation is called a parton shower (box 3) and creates a spray of particles in the direction of the outgoing partons (partonic jets). At some point during this evolution the particles can no longer be resolved perturbatively and the showering process thus cannot be traced any further.

Box 2: Parton distribution functions

PDFs describe the composition of partons inside a hadron at a probing scale or virtuality, Q^2 , and for a fraction of hadron momentum carried by the partons, x . A large virtuality allows for smaller regions of the hadron to be probed, thus finer details are resolved. Given a distribution $f(x, Q^2)$ at a scale Q_0^2 the DGLAP evolution equations [3–6] evolve this distribution to a different Q^2 scale.

$$\frac{df_b(x, Q^2)}{d \log(Q^2)} = \frac{\alpha_S(Q^2)}{2\pi} \sum_a \int_x^1 \frac{dz}{z} f_a(y, Q^2) P_{a \rightarrow bc} \left(z = \frac{x}{y}, Q^2 \right), \quad (7)$$

with $P_{a \rightarrow bc}$ the splitting kernels, given as

$$P_{q \rightarrow qg}(z, Q^2) = \frac{4}{3} \frac{1+z^2}{1-z}, \quad (8)$$

$$P_{g \rightarrow gg}(z, Q^2) = 3 \frac{(1-z)(1-z)^2}{z(1-z)}, \quad (9)$$

$$P_{g \rightarrow q\bar{q}}(z, Q^2) = \frac{n_f}{2} (z^2 + (1-z)^2), \quad (10)$$

with n_f the number of quark flavours. The initial state of the PDFs at low scale Q_0 is not described, however, so one has to parametrize this in some way. No predictions of the initial state can be made from first principles, but a simple approximation could be of the form $(1-x)^a x^{-b}$. This function vanishes at $x \rightarrow 1$, the limit where the entire momentum of the hadron is carried by a single parton. The parameters a, b are phenomenological model parameters and have to be fitted to data.

Some parts of the initial state are known. If the probing scale Q^2 is small, we are primarily

probing the valence content of the hadron. Increasing the probing scale makes the virtual fluctuations visible, such that gluon emissions and virtual quark-antiquark pairs can be seen. These virtual particles are called the sea-constituents of the hadron. In a perfect world a PDF for every single hadron would be defined. In reality often the same PDF is employed for several different hadrons provided their valence content is equivalent. This is because the construction of the PDFs requires a great amount of data as there are a lot of free parameters that need to be tuned. Even for particles that are considered elementary, PDFs may often be constructed. This is the case for the photon, as it has a non-zero probability to fluctuate into a quark-antiquark pair. If we were to collide a particle with the photon in exactly this moment, the particle probing the photon would instead see a mesonic state. Thus we can describe the photon as a meson under certain circumstances, with significant consequences for the scattering processes available.

Complementary to the evolution in virtuality, an evolution in x can be performed. This is known as the BFKL evolution [7, 8] and corresponds to filling up the hadrons with partons of smaller and smaller energy fractions. At some point we expect to obtain so many partons, that they will overlap. This creates a probability of recombining, such that two partons merge to form one. This region of recombination is called the saturation region, and is not included in the DGLAP evolution. Paper IV introduces the BFKL evolution in a Monte Carlo and discusses some of the aspects related to saturation in such an evolution.

This is not the end of the story. As many other processes give rise to two jets — and as it is extremely hard to distinguish between jets of different content — one has to include *all* partonic processes that give rise to two jets in the final state, before comparisons to data can be carried out. But we also have to combine the partons in the event to measurable hadrons, the aforementioned hadronization process. Several hadronization models exist but two are widely used: the Lund string model [9] and the cluster model [10].

Box 3: Parton showers

The radiation off colored partons can be described with a parton shower. The parton shower is exact in the collinear limit, where the splitting angle is very small, but can be used as an approximation of the complete answer in the entire phase space. The probability for a $q\bar{q}$ pair to emit an additional gluon can be calculated by studying the ratio of matrix elements $d\sigma(e^+e^- \rightarrow q\bar{q}g)/d\sigma(e^+e^- \rightarrow q\bar{q})$. In the collinear limit, the probability reduces to the aforementioned splitting kernels also used in the PDFs. The splitting probability is,

$$\frac{dP_{a \rightarrow bc}}{dz} = \frac{\alpha_S(Q^2)}{2\pi} \frac{dQ^2}{Q^2} P_{a \rightarrow bc}(z, Q^2), \quad (11)$$

with $P_{a \rightarrow bc}$ given by eqs. (8–10).

The choice of evolution variable Q is not unique, some use p_\perp , others (energy-weighted) angles. The probability is applied to all colored partons in the event until some minimal stopping scale is reached, usually around $Q \sim 1$ GeV. If $Q^2 > 0$ the shower is time-like and describes final state radiation, while $Q^2 < 0$ gives a space-like shower

and describes initial state radiation. In the latter case, the relation to PDFs become evident, as the initial state shower evolves the partons to larger Q^2 .

The parton shower is developed in the $N_C = \infty$ limit, with N_C the number of colors, where the expressions simplify a lot. In order to mimic a full-color ($N_c = 3$) parton shower, a dynamical color evolution (color reconnections) is often applied after the showering process. This shuffles the color structure of the event, required to get better agreement between data and predictions from event generators. Color reconnections can also arise in other ways, for instance in W -pair production when both W 's decay to quark pairs. Here, the decay products form color singlets, and one would naïvely not expect any connection between the two decay products. This, however, is not what is observed in experiments: at LEP the best overall description of data was found with models introducing moderate color reconnections in roughly half of the events [11].

The Lund string model is based on imagining the color-electric field as a string stretched between a color and an anticolor, cf. section 1, with κ assumed constant. This gives rise to a linear potential and the breaking of the string can occur when the potential energy in the string is sufficiently high to create a new quark-antiquark pair. The string between an initial quark-antiquark pair can fragment into several new pairs, and these are then combined into hadrons systematically, such that a quark and an antiquark from adjacent breaks are combined to form a hadron. Gluons are in this model treated as kinks on the string stretched between the quark-antiquark pair. As antiquarks can be approximated by a diquark system (anti-red can be formed by a green-blue diquark system) and vice versa, both baryons and antibaryons can be created in the string breaking as well. As the strings have transverse size different from zero, it is likely that overlapping strings will modify the hadronization model. A model introducing such modifications, the string shoving model [12], has recently been developed, enhancing the string tension in dense regions.

In the cluster model all gluons are forced to split into a quark-antiquark pair before each of these pairs are combined to form color singlet objects called clusters. The clusters have masses according to the momenta of its constituents, and high-mass clusters are allowed to decay into lighter clusters. These clusters are then allowed to decay into two hadrons with a probability based on the spin and mass of the hadrons and the mass of the cluster itself.

Although much progress has been made in recent years, we are still far from understanding all aspects of particle collisions. So far, the focus here has been on leading order calculations. Much progress has been made to go beyond this by e.g. introducing NLO matrix elements

in the hard scattering. At NLO two types of diagrams are added to figure 2: additional radiation off the incoming and outgoing partons and loop diagrams, where virtual gluons or quark-antiquark pairs are emitted and absorbed. Both give rise to new propagators, thus further complicating the phase-space integration. In recent years several dedicated event generators have become available that not only calculate (almost all) processes to LO, but also to higher orders in QCD and some even include EW corrections as well. This is an astonishing accomplishment that allows for extremely precise predictions, showing to a large extent better agreement with data than the LO predictions.

Increased precision has also been achieved through matching and merging techniques. The processes of interest are often multi-jet events, where the goal is to improve the description of well separated n jet states through n -parton matrix elements calculations. Multi-jet merging introduces a scale μ above which the n -parton matrix element is used, and below which the parton shower is employed. The matching techniques make sure that the lowest multiplicity states include fixed-order corrections, often taking all NLO corrections into account. The parton shower is then used to handle additional soft radiation off such matrix elements. Both matching and merging techniques require information of higher order corrections to a given process at a desired accuracy, often included through the dedicated matrix element generators. Further improvements to the event generation could be introduced by e.g. developing a full NLO parton shower, or taking the full color structure of the parton shower into account.

To summarize, the following steps have been taken in order to arrive at a measurable quantity:

- The hard process of interest has been identified and calculated to some perturbative order.
- The incoming partons have been extracted from the colliding hadrons using PDFs.
- Subsequent radiation off the incoming and outgoing partons have been dealt with in the parton shower (with or without matching and merging schemes).
- The partons have been hadronized to form measurable particles.

Again we note that these are not *all* the steps included in an event generator. Beam remnants and decays of unstable particles also have to be treated. Specialized effects, such as Bose-Einstein correlations and hadronic scatterings in the final state, can also be included. One component neglected in the list above, the MPIs, is crucial for this thesis and is presented in section 3.

In order to compare predictions from Monte Carlo event generators and data from experiments, both sides of the community have to agree on what is actually measured. This includes agreeing on particle definitions (how do we define a lepton in a detector? Should it include any additional radiation in a small cone close by?), agreeing on what cuts have

been used in the experimental analysis (is it really possible to measure a particle p_{\perp} down to zero, or is there a minimal threshold because of detector noise?), and also — very importantly — agreeing if detector effects should be mimicked in the event generator, or subtracted from data. During my Ph.D. I have been active in the development of the Rivet framework [13]. This is a toolkit for validating (and tuning) Monte Carlo event generators against experimental data analyses, many of which are provided by the experiments themselves. It addresses all of the questions above and provides a diverse set of functions and particle definitions, such that the definitions on the event generator-side agree best with the experimental definitions. I have primarily developed tools and functions for studies of diffraction as well as included some diffractive analyses to the Rivet framework. But I have also contributed to the upgrade of Rivet in order to facilitate heavy ion analyses [14]. These analyses often have a very different definition of observables and require several other tools, such as cumulant calculators for flow-variables. Both upgrades are available from the Rivet homepage [15]. Most figures presented in the forthcoming papers are produced with Rivet, as this provides a fast and efficient way of comparing results from Monte Carlo to data.

3 Multiparton interactions

An essential part of this thesis uses the concept of MPIs. MPIs are based on the idea that several partonic collisions can occur in the same hadron-hadron scattering, but that the majority of these collisions are of the soft QCD type, just barely described by perturbation theory. The idea begins with the view of two Lorentz-contracted hadrons — pancakes — colliding. The reasoning is now that several subcollisions between the partons inside these pancakes can happen essentially simultaneously. The number of subcollisions depend on the overlap, or impact parameter b , of these two pancakes, albeit not being fixed by the impact parameter, as random fluctuations occur even for fixed b .

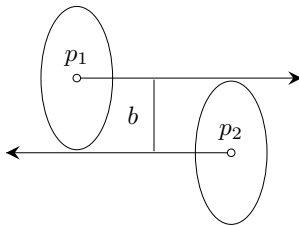


Figure 3: The impact parameter b of the collision between two contracted protons p_1, p_2 . The open circles represent the center of the two protons, while the arrows indicate their motion.

MPIs were originally introduced to explain the discrepancies between the successful Lund string hadronization model and data from $p\bar{p}$ collisions [16]. It was observed that the implementation of the initial- and final-state showers on top of a partonic $2 \rightarrow 2$ matrix element improved the jet observables, but not the description of the underlying event, i.e.

the additional hadronic activity outside of the jets. This led to the development of the MPI framework, such that not only one partonic scattering can occur, but several. The idea is an extension of the concept of double parton scattering (DPS) that theoreticians had explored earlier, although not restricted to only contain two scatterings. It is also inspired by pictures of multi-Pomeron exchanges in pp collisions, where the Pomeron will be explained in detail in a forthcoming section.

As the basic concepts of MPIs were developed within the Lund group and implemented into the early versions of PYTHIA (current version being 8.2 [17]), we will here focus on this description of MPIs. Other descriptions are available, e.g. the BFKL-inspired DIPSY model [18] and the eikonal model developed in HERWIG++ (see [19] and references therein). Many of these are equally successful in describing data as the MPI model described below.

The Lund MPI model [20, 21] begins with the differential perturbative QCD $2 \rightarrow 2$ scattering cross section,

$$\frac{d\sigma}{dp_{\perp}^2} = \sum_{i,j,k} \int \int \int f_i(x_i, Q^2) f_j(x_j, Q^2) \frac{d\hat{\sigma}_{ij}^k}{d\hat{t}} \delta\left(p_{\perp}^2 - \frac{\hat{t}\hat{u}}{\hat{s}}\right) dx_i dx_j d\hat{t}, \quad (12)$$

where $Q^2 = p_{\perp}^2$, and the differential cross section $\frac{d\hat{\sigma}_{ij}^k}{dp_{\perp}^2}$ is exactly the cross section giving rise to two jets as explained in section 2. When integrated this gives the interaction cross section,

$$\sigma_{\text{int}}(p_{\perp\text{min}}) = \int_{p_{\perp\text{min}}^2}^{s/4} \frac{d\sigma}{dp_{\perp}^2} dp_{\perp}^2. \quad (13)$$

Here, the integration is performed with a sharp cutoff, $p_{\perp\text{min}}$, below which the partonic cross section is not evaluated. If we let $p_{\perp\text{min}} \rightarrow 0$, at some point the interaction cross section will exceed the total cross section. The novel idea here is that the fact that the interaction cross section exceeds the total cross section for small $p_{\perp\text{min}}$ -values means that we have *more* than one such interaction per event, i.e. that we have multiple partonic interactions. Assuming that we only get jets from “regular” events (formally the inelastic nondiffractive events, where the particles are evenly distributed in the detector), a single hadron-hadron scattering is expected to give an average number of hard interactions above $p_{\perp\text{min}}$ as,

$$\langle n_{\text{MPI}}(p_{\perp\text{min}}) \rangle = \frac{\sigma_{\text{int}}(p_{\perp\text{min}})}{\sigma_{\text{ND}}}, \quad (14)$$

with σ_{ND} being the total inelastic nondiffractive cross section. The hard scattering of interest is then actually considered the “first” or hardest MPI.

From the $qq' \rightarrow qq'$ example in section 2 we know that the $2 \rightarrow 2$ QCD cross section diverges for $p_{\perp \min} \rightarrow 0$,

$$\frac{d\hat{\sigma}}{d\hat{t}} = \frac{4\pi\alpha_s^2(Q^2)}{9\hat{s}^2} \frac{\hat{s}^2 + \hat{u}^2}{\hat{t}^2} \underset{\hat{t} \rightarrow 0}{\sim} \frac{\alpha_s^2(Q^2)}{\hat{t}^2} \sim \frac{\alpha_s^2(p_{\perp}^2)}{p_{\perp}^4}, \quad (15)$$

where for $\hat{t} \rightarrow 0$ we have $\hat{t} \sim p_{\perp}^2$. Here, however, we have assumed that the partons are asymptotically free states, which we know is not correct. The partons have to be confined within a hadron, and thus the above relation cannot be the entire story. Naively we would expect a breakdown at around the hadron radius, giving a minimal p_{\perp} of the order $p_{\perp \min} \sim 1/r_h$. But, as we do not fully understand low- p_{\perp} physics, and we do not know what the actual form of the physical (measurable) cross section looks like for $p_{\perp} \rightarrow 0$, we instead introduce a screening parameter, $p_{\perp 0} \sim 1/d$ with d a color screening length scale, to avoid the divergency. In the Lund model the partonic cross section is thus dampened at small p_{\perp} with a factor of

$$\left(\frac{\alpha_s(p_{\perp 0}^2 + p_{\perp}^2)}{\alpha_s(p_{\perp}^2)} \frac{p_{\perp}^2}{p_{\perp 0}^2 + p_{\perp}^2} \right)^2, \quad (16)$$

which then modifies the cross section as,

$$\frac{d\hat{\sigma}}{dp_{\perp}^2} \rightarrow \frac{\alpha_s^2(p_{\perp 0}^2 + p_{\perp}^2)}{(p_{\perp 0}^2 + p_{\perp}^2)^2}, \quad (17)$$

which instead of diverging is finite. In the case where the dampening factor is introduced, the interactions can occur all the way to $p_{\perp} = 0$ GeV, but the characteristic scale for such low- p_{\perp} partons would be around $p_{\perp 0}$.

Although the MPIs are expected to occur simultaneously, it is convenient to order them in a sequence of decreasing p_{\perp} values, such that $p_{\perp 1} > p_{\perp 2} > p_{\perp 3} \dots$. Each of the successive MPIs with p_{\perp} 's less than the hardest scattering, can then be generated in a downwards evolution in p_{\perp} similar to the parton shower,

$$\frac{dP}{dp_{\perp i}} = \frac{1}{\sigma_{\text{ND}}} \frac{d\sigma}{dp_{\perp i}} \exp \left(- \int_{p_{\perp i}}^{p_{\perp i-1}} \frac{1}{\sigma_{\text{ND}}} \frac{d\sigma}{dp'_{\perp i}} dp'_{\perp i} \right), \quad (18)$$

where the exponential is the Sudakov (cf. box 4) factor giving the no-interaction probability between $p_{\perp i-1}$ and $p_{\perp i}$. As the PDFs of the incoming hadrons appear in the differential cross section, special care has to be taken. This is because of the fact that, say, a valence quark removed in a “previous” MPI cannot be used as an incoming parton in a “later” MPI.⁴ Similarly, an MPI initiated by a sea quark gives rise to the appearance of the companion sea

⁴The times here are in quotation marks, as they refer to the evolution variable and not proper time.

antiquark in the PDF of the hadron, as these always come in pairs. Energy and momentum also has to be conserved in the evolution, and thus a sophisticated scaling and normalization scheme for the PDFs is implemented in the MPI evolution. These are issues not considered in a standard PDF parametrization, which only address the hardest scattering.

Box 4: The Sudakov method

The Sudakov method is widely used in Monte Carlo event generators whenever some form of evolution is considered. It can be derived from general consideration of decays or emissions: at a given time t in the evolution, either the particle has decayed or not. Conservation of probability thus requires the no-decay probability, P_{nd} , to be given as

$$P_{nd} = 1 - P_d, \quad (19)$$

with P_d the decay or emission probability. Dividing the time scale considered ($0 < t < T$) into two, ($0 < t < T_1$) and ($T_1 < t < T$), gives a new no-decay probability,

$$P_{nd}(0, T) = P_{nd}(0, T_1) P_{nd}(T_1, T). \quad (20)$$

Dividing the scale t into n equal-sized steps between 0 and T thus gives

$$\begin{aligned} P_{nd}(0, T) &= \lim_{n \rightarrow \infty} \prod_{i=0}^{n-1} P_{nd}(T_i, T_{i+1}) \\ &= \lim_{n \rightarrow \infty} \prod_{i=0}^{n-1} (1 - P_d(T_i, T_{i+1})) \\ &= \exp\left(-\int_0^T \frac{dP_d}{dt} dt\right) \\ &\equiv \Delta(0, T). \end{aligned} \quad (21)$$

The probability for having the first emission at scale T is then the product of the emission probability at that scale and the Sudakov:

$$P(T) = P_d(T) \Delta(0, T). \quad (22)$$

If each MPI occurs independently, the probability of having at least one such MPI is given by Poissonian statistics as,

$$P_{\text{int}} \equiv P_{n \geq 1} = 1 - P_0 = 1 - \exp(-\langle n_{\text{MPI}} \rangle). \quad (23)$$

It is easily imagined that a head-on collision of the two hadrons gives rise to more activity, i.e. more MPIs, than a peripheral collision. This means the interaction probability should depend on the impact parameter b of the collision. An impact parameter of zero would imply a head-on collision, while a larger impact parameter implies a more peripheral collision. Assuming a relation between the average number of MPIs and the overlap function $f(b)$ of the two (assumed) spherically symmetric hadrons, given as $\langle n_{\text{MPI}} \rangle = k f(b)$, the interaction probability thus becomes dependent on b ,

$$P_{\text{int}}(b) = 1 - \exp(-k f(b)), \quad (24)$$

The overlap function itself can be found using the matter distributions $\rho(\vec{x})$ of the colliding hadrons,

$$f(b) \propto \int \int d^3\vec{x} dt \rho(x, y, z) \rho(x, y, z - \sqrt{b^2 + t^2}), \quad (25)$$

or it can be set directly without an underlying assumption of the matter distributions. The evolution equation thus becomes dependent on the impact parameter through

$$\frac{dP}{d^2b \, dp_{\perp i}} = \frac{f(b)}{\langle f(b) \rangle} \frac{1}{\sigma_{\text{ND}}} \frac{d\sigma}{dp_{\perp i}} \exp \left(-\frac{f(b)}{\langle f(b) \rangle} \int_{p_{\perp i}}^{p_{\perp i}-1} \frac{1}{\sigma_{\text{ND}}} \frac{d\sigma}{dp'_{\perp i}} dp'_{\perp i} \right), \quad (26)$$

where $\langle f(b) \rangle = \int f(b) d^2b / \int P_{\text{int}} d^2b$. The factor of $f(b)/\langle f(b) \rangle$ gives rise to an enhancement at small impact parameter and a depletion at large.

Several choices for the matter distributions appearing in the overlap functions can be made in the Lund model, but same for all is that the incoming hadrons are considered spherically symmetric. Denser regions of the protons can be introduced, e.g. by choosing a double Gaussian matter distribution, mimicking hot-spots around the valence quarks of the proton. The option to choose an x -dependent distribution also exists, but in general asymmetries and fluctuations in the initial state are not considered. This thesis introduces a method to create some initial-state fluctuations in Paper IV. The new model is utilized in the MPI framework only though assigning spatial vertices to the MPIs, thus does not affect any other parts of the MPI framework presently. The new model could, however, be used as input for the MPI framework: it predicts the size of the nondiffractive cross section as well as the sizes of the colliding protons. The former could then replace σ_{ND} in eq. (26), while the latter could be connected to $p_{\perp 0}$.

4 Detecting events

As the strong coupling is much larger than the electroweak one, we expect that the majority of partonic scatterings in high-energy pp collisions involve colored particles. The simplest possible collisions in QCD are exactly the $2 \rightarrow 2$ collisions that we considered in section 2, thus we expect these to be the dominant processes. Combining eq. (6) and the relation in eq. (15) we find

$$\frac{d^3\sigma(pp \rightarrow qq')}{dx_1 dx_2 dp_{\perp}^2} \sim f_q(x_1, p_{\perp}^2) f_{q'}(x_2, p_{\perp}^2) \frac{\alpha_s^2(p_{\perp})}{p_{\perp}^4}. \quad (27)$$

The PDFs are peaked at small x , while the hard scattering is peaked at low p_{\perp} . Hence it is evident that the majority of scatterings in high-energy pp collisions occur at low x and with low p_{\perp} — in the soft QCD regime!

In the longitudinal rest frame of the $qq' \rightarrow qq'$ collision, the quarks are created back-to-back at a given scattering angle. If we neglect parton showers, the gluon exchange between the two quarks causes two color strings to be stretched between either of the quarks back to the opposite beam remnant, cf. figure 4 (a). The fragmentation or breaking of a single

string will cause hadrons to be produced more or less evenly along this string, hence we expect the number of particles per string per unit rapidity⁵ to be roughly constant, giving rise to a rapidity plateau: a roughly flat distribution of particles per unit rapidity, cf. the red lines in figure 4 (b). The total number of particles per unit rapidity is then the sum of particles produced by both strings in the $qq' \rightarrow qq'$ scattering.

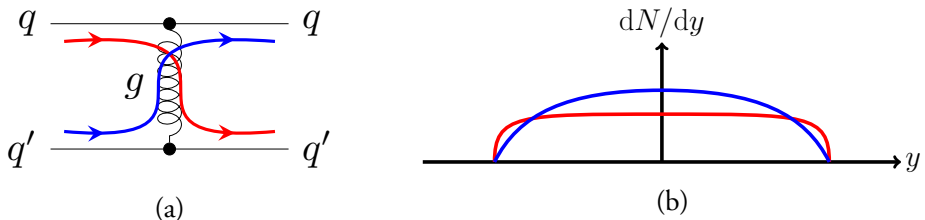


Figure 4: (a) The color flow in a $qq' \rightarrow qq'$ process. (b) A schematic view of the particle production as a function of rapidity produced by two strings (red lines) compared to a full event containing MPIs (blue lines).

The full event includes showers and MPIs as well. MPIs tend to favour the central region, thus additional MPIs will increase the plateau slightly towards central rapidity, cf. the blue distribution in figure 4 (b). The parton shower creates a spray of particles in the direction of each of the outgoing partons. For the MPIs, this does not affect the particle density per unit rapidity much, as these events usually have low p_\perp , leaving less room for particle production. Where the parton shower does have an effect, however, is if the hardest scattering has a relatively high p_\perp . Here, jets are formed in the direction of the high- p_\perp quarks (in our $qq' \rightarrow qq'$ example), and we will see two spikes in the dN/dy -distribution where the jets are located. Thus, while low- p_\perp physics dominate, an event with a hard scattering contains the signal (here the jets) along with an underlying event, the rapidity plateau formed by the MPIs.

Other processes give rise to different event topologies. Imagine for instance Higgs production by $W^+ W^-$ fusion [22]. As the W -bosons are color-neutral particles, no color is exchanged between the beams, so naïvely no particles should be produced centrally except for the Higgs decay products. This means that this process should have two rapidity gaps on either side of the decay products, i.e. parts of phase space void of any particle production. But because of the additional MPIs between the protons, these gaps will be filled with particles. Due to the probabilistic nature of the MPIs, a fraction of the events should contain no MPIs besides the hard scattering. This introduces the concept of a rapidity gap survival factor, a subject largely explored in this thesis. We will return to this later.

Rapidity gaps are also expected in other systems. Many soft processes gives rise to such gaps, most strikingly is of course elastic scattering, where only the two elastically scattered

⁵Rapidity is defined as $y = \frac{1}{2} \log((E + p_z)/(E - p_z))$. It can be related to the pseudorapidity $\eta = -\log(\tan \theta/2)$ where θ is the scattering angle w.r.t. the beam, as $\eta = y$ for massless particles and, approximately, for massive ones provided $p_\perp > m$.

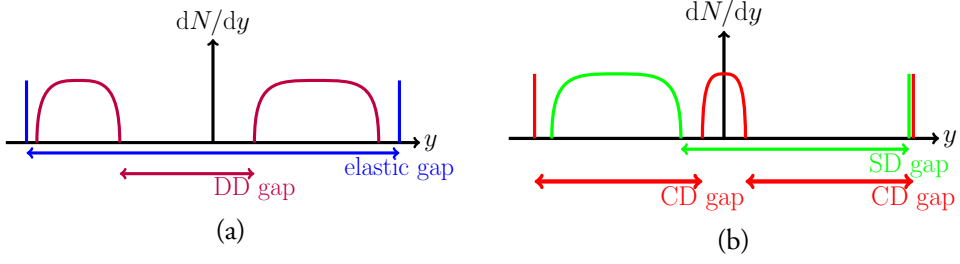


Figure 5: A schematic view of elastic (blue lines) and diffractive processes: single diffraction (SD, green lines), double diffraction (DD, purple lines) and central diffraction (CD, red lines). The picture shows how the particles are distributed in rapidity y , and the rapidity gaps present.

protons are detectable, with a single rapidity gap in between. Another type of soft processes, the diffractive processes, are also expected to contain rapidity gaps, visualized in figs. 5(a,b) along with the familiar elastic scattering process. The definitions of the soft processes used in this thesis are given in box 5.

Box 5: Types of soft collisions

The types of soft collisions used in this thesis have the following definitions. Examples are given for pp collisions.

- Elastic collisions (el), where the incoming and outgoing particles are of the same type.
 $p + p \rightarrow p + p$
- Single diffractive collisions (SD), where one of the outgoing particles have been diffractively excited.
 $p + p \rightarrow p + X$
- Double diffractive collisions (DD), where both of the outgoing particles have been diffractively excited.
 $p + p \rightarrow X + Y$

- Central diffractive collisions (CD), where the final state includes the two incoming particles and a diffractively excited system.

$$p + p \rightarrow p + X + p$$

- Nondiffractive collisions (ND), which is usually "the remainder" ($\sigma_{ND} = \sigma_{tot} - \sigma_{el} - 2\sigma_{SD} - \sigma_{DD} - \sigma_{CD}$) and contains both hard and soft collisions.

$$p + p \rightarrow X$$

The "+" in the final state indicates a rapidity gap, and "diffractively excited" here equates systems with the same quantum numbers as the proton, with a smooth transition between excited proton states and systems of higher mass.

The distinction between these soft processes, however, is marred by large uncertainties. Theoretically, diffraction and elastic scattering can be defined by the exchange(s) of a color-neutral object(s), collectively called Reggeons. The aforementioned Pomeron is one of these Reggeons, and the one dominating at high energies. Such exchanges of color-neutral Pomerons are depicted in figure 6, thus diagrammatically showing the definitions of box 5. Experimentally, these processes are defined by the detection of the rapidity gap produced by the color-neutral exchange, and/or by the detection of elastically scattered proton(s). But, as the size of the diffractive system depends on its mass, one could imagine that very large systems are very wide in rapidity. This means that the rapidity gaps, parts of the diffractive systems and the surviving proton(s) often escape detection due to the finite extent of the

experimental detectors. This introduces a possibility for mis-identification of the diffractive events.

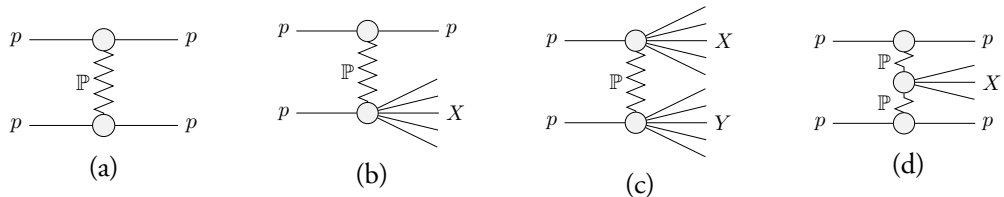


Figure 6: The elastic (a) and single (b), double (c) and central (d) diffractive processes in pp collisions. Here p is a proton and \mathbb{P} a Pomeron, the “particle” responsible for the momentum transfer. X, Y are diffractive systems.

Diffractive systems are also expected to have some MPI activity. One could here imagine two different scenarios for MPIs: between the elastically scattered proton and the diffractive system, and within the diffractive system itself. The former would likely destroy the rapidity gap, similar to the Higgs example, and thus this type of MPIs would kill the experimental classification of diffraction. The model for hard diffraction developed in Paper I exploits the probabilistic nature of the MPIs. A no-MPI requirement is enforced between the elastically scattered proton and the diffractive system, such that an event is *only* classified as diffractive if no MPIs occurred. This reduces the number of diffractive events, and effectively introduces a gap survival factor. Unlike other methods of gap survival, where an overall suppression factor is more commonly used (see e.g. the approaches used in [23–26]), the method presented in Paper I is performed on an event-by-event basis, thus a is dynamical effect.

The MPIs formed within the diffractive system contain no restrictions, but are unfortunately marred with open questions, such as

- what cross section should be used in place of the inelastic nondiffractive cross section in eq. (26)?
- What should be the overlap function — or the matter distribution — of the Pomeron?
- What should one use in place of the hadronic PDFs in the evolution?

Before these questions can be answered, we first have to delve deeper into what a diffractive system is and how we can model these phenomenologically. Thus the answers to these questions are postponed to section 5.6.

5 Models for soft collisions

The aim of this section is to be able to describe (differential) cross sections for the soft processes given in box 5. In general there are two approaches to calculate cross sections

for soft QCD processes: geometrical models and diagrammatical models. These are also called s - and t -channel approaches respectively, where s, t are the Mandelstam variables.⁶ Geometrical models emphasize the impact-parameter aspects, and often relate diffraction to peripheral collisions. The diagrammatical methods usually build a Feynman diagram-like recipe (similar to the diagrams in figure 6) for calculating the cross sections, and from these increase complexity e.g. by adding new components.

5.1 The S-matrix approach

Both the s - and t -channel approaches arise from general considerations of the scattering matrix (S-matrix), the operator that takes an initial state and transforms it into a final state. In the S-matrix approach, the analytical properties of the scattering matrix is evaluated instead of calculating matrix elements from Feynman diagrams as in the QFT approach. With a small set of assumptions, a large variety of properties can be deduced from the S-matrix. The following properties of the S-matrix are usually assumed:

- it is relativistically invariant,
- linearity,
- unitarity,
- analyticity,
- crossing.

The first property states that it must only depend on Lorentz-invariant combinations of the kinematical variables and the second arises from the superposition principle. Conservation of probabilities requires unitarity, while analyticity means that the S-matrix elements are analytical functions of the kinematical variables (specifically the Mandelstam variables s, t, u). The idea of crossing relates certain specific cross sections to each other, and arise from the fact that an incoming particle can be viewed as an outgoing antiparticle with negative momentum. Thus the cross section of two different processes can be described by the same analytic function, but in different regions of phase space. From these basic assumptions, of which a few of them will be described further below, a wide variety of information can be extracted from the S-matrix.

The S-matrix is the linear operator that takes an initial state $|i\rangle$, into a final state $|f\rangle$,

$$S |i\rangle = |f\rangle . \quad (28)$$

From this we can define a probability for the measuring the state $|i\rangle$ before the scattering and the state $|f\rangle$ after,

$$P_{fi} = |\langle f | S | i \rangle|^2 = \langle i | S^\dagger | f \rangle \langle f | S | i \rangle , \quad (29)$$

⁶Note that from now on we will drop the *hat* on the Mandelstam variables.

where $\langle f | S | i \rangle$ are the matrix elements of S . Conservation of probability implies a sum over all possible final states,

$$1 = \sum_f P_f = \sum_f \langle i | S^\dagger | f \rangle \langle f | S | i \rangle = \langle i | S^\dagger S | i \rangle = \langle i | i \rangle, \quad (30)$$

for any $| i \rangle$. Thus we have required that the S-matrix is a unitary matrix, $1 = S^\dagger S = S S^\dagger$.

We can now introduce the transition matrix T and the scattering amplitude A as

$$S = 1 + i T = 1 + i (2\pi)^4 \delta^4(p_i - p_f) A, \quad (31)$$

allowing us to rewrite all of the above in terms of actual transitions or scatterings $| i \rangle \rightarrow | f \rangle$ described by T or A , not including the process where nothing happens, $| i \rangle \rightarrow | i \rangle$ described by unity. Thus we can write the unitarity relation of the S-matrix in terms of the transition matrix,

$$i(T^\dagger - T) = T^\dagger T. \quad (32)$$

The matrix element of the left-hand side is

$$i \langle f | (T^\dagger - T) | i \rangle = 2\text{Im}[T_{fi}], \quad (33)$$

while inserting a complete set of intermediate states $| n \rangle$ on the right-hand side gives

$$\langle f | T^\dagger T | i \rangle = \sum_{\{n\}} \langle f | T^\dagger | n \rangle \langle n | T | i \rangle = \sum_{\{n\}} T_{fn}^* T_{ni}. \quad (34)$$

Combining the two we obtain the unitarity equations in terms of T or A , also visualized in figure 7:

$$2\text{Im}[T_{fi}] = \sum_{\{n\}} T_{fn}^* T_{in}, \quad (35)$$

$$2\text{Im}[A(i \rightarrow f)] = \sum_n \int d\Phi_n A^*(n \rightarrow f) A(i \rightarrow n). \quad (36)$$

To arrive at eq. (36) we have used that

$$\sum_{\{n\}} = \sum_n \int \prod_{j=1}^n \frac{d^3 p_j}{(2\pi)^3 2E_j}, \quad (37)$$

giving the n -body phase space, $d\Phi_n$, when the delta function is extracted from the T-matrix:

$$d\Phi_n = \prod_{j=1}^n \frac{d^3 p_j}{(2\pi)^3 2E_j} (2\pi)^4 \delta^4(p_i - p_f), \quad (38)$$

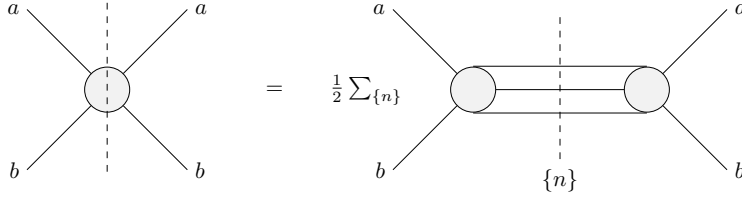


Figure 7: A visualization of the unitarity equations. Grey blobs represent an unspecified scattering. Solid lines represent physical particles (of which n are intermediate on the right hand side). The vertical dashed line represents a final-state cut (cf. section 5.5).

General considerations of a $2 \rightarrow n$ scattering process allow us to write the differential cross section,

$$\frac{d\sigma}{d\Phi_n} = \frac{|A|^2}{N}, \quad (39)$$

where N is a normalization factor and $d\Phi_n$ is the n -body phase-space. In the case of high-energy $2 \rightarrow 2$ scatterings this reduces to

$$\frac{d\sigma}{dt} = \frac{|A(s, t)|^2}{16\pi s^2}. \quad (40)$$

If the $2 \rightarrow 2$ scattering above is elastic, i.e. that the incoming particles are of the same type as the outgoing, we can derive the optical theorem (cf. box 6), which relates the imaginary part of the elastic amplitude to the total cross section — a very powerful relation.

Box 6: The optical theorem

For $2 \rightarrow 2$ elastic scattering at vanishing scattering angle we have $|f\rangle = |i\rangle$ and we use eq. (36) to obtain the optical theorem

$$\sigma_{\text{tot}} = \frac{2}{\Phi} \text{Im}[A_{\text{el}}(s, t=0)]. \quad (41)$$

as the right-hand side of eq. (36) can be recognized as the total cross section, σ_{tot} , times the incident flux, $\Phi = 2E_1 2E_2 |\mathbf{v}_1 - \mathbf{v}_2| \simeq 2s$ with the latter equality valid in the high-energy limit for

collinear incoming particles.

Taking the square on both sides gives the differential cross section for elastic scattering,

$$\left. \frac{d\sigma_{\text{el}}}{dt} \right|_{t=0} = \frac{\sigma_{\text{tot}}^2}{16\pi} (1 + \rho^2), \quad (42)$$

where ρ is the ratio of the real to the imaginary part of the elastic scattering amplitude at $t=0$.

In relativistic field theory we can view an incoming particle with momentum p as an outgoing antiparticle with momentum $-p$. Thus the same diagram for a $2 \rightarrow 2$ scattering can be used to describe different processes, cf. figure 8 (a). This relates the following processes to each other,

$$a + b \rightarrow c + d, \quad (43)$$

$$a + \bar{c} \rightarrow \bar{b} + d, \quad (44)$$

$$a + \bar{d} \rightarrow c + \bar{b}. \quad (45)$$

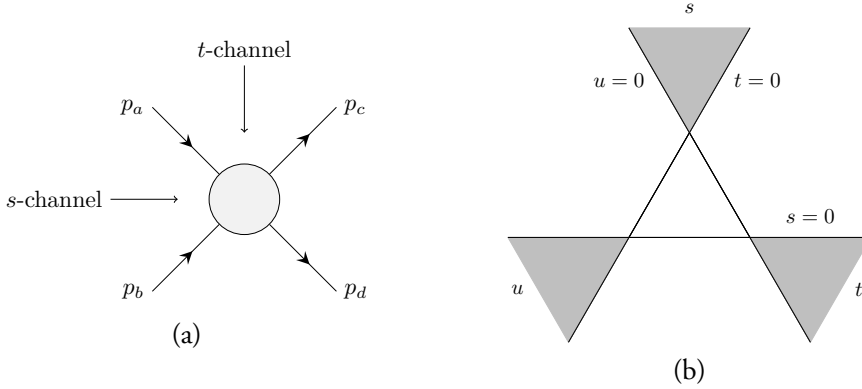


Figure 8: (a) A two-body scattering process $a + b \rightarrow c + d$ with momentum indicated as p_i . The arrows with the text "s-channel" or "t-channel" indicate the time-direction in the respective channels. (b) The physical regions for equal-mass scatterings.

In the case where the scattering in figure 8 (a) only includes a single intermediate particle, we obtain the definitions of the s -, t - and u -channels. These are shown in figure 9.

For the s -channel process, the physical region is given by requiring that $s \geq (m_a + m_b)^2$ and $|\cos \theta| \leq 1$, which in the equal-mass case gives

$$s \geq 4m^2, \quad t, u \leq 0 \quad (s\text{-channel}), \quad (46)$$

where the Mandelstam variables are related by

$$s + t + u = 4m^2. \quad (47)$$

The physical regions for the t - and u -channels are found by exchanging s and t in the former case and s and u in the latter. These regions are shown in figure 8 (b). If a scattering amplitude, $A(s, t)$, is found in one region, crossing postulates that the same amplitude can be continued to other regions of figure 8 (b), and describe the scattering amplitude there.

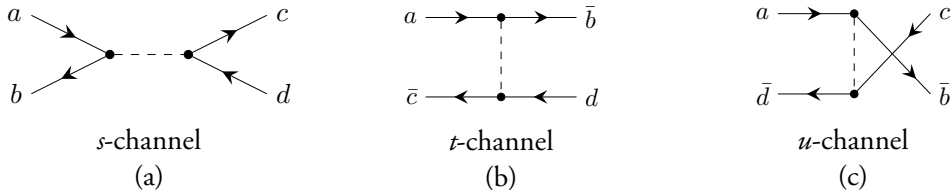


Figure 9: The s - (a), t - (b) and u -channels (c) obtained if the scattering of figure 8 (a) contains a single intermediate particle.

In the attempt to construct such a scattering amplitude, it is natural to turn to a simpler theory first. From quantum mechanics we know that a scattering amplitude for spherically

symmetric potentials can be expanded into partial waves,

$$A(k, \cos \theta) = \sum_{l=0}^{\infty} (2l+1) a_l(k) P_l(\cos \theta) , \quad (48)$$

with k the momentum of the incoming wave, θ the scattering angle, $l = 0, 1, 2, \dots$ denoting the angular momentum of the partial waves, P_l are the Legendre polynomials of the first kind and a_l the partial wave amplitudes at a given angular momentum. The same expansion is applicable for relativistic high-energy scatterings. For $2 \rightarrow 2$ processes with particles of equal mass, the s -channel scattering amplitude can thus be written as

$$A(s, z_s(s, t)) = \sum_{l=0}^{\infty} (2l+1) A_l(s) P_l(z_s(s, t)) , \quad (49)$$

now with A_l as the partial wave amplitudes at a given angular momentum and z_s the scattering angle of the process in the s -channel,

$$z_s(s, t) \equiv \cos \theta_s = 1 + \frac{2t}{s - 4m^2} . \quad (50)$$

The scattering amplitude, eq. (49), contains singularities on the real s -axis. It is most easily visualised in the s -channel, where discontinuities appear corresponding to the exchange of *physical* particles with mass m , cf. figure 7. The first term of the sum on the right-hand side of figure 7 is single-particle production, where a simple pole arises from the propagator of the intermediate particle. If the particle has mass m , then the propagator, $1/(s - m^2)$, is divergent for $s = m^2$. The second term in the sum is two-particle production. It is possible to perform parts of the two integrals required here, thus giving a term proportional to $\sqrt{s/4 - m^2}$ on the right-hand side. Because $x = 0$ is a branch point of \sqrt{x} , we can identify $s = (2m)^2$ as a branch point in the s -plane. Thus the singularities of the s -plane are,

$$\begin{aligned} &\text{pole at } s = m^2 , \\ &\text{branch points at } s = (2m)^2, (3m)^2, \dots , \end{aligned} \quad (51)$$

where the branch points correspond to $n \geq 2$ particles exchanged in figure 7.

Similar singularities can of course be found in the t - and u -channels, when exchanging either $s \rightarrow t$ or $s \rightarrow u$ in the above. Because the Mandelstam variables are related through eq. (47), the poles of the other channels can also appear in the s -channel scattering amplitude. Keeping t fixed, the u -channel poles and branch points also appear in the s -plane at,

$$\begin{aligned} &\text{pole at } u = m^2 \Rightarrow s = 3m^2 - t , \\ &\text{branch points at } u = (2m)^2, (3m)^2, \dots \Rightarrow s = -t, -t - 5m^2, \dots . \end{aligned} \quad (52)$$

So now we have written a scattering amplitude valid in the s -channel, and located all the discontinuities on the real s -axis in the complex s -plane. All of these poles are contained within the partial wave amplitude, $A_l(s)$, as the Legendre polynomials are convergent in the physical domain of s , i.e. for $s \geq 4m^2$, $t \leq 0$. It would thus be natural to try to extend eq. (49) to, say, the t -channel to obtain a crossing symmetric scattering amplitude. In the t -channel the roles of s and t are reversed, such that the scattering angle in the t -channel goes roughly as $z_t \sim s$. This is to be inserted into the Legendre polynomials. In the high-energy limit, s is large, and as the Legendre polynomials behave as $P_n(x) \sim x^n$ for large arguments, the series of eq. (49) will not converge in the t -channel. This means we must conclude that the present form of eq. (49) cannot be extended to the other channels, and thus cannot be a matrix element of the S-matrix as crossing is postulated.

5.2 The Regge formalism

In the presence of only a single resonance, the sum in eq. (49) reduces to only one term, $l = l_0$, and we avoid the trouble of a divergent series. Thus we can continue eq. (49) to the t -channel and study the exchange of a single resonance of angular momentum l_0 ,

$$A(s, t) = (2l_0 + 1)A_{l_0}(t)P_{l_0} \left(1 + \frac{2s}{t - 4m^2} \right) , \quad (53)$$

where we have interchanged s and t in eq. (50) to obtain the t -channel scattering angle $z_t(s, t)$. In the high-energy limit, we can use the large-argument form of the Legendre polynomials to obtain

$$A(s, t) \sim f(t)s^{l_0} , \quad (54)$$

where we have collected all terms depending on t in the function $f(t)$. The total cross section is then obtained from the optical theorem,

$$\sigma_{\text{tot}} \sim s^{l_0-1} . \quad (55)$$

Thus for the exchange of particles with spin equal to $l_0 = 0, 1, 2$, we get the following total cross sections:

$$\sigma_{\text{tot}} \sim \frac{1}{s} , \quad l_0 = 0 , \quad (56)$$

$$\sigma_{\text{tot}} \sim \text{const} , \quad l_0 = 1 , \quad (57)$$

$$\sigma_{\text{tot}} \sim s , \quad l_0 = 2 . \quad (58)$$

Unfortunately, neither of these behaviours are seen in measurements, where at large energies the behaviour is approximately $\sigma_{\text{tot}} \sim s^{0.1}$ for pp collisions. It thus is evident that it

is necessary to include more than one resonance in the sum of eq. (49) to describe the behaviour of the total cross section in pp collisions.

To find a crossing symmetric scattering amplitude, a special trick has to be invoked. This is the idea of complex angular momentum. In the late 1950's and early 1960's Regge proposed this idea to study the bound states of spherically symmetric potentials in quantum mechanics. The bound states of such a potential falls into families of increasing angular momentum and energy, and appear as poles of the partial wave amplitudes for positive integer angular momentum l and wavenumber k . By continuing l to complex values, an interpolating function $a(l, k)$ could be found that reduced to the partial wave amplitudes at physical l , i.e. $a(l, k) \rightarrow a_l(k)$ for $l = 0, 1, 2, \dots$. What Regge noted was that the singularities of the interpolating function $a(l, k)$ are poles located at $l = \alpha(k)$, with $\alpha(k)$ called the Regge trajectory. Each family of bound states has its own Regge trajectory.

As the partial wave amplitude is also defined for high-energy particle scattering, Regge's ideas were extended to this regime as well. The full derivation of the relativistic scattering amplitude and the interpolating function in terms of complex l is not necessary for this thesis, so it will not be pursued here. The interested reader can consult e.g. [27–31]. Instead we will briefly sketch the consequences of constructing a crossing symmetric amplitude in this regime. In relativistic scattering theory it becomes necessary to introduce two partial wave amplitudes, $A^\pm(l, t)$, where

$$A^+(l, t) \rightarrow A_l(t) \quad \text{for } l \text{ even}, \quad A^-(l, t) \rightarrow A_l(t) \quad \text{for } l \text{ odd}. \quad (59)$$

Then the t -channel partial wave expansion is given as [31],

$$A(z_t, t) = A^+(s, t) + A^-(s, t), \quad (60)$$

$$A^\pm(z_t, t) \sim \sum_{l=0}^{\infty} (2l+1) A_l(t) (P_l(z_t(s, t)) \pm P_l(-z_t(s, t))). \quad (61)$$

Because of the property of the Legendre polynomials, $P(-x) = (-1)^l P_l(x)$, the scattering amplitude $A^+(s, t)$ only gets contributions from even l , and $A^-(s, t)$ only from odd l . We can thus introduce a new quantum number, the signature $\xi = \pm 1$, that determines whether even or odd angular momentum is exchanged. The end result in the small- t , large- s limit (the Regge limit) is the signature amplitudes,

$$A^\xi(s, t) \sim \sum_i \beta_i(t) \eta_i(\xi, t) s^{\alpha_i(t)}, \quad (62)$$

where $\eta_i(\xi, t)$ is called the signature factor, β_i is the residue and $\alpha_i(t)$ the location of the i th pole. To lowest order, we can ignore all exchanges but the one with the largest real part in the l -plane — this is called the leading pole. In this case we obtain the scattering

amplitude,

$$A(s, t) \sim \beta(t)\eta(t)s^{\alpha(t)} , \quad (63)$$

where $\beta(t)$ and $\alpha(t)$ are the residue and location (or Regge trajectory) of the leading pole. In simple models the signature factor is often approximated with the imaginary unit, $\eta(t) \sim i$. The residue $\beta(t)$ is unknown and has to be modeled somehow, and the Regge trajectory (or Reggeon (\mathbb{R})) $\alpha(t)$ has to be determined from experimental data.

To check if we actually obtain bound states with such an amplitude, we can further examine the behaviour of the interpolating function near the leading pole at $l = \alpha(t)$. Here we find the behaviour,

$$A(l, t) \sim \frac{1}{l - \alpha(t)} . \quad (64)$$

Assume now that for some t_0 the Regge trajectory behaves as,

$$\alpha(t_0) = l + i\epsilon , \quad (65)$$

with ϵ a (small) number and l integer. A Taylor expansion near this point gives,

$$\alpha(t) \simeq \alpha(t_0) + \alpha'(t_0) \cdot (t - t_0) = l + i\epsilon + \alpha'(t_0)(t - t_0), \quad (66)$$

resulting in the following behaviour of the interpolating function,

$$A(l, t) \sim \frac{1}{t - t_0 + i\epsilon/\alpha'(t_0)} . \quad (67)$$

This can be recognized as a Breit-Wigner term for a resonance with mass $\sqrt{t_0}$ and width $\Gamma = \epsilon/\alpha'(t_0)$ for ϵ finite, but different from zero. If $\epsilon = 0$ then the interpolating function describes a stable bound state of mass $\sqrt{t_0}$. So now we actually see, that the poles in the interpolating function $A(l, t)$ represent resonances and stable bound states of increasing angular momentum l . Combining this knowledge with the form of eqs. (60) and (62), we deduce the main point to take from the Regge theory: the asymptotic behaviour of the s -channel scattering amplitude is determined by the exchange of a family of resonances in the t -channel.

Strikingly, experimental results show that the Regge trajectories lie on straight lines in the $t, \alpha(t)$ -plane, see figure 10. Thus we can write

$$\alpha(t) = \alpha(0) + \alpha' t , \quad (68)$$

for all known mesonic and baryonic trajectories. From this Regge trajectory we can approximate the total cross section as

$$\sigma_{\text{tot}} \sim s^{\alpha(0)-1} , \quad (69)$$

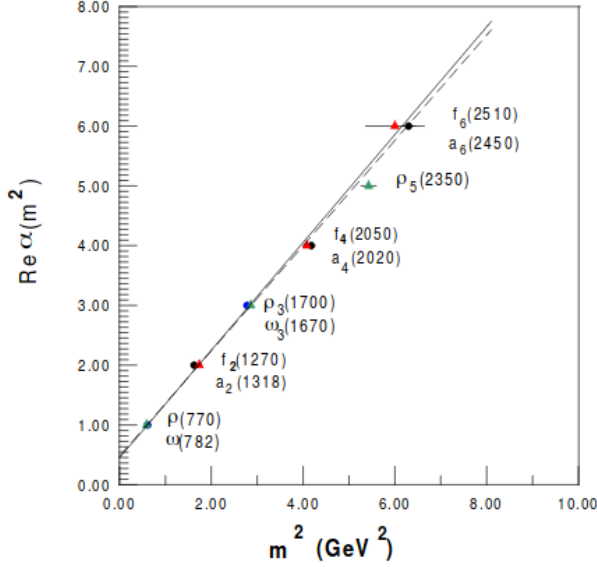


Figure 10: The Regge trajectories for the ρ, ω families along with the observed mesons [32].

i.e. it depends *only* on the intercept of the Regge trajectory. Experimental results show that the leading mesonic resonances all have intercepts at around $\alpha(0) \sim 0.5$, while the leading baryonic ones (not shown in figure 10) have smaller intercepts. Thus neither of these predict a total cross section similar to what is observed. Hence, we must find a Regge trajectory with $\alpha(0) > 1$ in order to describe the high-energy behaviour of the total pp cross section. This trajectory is known as the Pomeron.

5.3 The Pomeron

Historically, the observation was that the total pp cross section seemed to approach a constant at high energies, i.e. it required a trajectory with $\alpha(0) = 1$. This trajectory was called the critical Pomeron named after Pomeranchuk, who introduced it. Later on, when the increase of the total cross section was observed, the supercritical Pomeron with $\alpha(0) > 1$ was introduced. Presently, often the terms hard and soft Pomerons are used, describing Pomerons with two different intercepts (as well as methods to find the intercepts).

As the Pomeron is supposed to be responsible for elastic scattering processes, this restricts its quantum numbers to be those of the vacuum. These can be obtained by an exchange of two gluons in the t -channel. This is the simplest (perturbative) picture of the Pomeron trajectory. Additional gluon exchanges between the two t -channel gluons are allowed, thus

creating a gluon-ladder. Such a ladder is exactly the BFKL Pomeron, derived from pQCD in the late 1970's [8, 33]. This is the Pomeron often referred to as the hard Pomeron. It has an intercept larger than one giving rise to an increasing total cross section, albeit at a larger rate than observed. The intercept can, however, be decreased by multiple Pomeron exchanges, or eikonalization, similar to the dampening occurring within the MPI formalism of section 3 (for a review of such approaches, see e.g. [30, 34]).

The BFKL Pomeron is one approximation — or interpretation — of the Pomeron trajectory. Another interpretation is that the Pomeron is a bound state of gluons — the glueball mentioned in section 1. The idea of a bound state of gluonic content was expanded in the Ingelman-Schlein approach [35], where the Pomeron is modelled similar to any other composite particle. To my knowledge, no trajectory has been analytically calculated for such bound states of gluons, but instead a fit to data is used to extract the intercept and slope for such soft Pomerons.

5.4 The Odderon

In 1973 Lukaszuk and Nicolescu proposed a partner to the Pomeron [36]. This trajectory was called the Odderon, as it was proposed to have the same quantum numbers as the Pomeron, except for having negative C and P parities. This set of quantum numbers can be obtained with the exchange of three gluons and its intercept was analytically calculated in 1999 [37]. The consequences of introducing this trajectory are vast, but most important is that the asymptotic behaviour of many observables changes. Where the asymptotic behaviour of the total cross section and the parameter ρ (defining the ratio of real to imaginary parts of the elastic scattering amplitude) become identical for pp and $p\bar{p}$ (or any hadron-hadron and hadron-antihadron) for processes without the Odderon, the introduction of an Odderon with intercept $\alpha_{\mathbb{O}} \leq 1$ changes this behaviour to the two becoming distinguishable.

For long, this Odderon was not believed to exist, as no experimental evidence pointed towards this. This, however, changed in 2017 when the TOTEM experiment [38, 39] measured ρ to be lower than what present models without Odderons predicted. Similarly, the total cross section was measured to be larger than predicted by the same models. Thus a tension between non-Odderon models and data was beginning to form. Quickly, papers began to appear stating that the TOTEM experiment had seen evidence of this Odderon, and not long after, the TOTEM experiment drew the same conclusions in a different observable [40]. Further analyses are however required before a definite conclusion can be made. Especially the long-awaited results from the ATLAS experiment are needed, as their last measurement of σ_{tot} at 8 TeV was lower than what was measured by TOTEM [41].

5.5 Cut and uncut trajectories

It should now be evident that to describe the total and elastic cross sections, one could construct a model with various Reggeons exchanged in the t -channel. The complexity of such a model can be increased by including e.g. pole terms (single-Reggeon exchanges) and branch cuts (multi-Reggeon exchanges). The method to handle such multi-Reggeon diagrams, was proposed by Gribov and is denoted the Gribov Regge calculus [42]. This method assigns a set of Feynman-like rules to any external and internal legs and vertices in a given scattering diagram. An internal Reggeon⁷ exchange obtains a propagator of the form $\eta(t)s^{\alpha(t)}$, while the incoming and outgoing hadrons have wave functions approximated by their form factor squared. This form factor is a measure of how likely it is for the hadron to stick together after the emission (or absorption) of a particle, i.e. when absorbing the recoil from the emitted particle. Thus in an elastic scattering at zero scattering angle, the form factor equals unity, as both the incoming and outgoing particles are of the same type. Each vertex is assigned a coupling strength: the hadron-hadron-Reggeon vertex has the strength $\beta(t)$, while the triple-Reggeon vertex has the strength $g_3(t)$. Thus diagrams containing several exchanges can be evaluated similar to when using Feynman diagrams in pQCD.

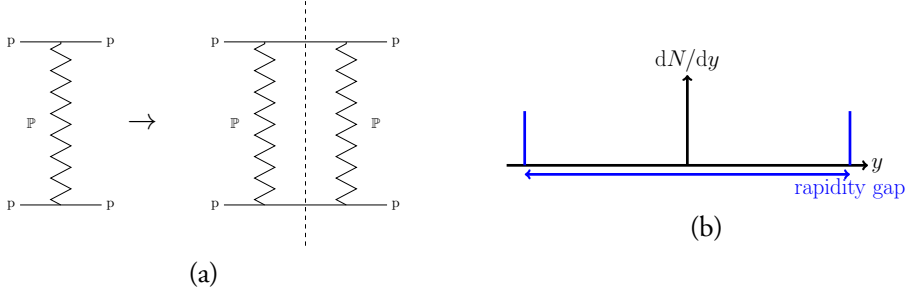


Figure 11: (a) The elastic amplitude (left of the arrow) and its cross section (right of the arrow). (b) The multiplicity as a function of rapidity for elastic scattering.

An elastic scattering is then visualized as in figure 11 (a). Here, the diagram on the left of the arrow show the elastic scattering amplitude, while the diagram on the right side shows the cross section obtained from the diagram on the left. Cross sections are diagrammatically visualized by placing a final-state cut (often a dashed line) in the diagram, where each side of the cut thus represents the amplitude and its complex conjugate. A cut as shown in figure 11 would not give rise to any particles in the final state, as this is an elastic scattering, cf. figure 11 (b). Imagine now the Pomeron as a two-gluon exchange, where the two gluons form a color singlet. Cutting through a Pomeron, i.e. cutting just between the two gluons, produces two color strings between the two hadrons and fragmentation of these strings gives rise to particle production, cf. figure 12. Thus a cut through a Pomeron gives rise to particle production, while uncut Pomerons gives rise to rapidity gaps.

⁷In this section, the term Reggeon also includes the Pomeron and Odderon

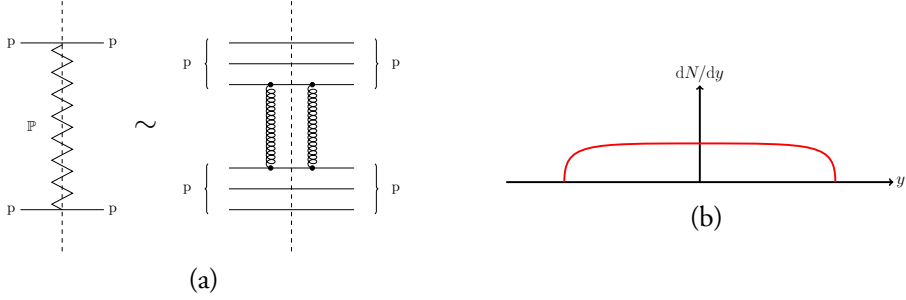


Figure 12: Cutting through a Pomeron approximately corresponds to cutting through two gluons (a). This gives rise to two color-strings stretched between the two hadrons, hence giving rise to particle production in the entire phase space (b).

Returning to the leading-pole approximation, an expression for the elastic pp scattering amplitude can be written,

$$A_{\text{el}}(s, t) = \beta_{p\mathbb{P}}^2(t) \eta_{\mathbb{P}}(t) s^{\alpha_{\mathbb{P}}(t)} . \quad (70)$$

This can now easily be turned into the total cross section,

$$\sigma_{\text{tot}}(s) \sim \frac{1}{s} \text{Im} A_{\text{el}}(s, 0) = \beta_{p\mathbb{P}}^2(0) s^{\alpha_{\mathbb{P}}(0)-1} , \quad (71)$$

where we have used the approximation $\eta(t) \sim i$. This expression can be used in a fit to measurements of the total cross section, and these fitted parameters can then afterwards be used to describe the elastic cross section, both differentially and integrated.

In 1992 Donnachie and Landshoff [43] proposed a model using a single Pomeron and a single Reggeon, and were able to describe the experimental measurements of the total cross section spanning energies from measurements at around 5 GeV up until the Tevatron energies of 1.8 TeV. It also made predictions for the LHC which, however, turned out to slightly undershoot data when measurements from LHC were published. This model was later combined with a model for differential elastic and diffractive scatterings by Schuler and Sjöstrand (the SaS model) [44], using only the Donnachie-Landshoff Pomeron in the elastic and diffractive scatterings. This described the small- t region of elastic scattering fairly well, but did not capture the observed structure at larger t — also known as the diffractive dip and shoulder regions. Diffraction was also reasonably well described by the SaS model, although a suppression factor later had to be introduced as the model gave too large diffractive cross sections at LHC energies. Several other authors (including the work presented in Paper II discussed in the next section) have created models describing all or a subset of these soft QCD processes with more or less success using Regge models, but to list them all here would be too great a task. Instead we proceed to show how such soft collisions look like in a detector, the hadronic event shapes of the soft QCD processes.

5.6 Hadronic event shapes

Once the cross sections of the soft QCD scatterings have been established, the next natural step is to make predictions for the hadronic event shapes of these systems. This section thus extends the simple sketch of section 4 with further details. The hadronic event shapes determine what the event looks like in a detector, i.e. how the particles are distributed in the phase space. This is an essential prediction for event generators, but one that is often neglected by the authors of the models describing the cross sections. Here we will follow the model implemented in the general purpose event generator PYTHIA 8 [17], used in all of the studies in this thesis. Other event generators use different approaches, and thus this section will not be a comprehensive introduction of how event shapes are created, but merely an introduction to the event shapes for soft QCD processes in PYTHIA 8.

The elastic systems are fairly simple to describe, as the incoming and outgoing particles are the same. This means that the only observable left to sample is the scattering angle θ , chosen probabilistically from the t -spectrum of the differential cross section, e.g. from an exponential in the simplest models. Diffraction is more complicated. The mass(es) of the diffractive system(s) and the squared momentum transfer(s) t are sampled based on the differential cross sections. Paper II presented in this thesis includes several new models for these differential cross sections, both the elastic and the diffractive. Preceding this work, the elastic cross section differential in t was the simple exponential described above, albeit with the possibility to include the Coulomb term for very low t values. This was extended to models that includes the dip-shoulder region at intermediate and high t -values. Two models were selected: the COMPAS [45] and ABMST [46] models. Both described the available total and elastic data. They differ in the number of included trajectories and cuts, but the difference is primarily seen in the large t tail, where almost no data exists. The former model includes new structures here, similar to the dip-shoulder region at intermediate t -values, whereas the latter shows no sign of such structure. Discriminating between the two would thus require measuring the elastic scattering process at large t -values.

Paper II included a new model for diffraction, originally proposed only for single diffraction, but extended to other diffractive topologies here. The model includes a high-mass regime containing two effective trajectories, \mathbb{P} , \mathbb{R} , as well as a term for pion exchange between the protons. The low-mass regime is modelled to include the first four excited states of the proton, all a unit of angular momentum higher than the former. These are placed on top of a smooth background containing the low-mass tail of the high-mass model. The new model, and a variation of it also introduced in Paper II, performs well at LHC energies, although data on diffraction is sparse and — unfortunately — disagrees between the two general purpose experiments, ATLAS and CMS. Thus experimental measurements both in different observables and at varying energies are required to test the models further.

Once the mass(es) and squared momentum transfer(s) have been chosen, the subsequent

evolution of the diffractive system(s) depend on its mass, as very low-mass diffractive systems are not energetic enough to be described with pQCD. PYTHIA 8 operates with two regimes (low- and high-mass systems) with a smooth transition between the two,

$$P_{\text{pert}} = 1 - \exp\left(-\frac{\max(0, M_X - m_{\text{min}})}{m_{\text{width}}}\right). \quad (72)$$

Here P_{pert} gives the probability for using a perturbative evolution of the diffractive system, M_X is the mass of the diffractive system and m_{min} , m_{width} are free parameters to be tuned to data. With this distribution, the probability for using the perturbative description vanishes when $M_X \leq m_{\text{min}}$, just as we want.

The nonperturbative, low-mass regime is again split into two regions. Very low mass systems, with masses near the mass of the incoming hadron ($M_X \leq m_h + 1$ GeV), can only decay isotropically into a two-hadron state, thus no evolution or hadronization is applied here. For masses above this limit, but still in the low-mass region, the collision is pictured as a Pomeron obtained from the other side kicking out either a valence quark or a gluon from the colliding hadron. The relative rate of which is kicked out is mass dependent,

$$\frac{P(q)}{P(g)} = \frac{N}{M_X^p}, \quad (73)$$

with N, p free parameters. If a quark is kicked out of the colliding hadron, a single string will be stretched from the quark to the remaining diquark in the hadron remnant. If a gluon is kicked out, two strings are connected from the kicked-out gluon and back to the hadron remnant. These strings are then allowed to hadronize using the string hadronization model described in section 2.

In the high-mass regime, a very different approach is taken. Here, the collision is viewed as a subcollision between a Pomeron and a hadron for single diffraction, as two such systems for double diffraction and a subcollision between two Pomerons for central diffraction. Such a picture was first proposed by Ingelman and Schlein [35], and was developed in conjunction with experimental measurements showing evidence of hard scales in diffractive systems, e.g. diffractive systems containing jets. In the Ingelman-Schlein approach, one factorizes the differential diffractive cross section, similar to the factorization done in any other nondiffractive process with a hard scale. This means that a flux of Pomerons and a Pomeron PDF is used in place of the regular hadron PDFs, and then the standard evolution framework is used with parton showers, multiple interactions and hadronization, just as described in section 2.

The Pomeron flux can be viewed as a probability for extracting a Pomeron from the incoming hadron, while the Pomeron PDF can be seen as a probability for extracting a parton from the Pomeron. Theoretically these two can be separated, as they depend on different variables. Experimentally, however, only the convolution of the two can be measured, and

this is what is provided by the experimental collaborations. In the event generator the two can be separated, and uncertainties related to the choice of either two probed. Note that the Pomeron PDF, although imagined to be primarily of gluonic content, also contains a sea of quarks and antiquarks, created by $g \rightarrow q\bar{q}$ splittings. Several uncertainties go into the extraction of these diffractive PDFs (dPDFs). The perturbative order of course matters, with an NLO description increasing the precision. Some experiments use a single Pomeron in their dPDFs, others use both Pomerons and Reggeons. The lack of fully differential measurements on diffractive systems results in the fits of the dPDFs to be less constrained than e.g. the proton PDFs, where plenty of data exists. Thus dPDFs should always be used with care and consideration.

The dPDFs are usually fitted to deep-inelastic scattering (DIS) data. In DIS, a highly virtual photon is emitted from an electron and can thus directly probe the content of the colliding particle — most often used to probe the content of the proton. In diffractive DIS (DDIS), the virtual photon is used to probe the content of the Pomeron instead. Two experiments at the German electron-proton collider HERA did dPDF measurements, using the factorization approach and fitting the dPDFs to DDIS data. But when these dPDFs were used in hadron-hadron collisions, the predicted cross sections completely failed to describe data. In some processes, the predictions with the dPDFs were about a factor of ten higher than measurements, see e.g. [41]. Thus the hadronic scattering data showed evidence of the breakdown of factorization in diffractive processes. This motivated the HERA experiments to measure diffraction in the photoproduction regime — a regime where the photon emitted from the electron can fluctuate into a hadronic state, which then interacts with a Pomeron extracted from the proton. Here, the experiments also observed that the dPDF predictions were too large as compared to data, although not by as large a factor as in pp and $p\bar{p}$. Thus the factorization breaking was seen in both $p\bar{p}$, pp and photoproduced ep data.

Several models for explaining this factorization breaking has been proposed. Most of them introduce a survival factor based on Regge theory, where additional uncut Pomerons between the two incoming hadrons reduce the cross section. But the effect is not easily calculated, and often gives rise to an overall normalization factor, whereas some data suggest that the suppression factor is observable-dependent, e.g. it depends on the p_{\perp} of the jets created in the diffractive system.

As a different approach we have in this thesis developed a model (Paper I) that evaluates the suppression factor on an event-by-event basis. The model discriminates between preliminary diffractive and purely diffractive events, where the former is exactly the Ingelman-Schlein approach. The difference in this model is that the events are only considered purely diffractive if no other MPIs are found in the hadron-hadron system, as these would destroy the rapidity gap created by the diffractive system. This creates a dynamical suppression, one that is also dependent on the kinematics of the event. The latest results from the CMS

experiment at CERN is shown in figure 13 [47]. Here it is evident that the model developed in this thesis (denoted “Pythia8-DG” in the figure) does a very good job at describing the data, thus hinting that the model might be on the right track. Furthermore, the model is easily extended to other beam-types, and can thus also explain the factorization breaking in photoproduced ep data. This extension was performed in Paper III and comparisons to HERA data showed good agreement. Predictions for ultra-peripheral pp and pA collisions (UPCs) was also given in Paper III, showing larger suppression compared to the ep suppression factors, because of the larger energies available in the photon-Pomeron system in UPCs. Measurements from the LHC on such diffractively produced dijets in UPCs would be an ideal place to constrain the model developed in Papers I and III.

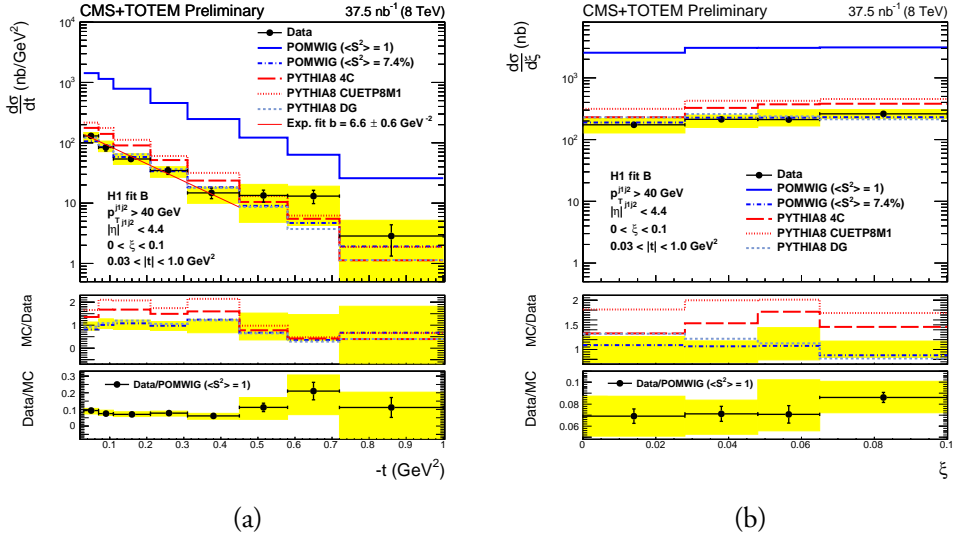


Figure 13: The latest results from CMS [47] on diffractive dijet production. (a) shows the differential cross section as a function of $-t$, while (b) shows it as a function of $\xi = x/x_F$. The model developed in this thesis is denoted “Pythia8 DG” in the plots and is shown with a light-blue dashed line.

5.7 The Good-Walker formalism

The following section leaves the t -channel approach behind and describes a single s -channel approach for calculating cross sections in soft collisions. The Good and Walker approach relates to the eikonal picture of high-energy scattering. The eikonal limit is the limit of large s and small scattering angles. Here, the amplitude found from the t -channel approach can be written as an integral over the impact parameter, b , between the two colliding particles as the angular momentum l can be related to the impact parameter b through the approximation $l \sim kb$, with k being the wavenumber of the incident wave. We thus obtain

a scattering amplitude,

$$A(s, t) = \frac{s}{4\pi} \int d^2\mathbf{b} e^{-i\mathbf{q}\cdot\mathbf{b}} A(s, b) \quad (74)$$

$$= 2is \int d^2\mathbf{b} e^{-i\mathbf{q}\cdot\mathbf{b}} \Gamma(s, b) , \quad (75)$$

with the squared momentum transfer being $t \simeq -\mathbf{q}^2$. In the second step we have defined the profile function $\Gamma(s, b)$ related to the phase-shift $\delta(s, b)$ in impact-parameter space,

$$\Gamma(s, b) = -\frac{i}{8\pi} A(s, b) = 1 - e^{2i\delta(s, b)} = 1 - e^{-\Omega(s, b)} , \quad (76)$$

where we in the last equality also have defined the opacity $\Omega(s, b)$ from the phase shift. If the potential has an azimuthal symmetry, the dot product can be evaluated ($\mathbf{q} \cdot \mathbf{b} = qb \cos \phi$), and the azimuthal integration performed,

$$\frac{1}{2\pi} \int_0^{2\pi} e^{iqb \cos \phi} d\phi = J_0(qb) , \quad (77)$$

with J_0 the zeroth order Bessel function. Thus we obtain the scattering amplitude,

$$A(s, t) = 4\pi is \int db b J_0(qb) \Gamma(s, b) . \quad (78)$$

This expression is the same as obtained in optics. From optics we know that when a plane wave hits an obstacle (or a hole in a screen) of size R , a pattern occurs on a different screen (or detector) at a distance D away from the obstacle. In optics, where diffraction simply means interference, two types of diffraction can occur: Fraunhofer diffraction, valid for $kR^2/D \ll 1$, and Fresnel diffraction, valid for $kR^2/D \approx 1$. The former type is most easily calculable, and luckily this is also the regime where high-energy particle diffraction exists.⁸ From the intensity of the incident and scattered light, the cross section for scattering and absorbtion can be found by integrating the profile function. The total cross section is then the sum of the two. Thus, as the scattering amplitude is the same in the eikonal limit of high-energy particle scattering as in optics, we can directly use the cross section from optics for elastic scattering (the scattering cross section in optics), inelastic scattering (the absorbtion cross section in optics) as well as the total cross section,

$$\sigma_{\text{el}}(s) = \int d^2\mathbf{b} |\Gamma(s, b)|^2 , \quad (79)$$

$$\sigma_{\text{in}}(s) = \int d^2\mathbf{b} (2\text{Re}[\Gamma(s, b)] - |\Gamma(s, b)|^2) , \quad (80)$$

$$\sigma_{\text{tot}}(s) = 2 \int d^2\mathbf{b} \text{Re}[\Gamma(s, b)] . \quad (81)$$

⁸In high-energy particle diffraction we are working on scales where $R \sim 1$ fm, $D \sim 1$ m and $k \sim \sqrt{s} \sim 1$ TeV, thus $kR^2/D \ll 1$.

In the limit $\Omega \rightarrow \infty$ (absolute blackness), one can set the profile function to unity for a given impact parameter $b \leq R$. This gives the black disk relations,

$$\sigma_{\text{el}} = \sigma_{\text{in}} = \frac{1}{2} \sigma_{\text{tot}} = \pi R^2, \quad (82)$$

that gives an upper limit for the elastic cross section.

In 1960 Good and Walker created a model for evaluating cross sections of low-mass diffractive scatterings [48]. The method has since been expanded and used in e.g. [49–51]. Here, a normalized and complete set of real particle states $\{|N\rangle\}$ with fixed quantum numbers is defined. Similarly, eigenstates of the scattering (or transition) matrix T with eigenvalues $T|n\rangle = t_n|n\rangle$ are defined, also forming a normalized and complete set of states ($\{|n\rangle\}$). Assume that we have two incoming beams, one left-moving $|L\rangle$ and one right-moving $|R\rangle$. These can now be diffracted onto the real particle states $|N\rangle$ and $|M\rangle$, where the former carries the quantum numbers of the left-moving beam particle and the latter carries the quantum numbers of the right-moving beam particle. The beam particles can be expressed in terms of the scattering eigenstates,

$$\begin{aligned} |L\rangle &= \sum_n c_n^L |n\rangle, \\ |R\rangle &= \sum_m c_m^R |m\rangle, \end{aligned} \quad (83)$$

and we can combine these into an incoming wavefunction $|\psi_I\rangle$:

$$|\psi_I\rangle = |R, L\rangle = \sum_{n,m} c_n^L c_m^R |n, m\rangle. \quad (84)$$

The scattered wavefunction can be written in terms of the outgoing beams denoted A and B, $|\psi_S\rangle = |A, B\rangle$. It is obtained by operating with the transition matrix on the incoming wavefunction,

$$|\psi_S\rangle = T|\psi_I\rangle = \sum_{n,m} c_n^L c_m^R T|n, m\rangle = \sum_{n,m} c_n^L c_m^R t_{nm} |n, m\rangle. \quad (85)$$

The inner product of the scattering wavefunction is then,

$$\begin{aligned} \langle\psi_S|\psi_S\rangle &= \langle\psi_I|T^\dagger T|\psi_I\rangle = \sum_{n,m} |c_n^L|^2 |c_m^R|^2 t_{nm}^2 \langle n, m|n, m\rangle \\ &= \sum_{n,m} |c_n^L|^2 |c_m^R|^2 t_{nm}^2 \equiv \langle t^2 \rangle_{RL}, \end{aligned} \quad (86)$$

where we have defined an average over both the left-moving and right-moving particles $\langle \rangle_{RL}$ and suppressed indices on t . Using the completeness relation,⁹ we can rewrite the above as

$$\begin{aligned} \langle \psi_S | \psi_S \rangle = & |\langle R, L | \psi_S \rangle|^2 + \sum_{A \neq R} |\langle A, L | \psi_S \rangle|^2 \\ & + \sum_{B \neq L} |\langle R, B | \psi_S \rangle|^2 + \sum_{A \neq R} \sum_{B \neq L} |\langle A, B | \psi_S \rangle|^2, \end{aligned} \quad (87)$$

i.e. the scattering process can return the incoming wave (elastic scattering), it can return an excited state of either the left- or right-moving particle (single diffraction) or both the left- and right-moving particles can be excited (double diffraction).

The profile function for elastic scattering at fixed s is then found from the first term of the right-hand side of eq. (87)

$$\Gamma_{\text{el}}(\mathbf{b}) = \langle R, L | \psi_S \rangle = \langle R, L | T | \psi_I \rangle = \sum_{n,m} |c_n^L|^2 |c_m^R|^2 t_{nm} \langle n, m | n, m \rangle \equiv \langle t \rangle_{RL}, \quad (88)$$

and the differential cross section is then obtained from the differential version of eq. (79)

$$\frac{d\sigma_{\text{el}}}{d^2\mathbf{b}} = \langle t \rangle_{RL}^2. \quad (89)$$

The profile function for obtaining the excited state A on the right-moving side at fixed s is given as,

$$\begin{aligned} \Gamma_{\text{SD}}^A(\mathbf{b}) = & \langle A, L | \psi_S \rangle = \langle A, L | T | \psi_I \rangle = \sum_{n,m} (c_m^A)^* (c_m^R) |c_n^L|^2 t_{nm} \langle n, m | n, m \rangle \\ = & \sum_m (c_m^A)^* (c_m^R) \langle t \rangle_L, \end{aligned} \quad (90)$$

where we have defined the expansion coefficients $c_m^{A,R}$ picked from either the incoming or outgoing waves and the single-side average $\langle \rangle_L$. Similarly the profile function for obtaining the excited state B on the left-moving side is,

$$\Gamma_{\text{SD}}^B(s, \mathbf{b}) = \sum_n (c_n^B)^* (c_n^L) \langle t \rangle_R. \quad (91)$$

Cross sections are obtained by squaring the profile function and summing over possible excited states A, B . For simplicity we add elastic scattering to the sum (i.e. $A = R$ in the

⁹ $\langle \alpha | \alpha \rangle = \sum_{\alpha'} |\langle \alpha' | \alpha \rangle|^2$

sum over A and $B = L$ in the sum over B), as we can then use the completeness relation of the beam-states $\{|B\rangle\}$,

$$\sum_B c_i^{B*} c_j^B = \delta_{ij} . \quad (92)$$

The final result must then include a subtraction of the elastic contribution, and we obtain

$$\begin{aligned} \frac{d\sigma_{\text{SD}}^R}{d^2\mathbf{b}} &= \sum_A |\Gamma_{\text{SD}}^A(\mathbf{b})|^2 - \frac{d\sigma_{\text{el}}}{d^2\mathbf{b}} = \sum_A \sum_{m,m'} (c_{m'}^A)^* (c_{m'}^R) (c_m^A) (c_m^R)^* \langle t \rangle_L^2 - \langle t \rangle_{RL}^2 \\ &= \sum_m |c_m^R|^2 \langle t \rangle_L^2 - \langle t \rangle_{RL}^2 = \langle \langle t \rangle_L^2 \rangle_R - \langle t \rangle_{RL}^2 . \end{aligned} \quad (93)$$

Similarly for the excitation of the left-moving side we obtain,

$$\frac{d\sigma_{\text{SD}}^L}{d^2\mathbf{b}} = \langle \langle t \rangle_R^2 \rangle_L - \langle t \rangle_{RL}^2 . \quad (94)$$

The double-diffractive cross section is most easily derived from eq. (87)

$$\begin{aligned} \frac{d\sigma_{\text{DD}}}{d^2\mathbf{b}} &= \langle \psi_S | \psi_S \rangle - \frac{d\sigma_{\text{SD}}^R}{d^2\mathbf{b}} - \frac{d\sigma_{\text{SD}}^L}{d^2\mathbf{b}} - \frac{d\sigma_{\text{el}}}{d^2\mathbf{b}} \\ &= \langle t^2 \rangle_{RL} - \langle \langle t \rangle_L^2 \rangle_R - \langle \langle t \rangle_R^2 \rangle_L + \langle t \rangle_{RL}^2 . \end{aligned} \quad (95)$$

The Good-Walker formalism thus derives diffractive excitations from the expectation value and width of the eigenvalues of the scattering matrix T . The expectation value is defined by a given incoming wavefunction. Hence expressions are required for both T and the wavefunctions of the beams in order to use this method. There is no clear method of calculating the central diffractive cross sections, as this would include two surviving protons and a diffractive system in a pp collision, thus essentially live inside the elastic cross section expression.

The Good-Walker framework was initially developed only for low-mass diffraction, but can be extended to higher masses, if a scattering matrix T can be defined in this region. In the case where the Good-Walker method is combined with the dipole description of QCD, T is well-defined and thus can be used for all diffractive masses.

5.8 The dipole description of QCD

One way to describe the evolution of the incoming particles, alternative to conventional ISR showers, is the Mueller dipole formalism [52]. Here, a quark-antiquark pair is seen as a

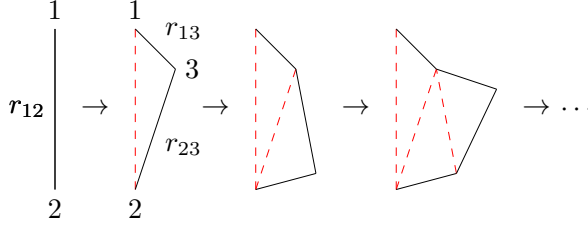


Figure 14: A schematic evolution in rapidity of a single dipole (solid, black lines) stretched between a quark-antiquark pair denoted 1, 2. The dipole emits a gluon (denoted 3) thus breaking into two new dipoles spanned between partons 1, 3 and 2, 3, respectively. The mother dipole is represented by dashed, red lines. Only one of the new dipoles are allowed to emit in each step of the process. Definitions of the lengths, r_{ij} , have been shown in the first and second step of the evolution.

the endpoints of a color-dipole, and the probability for emitting a soft gluon is calculated. In Mueller's original formalism, the calculation is performed in the eikonal approximation, such that the emitters do not obtain any recoil from the emission of the gluon, i.e. there is no energy or momentum conservation. The dipole splitting probability is found by adding the contribution from emitting the gluon from either the quark or antiquark with the interference effects,

$$\frac{dP}{d^2\mathbf{r}_3 dy} = \frac{3\alpha_S(Q^2)}{2\pi^2} \frac{r_{12}^2}{r_{13}^2 r_{23}^2}, \quad (96)$$

with r_{ij} the lengths of the dipoles, see figure 14. The evolution is performed in transverse coordinate space ($\mathbf{r}_3 = (r_x, r_y)$ are the transverse coordinates of the emitted gluon) and in gluon rapidity, y , defined by

$$y = \log \frac{p_+}{p_\perp}, \quad (97)$$

with p_\perp the transverse momentum of the emitted gluon and p_+ its positive lightcone momenta, $p_\pm = E \pm p_z$. Note, however, that the splitting kernel, eq. (96), diverges for dipole sizes approaching zero, thus requiring a cutoff for small dipole lengths, $r_{ij} \geq \rho$.

Introducing the no-emission Sudakov to the splitting kernel allows for an iterative sampling of the transverse coordinates and rapidities, similar to the sampling of new emissions in a parton shower,

$$\frac{dP}{d^2\mathbf{r}_3 dy} = \frac{3\alpha_S(Q^2)}{2\pi^2} \frac{r_{12}^2}{r_{13}^2 r_{23}^2} \Delta(y_0, y), \quad (98)$$

where y_0 is the rapidity of the initial dipole. The allowed rapidity range for a single dipole evolution depends on the type and energy of the colliding beams, $y_{\max} \sim 1/2 \log(s/m^2)$.

With this description one can evolve a initial-state system in rapidity, to find the distribution of dipoles inside two colliding particles just before the collision. In order to calculate

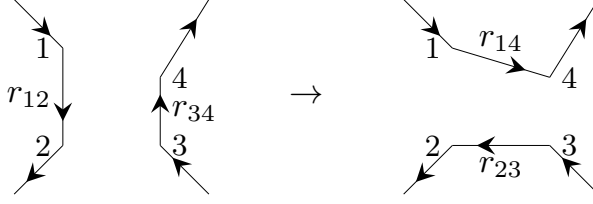


Figure 15: A schematic view of a dipole-dipole interaction. Here the dipole spanned between partons 1,2 interact with the dipole spanned between partons 3,4. The scattering probability of these two dipoles depends on the lengths between the endpoints r_{ij} . In this figure the lengths r_{12} , r_{34} , r_{14} , r_{23} are shown, while lengths r_{13} , r_{24} have been omitted for simplicity.

cross sections, two additional ingredients are needed. Firstly, the dipole-dipole scattering amplitude is required. This is given as,

$$f_{ij} = \frac{\alpha_s^2(Q^2)}{2} \log^2 \left[\frac{r_{14}r_{23}}{r_{24}r_{13}} \right], \quad (99)$$

with r_{ij} being the distances between the endpoints of the two dipoles, see figure 15. Provided that the real part of a scattering amplitude is zero, we can directly treat these scattering amplitudes as cross sections or probabilities. So, imagine now a projectile consisting of a single dipole colliding with a target containing three dipoles. The total interaction probability corresponds to the probability of interacting with each of the dipoles in the targets independently, but subtracting double-counting terms. This gives the following scattering probability,

$$\begin{aligned} P_{\text{int}} &= f_1 + f_2 + f_3 - f_1f_2 - f_2f_3 - f_1f_3 + f_1f_2f_3 \\ &= 1 - (1 - f_1)(1 - f_2)(1 - f_3) \\ f_i \text{ small} &\simeq 1 - \prod \exp(-f_i) = 1 - \exp\left(-\sum_i f_i\right). \end{aligned} \quad (100)$$

This can be directly transferred to projectile and targets with an arbitrary number of dipoles, thus giving the total interaction probability (also called the eikonalized scattering amplitude)

$$P_{\text{int}} = 1 - \exp\left(-\sum_{ij} f_{ij}\right). \quad (101)$$

Secondly, we need an expression for the wavefunction of the initial particles. It turns out [51], that the wavefunction of the proton can be approximated by an initial state consisting of three dipoles in a triangle configuration. An examples of such an initial state along with the evolved proton state os shown in figure 16. For other particles, e.g. the photon, other wave functions have to be used, see e.g. Paper IV.

This dipole formalism can be used directly along with the Good-Walker method for obtaining cross sections, and have been implemented in the Monte Carlo event generators

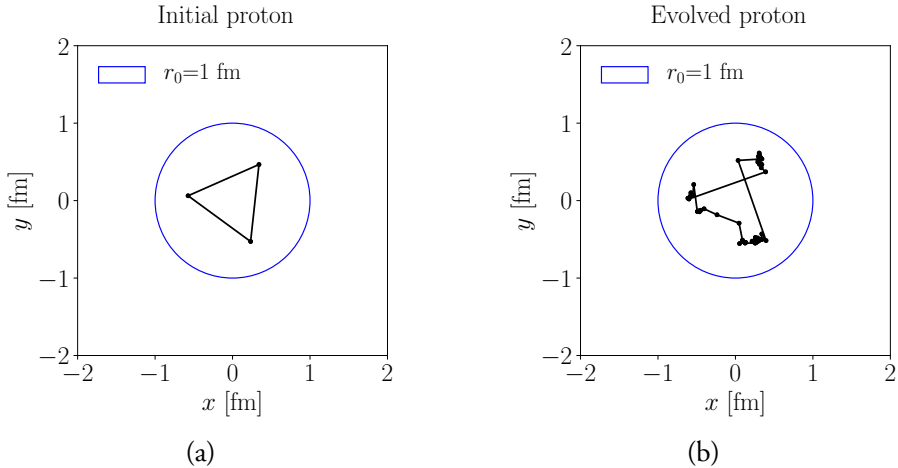


Figure 16: An initial state proton consisting of three dipoles in an equilateral triangle configuration (a). After a full evolution in rapidity ($y_{max} = 9$) the three dipoles have evolved into several smaller ones in (b). In both figures $r_0 = 1$ fm is the size of the initial dipoles.

DIPSY [18] and OEDIPUS [53]. The latter did not contain any energy and momentum conservation, and contained problems with a rapidly growing number of dipoles in the evolution. The former introduced (amongst other things) energy and momentum conservation, and thus could decrease the number of dipoles in the evolution. The dipole model introduced in Paper IV contains some of the aspects used in the former model. In the dipole model of Paper IV, fluctuations in the matter distributions of the protons are created by evolving an initial state proton, parametrised by a triangle configuration of dipoles, in rapidity. If two such asymmetric protons are collided, then the overlap between these two protons will also be asymmetrically distributed, as opposed to the symmetric distribution used in the MPI framework of section 3. The impact of such asymmetric initial states can then be studied in observables related to collective effects.

In heavy-ion collisions, a linear response between the flow-coefficients and the initial eccentricity has been observed for both elliptic (v_2) and triangular (v_3) flow coefficients [54], i.e. $v_n \sim k_n \epsilon_n$. In Paper IV parton-level eccentricities, i.e. eccentricities measured on parton-level objects such as quarks and gluons, are studied using both the symmetric and asymmetric models in different collision systems. Ratios of these eccentricities can be directly compared to ratios of the flow-coefficients, as the response is removed here. Paper IV shows that the dipole model gives rise to larger eccentricities than the symmetric model, but distinguishing between the two models is difficult with the present data available.

6 Outlook

The papers presented in this thesis could be used as a starting point for further studies. In this section, some ideas are given in case the reader has become inspired to continue the work.

6.1 Hard diffraction

The model developed in this thesis is currently limited to single diffractive events. It would be possible to extend this to both double and central diffraction, although not much data is available for these processes. The model could be constrained significantly in UPC processes, as stated in Paper III. Constraining the modelling of the diffractive systems, e.g. the MPI parameters in the Pomeron-proton system, would require detailed measurements of the diffractive system: new measurements should not only measure the differential distributions for the dijet system, but also the underlying event. Presently, the model has been used in connection with double parton scattering in proton-lead collisions, where the total double parton scattering is enhanced because of these hard diffractive events (see e.g. a talk by O. Fedkevyeh [55]).

6.2 Central exclusive production

Currently, the production of a subset of the central exclusive processes (CEP) are available in PYTHIA 8 with a plugin developed using the Durham method [56]. The Durham method creates CEP using additional gluon exchanges, such that the net color charge between the colliding protons is zero. Such an approach is different from the Pomeron-exchange approach used in PYTHIA 8. The end goal is to be able to describe low mass central diffraction as well as CEP internally in PYTHIA 8, as these are presently ignored. One could argue that the CEP plugin could be used internally for low-mass central diffraction, but the merging of the two methods is not obvious, because of the different physics approaches. A study on the production of central diffractive dijet events using the hard diffraction model and this CEP plugin could highlight the differences between the two approaches, and thus be used as a starting point for the inclusion of low-mass central diffraction.

6.3 Diffraction in cosmic rays

Highly energetic cosmic rays creates a cascade of particles during the passing through the Earths atmosphere. Describing these rays requires models applicable for both very high

energies at the start of the cascade, as well as the lower energies near the end of the cascade. The hadronic cascades include diffractive events, thus requires modelling of these events at a large range of energies. The improved description of such events presented in Paper II could be used as input for dedicated air shower generators, thus likely improving their predictions. Similarly, the models of Paper II could be extended to πp , Kp and proton-air collisions, and again be used as input for dedicated cosmic ray generators. Using PYTHIA 8 as a cosmic ray generator could also be feasible in the future.

6.4 The dipole evolution model

The dipole evolution model implemented in Paper IV is extremely flexible. First off, by defining the response function, e.g. using the string shoving mechanism [12], one could directly compare to measured flow coefficients, instead of comparing ratios of flow coefficients as done in Paper IV. As wave functions can be defined for most particles, it is possible to use the dipole model not only for collisions of protons, but also collisions of photons or mesons. With the photon fluxes defined in Paper III, the dipole model could be used for predictions in UPCs. Expanding the photon wave function in Paper IV opens up for studies on vector meson production in ep collisions. Diffraction could also be studied using the Good-Walker method described in section 5.7. A combination of the dipole model and the recent extension to heavy ions within the PYTHIA framework, the ANGANTYR model [57, 58], opens up for predictions for electron-ion collisions — a work that was initiated in Paper IV. And finally, models for saturation in the dipole cascade could be studied and compared to other approaches, such as the CGC method [59].

References

- [1] W. Ochs, J. Phys. G **40**, 043001 (2013) doi:10.1088/0954-3899/40/4/043001 [arXiv:1301.5183 [hep-ph]].
- [2] <http://pdg.lbl.gov/2018/figures/qcd/figures/asq-2015.eps>
- [3] L. N. Lipatov, Sov. J. Nucl. Phys. **20**, 94 (1975) [Yad. Fiz. **20**, 181 (1974)].
- [4] V. N. Gribov and L. N. Lipatov, Sov. J. Nucl. Phys. **15**, 438 (1972) [Yad. Fiz. **15**, 781 (1972)].
- [5] G. Altarelli and G. Parisi, Nucl. Phys. B **126**, 298 (1977). doi:10.1016/0550-3213(77)90384-4
- [6] Y. L. Dokshitzer, Sov. Phys. JETP **46**, 641 (1977) [Zh. Eksp. Teor. Fiz. **73**, 1216 (1977)].
- [7] E. A. Kuraev, L. N. Lipatov and V. S. Fadin, Sov. Phys. JETP **45**, 199 (1977) [Zh. Eksp. Teor. Fiz. **72**, 377 (1977)].
- [8] I. I. Balitsky and L. N. Lipatov, Sov. J. Nucl. Phys. **28**, 822 (1978) [Yad. Fiz. **28**, 1597 (1978)].
- [9] B. Andersson, G. Gustafson, G. Ingelman and T. Sjöstrand, Phys. Rept. **97**, 31 (1983). doi:10.1016/0370-1573(83)90080-7
- [10] B. R. Webber, Nucl. Phys. B **238**, 492 (1984). doi:10.1016/0550-3213(84)90333-X
- [11] S. Schael *et al.* [ALEPH and DELPHI and L3 and OPAL and LEP Electroweak Collaborations], Phys. Rept. **532**, 119 (2013) doi:10.1016/j.physrep.2013.07.004 [arXiv:1302.3415 [hep-ex]].

- [12] C. Bierlich, G. Gustafson and L. Lönnblad, Phys. Lett. B **779**, 58 (2018) doi:10.1016/j.physletb.2018.01.069 [arXiv:1710.09725 [hep-ph]].
- [13] A. Buckley, J. Butterworth, L. Lönnblad, D. Grellscheid, H. Hoeth, J. Monk, H. Schulz and F. Siegert, Comput. Phys. Commun. **184**, 2803 (2013) doi:10.1016/j.cpc.2013.05.021 [arXiv:1003.0694 [hep-ph]].
- [14] Christian Bierlich et al., In preparation.
- [15] <https://rivet.hepforge.org>
- [16] T. Sjöstrand, FERMILAB-PUB-85-119-T.
- [17] T. Sjöstrand *et al.*, Comput. Phys. Commun. **191**, 159 (2015) doi:10.1016/j.cpc.2015.01.024 [arXiv:1410.3012 [hep-ph]].
- [18] C. Flensburg, G. Gustafson and L. Lönnblad, JHEP **1108**, 103 (2011) doi:10.1007/JHEP08(2011)103 [arXiv:1103.4321 [hep-ph]].
- [19] M. Bahr *et al.*, Eur. Phys. J. C **58**, 639 (2008) doi:10.1140/epjc/s10052-008-0798-9 [arXiv:0803.0883 [hep-ph]].
- [20] T. Sjöstrand, FERMILAB-PUB-85-119-T.
- [21] T. Sjöstrand and M. van Zijl, Phys. Lett. B **188**, 149 (1987). doi:10.1016/0370-2693(87)90722-2
- [22] Y. L. Dokshitzer, V. A. Khoze and T. Sjöstrand, Phys. Lett. B **274**, 116 (1992). doi:10.1016/0370-2693(92)90312-R
- [23] J. D. Bjorken, Phys. Rev. D **47**, 101 (1993). doi:10.1103/PhysRevD.47.101
- [24] V. A. Khoze, A. D. Martin and M. G. Ryskin, Eur. Phys. J. C **18**, 167 (2000) doi:10.1007/s100520000494 [hep-ph/0007359].
- [25] E. Gotsman, E. Levin, U. Maor, E. Naftali and A. Prygarin, hep-ph/0511060.
- [26] S. P. Jones, A. D. Martin, M. G. Ryskin and T. Teubner, JHEP **1311**, 085 (2013) doi:10.1007/JHEP11(2013)085 [arXiv:1307.7099 [hep-ph]].
- [27] P. D. B. Collins, “An Introduction to Regge Theory and High-Energy Physics,” doi:10.1017/CBO9780511897603
- [28] M. L. Perl, “High Energy Hadronic Physics”, Wiley-Interscience (1974), ISBN 0-471-68049-4.

- [29] J. R. Forshaw and D. A. Ross, “Quantum chromodynamics and the pomeron,” Cambridge Lect. Notes Phys. **9**, 1 (1997).
- [30] V. Barone and E. Predazzi, “High-Energy Particle Diffraction,” Springer (2002).
- [31] S. Donnachie, H. G. Dosch, O. Nachtmann and P. Landshoff, “Pomeron physics and QCD,” Camb. Monogr. Part. Phys. Nucl. Phys. Cosmol. **19**, 1 (2002).
- [32] V. A. Petrov, AIP Conf. Proc. **1105**, no. 1, 266 (2009) doi:10.1063/1.3122190 [arXiv:0812.0996 [hep-ph]].
- [33] E. A. Kuraev, L. N. Lipatov and V. S. Fadin, Sov. Phys. JETP **44**, 443 (1976) [Zh. Eksp. Teor. Fiz. **71**, 840 (1976)].
- [34] G. Matthiae, Rept. Prog. Phys. **57**, 743 (1994). doi:10.1088/0034-4885/57/8/001
- [35] G. Ingelman and P. E. Schlein, Phys. Lett. **152B**, 256 (1985). doi:10.1016/0370-2693(85)91181-5
- [36] L. Lukaszuk and B. Nicolescu, Lett. Nuovo Cim. **8**, 405 (1973). doi:10.1007/BF02824484
- [37] J. Bartels, L. N. Lipatov and G. P. Vacca, Phys. Lett. B **477**, 178 (2000) doi:10.1016/S0370-2693(00)00221-5 [hep-ph/9912423].
- [38] G. Antchev *et al.* [TOTEM Collaboration], Eur. Phys. J. C **79**, no. 2, 103 (2019) doi:10.1140/epjc/s10052-019-6567-0 [arXiv:1712.06153 [hep-ex]].
- [39] G. Antchev *et al.* [TOTEM Collaboration], arXiv:1812.04732 [hep-ex].
- [40] G. Antchev *et al.* [TOTEM Collaboration], arXiv:1812.08610 [hep-ex].
- [41] M. Aaboud *et al.* [ATLAS Collaboration], Phys. Lett. B **761**, 158 (2016) doi:10.1016/j.physletb.2016.08.020 [arXiv:1607.06605 [hep-ex]].
- [42] V. N. Gribov, Sov. Phys. JETP **26**, 414 (1968) [Zh. Eksp. Teor. Fiz. **53**, 654 (1967)].
- [43] A. Donnachie and P. V. Landshoff, Phys. Lett. B **296**, 227 (1992) doi:10.1016/0370-2693(92)90832-O [hep-ph/9209205].
- [44] G. A. Schuler and T. Sjöstrand, Phys. Rev. D **49**, 2257 (1994). doi:10.1103/PhysRevD.49.2257
- [45] C. Patrignani *et al.* [Particle Data Group], Chin. Phys. C **40**, no. 10, 100001 (2016). doi:10.1088/1674-1137/40/10/100001

- [46] R. B. Appleby, R. J. Barlow, J. G. Molson, M. Serluca and A. Toader, Eur. Phys. J. C **76**, no. 10, 520 (2016) doi:10.1140/epjc/s10052-016-4363-7 [arXiv:1604.07327 [hep-ph]].
- [47] CMS Collaboration [CMS Collaboration], CMS-PAS-FSQ-12-033.
- [48] M. L. Good and W. D. Walker, Phys. Rev. **120**, 1857 (1960). doi:10.1103/PhysRev.120.1857
- [49] H. I. Miettinen and J. Pumplin, Phys. Rev. D **18** (1978) 1696. doi:10.1103/PhysRevD.18.1696
- [50] Y. Hatta, E. Iancu, C. Marquet, G. Soyez and D. N. Triantafyllopoulos, Nucl. Phys. A **773** (2006) 95 doi:10.1016/j.nuclphysa.2006.04.003 [hep-ph/0601150].
- [51] E. Avsar, G. Gustafson and L. Lönnblad, JHEP **0712** (2007) 012 doi:10.1088/1126-6708/2007/12/012 [arXiv:0709.1368 [hep-ph]].
- [52] A. H. Mueller and B. Patel, Nucl. Phys. B **425**, 471 (1994) doi:10.1016/0550-3213(94)90284-4 [hep-ph/9403256].
- [53] G. P. Salam, Comput. Phys. Commun. **105**, 62 (1997) doi:10.1016/S0010-4655(97)00066-0 [hep-ph/9601220].
- [54] H. Niemi, G. S. Denicol, H. Holopainen and P. Huovinen, Phys. Rev. C **87**, no. 5, 054901 (2013) doi:10.1103/PhysRevC.87.054901 [arXiv:1212.1008 [nucl-th]].
- [55] https://agenda.irmp.ucl.ac.be/event/3217/contributions/3730/attachments/1887/2216/Louvain_Fedkevych_pA_v1_0_2.pdf
- [56] L. Lönnblad and R. Žlebčík, Eur. Phys. J. C **76**, no. 12, 668 (2016) doi:10.1140/epjc/s10052-016-4513-y [arXiv:1608.03765 [hep-ph]].
- [57] C. Bierlich, G. Gustafson and L. Lönnblad, JHEP **1610**, 139 (2016) doi:10.1007/JHEP10(2016)139 [arXiv:1607.04434 [hep-ph]].
- [58] C. Bierlich, G. Gustafson, L. Lönnblad and H. Shah, JHEP **1810**, 134 (2018) doi:10.1007/JHEP10(2018)134 [arXiv:1806.10820 [hep-ph]].
- [59] E. Iancu, K. Itakura and S. Munier, Phys. Lett. B **590**, 199 (2004) doi:10.1016/j.physletb.2004.02.040 [hep-ph/0310338].

7 Publications

Paper I

Christine O. Rasmussen, Torbjörn Sjöstrand: **Hard diffraction with dynamic gap survival**, JHEP **1602** (2016) 142 [arXiv:1512.05525 [hep-ph]].

The main ideas behind the model were developed by Torbjörn Sjöstrand. The implementation of the model, the validation of it and the results used in the paper were carried out by myself.

The introduction and summary was written by Torbjörn Sjöstrand, the model description was written in collaboration, and I wrote the validation and results sections.

Paper II

Christine O. Rasmussen, Torbjörn Sjöstrand: **Models for total, elastic and diffractive cross sections**, Eur. Phys. J. C **78** (2018) no.6, 461 [arXiv:1804.10373 [hep-ph]].

The initiation of the upgrade of the cross sections was proposed by Torbjörn Sjöstrand. The choice of models was decided on in collaboration and initial studies were done in parallel as validation of the models. Further validation and extensions to other topologies was done by myself, while the final implementation was performed by Torbjörn Sjöstrand. All results and figures have been produced by myself.

The introduction was written by Torbjörn Sjöstrand while I wrote the remainder with Torbjörn Sjöstrand proofreading.

Paper III

Ilkka Helenius, Christine O. Rasmussen: **Hard diffraction in photoproduction with PYTHIA 8**, Eur. Phys. J. C **79** (2019) no.5, 413 [arXiv:1901.05261 [hep-ph]].

The ideas behind the model were developed in Paper I, while the proposal for the extension was put forth by Ilkka Helenius. The hard diffraction model for photon collisions was implemented by myself, while Ilkka Helenius allowed for lepton-hadron and lepton-lepton collisions. Validation and results was done in collaboration.

The main body of the paper was written in collaboration.

Paper IV

Christian Bierlich, Christine O. Rasmussen: **Dipole evolution: perspectives for collectivity and γ^*A collisions**, submitted to JHEP, [arXiv:1917.12871 [hep-ph]].

The proposal to implement the dipole model was put forth by Christian Bierlich. The implementation of the models was done by myself, while Christian Bierlich developed the framework for measuring the eccentricities. All figures, except for the eA ones, was produced by myself.

The main body of the paper was written in collaboration.

Further published work

During my Ph.D. I have also published the following work, not included in the thesis, but listed here for the sake of completeness:

Paper V

Torbjörn Sjöstrand et al., **An introduction to PYTHIA 8.2**,
Comput.Phys.Commun.191 (2015) 159-177 [arXiv:1410.3012[hep-ph]].
PYTHIA 8.2 manual.

Paper VI

Christine O. Rasmussen, **Hard Diffraction in PYTHIA 8**,
Acta. Phys. Polon. Supp. 8 (2015) 849-854 [arXiv:1509.03115 [hep-ph]].
Conference proceedings, EDS Blois 2015, talk given by myself.

Paper VII

Christine O. Rasmussen, **Hard Diffraction in PYTHIA 8**.
EPJ Web. Conf. 120 (2016) 02002 [arXiv:1512.05872 [hep-ph]].
Conference proceedings, ISMD 2015, talk given by myself.

Paper VIII

I. Helenius, J.R. Christiansen, C.O. Rasmussen, **Hard Diffraction, Colour Reconnection and $\gamma\gamma$ collisions.**

arxiv:1604.07996[hep-ph].

Conference proceedings, MPI@LHC 2015, talk given by I. Helenius.

Paper IX

Christian Bierlich et al., **Confronting exclusive heavy ion models with data.**

In preparation.

User manual for the RIVET-2.7 upgrade for heavy ions.

8 Acknowledgments

Several people deserve a great big thank you. First of all Torbjörn for giving me the opportunity to work in such an incredible area of physics and for the patience and confidence in my abilities. I appreciate the time you have put into explaining things over and over again.

Thank you to Gösta for listening and explaining everything I did not understand, and Leif for several useful discussions during the work for Paper IV. Thank you to Christian, Ilkka, Johannes and Stefan for valuable collaboration and discussions both at the office and outside in real life. I appreciate your nodding and (silent) agreeing when I was complaining or being a feminist killjoy. I could not have finished this Ph.D. without you.

To my officemates, Christian, Jesper, Johan, Joel and Johannes, thank you for always making the vibe better. Thank you to the rest of the team in Lund for being incredible colleagues. Thanks as well to all of the members in the MCnet collaboration for making the meetings and the conferences so much more fun. Several other people has also helped along the way. Most are mentioned in the acknowledgments of the papers, but some have unfortunately been left out: Robert Cisielski, thanks for the good times in New York, You Zhou and Vytautas Vislavicius for many discussions on all things heavy ion and the ALICE and ATLAS groups in Copenhagen for providing a desk when needed. And thanks as well to the proofreaders: Torbjörn, Gösta, Christian and Sofie.

Thank you to my family and friends for all of the help along the way. And finally to Morten, for keeping my sanity and for always being there.

I

Hard Diffraction with Dynamic Gap Survival

Christine O. Rasmussen¹ and Torbjörn Sjöstrand¹.

JHEP, 1602 (2016) 142

doi:10.1007/JHEP02(2016)142

e-Print: arXiv:1512.05525[hep-ph]

MCnet-15-36 LU-TP 15-56

¹ Dept. of Astronomy and Theoretical Physics, Lund University, Sölvegatan 14A, SE-223 62 Lund, Sweden.

ABSTRACT:

We present a new framework for the modeling of hard diffraction in pp and p \bar{p} collisions. It starts from the approach pioneered by Ingelman and Schlein, wherein the single diffractive cross section is factorized into a Pomeron flux and a Pomeron PDF. To this it adds a dynamically calculated rapidity gap survival factor, derived from the modeling of multiparton interactions. This factor is not relevant for diffraction in ep collisions, giving non-universality between HERA and Tevatron diffractive event rates. The model has been implemented in PYTHIA 8 and provides a complete description of the hadronic state associated with any hard single diffractive process. Comparisons with p \bar{p} and pp data reveal improvement in the description of single diffractive events.

I Introduction

The nature of diffractive excitation in hadron-hadron collisions remains a bit of a mystery. We may motivate *why* it happens, e.g. based on the optical analogy that lies behind its name, or in the related Good-Walker formalism [1]. But to explain *how* diffractive events are produced, and with what properties, is a longer story. In a first step the single diffractive cross section should be describable as a function of the diffractive mass M and the squared momentum transfer t . In a second step the generic properties of a diffractive system of a given mass should be explained: multiplicity distributions, rapidity and transverse momentum spectra and other event characteristics. In a third step the existence and character of exclusive diffractive processes and the underlying events associated therewith should be understood.

Over the years much data has accumulated, and many models have been presented, but so far without any model that explains all aspects of the data, and without any consensus which models are the most relevant ones. It is beyond the scope of the current article to review all the data and models; for a selection of relevant textbooks and reviews see [2–8].

For the path we will follow in this article, Regge theory provides the basic mathematical framework. In it, poles in the plane of complex spin α may be viewed as the manifestations of hadronic resonances in the crossed channels. A linear trajectory of poles $\alpha(t) = \alpha(0) + \alpha' t$ corresponds to a $\sigma_{\text{tot}} \sim s^{\alpha(0)-1}$. Several trajectories appear to exist, but for high-energy applications the most important is the Pomeron (\mathbb{P}) one, which with its $\alpha(0) > 1$ is deemed responsible for the observed rise of the total cross section, and in modern terminology would correspond to a set of glueball states. With single-Pomeron exchange as the starting point, higher orders involve multiple Pomeron exchanges, and also interactions between the Pomerons being exchanged, driven by a triple-Pomeron vertex. Out of this framework the cross section for various diffractive topologies can be derived, differentially in mass and t , given a set of numbers that must be extracted from data.

Such models do not address the structure of the diffractive system. The fireball models of older times implied isotropic decay in the rest frame of the diffractive system, or possibly elongated along the collision axis, but without internal structure. The Ingelman-Schlein (IS) model [9] made the bold assumption that the exchanged Pomeron could be viewed as a hadronic state, and that therefore a diffractive system could be described as a hadron-hadron collision at a reduced energy. This implied the existence of Parton Distribution Functions (PDFs) for the Pomeron. Thereby also hard processes became available, confirmed by the observation of jet production in diffractive systems [10]. The PomPyt program [11] combined Pomeron fluxes and PDFs, largely determined from HERA data, with the PYTHIA event generator of the time [12] to produce complete hadronic final states, and PomWig [13] did similarly for Herwig [14].

One limitation of these models is that they are restricted to the exchange of one Pomeron per hadron-hadron collision, not the multiple ones expected in Regge theory. Translated into a QCD-based, more modern view of such collisions, Multiple Partonic Interactions (MPIs) occur between the incoming hadrons [15]. That is, since hadrons are composite objects, there is the possibility for several partons from a hadron to collide, predominantly by semisoft $2 \rightarrow 2$ QCD interactions. These together create color flows (strings [16]) criss-crossing the event, typically filling up the whole rapidity range between the two beam particles with hadron production. Thereby a “basic” process containing a rapidity gap can lose that by MPIs. (MPIs and soft color exchanges could also be sources of gaps [17, 18], a possibility we will not study further in this article, so as to keep the discussion focused.)

A spectacular example is Higgs production by gauge-boson fusion, $W^+W^- \rightarrow H^0$ and $Z^0Z^0 \rightarrow H^0$, where the naive process should result in a large central gap only populated by the Higgs decay products, since no color exchange is involved. Including MPIs, this gap largely fills up [19], although a fraction of the events should contain no further MPIs [20], a fraction denoted as the Rapidity Gap Survival Probability (RGSP). Such a picture has been given credence by the observation of “factorization breaking” between HERA and the Tevatron: the Pomeron flux and PDFs determined at HERA predicts about an order of magnitude more QCD jet production than observed at the Tevatron, e.g. [21].

In this article the intention is to provide a dynamical description of such factorization breaking, as a function of the hard process studied and its kinematics, and to predict the resulting event structure for hard diffraction in hadronic collisions. This is done in three steps. Firstly, given a hard process selected based on the inclusive PDFs, the fraction of a PDF that should be associated with diffraction is calculated, as a convolution of the Pomeron flux and its PDFs. Secondly, the full MPI framework of PYTHIA, including also the effects of initial- and final-state radiation, is applied to find the fraction of events without any further MPIs. Those events that survive these two steps define the diffractive event fraction, while the rest remain as regular nondiffractive events. Thirdly, diffractive events may still have MPIs within the $\mathbb{P}\mathbb{P}$ subsystem, and therefore the full hadron-hadron underlying-event generation machinery is repeated for this subsystem. The nondiffractive events are kept as they are in this step.

One should not expect perfect agreement with data in this approach; there are too many uncertainties that enter in the description. Nevertheless a qualitative description can be helpful, not only to understand the trend of existing data, but also to pave the way for future studies. The new framework we present here has been implemented as an integrated part of the PYTHIA 8.2 event generator [22], and can be switched on for any standard hard process. It thereby complements the already existing modeling of soft diffraction, i.e. of diffractive events with no discernible hard process. The dividing line between these two descriptions is not sharp, and in the future we will explore tensions between the two.

As should be clear from this introduction, our model is “just” a combination of the existing IS and RGSP ideas, and thus not anything fundamentally new. The devil lies in the details, however, and to the best of our knowledge nobody has previously worked out a complete model of this character.

The article is structured as follows. In section 2 we introduce the new model framework, which then is validated in section 3. Some tentative comparisons with data are presented in section 4. The article concludes with a summary and outlook in section 5.

2 The model

In this article we study hard diffraction, so this means we assume the presence of some hard process in the events of interest. Standard examples would be jet, Z^0 and W^\pm production. By factorization a cross section involving partons i, j from incoming beams A, B can be written as

$$\sigma = \sum_{i,j} \iint dx_1 dx_2 f_{i/A}(x_1, Q^2) f_{j/B}(x_2, Q^2) \hat{\sigma}_{ij}(\hat{s} = x_1 x_2 s, Q^2), \quad (\text{I.1})$$

where $\hat{\sigma}$ is the parton-level cross section, integrated over relevant further degrees of freedom, like a p_\perp range for jets.

Assuming Pomerons to have some kind of existence inside the proton, in the Ingelman-Schlein spirit, we introduce a Pomeron flux $f_{\mathbb{P}/p}(x_{\mathbb{P}}, t)$, where $x_{\mathbb{P}}$ is the \mathbb{P} momentum fraction and t its (spacelike) virtuality. The \mathbb{P} has a partonic substructure, just like a hadron, and thus we can define PDFs $f_{i/\mathbb{P}}(x, Q^2)$. The PDF could also depend on the t scale, just like the photon has a PDF strongly dependent on its virtuality. For lack of a model for such a dependence we assume the \mathbb{P} PDF is a suitable average over the t range probed. As a consequence we will not need t for most of the studies, and so it can be integrated out of the flux, $f_{\mathbb{P}/p}(x_{\mathbb{P}}) = \int f_{\mathbb{P}/p}(x_{\mathbb{P}}, t) dt$.

Given the ansatz with Pomeron flux and PDF, the PDF of a proton can be split into one regular nondiffractive (ND) and one \mathbb{P} -induced diffractive (D) part,

$$f_{i/p}(x, Q^2) = f_{i/p}^{\text{ND}}(x, Q^2) + f_{i/p}^{\text{D}}(x, Q^2), \quad (\text{I.2})$$

where

$$\begin{aligned} f_{i/p}^{\text{D}}(x, Q^2) &= \int_0^1 dx_{\mathbb{P}} f_{\mathbb{P}/p}(x_{\mathbb{P}}) \int_0^1 dx' f_{i/\mathbb{P}}(x', Q^2) \delta(x - x_{\mathbb{P}} x') \\ &= \int_x^1 \frac{dx_{\mathbb{P}}}{x_{\mathbb{P}}} f_{\mathbb{P}/p}(x_{\mathbb{P}}) f_{i/\mathbb{P}}\left(\frac{x}{x_{\mathbb{P}}}, Q^2\right). \end{aligned} \quad (\text{I.3})$$

The assumption that the diffractive part $f_{i/\mathbb{P}}^{\text{D}}(x, Q^2; x_{\mathbb{P}}, t)$ of the full PDF can be decomposed in this way is in approximate agreement with the HERA data [23].

For two incoming protons (or antiprotons, or other hadrons) A and B , an initial probability for diffraction $\mathcal{P}^{\text{D}} \approx \mathcal{P}_A^{\text{D}} + \mathcal{P}_B^{\text{D}}$ is obtained from the ratio of diffractive to inclusive PDFs,

$$\begin{aligned}\mathcal{P}_A^{\text{D}} &= \frac{f_{i/B}^{\text{D}}(x_B, Q^2)}{f_{i/B}(x_B, Q^2)} \quad \text{for } AB \rightarrow XB, \\ \mathcal{P}_B^{\text{D}} &= \frac{f_{i/A}^{\text{D}}(x_A, Q^2)}{f_{i/A}(x_A, Q^2)} \quad \text{for } AB \rightarrow AX,\end{aligned}\tag{I.4}$$

where $\mathcal{P}_{A/B}^{\text{D}}$ is the probability for side A/B to be the diffractive system, thus being dependent on the variables of the opposite side.

This probability is used to determine, on an event-by-event basis, the nature of the selected hard scattering, whether diffractive or not. Currently we concentrate on single diffraction. A natural extension would be to associate the product $\mathcal{P}_A^{\text{D}}\mathcal{P}_B^{\text{D}}$ with central diffraction (CD), where two Pomerons collide and one parton is extracted from each \mathbb{P} . It would also be possible to extend the formalism such that part of the SD rate is reassigned as double diffraction (DD), where the hard collision happens inside one of the two diffractive systems. Neither CD nor DD are considered in this first study, however. Instead, for the fraction $\mathcal{P}_A^{\text{D}}\mathcal{P}_B^{\text{D}}$ of events, which normally is small anyway, a random choice is made between $AB \rightarrow AX$ and $AB \rightarrow XB$.

The key aspect of the model is now that it contains a dynamical gap survival. This means that we do not allow any further MPIs to occur between the two incoming hadrons, so as to ensure that the gap survives. In practice the tentative classification as diffractive, based on eq. (I.4), initially has no consequences: all events are handled as if they were nondiffractive hadron-hadron collisions.

Only if no additional MPIs occur does a diffractive classification survive and only then is the $\mathbb{P}\mathbb{P}$ subsystem set up. Specifically the $x_{\mathbb{P}}$ value is selected according to the distribution implied by eq. (I.4), and also a t value is selected for the outgoing proton. Technically, it is only at this stage that “pure” samples of diffractive events can be selected, should one wish to single out such events.

Once the $\mathbb{P}\mathbb{P}$ system has been set up, it is allowed to develop a partonic structure just like any hadron-hadron collision. Both initial-state radiation (ISR) and final-state radiation (FSR) thereby dress the original hard process by the emission of further softer partons. Also further MPIs inside this system are allowed, based on the $f_{i/\mathbb{P}}(x, Q^2)$ PDFs, successively modified to take into account the momentum and flavors already carried away by the MPI, ISR and FSR activity at p_{\perp} scales above the currently considered one, just like for nondiffractive systems.

The ISR/FSR/MPI description is based on the perturbative parton picture. Nonperturbative aspects have to be added to this. Beam remnants carry the momentum not kicked out of the incoming \mathbb{P} and p . For the former a fictitious “valence quark” content of either $d\bar{d}$ or $u\bar{u}$ is chosen at random for each new event. It is essentially equivalent to having a gluon as remnant, but is slightly more convenient. All outgoing partons are color-connected by color flux lines - strings - that fragment to produce the primary hadrons of the final state. The color flow in an event is not unambiguously determined, however, and data suggest that colors tend to be more correlated than naively comes out of the perturbative picture, a phenomenon known as Color Reconnection (CR).

We can by combining these two simple ideas give an explanation of the discrepancies between Tevatron and HERA. The dynamical gap survival introduces an additional suppression factor, reducing the number of diffractive events without any additional parameters.

2.1 Pomeron fluxes and PDFs

For numerical studies it is necessary to specify Pomeron flux and PDF parametrizations. There are currently seven parametrizations/models for the former and five for the latter available in PYTHIA.

The parametrizations for the Pomeron flux $f_{\mathbb{P}/p}(x_{\mathbb{P}}, t)$ are

- Schuler-Sjöstrand model (SaS) [24],
- the Bruni-Ingelman model [25],
- the Strengh-Berger model [26],
- the Donnachie-Landshoff model [27],
- the Minimum Bias Rockefeller model (MBR) [28] with an option to renormalize the flux, and
- the H1 models Fit A and B [29, 30].

All have to obey an approximate form $f_{\mathbb{P}/p}(x_{\mathbb{P}}) \sim 1/x_{\mathbb{P}}$ in order to obtain an approximate diffractive mass spectrum $\sim dM_X^2/M_X^2$, as required by Regge theory and by data. Just like the rise of the total cross section requires a supercritical Pomeron $\alpha(0) = 1 + \epsilon > 1$, with $\epsilon \approx 0.08$, several of the fluxes have adapted this steeper slope $f_{\mathbb{P}/p}(x_{\mathbb{P}}) \sim 1/x_{\mathbb{P}}^{1+2\epsilon}$ (where the factor of 2 in front of ϵ comes from the optical theorem). There are also some attempts to account for an excess in the low-mass resonance region. The t dependence is typically parametrized as a single exponential $f_{\mathbb{P}/p}(x_{\mathbb{P}}, t) \sim \exp(B_{SD}t)$, but also as a sum of two

exponentials, or as a (power-like) dipole form factor. The MBR model differs from the others, since the model renormalizes the flux to unity. This renormalization suppresses the flux, thus making the dynamical gap survival obsolete. In order to make direct comparisons to the other available flux-models, we have implemented the renormalization as an option with the default being the non-renormalized flux.

The parametrizations for the Pomeron PDFs $f_{i/\mathbb{P}}(x, Q^2)$ are

- PomFix, a simple (toy) Q^2 -independent parametrization,
- the H1 Fit A and B NLO PDFs [29],
- the H1 Jets NLO PDF [31], and
- the H1 Fit B LO PDF [29],
- the ACTW B PDF with $\epsilon = 0.14$ [32],
- the ACTW D PDF with $\epsilon = 0.14$ [32],
- the ACTW SG PDF with $\epsilon = 0.14$ [32],
- the ACTW D PDF with $\epsilon = 0.19$ [32].

The first of these has a momentum sum of unity, whereas the latter are not normalized to any specific value, the argument used being that the Pomeron is not a real particle and so does not obey that kind of constraints [33, 34]. (Technically H1 chose to normalize the \mathbb{P} flux to unity at $x_{\mathbb{P}} = 0.003$, and then let the PDF normalization float. No normalization constraints are included in the ACTW PDFs, as this is primarily set by the normalization of the DL flux. Thus the momentum sum of these PDFs range from 0.5 to 2, depending on fit.) Pragmatically it could be argued that what is measured is the convolution of the \mathbb{P} flux and the \mathbb{P} PDF, so that it is feasible to shuffle any constant number between the two. Unfortunately this makes it less trivial to mix freely, and makes it almost a necessity to combine H1 PDFs with H1 fluxes. In PYTHIA 8, it is only allowed to combine the ACTW PDFs with the DL flux, as these have been fitted together, and each of the fits uses different ϵ values.

No attempts have been made to exclude or validate different flux–PDF combinations in the light of more recent HERA data than available at the time of the fits; this would be a separate project. We do note, however, that a more recent ZEUS article [35] compares a new ZEUS DPDF SJ fit with the H1 Fit B, showing disagreements on the 10–20% level. For our purposes this is an acceptable uncertainty, and we will often use Fit B as a reference, but keep an open mind to variations.

This is not the end of the story from an event-generator point of view, however. In most of the available PDF parametrizations the momentum sums to approximately 0.5, but this does not mean that half of the \mathbb{P} momentum in the $\mathbb{P}p$ collision can just be thought away. At the very least this other half has to be considered as an inert component that sails through without interacting, but is present in the beam remnant. A further complication arises when MPIs are introduced. Normally these are generated in a sequence of decreasing p_\perp , with the PDFs for an MPI adjusted to take into account the momentum and flavors carried away by the preceding MPIs. So if 0.4 of the \mathbb{P} momentum has already been taken, does it mean that 0.1 or 0.6 of it remains? This is an issue that did not exist at HERA, where MPIs are negligible outside of the photoproduction region. The choice made in PYTHIA is to assume that the full \mathbb{P} momentum is available for MPIs. Furthermore we allow the option to rescale the PDFs by a constant factor so as to change the momentum, notably by a factor of two to restore (approximately) the momentum sum rule. This should then be compensated by a corresponding rescaling of the \mathbb{P} flux in the opposite direction. That way the \mathbb{P} can be brought closer to an ordinary hadron, and more \mathbb{P} flux-PDF combinations can be used.

Another problem is that most PDF fits are NLO ones. Given the sparsity of data, it should be clear that “NLO accuracy” does not mean the same thing as it does for the inclusive proton PDF. Since PYTHIA only contains LO matrix elements (MEs) for QCD processes there is no extra bonus for using NLO PDFs. Worse, it is well known that the gluon PDF (of the proton) is much smaller in NLO than in LO for small x and Q^2 ; in principle it can even become negative. This behavior compensates for the NLO MEs being larger than the LO ones in this region, but the compensation is nontrivial. Therefore an all-LO description, for all its weaknesses, is more robust in the small- p_\perp region, which is where the MPI machinery largely operates. The default choice thus is H1 Fit B LO.

Finally also the inclusive proton PDF $f_{i/p}(x, Q^2)$ should be chosen. Here several options come with PYTHIA, and many more can be obtained via the interfaces to LHAPDF5 and LHAPDF6 [36, 37]. The current default set is the NNPDF 2.3 QCD+QED LO one with $\alpha_s(M_Z) = 0.130$ [38]. The argument for using LO has already been outlined above. Since the proton PDF is much better constrained than that of the \mathbb{P} , there is less of a point in varying it between different options consistent with current p data. Note that, for diffractive events, the dependence on the original choice of proton PDF is largely removed on the \mathbb{P} side by applying eq. (I.4). It does remain on the proton side, and in the dynamical calculation of rapidity gap survival, however.

2.2 MPI phenomenology

The QCD $2 \rightarrow 2$ processes are dominated by t -channel gluon exchange, which gives a perturbative cross section $d\hat{\sigma}/dp_\perp^2 \sim \alpha_s^2(p_\perp^2)/p_\perp^4$ that diverges in the $p_\perp \rightarrow 0$ limit. Two

modifications are needed to make sense out of this divergence.

Firstly a divergent integrated QCD cross section should not necessarily be construed as a divergent total pp cross section. Rather a $\mu = \sigma_{2 \rightarrow 2}^{\text{tot}} / \sigma_{\text{pp}}^{\text{tot}} > 1$ for $p_{\perp} > p_{\perp \text{min}}$ should be interpreted as implying an average of μ such partonic interactions per pp collision. Overall energy-momentum conservation will reduce the naively calculated rate, but would still kick out essentially all beam momentum if we allow $p_{\perp \text{min}} \rightarrow 0$, in contradiction with the presence of well-defined beam jets wherein a single particle can carry an appreciable fraction of the incoming beam momentum.

Secondly, therefore, it is important to note the presence of a screening mechanism: whereas standard perturbation theory is based on asymptotically free incoming states, reality is that partons are confined inside color singlet states. This introduces a nonperturbative scale of the size of a hadron, or rather of the average distance d between two opposite-color charges. In this spirit we introduce a free parameter $p_{\perp 0} \sim 1/d$ that is used to dampen the cross section

$$\frac{d\sigma}{dp_{\perp}^2} \propto \frac{\alpha_s^2(p_{\perp}^2)}{p_{\perp}^4} \longrightarrow \frac{\alpha_s^2(p_{\perp 0}^2 + p_{\perp}^2)}{(p_{\perp 0}^2 + p_{\perp}^2)^2}. \quad (\text{I.5})$$

Technically the dampening is implemented as an extra factor multiplying the standard QCD $2 \rightarrow 2$ cross sections, but could equally well have been associated with a dampening of the PDFs; it is only the product of these that enters in measurable quantities.

Empirically, a $p_{\perp 0}$ scale of 2 – 3 GeV is required to describe data. This scale is larger than expected from the proton size alone, and is also in a regime where normally one would expect perturbation theory to be valid. The $p_{\perp 0}$ scale appears to increase slowly with energy, which is consistent with the growth of the number of gluons at smaller x values, leading to a closer-packing of partons and thereby a reduced screening distance d . A similar parametrization is chosen as for the rise of total cross section

$$p_{\perp 0}(E_{\text{CM}}) = p_{\perp 0}^{\text{ref}} \times \left(\frac{E_{\text{CM}}}{E_{\text{CM}}^{\text{ref}}} \right)^{E_{\text{CM}}^{\text{pow}}}, \quad (\text{I.6})$$

with $E_{\text{CM}}^{\text{pow}}$ and $p_{\perp 0}^{\text{ref}}$ being tunable parameters and $E_{\text{CM}}^{\text{ref}}$ a reference energy scale.

With the protons being extended objects, the amount of overlap between two incoming ones strongly depends on the impact parameter b . A small b will allow for many parton-parton collisions, i.e. a high level of MPI activity, and a close-to-unity probability for the incoming protons to interact. A large b , on the other hand, gives less average activity and a higher likelihood that the protons pass by each other unaffected. Diffractive events predominantly occur in peripheral collisions, a concept well-known already from the optical point of view. In our approach it comes out naturally since we only allow one interaction to occur, namely the hard process of interest; if there is a second one this will fill the rapidity gap and kill the diffractive nature.

The shape of the proton and the resulting overlap – the convolution of the two incoming proton distributions – is not known in any detail. The proton electric charge distribution may give some hints, but measures quarks only and not gluons, and is in the static limit. Instead a few different simple parametrizations can be chosen:

- a simple Gaussian, offering no free parameters,
- a double Gaussian, i.e. a sum of two Gaussians with different radii and proton momentum fractions, and
- an overlap of the form $\exp(-b^p)$ (which does not correspond to a simple shape for the individual proton), with p a free parameter.

(A further option is a Gaussian with an x -dependent width, but this has not been implemented in a diffractive context.) All are normalized to unit momentum sum for the incoming partons, and an overall radius normalization factor is fixed by the total cross section.

The more uneven the matter distribution, the broader will the charged multiplicity distribution be. Notably the higher the overlap for central collisions, the higher the tail to very large multiplicities. Also other measures, like forward-backward correlations, probe the distribution. Unfortunately it is always indirectly, and closely correlated with other model details. As an example we can mention that the earliest tunes worked with a much lower $p_{\perp 0}$ than today and with double Gaussians rather far away from the single-Gaussian behavior. This changed when more modern PDFs started to assume a steeper rise of the gluon PDF at small x , and when the PYTHIA parton showers were extended to apply to all MPIs rather than only the hardest one, and for some other improvements over the years. Currently best fits are not very far away from a simple Gaussian, e.g. with an overlap like $\exp(-b^{1.85})$, but still on the side of more peaked than a Gaussian.

An event that contains a high- p_{\perp} interaction is likely to be more central than one that does not, since the former has more MPIs and therefore more chances that the hardest of these reaches a high p_{\perp} . This bias effect is included in the choice of a b for an event where the hardest interaction has been given, and is used in the subsequent generation of MPIs. For the current study of hard diffraction this means that the hard process is initially picked biased towards smaller b values, but afterwards the central b region is strongly suppressed because the likelihood of several MPIs is so big there.

Starting from a hard interaction scale, and a selected b , the probability for an MPI at a lower scale has the characteristic form

$$\frac{d\mathcal{P}}{dp_{\perp}^2} = O(b) \frac{1}{\sigma_{\text{ref}}} \frac{d\sigma_{\text{QCD}}}{dp_{\perp}^2} . \quad (\text{I.7})$$

Here $O(b)$ is the overlap enhancement/depletion factor, $d\sigma_{\text{QCD}}$ the differential cross section for all $2 \rightarrow 2$ QCD processes, and σ_{ref} the total cross section for the event classes affected by the QCD processes. Historically σ_{ref} has been equated with the nondiffractive cross section in PYTHIA, on the assumption that diffraction only corresponds to a negligible fraction of $d\sigma_{\text{QCD}}$. Within the current framework a reformulation to use the full inelastic cross section would make sense, but would require further work and retuning, and is therefore left aside for now.

Given eq. (I.7) as a starting point, MPIs can be generated in a falling p_{\perp} sequence, using a Sudakov-style formalism akin to what is used in parton showers. Actually, in the complete generation the MPI, ISR and FSR activity is interleaved into one common p_{\perp} -ordered chain of interactions and branchings, with one common “Sudakov form factor”, down to the respective cutoff scales.

In the current case, the MPI formalism is used twice. Firstly, to determine whether an event is diffractive, and if not to generate the complete nondiffractive event. Secondly, for diffractive events, to determine the amount of MPI activity within the $\mathbb{P}p$ system. Here eq. (I.7) can be reused, but with new meaning for the components of the equation.

- The $d\sigma_{\text{QCD}}/dp_{\perp}$ is now evaluated using the \mathbb{P} PDF on one side, but with the same damping as in eq. (I.5), where E_{CM} in eq. (I.6) is now the $\mathbb{P}p$ invariant mass. If the \mathbb{P} is supposed to have a smaller size than the proton then this could be an argument for a higher $p_{\perp 0}$ in this situation, but we have not here pursued this.
- The σ_{ref} now represents the $\mathbb{P}p$ total cross section, an unknown quantity that relates to the normalizations of the \mathbb{P} flux and \mathbb{P} PDF. By default it is chosen to have a fixed value of 10 mb, higher than is normally quoted in literature. This way, with other quantities at their default settings, the charged multiplicity of a $\mathbb{P}p$ collision agrees reasonably well with that of a nondiffractive pp one at the same invariant mass. This may not be the best of arguments, but is a reasonable first choice that is experimentally testable, at least in principle.
- The $O(b)$ factor may be changed, see next.

The impact parameter $b_{\mathbb{P}p}$ of the $\mathbb{P}p$ subcollision does not have to agree with the b_{pp} of the whole pp collision. It introduces the transverse matter profile of the Pomeron, even less known than that of the proton. Generally a Pomeron is supposed to be a smaller object in a localized part of the proton, but one should keep an open mind. For lack of better, three possibilities have been implemented, which can be compared to gauge the impact of this uncertainty.

- $b_{\mathbb{P}p} = b_{pp}$. This implicitly assumes that a Pomeron is as big as a proton and centered

in the same place. Since small $b_{\mathbb{P}\mathbb{P}}$ values already have been suppressed, by the MPI selection step, it implies that few events will have high enhancement factors.

- $b_{\mathbb{P}\mathbb{P}} = \sqrt{b_{\mathbb{P}\mathbb{P}}}$ (where normalization is such that $\langle b \rangle = 1$ for minimum-bias events). This can crudely be motivated as follows. In the limit that the \mathbb{P} is very tiny, such that the proton matter profile varies slowly over the width of the \mathbb{P} , then what matters is where the Pomeron strikes the other proton. Thus the variation of $O(b)$ with b is that of one proton, not two, and so the square root of the normal variation, loosely speaking. Technically this is messy to implement, but the current simple recipe provides the main effect of reducing the variation, bringing all b values closer to the average.
- Pick a completely new $b_{\mathbb{P}\mathbb{P}}$, as was done with $b_{\mathbb{P}\mathbb{P}}$ in the first place. This allows a broad spread from central to peripheral values, and thereby also a larger and more varying MPI activity inside the diffractive system than the other two options, and thereby offers a useful contrast.

3 Validation

In this section we summarize some of the tests and sanity checks we have performed on the model implementation. This provide insight into how the model operates and with what general results, but also highlights the uncertain nature of many of the components of the model.

In the model we have two options for when an event is classified as diffractive: either right after the event has passed the PDF selection criterion, eq. (I.4), or after passing the further MPI criterion. Results using only the former will from now on be denoted “PDF selected”, and with the latter in addition “MPI selected”. Our full model for hard diffraction corresponds to the latter, but the intermediate level is helpful in separating the effects of these two rather different physics components.

Notably, many distributions tend to be mainly determined by one of the two criteria. Those mainly sensitive to the PDF selection include the $x_{\mathbb{P}}$ and thereby the mass of the diffractive system, and the squared momentum transfer t of the process and thereby the scattering angle θ of the outgoing proton. In particular we will explore the dependence on Pomeron fluxes and PDFs. Aspects that depend on the details of the MPI model include several particle distributions, such as multiplicities, and that will also be highlighted.

The key number where both components are comparably important is the overall diffractive rate, where each of them gives an order-of-magnitude suppression, resulting in a $\sim 1\%$

fraction of hard events being of a diffractive nature. This number thereby receives a considerable overall uncertainty.

3.1 The Pomeron flux and PDF

We begin by studying the effects of variations of the \mathbb{P} parametrizations. In figures I.1a and I.1b the seven different Pomeron fluxes are compared. As can be seen there is a considerable spread. Even in the region of medium $x_{\mathbb{P}}$ values, $x_{\mathbb{P}} \sim 0.1$, this corresponds to more than a factor of two between the extremes. The dramatic differences at large $x_{\mathbb{P}}$ are not readily visible, since a large- $x_{\mathbb{P}}$ event usually corresponds to a small rapidity gap and therefore is difficult to discern from non-diffractive events. The limit of small $x_{\mathbb{P}}$ generally is more interesting, tying in with the intercept of the Pomeron trajectory, but plays a lesser role for the current study of hard diffraction.

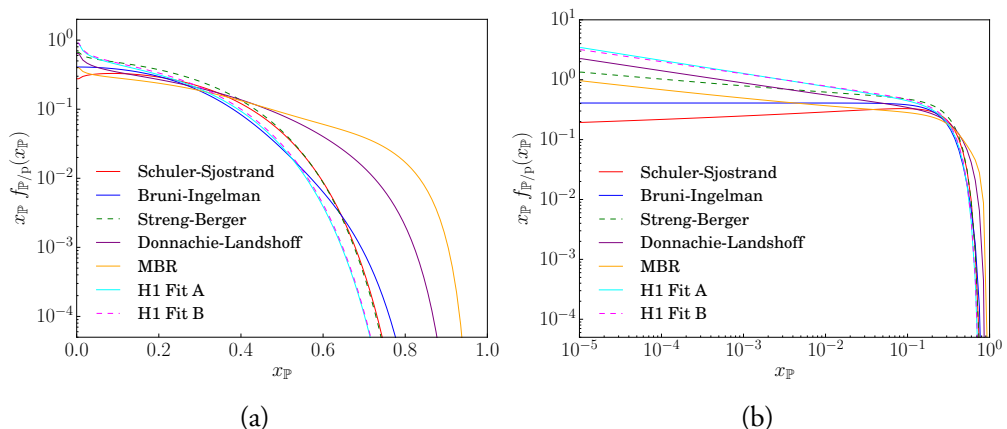


Figure I.1: The seven different Pomeron fluxes included in Pythia on linear (a) and logarithmic scale (b). Note that the MBR flux has not been renormalized (see [28]).

Turning to the Pomeron PDFs, a detailed comparison would entail the separate quark and gluon distributions at varying Q^2 scales. To simplify we show the QCD-charge-weighted sum

$$F_{\mathbb{P}}(x, Q^2) = \frac{4}{9} \sum_{i=q,\bar{q}} x f_{i/\mathbb{P}}(x, Q^2) + x g_{\mathbb{P}}(x, Q^2) \quad (\text{I.8})$$

at a single value $Q^2 = 100 \text{ GeV}^2$, figures I.2a to I.2d. We notice that they all tend to be significantly harder than the corresponding proton PDF, here represented by the NNPDF 2.3 QCD+QED LO one. (The PomFix option is just a toy one, shown for completeness, but not used in the following.) For the gluon on its own, the \mathbb{P} is significantly harder than the p, consistent with the idealized picture of a \mathbb{P} as a glueball state with two “valence gluons”, figures I.3a, b and I.4a, b. Surprisingly, also the quark PDFs of the \mathbb{P} (figures I.3c, d and

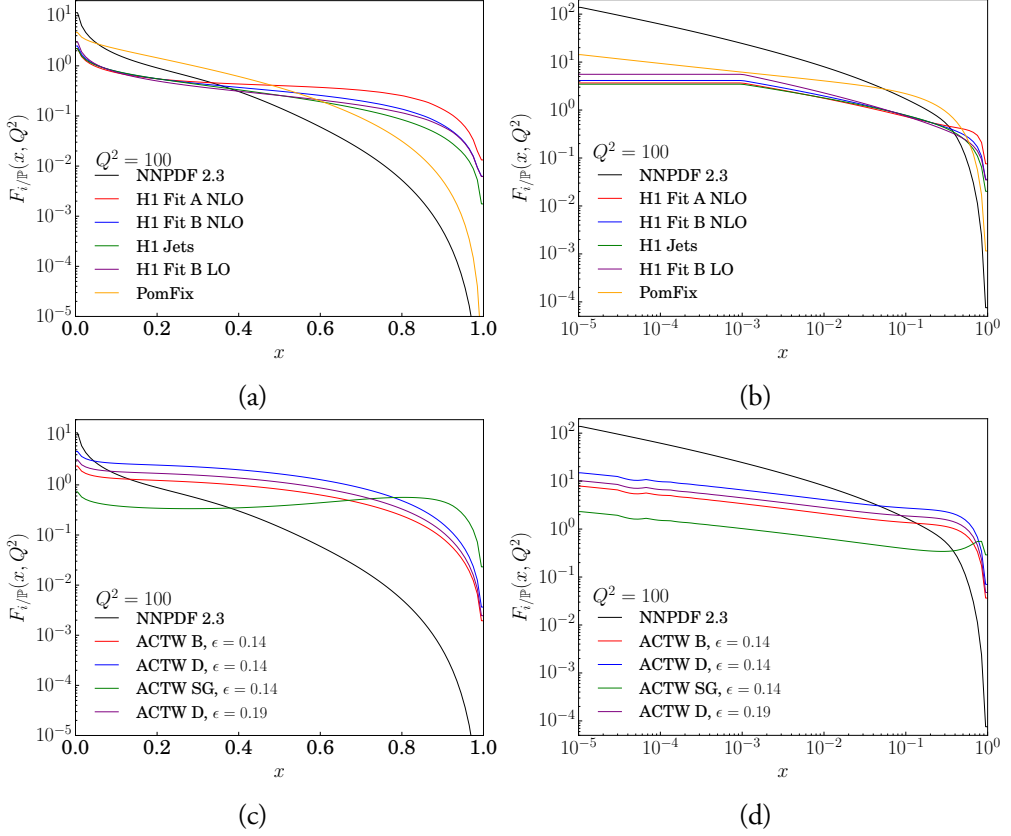


Figure I.2: The QCD charge-weighted sum, eq. (I.8), of the H1 PDFs and the toy PDF PomFix compared to the NNPDF 2.3 proton PDF on linear (a) and logarithmic scale (b). The QCD charge-weighted sum, eq. (I.8), of the ACTW PDFs compared to the NNPDF 2.3 proton PDF on linear (c) and logarithmic scale (d).

I.4c, d) are harder than proton ones, suggesting the presence of “valence quarks” in the \mathbb{P} , although an order of magnitude below the gluons. Another observation is that the \mathbb{P} PDF sets we compare are all primarily based on H1 analyses, with largely the same data and with correlated assumptions for the definition of diffractive events. This is especially notable in the quark distributions, which are close to identical. Also the close affinity of gluons at lower x values should not be overstressed. The slightly larger variations in the ACTW PDFs are due to both the different values of the flux-parameter ϵ , as well as different parametrizations of the PDFs. Finally, note that the H1 parametrizations only apply down to $x = 10^{-3}$, and are frozen below that. This is likely to underestimate the low- x rise of PDFs, which as well could have been of the same shape as in the proton. A small kink in the ACTW PDFs around $x = 10^{-4}$ is due to regions of phase space where the parametrization of the initial quark distribution would become negative and has been reset to vanish.

In the end, what matters is the convolution of the \mathbb{P} flux with its PDFs, and that is shown

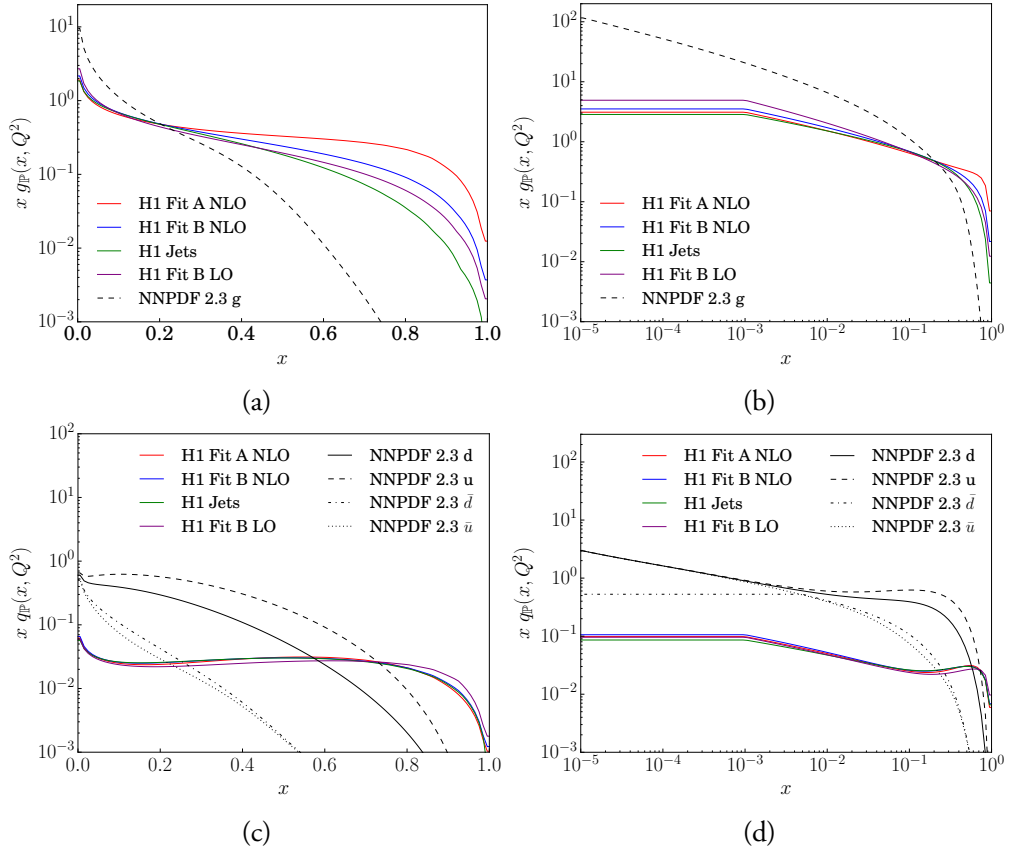


Figure I.3: The H1 \mathbb{P} gluon distribution on linear (a) and logarithmic (b) scale. The H1 \mathbb{P} quark and antiquark distributions on linear (c) and logarithmic (d) scale. Both compared to the NNPDF 2.3 proton PDF distributions. Note that for the \mathbb{P} we have $d = u = s = \bar{d} = \bar{u} = \bar{s} (= c = \bar{c})$, where the c, \bar{c} are only included in H1Jets.

in figure I.5. There would be too many combinations possible to show individually, so we only indicate the range of possibilities and a few specific combinations. This may be on the extreme side, since some fluxes and PDFs come as fixed pairs, not really intended to be mixed freely. The key feature to note is that in this convolution the Pomeron part is now falling steeper at large x than the proton as a whole. This has the immediate consequence that diffractive hard subcollisions are not necessarily going to be produced more in the forwards direction than the bulk of corresponding nondiffractive ones, but on the contrary may be more central. The difference is not all that dramatic, however. It is also partly compensated by a somewhat slower increase of the \mathbb{P} towards lower x values, a feature that for the H1 \mathbb{P} PDF derives from the artificial freezing of below $x = 10^{-3}$. Note that the four different ACTW PDFs differ by up to an order of magnitude. The two D fits are similar in shape and size as expected, but especially the SG fit stands out being up to a factor 10 smaller than the D fits. Most of this discrepancy is also seen in figure I.2c,d but also arise

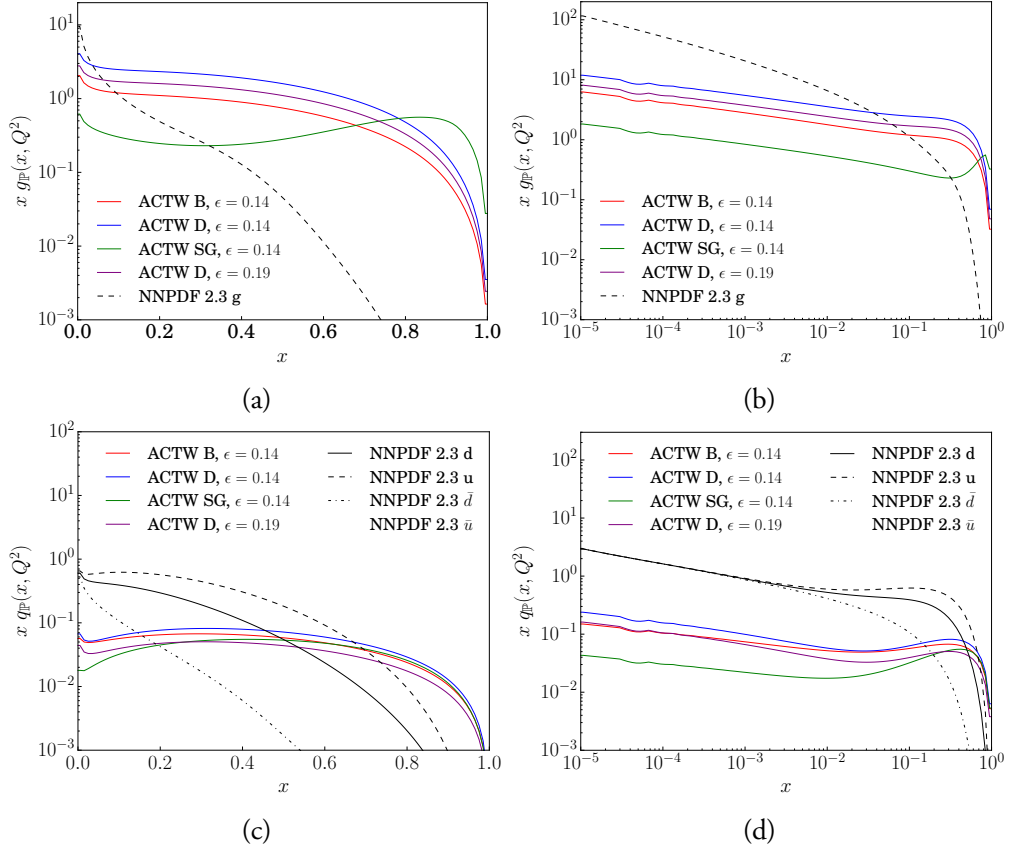


Figure I.4: The ACTW \mathbb{P} gluon distribution on linear (a) and logarithmic (b) scale. The ACTW \mathbb{P} quark and antiquark distributions on linear (c) and logarithmic (d) scale. Both compared to the NNPDF 2.3 proton PDF distributions. Note that for the \mathbb{P} we have $d = u = s = \bar{d} = \bar{u} = \bar{s} (= c = \bar{c})$, where the c, \bar{c} are only included in H1Jets.

from the difference in normalization, the D and SG fits having momentum sums of ~ 1.8 and ~ 0.5 , respectively. The lack of major shape differences between the \mathbb{P} part and the rest will be visible in the more detailed studies later on. Because of the close similarity of most of the different (but related) \mathbb{P} PDFs at low-to-medium x , the bulk of the differences come from the \mathbb{P} fluxes. We have chosen to exemplify this for $2 \rightarrow 2$ QCD processes with $p_{\perp} > 20$ GeV in $\sqrt{s} = 8$ TeV pp collisions, with the diffractive fractions for a few combinations shown in table I.I.

Note that changing the Pomeron parametrizations changes the fraction of events passing the PDF selection, but that the suppression factor introduced by the dynamical gap survival is about ~ 0.07 for all combinations in table I.I. This reflects the fact that neither the MPI model nor the proton PDF are influenced by the Pomeron parametrization, hence the probability for obtaining no additional MPIs in the pp system should not change. (This does not have to hold in general, but here we compare very similar distributions of x and

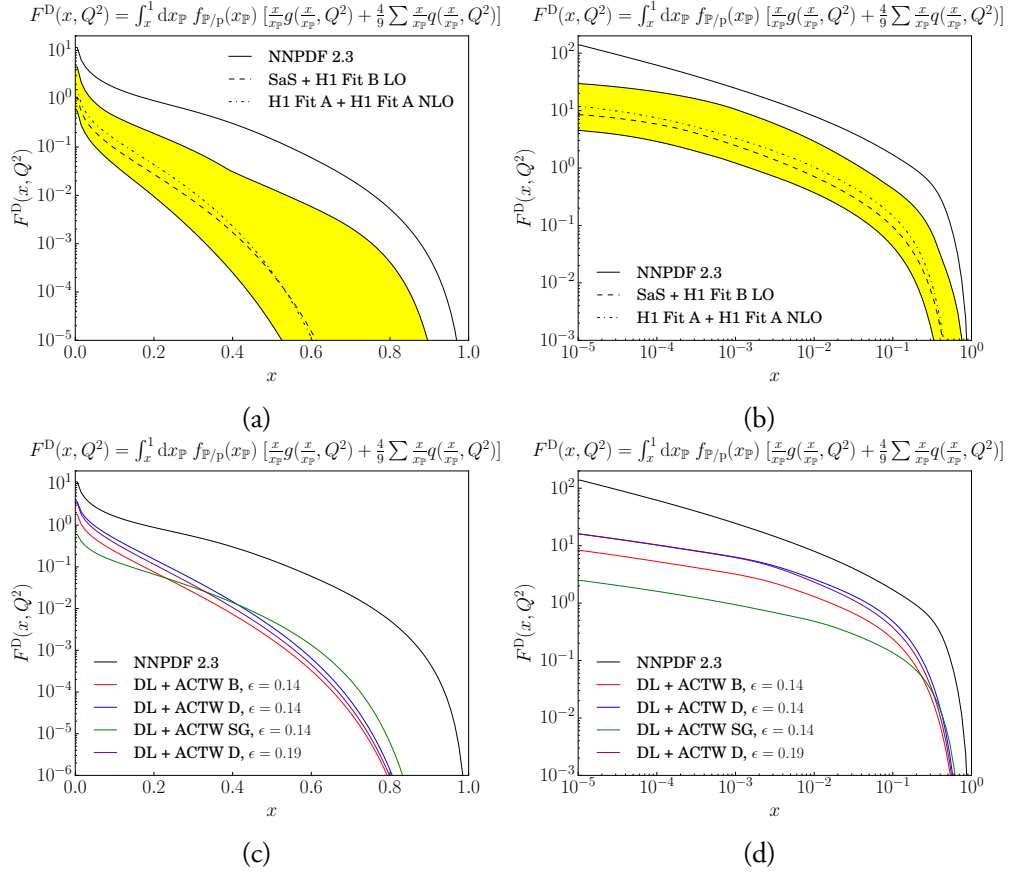


Figure I.5: The convolution of Pomeron fluxes and H1 PDFs for a few cases, with the range between the extremes marked in yellow; (a) linear and (b) logarithmic x scale. The convolution of DL flux and ACTW PDFs on (c) linear and (d) logarithmic x scale.

p_{\perp} values of the hard interaction, and then also the MPI effects are closely the same.) Note also that some of the ACTW PDFs gives substantially larger fractions than the HERA PDFs. This is related to the fact that the intercept of the \mathbb{P} trajectory is larger in ACTW fits than in the H1 ones, $\epsilon = 0.14 - 0.19$ vs. 0.085 . This gives a larger flux at high-energy hadron colliders. A similar flux increase can of course be obtained for the H1 PDFs, with the caveat that the flux might not be able to describe the total cross section and other associated quantities. Additionally the gluon is only probed indirectly in DIS, and so is poorly constrained, while it dominates for QCD jet rates.

Differential distributions of the diffractive events are also affected, since the kinematics of the $\mathbb{P}p$ system is set up using the Pomeron flux parametrizations. A subset of these distributions is shown in figure I.6, for some of the same combinations as in table I.1. As expected, \mathbb{P} PDF variations do not have a large impact on the shapes (cf. figure I.6), while

Table I.1: Diffractive fractions for the $2 \rightarrow 2$ QCD processes with $p_{\perp} > 20$ GeV obtained with Pythia 8. The samples have been produced without any phase-space cuts.

Diffractive fractions pp collisions at $\sqrt{s} = 8$ TeV		
\mathbb{P} PDF \mathbb{P} flux	PDF selection	MPI selection
H1 Fit B LO SaS	$(14.33 \pm 0.11) \%$	$(0.98 \pm 0.03) \%$
H1 Fit B LO MBR	$(14.79 \pm 0.11) \%$	$(0.96 \pm 0.03) \%$
H1 Jets SaS	$(13.70 \pm 0.11) \%$	$(0.92 \pm 0.03) \%$
H1 Fit A NLO H1 Fit A	$(20.55 \pm 0.13) \%$	$(1.35 \pm 0.04) \%$
H1 Fit B LO H1 Fit A	$(18.49 \pm 0.12) \%$	$(1.32 \pm 0.04) \%$
ACTW D14 DL	$(46.54 \pm 0.16) \%$	$(3.18 \pm 0.06) \%$
ACTW SG14 DL	$(11.82 \pm 0.10) \%$	$(0.81 \pm 0.03) \%$
ACTW D19 DL	$(42.09 \pm 0.16) \%$	$(2.89 \pm 0.05) \%$

the \mathbb{P} flux gives rise to large effects in $x_{\mathbb{P}}$, hence on the broadening of the mass spectrum and on the tails of the t and θ distributions. In view of these observations, we do not expect to be able to discriminate between the available Pomeron PDFs when comparing to data. Thus we will leave out this variation from now on, and focus on variations in the Pomeron flux.

The diffractive event fraction is not process-independent. One reason is that processes may be dominated by different initial states, another that different x and Q^2 scales are probed. In table I.2 we show the fraction of events passing either selection for various hard processes available in PYTHIA 8 using the SaS flux and the H1 Fit B LO PDF. Firstly we note that a smaller fraction of events pass the PDF selection than in table I.1, owing to the larger x needed to produce these particles, cf. figures I.1, I.2. This is why top, being the heaviest, has the smallest diffractive fraction. In addition there is a notable difference between the gluon-dominated Higgs production and the quark-induced production of $W^{\pm}/\gamma^*/Z^0$, owing to the hard gluon PDF in the \mathbb{P} . If top production is considered separately for $q\bar{q} \rightarrow t\bar{t}$ and $gg \rightarrow t\bar{t}$, the PDF survival rate is $(9.74 \pm 0.09)\%$ and $(10.55 \pm 0.10)\%$, respectively, displaying the difference between the two production channels.

In figure I.7 we show the rapidity of the W-boson produced in the process $q\bar{q} \rightarrow W^{\pm}$ at an 8 TeV pp collision, comparing three samples; nondiffractive, PDF selected and MPI selected. It is observed that the diffractive W's are slightly more central than the nondiffractive in the CM frame, as expected from figure I.5. The differences are small, however, being

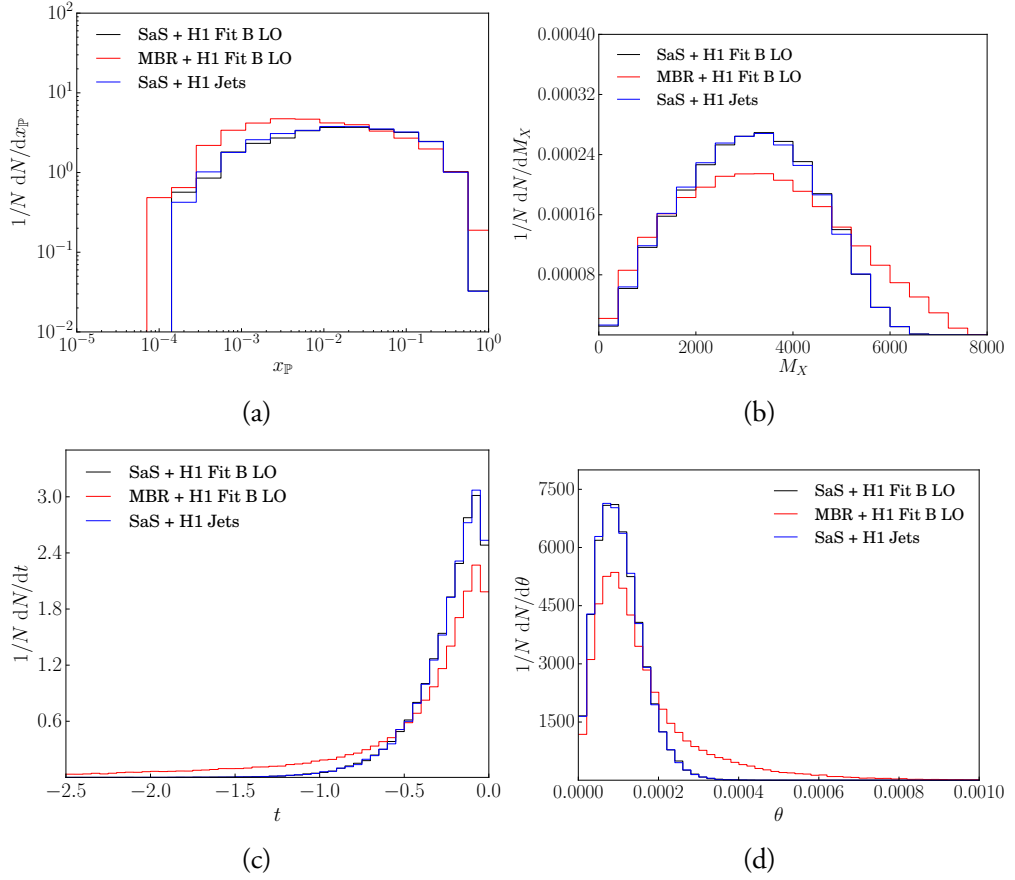


Figure 1.6: Some kinematics distributions obtained with variations of the Pomeron parametrizations: (a) x_p , (b) M_X , (c) t and (d) θ .

Table 1.2: Diffractive fractions obtained with Pythia without any phasespace cuts at $\sqrt{s} = 8$ TeV for various hard processes. Pythia is run with the SaS flux and the H1 Fit B LO PDF.

Diffractive fractions pp collisions at $\sqrt{s} = 8$ TeV		
	PDF selection	MPI selection
$q\bar{q} \rightarrow W^\pm$	$(11.16 \pm 0.10) \%$	$(0.70 \pm 0.03) \%$
$q\bar{q} \rightarrow \gamma^*/Z^0$	$(10.69 \pm 0.10) \%$	$(0.76 \pm 0.03) \%$
Single top and top pair production	$(8.51 \pm 0.09) \%$	$(0.62 \pm 0.02) \%$
SM Higgs production	$(12.37 \pm 0.10) \%$	$(0.86 \pm 0.03) \%$

on the order of (5-10)%, and might reduce when phase-space cuts are introduced. We will study this process further in section 4.1.

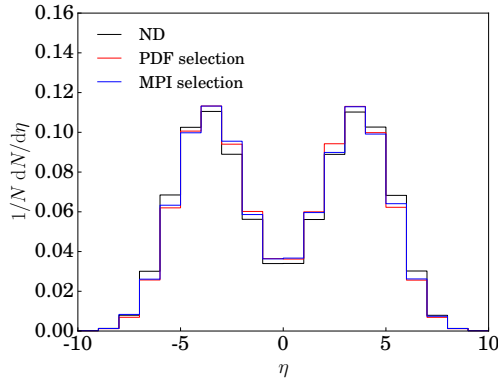


Figure I.7: The rapidity of the W-boson produced in $q\bar{q} \rightarrow W^\pm$ at $\sqrt{s} = 8$ TeV.

3.2 The dynamical gap survival and MPI models

In the above section we studied how the parametrization of the Pomeron flux and PDF affected the diffractive fractions and distributions, and notably by the choice of \mathbb{P} flux. By contrast, we saw that the survival fraction in the MPI selection step was not significantly affected by these choices. A dependence does enter both via the x and the p_\perp distributions of a process: larger x scales leaves less energy for MPIs and thereby gives a higher MPI survival probability, whereas larger p_\perp values gives a longer MPI evolution range and thereby a lower MPI survival. Such effects are not too prominent, however, and tend to be overshadowed by the sensitivity to the parameters of the MPI model. These enter twice. Firstly, for the MPI selection, since the dynamical gap survival is tied to the number of MPIs in the pp system. Secondly, for the properties of the diffractive system, where the number of MPIs affects e.g. charged multiplicities.

The probability for obtaining MPIs is given by eq. (I.7), and hence depends on both the overlap function and the regulator $p_{\perp 0}^{\text{ref}}$. The related parameters are primarily tuned to minimum bias and underlying event data, e.g. charged particle pseudorapidity $dn/d\eta$, multiplicity $P(n)$ and transverse momenta dn/dp_\perp and $\langle p_\perp \rangle(n_{\text{ch}})$ spectra of charged particles. This means that a change of MPI parameters for the diffractive studies would spoil agreement with nondiffractive data. Nevertheless, it is interesting to study how the survival rate changes with these parameters for the pp collision itself.

The MPI modeling of the $\mathbb{P}p$ collision can be decoupled from that of the pp one. Then the MPI survival rate would not be affected by changes, but only the particle distributions in the diffractive system. One inevitable free parameter is the effective $\mathbb{P}p$ total cross section. It is currently set always to be 10 mb, but could be made to depend on the mass of the diffractive system. Also the relative normalization of \mathbb{P} flux and PDFs can influence the event activity. We will study the normalization dependence in the last part of this section.

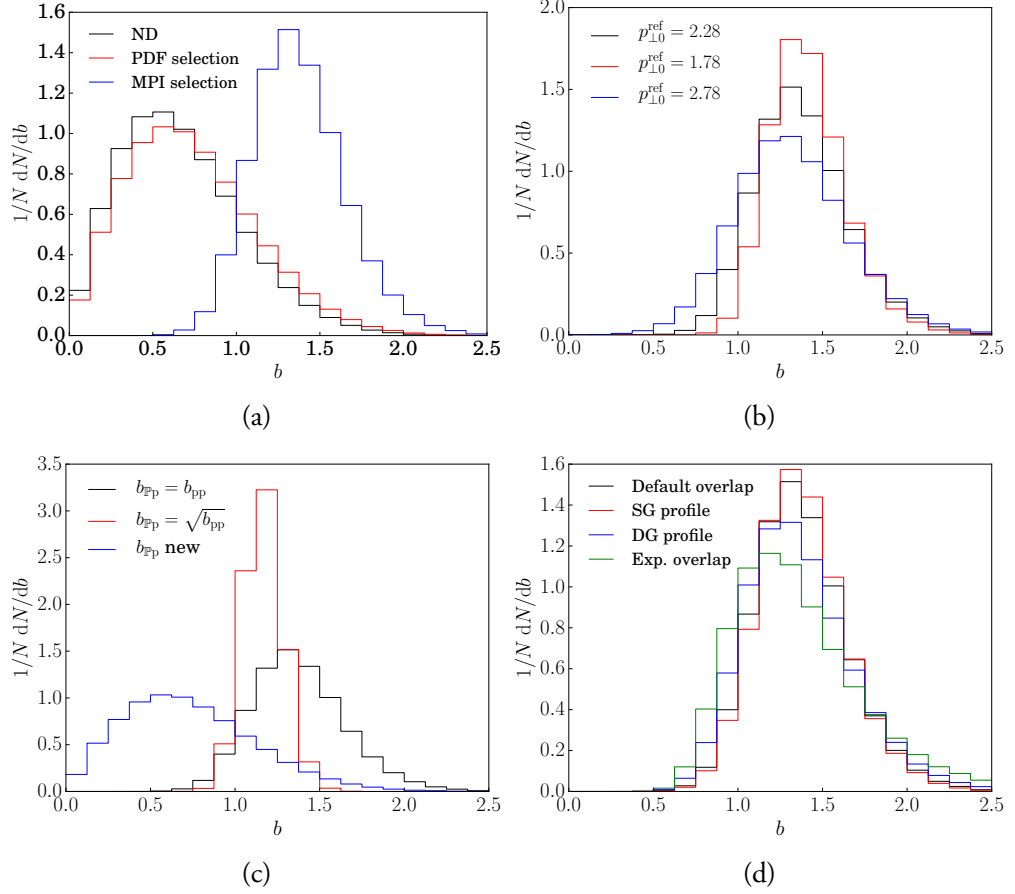


Figure I.8: Impact-parameter distribution of $2 \rightarrow 2$ QCD processes with $p_{\perp} > 20$ GeV in $\sqrt{s} = 8$ TeV pp collisions. (a) The change during the selection steps. (b) The dependence on $p_{\perp 0}^{\text{ref}}$. (c) The distribution in the \mathbb{P}_p subcollision. (d) The dependence on impact-parameter profile.

To begin with, consider the impact-parameter picture associated with hard collisions in our model, figure I.8a. The b scale is normalized such that $\langle b \rangle = 1$ for inclusive minimum-bias events. Events with a hard interaction tend to be more central than that, since central events have more MPIs in general and thereby a bigger likelihood that at least one of them is at large p_{\perp} . The PDF selection step does not have a significant impact, but the MPI one kills most low- b events and pushes $\langle b \rangle$ above unity. The reason is obvious: for central events the average number of MPIs is high, and thus the likelihood of only having the trigger hard process and no further MPIs is small, while more peripheral collisions give fewer MPIs and thereby a higher surviving fraction. Ultimately, when $\langle n_{\text{MPI}}(b) \rangle \ll 1$, most protons pass by each other without colliding at all. Thus the interesting region for diffraction is where $\langle n_{\text{MPI}}(b) \rangle \sim 1$.

The $p_{\perp 0}^{\text{ref}}$ regulator is by default 2.28 GeV. Since an increase in this parameter gives less MPI in the pp system, we expect an increase in the diffractive fractions, and vice versa. table I.3 confirms that this is indeed the case: variations of ± 0.5 GeV around the default $p_{\perp 0}^{\text{ref}}$ value gives about a factor of two in the MPI selection rate. This major $p_{\perp 0}^{\text{ref}}$ dependence holds also for many other nondiffractive event properties, however; keeping everything else fixed even a variation of ± 0.1 GeV would be unacceptable. In figure I.9 we show the charged multiplicity distribution, when we change the regulator $p_{\perp 0}^{\text{ref}}$ for both diffractive and nondiffractive events, with minor/major effects for the former/latter. The stability in the diffractive case is because a change in the regulator also affects the impact parameter picture. Specifically, in this case $b_{\mathbb{P}\mathbb{P}} = b_{\text{pp}}$ has been assumed. A lower value of the regulator, giving rise to a larger number of MPIs in the pp system, pushes $\langle b_{\text{pp}} \rangle$ to larger values for those events that survive the diffractive MPI criterion, figure I.8b. More precisely, the change is to b values where the average pp MPI activity is restored to its original level. With $b_{\mathbb{P}\mathbb{P}} = b_{\text{pp}}$ the same then holds when MPI activity is generated in the diffractive system, such that the effects of a smaller regulator and a larger impact parameter almost completely cancel.

Table I.3: Diffractive fractions for the $2 \rightarrow 2$ QCD processes with $p_{\perp} > 20$ GeV in $\sqrt{s} = 8$ TeV pp collisions. Pythia is run with the SaS flux and the H1 Fit B LO PDF.

Diffractive fractions pp collisions at $\sqrt{s} = 8$ TeV		
	PDF selection	MPI selection
$p_{\perp 0} = 1.78$	$(14.50 \pm 0.11) \%$	$(0.39 \pm 0.02) \%$
$p_{\perp 0} = 2.28$	$(14.33 \pm 0.11) \%$	$(0.98 \pm 0.03) \%$
$p_{\perp 0} = 2.78$	$(14.19 \pm 0.11) \%$	$(2.00 \pm 0.04) \%$

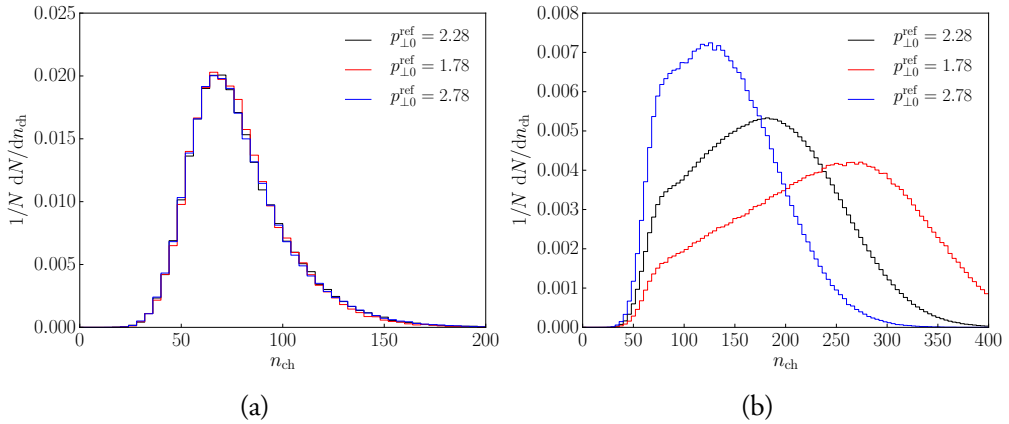


Figure I.9: Charged multiplicity distributions in the (a) $\mathbb{P}\mathbb{P}$ subsystem for diffractive events, (b) pp system for nondiffractive events, in $2 \rightarrow 2$ QCD processes with $p_{\perp} > 20$ GeV as before.

As we have already discussed, the modeling of the \mathbb{P} size could also affect the MPI machinery

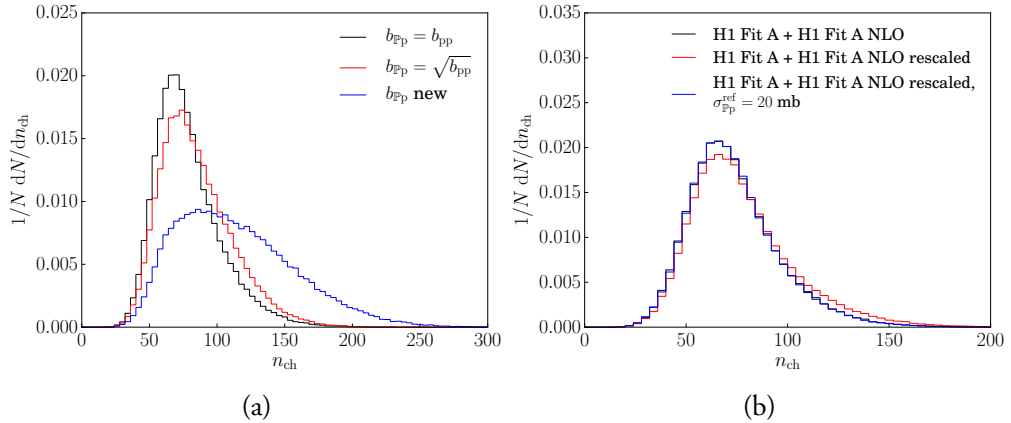


Figure I.10: Charged multiplicity distribution distributions for the $\mathbb{P}p$ diffractive subsystem, for events with $2 \rightarrow 2$ QCD processes with $p_{\perp} > 20$ GeV as before. (a) For three different $b_{\mathbb{P}p}$ impact-parameter profiles. (b) With or without rescaled \mathbb{P} flux and PDFs, see text.

for the $\mathbb{P}p$ subcollision via the impact parameter $b_{\mathbb{P}p}$. The currently implemented three alternatives are compared in figure I.8c. The maybe less realistic last option of picking a new $b_{\mathbb{P}p}$ value at random implies a significant fraction of events with small $b_{\mathbb{P}p}$ and thereby the possibility of many MPIs. The average $\langle n_{\text{MPI}} \rangle$ for the three options is 1.66, 2.04 and 4.09, respectively, thus giving rise to 0.66, 1.04 and 3.09 additional MPIs besides the hardest process. This is reflected notably in the charged multiplicity distribution, figure I.10a.

Table I.4: Diffractive fractions for the $2 \rightarrow 2$ QCD processes with $p_{\perp} > 20$ GeV in $\sqrt{s} = 8$ TeV pp collisions. Pythia is run with the SaS flux and the H1 Fit B LO PDF.

Diffractive fractions pp collisions at $\sqrt{s} = 8$ TeV		
	PDF selection	MPI selection
No impact parameter dependence	$(14.36 \pm 0.11) \%$	$(0.38 \pm 0.02) \%$
Single Gaussian matter profile	$(14.25 \pm 0.11) \%$	$(0.93 \pm 0.03) \%$
Double Gaussian matter profile	$(14.24 \pm 0.11) \%$	$(1.04 \pm 0.03) \%$
Default overlap	$(14.33 \pm 0.11) \%$	$(0.98 \pm 0.03) \%$
Exponential overlap	$(14.50 \pm 0.11) \%$	$(1.28 \pm 0.04) \%$

The MPI survival rate is highly dependent on the proton matter profile, table I.4 and figure I.8d. Diffraction thrives when $\langle n_{\text{MPI}}(b) \rangle \sim 1$, so this b region should be as broad as possible for a large diffractive rate. Conversely, a sharp proton edge implies less diffraction. The default overlap function $\exp(-b^{1.85})$ is close to a Gaussian, and the two have about the same MPI selection rate. The double Gaussian and the exponential overlap are examples of broader distributions, thus with more diffraction, whereas the option without any b dependence represents the other extreme (not shown in figure I.8d), with less diffraction. Overall the variation is not so dramatic, however, if only experimentally acceptable

variations are considered.

Finally we turn to the relative normalization of the \mathbb{P} PDF and flux. From eq. (I.3) we know that the PDF selection step depends on the convolution of the \mathbb{P} flux and PDFs. Thus it has no net effect if the flux is scaled down by a factor of two and the PDFs are scaled up by the same amount, so as to bring the H1 PDFs to be approximately normalized to unit momentum sum. It does have consequences for the MPI selection step, however, since the average MPI rate comes up in the \mathbb{P}_p system.

Compared with the (1.35 ± 0.04) % MPI selection rate in table I.1 for the H1 Fit A flux+PDF combination, such a rescaling changes the rate to (1.40 ± 0.04) %, i.e. no effects are seen. The rescaling however, does change the multiplicity distribution, figure I.10b, as a consequence of the increased $d\sigma_{\text{MPI}}$ in eq. (I.7). This could be compensated by a corresponding increase of σ_{ref} from the default 10 mb to 20 mb, thereby restoring both the MPI selection rate and the multiplicity distribution, cf. the blue line in figure I.10b.

3.3 Energy and scale dependence

Here we study the model dependence on the scales in the hard process and the energy of the collision.

In figure I.11 the diffractive fractions are compared at different collision energies, \sqrt{s} , for $2 \rightarrow 2$ QCD processes with $p_{\perp} > 20$ GeV, and for W^{\pm} production. In the PDF selection step the diffractive rate increases with energy. The difference between the two processes indicates that this rise can depend on the incoming flavors and the relevant ranges of x values. Depending on the \mathbb{P} flux and PDF, such as a freezing of the latter at small x , the fraction might even decrease with energy.

A larger collision energies also implies a higher average number of MPIs, in addition to the hardest collision, thus implying a reduced fraction of events passing the MPI criterion, see figure I.11. There is a compensatory effect of diffraction shifting to larger impact parameters, as already discussed for the $p_{\perp 0}^{\text{ref}}$ variations. For the close-to-Gaussian default overlap the relative size of the $\langle n_{\text{MPI}} \rangle \approx 1$ region decreases with energy, however, resulting in the trend shown. By comparison an exponential overlap decreases slower than the close-to-Gaussian, hence resulting in less suppression with increasing energy.

Finally, table I.5 shows the number of events passing the PDF and MPI selections when the mass of the produced particle is changed. In the PDF selection step heavier particles are less likely to be produced diffractively, as they require larger x -values, where the probability for diffraction is lower (cf. figure I.5). The same trend was observed in table I.2, but was there mixed up by the use of different production channels. After the MPI selection step the mass dependence is not as clearly visible. A partial compensation can indeed occur, since a

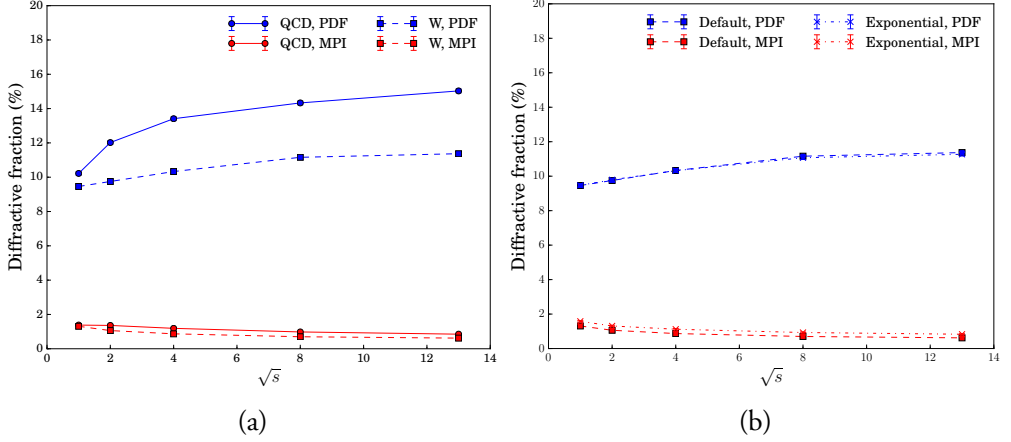


Figure I.11: (a) The diffractive fractions obtained in $2 \rightarrow 2$ QCD processes with $p_{\perp} > 20$ GeV (circles and solid lines) and $q\bar{q} \rightarrow W^{\pm}$ (squares and dashed lines) in pp collisions at different energies. (b) The diffractive fractions obtained in $q\bar{q} \rightarrow W^{\pm}$ with the default overlap function (squares and dashed lines) and the exponential overlap function (crosses and dashed-dotted lines). Pythia is run with the SaS flux and the H1 Fit B LO PDF.

higher subcollision mass implies more momentum taken out of the incoming protons and thereby less left for subsequent collisions.

Table I.5: Diffractive fractions for the process $q\bar{q} \rightarrow Z^0$ in $\sqrt{s} = 8$ TeV pp collisions. Pythia is run with the SaS flux and the H1 Fit B LO PDF.

Diffractive fractions pp collisions at $\sqrt{s} = 8$ TeV		
	PDF selection	MPI selection
$M_W = 50$ GeV	$(11.52 \pm 0.10) \%$	$(0.72 \pm 0.03) \%$
$M_W = 80.385$ GeV	$(10.69 \pm 0.10) \%$	$(0.70 \pm 0.03) \%$
$M_W = 150$ GeV	$(10.46 \pm 0.10) \%$	$(0.72 \pm 0.03) \%$
$M_W = 500$ GeV	$(9.47 \pm 0.09) \%$	$(0.65 \pm 0.03) \%$

3.4 Comparison with soft diffraction

The new model for hard diffraction complements the existing one for soft (or rather inclusive) diffraction. The latter already has a hard component arising from the MPI model, which is used to pick the hardest process and all subsequent scatterings in the $\mathbb{P}p$ system, except for low-mass diffractive systems where no perturbative framework can be applied. The soft diffractive model only allows for $2 \rightarrow 2$ QCD processes, unlike the new hard one, but for QCD processes a comparison between the two is meaningful. To this end, the p_{\perp} of the hardest process in an event will be used. This is not a physically measurable observable, unlike e.g. the closely related p_{\perp} of the hardest jet in an event, but for the relative

comparison of hard and soft diffraction it is cleaner.

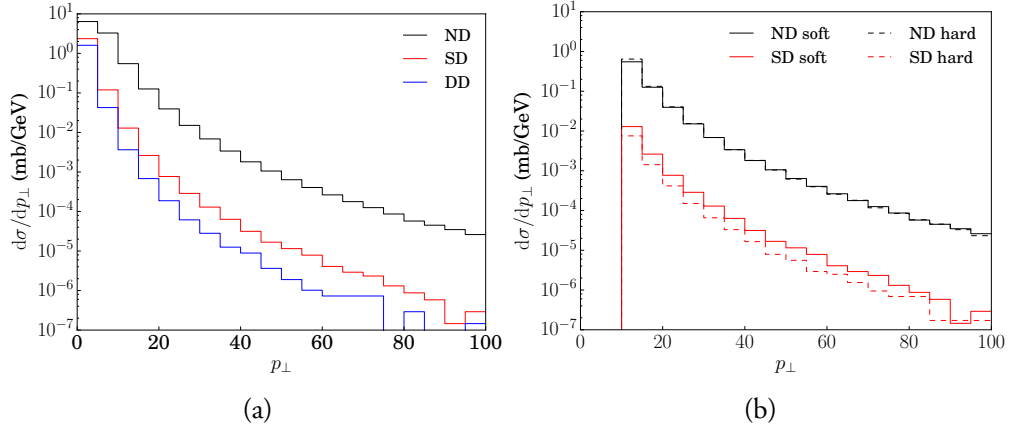


Figure I.12: The p_{\perp} of the hardest process obtained with (a) the soft (or inclusive) diffraction framework, and (b) both the soft and hard diffraction frameworks for events with $p_{\perp} > 10$ GeV.

The MPI framework predominantly gives low- p_{\perp} interactions, be it for diffractive or non-diffractive events. Thus only a small fraction of the events will have p_{\perp} values at ~ 10 GeV or more, see figure I.12a. Note that the p_{\perp} spectrum falls faster for diffractive than nondiffractive events, mainly as a consequence of the former having a $\mathbb{P}\mathbb{P}$ invariant mass spectrum peaked towards lower values.

Table I.6: Cross sections obtained with the two diffractive frameworks. Extracted from figure I.12 by integration.

Cross sections pp collisions at $\sqrt{s} = 8$ TeV		
	Soft diffraction	Hard diffraction
ND sample, $p_{\perp} > 10$ GeV (mb)	3.730	4.239
ND sample, $p_{\perp} > 20$ GeV (mb)	0.348	0.353
SD sample, $p_{\perp} > 10$ GeV (mb)	0.084	0.048
SD sample, $p_{\perp} > 20$ GeV (mb)	0.0066	0.0035

In figure I.12b the p_{\perp} of the hardest process for the two samples is compared. One is obtained by generating inclusive (soft) events and keeping only those with large enough p_{\perp} , the other by generating only hard events above 10 GeV. Nondiffractive events are shown as a sanity check, as for them the two approaches should give the same results. A closer look at integrated cross sections, table I.6, shows a small discrepancy for the $p_{\perp} > 10$ GeV case, while the $p_{\perp} > 20$ GeV agree much better. This discrepancy is caused by not having a “Sudakov factor” in the hard model. That is, in the soft model the rate at lower p_{\perp} scales is reduced by the requirement of not having an interaction at a higher p_{\perp} scale, whereas no such reduction is implemented in the hard framework, which only uses pure matrix

elements.

The single diffractive events show differences in the normalization, while the shape of the p_{\perp} distributions agree between the two frameworks. The normalization differences arise from the two different ways of handling the survival rate. The soft diffractive framework assumes an effective flux of \mathbb{P} 's inside the proton, rescaled to get the desired total diffractive cross section, and thereby implicitly includes an average rapidity gap survival factor. The hard diffractive framework has a higher initial \mathbb{P} flux but then explicitly implements a dynamical event-by-event survival factor. As it works out, single diffractive high- p_{\perp} events are somewhat more suppressed in the latter case. This is indeed what we would expect: there should be more MPIs in high- p_{\perp} (and high-mass) events than in low- p_{\perp} ones, and thus more MPI survival suppression. Put another way, the soft implementation overestimates the suppression at low p_{\perp} and underestimates it at high p_{\perp} . (Assuming our new model is the right way to view the matter.)

In the future it would be desirable to include such dynamical effects also in the soft framework, so that the two descriptions can be made to agree in the high- p_{\perp} region. This is not a trivial task, however.

4 Comparisons with data

In this section we compare the new model for hard diffraction with some available data. While many results have been presented for soft diffractive processes, less is available on hard ones.

At the Tevatron, both the CDF and D0 collaborations studied hard diffractive events. We have chosen here to compare with two analyses, one in which only the diffractive fractions are measured, the other in which also the distributions of the hard collisions are reported.

At the LHC, diffraction has been studied both by ATLAS [39–41] and CMS [42–44]. One key observation there is that the PYTHIA default \mathbb{P} flux shape does not describe the rapidity gap distribution so well, suggesting that a new parametrization may be needed. In other respects the model seems to do a reasonable job. For hard diffraction we will compare to the latest ATLAS study, [41], and a similar CMS study, [43].

Unfortunately, neither of the studies at hand are implemented as Rivet [45] analyses, so we have tried to apply the relevant experimental cuts as best as we can. This makes comparisons with data less than reliable, and results should therefore be taken as a first indication only. At least for LHC the intention is that the new PYTHIA options can be directly tested by the experimental community, to allow more precise comparisons in the future.

Table I.7: Cuts used in [46]. Number of events listed in each of the samples are based on Monte Carlo truth obtained when generating 10^6 inclusive events. A blank means that a specific cut was not relevant.

CDF cuts	W sample			Z sample		
	ND	SD	$\frac{SD \times 2}{ND} (\%)$	ND	SD	$\frac{SD \times 2}{ND} (\%)$
Lepton $E_T^{(p_T^\mu)} > 25$ GeV	670602	2827	0.84	667851	2466	0.74
Missing $E_T > 25$ GeV	595236	2490	0.84	-	-	-
One electron in $ \eta < 2.8$	-	-	-	642250	2366	0.74
One lepton in $ \eta < 1.1$	331316	1374	0.83	366566	1397	0.76
$M_T^W = [40, 120]$ GeV	327671	1361	0.83	-	-	-
$M_Z = [66, 116]$ GeV	-	-	-	36814	1397	0.76
$ t < 1$ GeV ²	-	1348	0.82	-	1383	0.75
$x_{\mathbb{P}} = [0.03, 0.1]$	-	366	0.23	-	346	0.19

4.1 Diffractive W/Z production at the Tevatron

CDF has measured the fraction of events with a diffractively produced W/Z boson at $\sqrt{s} = 1.96$ TeV [46]. The surviving antiproton was measured in a Roman Pot forward spectrometer, and the boson decay products in the central detector. The observed fraction of events with forward antiprotons was doubled, to compensate for there being no Roman Pots on the proton side. Only the e and μ leptonic decays of the bosons were taken into account. The cuts used in the analysis are listed in table I.7, along with the number of events that survive after each step. To this end, the internal W- and Z-finder projections available in Rivet [45] have been used as a starting point; these have previously been validated for other CDF analyses. In addition the diffractive properties are derived from the measured antiproton as

$$t = -p_{\perp}^2 \quad (\text{I.9})$$

$$x_{\mathbb{P}}^{\text{RPS}} = 1 - \frac{2|p_z|}{\sqrt{s}} \quad (\text{I.10})$$

which has been compared to Monte Carlo truth, giving good agreement.

The results in table I.7 are obtained with PYTHIA 8 using the SaS flux and the H1 Fit B LO PDF, starting out from an inclusive MPI-selected sample. We note that a large fraction of the diffractive events do not pass the experimental $x_{\mathbb{P}}$ cut. Therefore, although we begin with a “Monte Carlo truth” fraction of $\sim 1\%$ diffractive W/Z, this is reduced to $\sim 0.2\%$ by the $x_{\mathbb{P}}$ cut. Results look better for other choices of \mathbb{P} flux, see table I.8, but even at best still with a factor two discrepancy. Note that it is the fluxes that rise fastest in the low- $x_{\mathbb{P}}$ region that gives fractions closer to data.

We can compare these values to the results from [32], where no gap survival factor is included. The authors only show results on W production and use different integration limits on $x_{\mathbb{P}}$. A subset of the results are listed in Table I.9. It is worth noting that the results using

Table I.8: Diffractive fractions for the $W \rightarrow l\nu$ and $Z \rightarrow l^+l^-$, $l = e, \mu$ in $\sqrt{s} = 1.96$ TeV $p\bar{p}$ collisions.

\mathbb{P} PDF		
\mathbb{P} flux	$(p\bar{p} \rightarrow \bar{p}' + W) \times 2$	$(p\bar{p} \rightarrow \bar{p}' + Z) \times 2$
CDF	$(1.0 \pm 0.11) \%$	$(0.88 \pm 0.22) \%$
H1 Fit B LO		
SaS	$(0.19 \pm 0.03) \%$	$(0.24 \pm 0.04) \%$
H1 Fit B LO		
MBR	$(0.29 \pm 0.04) \%$	$(0.20 \pm 0.03) \%$
H1 Jets		
SaS	$(0.29 \pm 0.04) \%$	$(0.24 \pm 0.04) \%$
H1 Fit A NLO		
H1 Fit A	$(0.46 \pm 0.05) \%$	$(0.35 \pm 0.04) \%$
H1 Fit B LO		
H1 Fit A	$(0.44 \pm 0.05) \%$	$(0.29 \pm 0.04) \%$

Table I.9: Diffractive fractions for the W production from [32].

\mathbb{P} PDF		
\mathbb{P} flux	$x_{\mathbb{P}} = 0.01$	$x_{\mathbb{P}} = 0.1$
CDF	-	$(1.0 \pm 0.11) \%$
Fit B		
DL, $\epsilon = 0.14$	0.14%	5.1%
Fit D		
DL, $\epsilon = 0.14$	0.18%	6.9%
Fit SG		
DL, $\epsilon = 0.14$	0.14%	4.1%

the lower integration limit are of the same order as the default settings of PYTHIA 8, whereas the high integration limit (which is that of CDF) are higher than both data and our model. This we interpret as being due to the lack of suppression factor, as their calculations do not take MPIs into account.

The diffractive fraction can also be increased by changing the free parameters of the MPI framework, with the caveat that nondiffractive events will then no longer describe data as well. Table I.10 shows the diffractive fractions obtained when varying some of the MPI parameters. This variation is still not sufficient when combined with the default flux and PDF in PYTHIA 8. If combined with some of the fluxes in table I.8 it would be possible to obtain fractions close to the experimentally observed values, however.

Table I.10: Diffractive fractions for the $W \rightarrow l\nu$ and $Z \rightarrow l^+l^-$, $l = e, \mu$ in $\sqrt{s} = 1.96$ TeV $p\bar{p}$ collisions.

Parameter	$(p\bar{p} \rightarrow \bar{p}' + W) \times 2$	$(p\bar{p} \rightarrow \bar{p}' + Z) \times 2$
CDF	$(1.0 \pm 0.11) \%$	$(0.88 \pm 0.22) \%$
$p_{\perp 0}^{\text{ref}} = 2.78$ GeV	$(0.59 \pm 0.06) \%$	$(0.49 \pm 0.05) \%$
Exponential overlap	$(0.25 \pm 0.04) \%$	$(0.24 \pm 0.04) \%$

Table I.11: Cuts used in [21].

CDF cuts	
Jet $E_T^{1,2}$	$> 7 \text{ GeV}$
Jet E_T^3	$> 5 \text{ GeV}$
Jet $ \eta^{1,2,3} $	< 4.2
ΔR	0.7
$ t $	$< 1 \text{ GeV}^2$
$x_{\mathbb{P}}^{\text{RPS}}$	$[0.035, 0.095]$

4.2 Diffractive dijets at the Tevatron

Another interesting measurement performed at CDF was the process $\bar{p}p \rightarrow \bar{p} + X_p$, $X_p \rightarrow X + J + J$, i.e. SD dijet production with a leading antiproton. CDF measured this at three different energies, $\sqrt{s} = 630, 1800$ and 1960 GeV [21, 47, 48]. Here not only the diffractive fractions were measured, but a number of differential distributions. Large discrepancies were found between the diffractive structure functions determined from CDF data and those extracted by the H1 Collaboration from diffractive deep inelastic scattering data at HERA. The discrepancies are both in normalization and shape and were interpreted as a breakdown of factorization.

Our comparison focuses on the 1800 GeV data ([21]), since this also includes a measurement of the diffractive structure function. The cuts used in the analysis are listed in table I.11. The jets are identified with the CDF cone algorithm as implemented in Rivet [45], with a cone radius of 0.7 . Jet energy scale corrections for underlying-event activity are done separately for diffractive and nondiffractive events, as outlined in the CDF article, but only has a minor impact on relative rates. The momentum transfer of the antiproton is evaluated using eq. (I.9) and the momentum loss of the antiproton using eq. (I.10).

We begin by evaluating the suppression factor introduced by the MPI framework. This is evaluated by running two samples of 10^6 events, one with and one without the MPI criterion, both using the cuts of table I.11 and the SaS flux and the H1 Fit B LO PDF. We obtain a suppression factor of 0.11 , to be compared with the quoted discrepancies from CDF of 0.06 ± 0.02 (0.05 ± 0.02) when using the H1 Fit 2 (Fit 3), respectively [21]. A similar suppression factor as for SaS is obtained when using the H1 Fit B flux, based on the same parametrization as the H1 Fit 2 and 3 fluxes, although with different values for the free parameters of the model. Using this flux, however, allows for approximately two times more events passing the experimental cuts. This is due to the fact that the H1 Fit B flux is less restrictive in the low- $x_{\mathbb{P}}$ region, where the experiment is performed. Hence we expect better agreement with data when using the H1 Fit B flux, as compared to SaS. We are not able to directly compare to the suppression factors obtained in [32], as these have been calculated with different kinematical cuts (eg. $E_T > 10 \text{ GeV}$ and $0.05 < x_{\mathbb{P}} < 0.1$), but the numbers

obtained are still interesting in their own right. Alvero et al. obtain suppression factors of 0.061 (fit B and DL flux, $\epsilon = 0.14$), 0.029 (fit D, same flux) and 0.12 (fit SG, same flux), thus ranging from the measured suppression factor to our one.

Results on kinematical distributions using both the SaS and the H1 Fit B flux are shown in figure I.13. The SD E_T^* distribution has a steeper falloff than the ND distribution, indicating a lower center-of-mass energy in the collision. Likewise the η^* distribution is shifted towards positive η , the proton direction, indicating a boost of the center-of-mass system. The final kinematical distribution here is the difference in azimuthal angle between the two leading jets. This observable was not shown in the 1800 GeV analysis but in the 1960 GeV one. The SD events there show a tendency to be more back-to-back than the ND ones. This can also be attributed to the lower energy in the $\mathbb{P}\mathbb{P}$ collision than in the full $p\bar{p}$ system, leaving less space for initial-state radiation.

The momentum fraction of the antiproton carried by the subcollision parton can be evaluated from the jets using

$$x = \frac{1}{\sqrt{s}} \sum_{i=1}^3 E_T^i e^{-\eta^i}, \quad (\text{I.11})$$

where the sum is over the two leading jets, plus a third if it has $E_T > 5$ GeV. The result is shown in figure I.14, for the two \mathbb{P} fluxes used in figure I.13. As expected the SaS flux, figure I.14a, suppress the diffractive events too much, as the suppression factor is too large compared to experimental value from CDF. With this flux, the PDF selected samples lie above the CDF data, but then drop by an order of magnitude by the MPI selection, to lie well below the data, by a factor of five. There is also some discrepancy in shape. Changing to the H1 Fit B flux, figure I.14b, the PDF selected sample lies above the data as expected, with the MPI selected sample a bit below, although only by a factor of three. The suppression is still too large, and shapes still disagree, but not as markedly as in figure I.14a.

There are some aspects of the CDF article that we don't understand, however. The key figure 4 of [21] is intended to show the H1 predictions for the diffractive structure function along with the experimentally measured one. The information provided on how the former prediction is obtained is inconsistent with the curve shown, however, in normalization and shape. In the end we therefore put more faith in the suppression factor between CDF and HERA, already presented above, than in absolute numbers. Assuming we could have reproduced the CDF curve intended to represent the predictions of the H1 PDFs, that then is suppressed by an average multiplicative factor of 0.05 – 0.06 in data but 0.11 in our model, we should have been a factor of ~ 2 above data, which is inconsistent with the outcome in figure I.14.

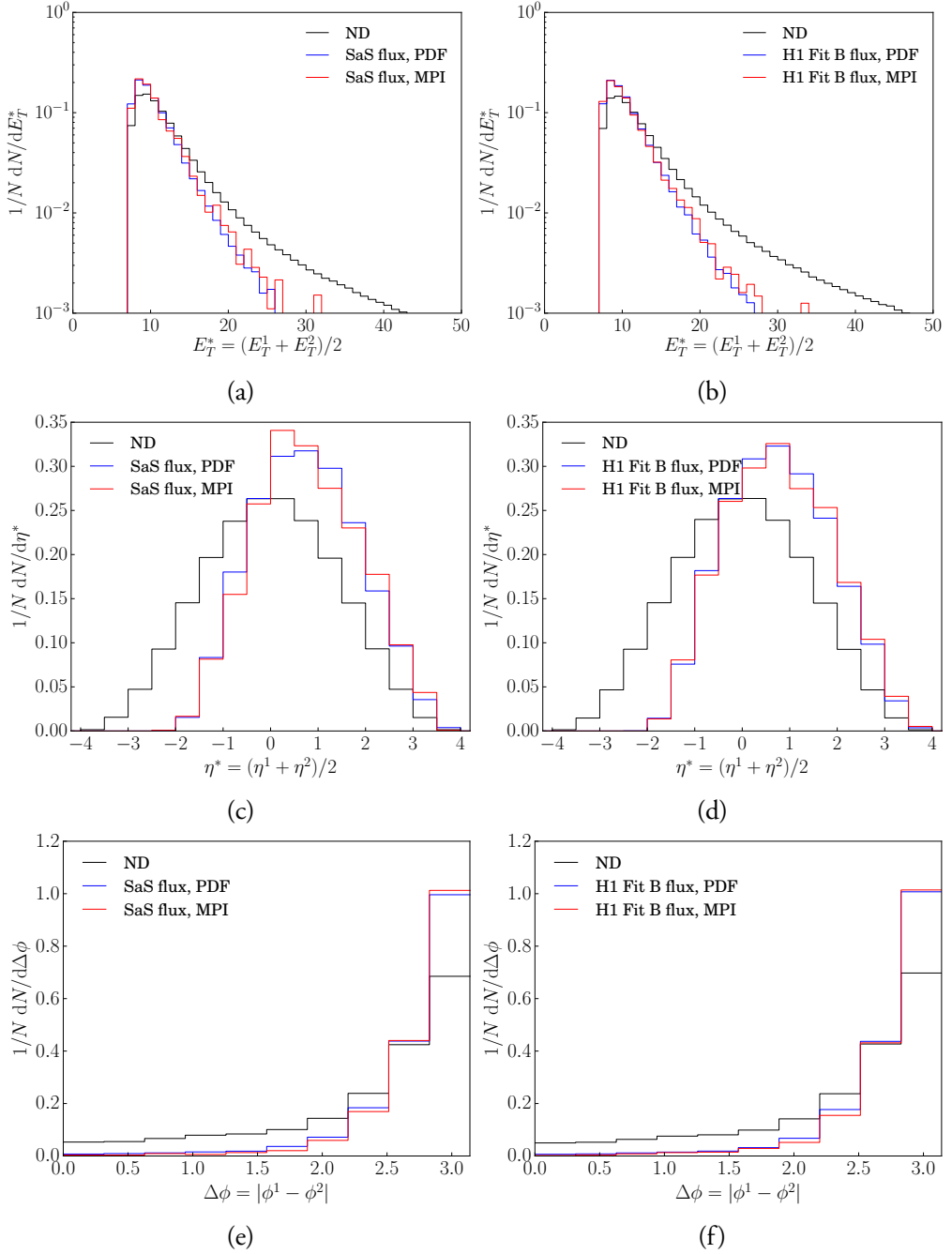


Figure I.13: The mean E_T of the leading jets in both SD and ND events using (a) the SaS and (b) the H1 Fit B flux. The mean η of the leading jets in both SD and ND events using (c) the SaS and (d) the H1 Fit B flux. The mean difference in ϕ between the leading jets in both SD and ND events using (e) the SaS and (f) the H1 Fit B flux.

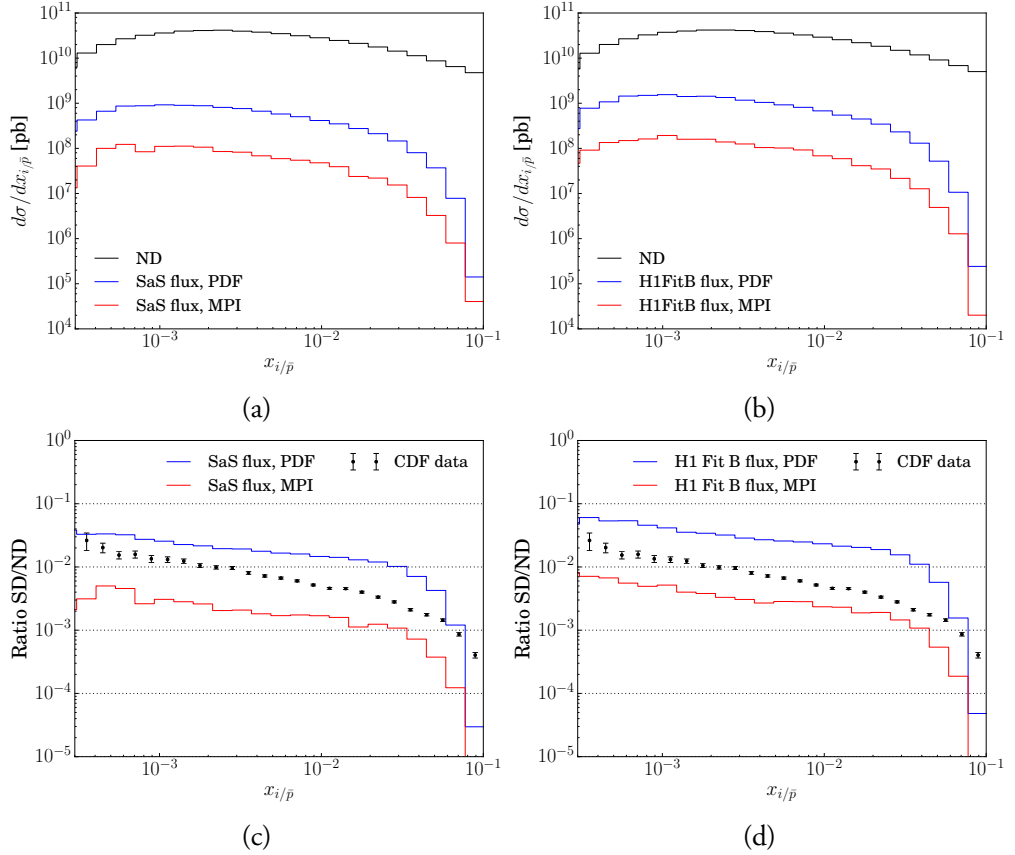


Figure I.14: The antiproton momentum fraction carried by the parton entering the hard collision, for Pythia 8 compared with CDF data. Pythia is run with the H1 Fit B LO PDF and (a) the SaS or (b) H1 Fit B flux. (c) and (d) shows the ratio SD to ND using (a) and (b).

4.3 CMS diffractive contribution to dijet production

CMS has studied the diffractive contribution to dijet events at $\sqrt{s} = 7$ TeV pp collisions [43]. The cross section is presented as a function of $\tilde{\xi}$, an approximation to the fractional momentum loss of the scattered proton corresponding to the $x_{\mathbb{P}}$ variable. Dijets were selected with $p_{\perp} > 20$ GeV in the $|\eta| < 4.4$ range using the anti- k_{\perp} algorithm with a cone size of $R = 0.5$ [49]. $\tilde{\xi}$ was reconstructed using particles in the region $|\eta| < 2.4$ with $p_{\perp} > 0.2$ GeV for charged particles as well as particles in the range $3.0 < |\eta| < 4.9$ with $E > 4$ GeV. To enhance the diffractive contribution additional requirements were introduced, such that the minimum rapidity gap was of 1.9 units (no particles was allowed in the region $|\eta| > 3$). Finally a cut on $\tilde{\xi} < 0.01$ was introduced.

With these cuts, rapidity gap survival probabilities are in the range 0.08 ± 0.04 (NLO) to

Table I.12: Cuts used in [41].

Jet cuts	
Jet $E_T^{1,2}$	$> 20 \text{ GeV}$
Jet $ \eta^{1,2} $	< 4.4
Anti- $k_\perp \Delta R$	0.6
Neutral particles	
$ p $	$> 200 \text{ MeV}$
$ \eta $	< 4.8
Charged particles	
$ p $	$> 500 \text{ MeV or}$
p_\perp	$> 200 \text{ MeV}$
$ \eta $	< 4.8

0.12 ± 0.05 (LO), where the NLO gap survival probability was found using PomPyT and PowHEG [50]+PYTHIA 8 and the LO gap survival probability was found using PomPyT and PomWig.

Implementing the same cuts in PYTHIA 8, using the SaS flux and the H1 Fit B LO PDF gives a rapidity gap survival probability of 0.06, compatible with the CMS results. Changing from the SaS flux to the H1 Fit B flux gives the same suppression factor, but allows for more events to pass the experimental cuts. We thus see the same trend as in the CDF analysis, where the SaS flux is too restrictive at low $x_{\mathbb{P}}$.

4.4 ATLAS dijets with large rapidity gaps

Recently, the ATLAS collaboration published a study of dijets with large rapidity gaps in $\sqrt{s} = 7 \text{ TeV}$ pp collisions [41]. Dijets were selected with $p_\perp > 20 \text{ GeV}$ in the $|\eta| < 4.4$ range, and the cross section was measured in terms of $\Delta\eta^F$, the size of the observed rapidity gap, as well as in $\tilde{\xi} = \sum p_\perp^i e^{\pm\eta^i} / \sqrt{s}$, the estimate of the fractional momentum loss deduced from charged and neutral particles in the ATLAS detector (the sign on η depends on where in the detector the largest gap is located). Cuts used in the analysis are listed in table I.12.

Experimental results were compared with the PYTHIA 8 soft diffractive framework, which predicts both the ND, SD and DD contributions to the dijet production. Three different flux models were compared: SaS, Donnachie-Landshoff and MBR. All three predict cross sections in the range of the data, without any need for additional gap survival probability factors. The PomWig generator [13], on the other hand, needed an additional suppression of $S^2 = 0.16 \pm 0.04(\text{stat}) \pm 0.08(\text{sys})$ in order to describe data.

In this section we use the new model for hard diffraction to study the same cross sections. The new model currently only includes the SD contribution, hence we will not be able to

describe all aspects of data, especially in the high- $\Delta\eta^F$ and low- $\tilde{\xi}$ -regions, where the SD and DD contributions are comparable in size, at least according to the soft diffraction model available in PYTHIA 8. We could also expect the normalization of the SD events obtained with the hard diffraction framework to be lower than in the soft one and thus in data, because of the difference in normalization between the two frameworks (cf. section 3.4). The ND contribution should not differ from the ATLAS analysis, however, since no changes have been implemented in this framework.

The ND distribution was normalized to data, where the normalization factor was found using the first bin of the $\Delta\eta^F$ distribution. This approach has also been used in our analysis, although when generating an inclusive sample (e.g. the purple distribution in figures I.15b and I.15d) this normalization is applied to the full sample, unlike in the ATLAS paper. In this sample, no classification of events occurs, hence the normalization cannot be performed only on the ND sample. In the exclusive samples, the distinction between ND and SD is performed, and we can apply the normalization to only the ND sample (cf. the black distribution in figures I.15b and I.15d).

In figure I.15 we show the results obtained with the model for hard diffraction. Three samples are compared: ND, PDF-selected SD and MPI-selected SD. Note that the MPI-selected sample lies about a factor of 10 below the PDF-selected one, as usual, and that the suppression due to the MPI-framework is constant over both intervals. The new model undershoots the data in the regions where the DD contribution is non-negligible ($\Delta\eta^F > 1$ and $\log_{10}\tilde{\xi} < -0.5$). When this contribution is included in the framework, a better agreement with data should be possible, and overall the picture should be consistent with the soft diffractive framework.

5 Summary and outlook

In this article we have studied hard diffraction by combining two concepts, the Ingelman–Schlein picture of a Pomeron and the PYTHIA model for multiparton interactions. The Pomeron fluxes and PDFs are mainly extracted from HERA data, while the MPI picture (and several other relevant physics components) makes use of a broader spectrum of Tevatron and LHC data. This combination allows us, in principle, to predict all physical quantities of hard diffractive events, from rapidity gap sizes to charged multiplicity distributions, but most importantly the fraction of diffractive events for any hard process.

Reality is not quite as simple, however. In this article we have studied the different assumptions that go into a detailed framework, and explored the inherent uncertainties. One part concerns the assumed Pomeron flux and PDFs, where particularly the latter is dominated by one source only, namely the H1 analyses, making it difficult to assess to full range of un-

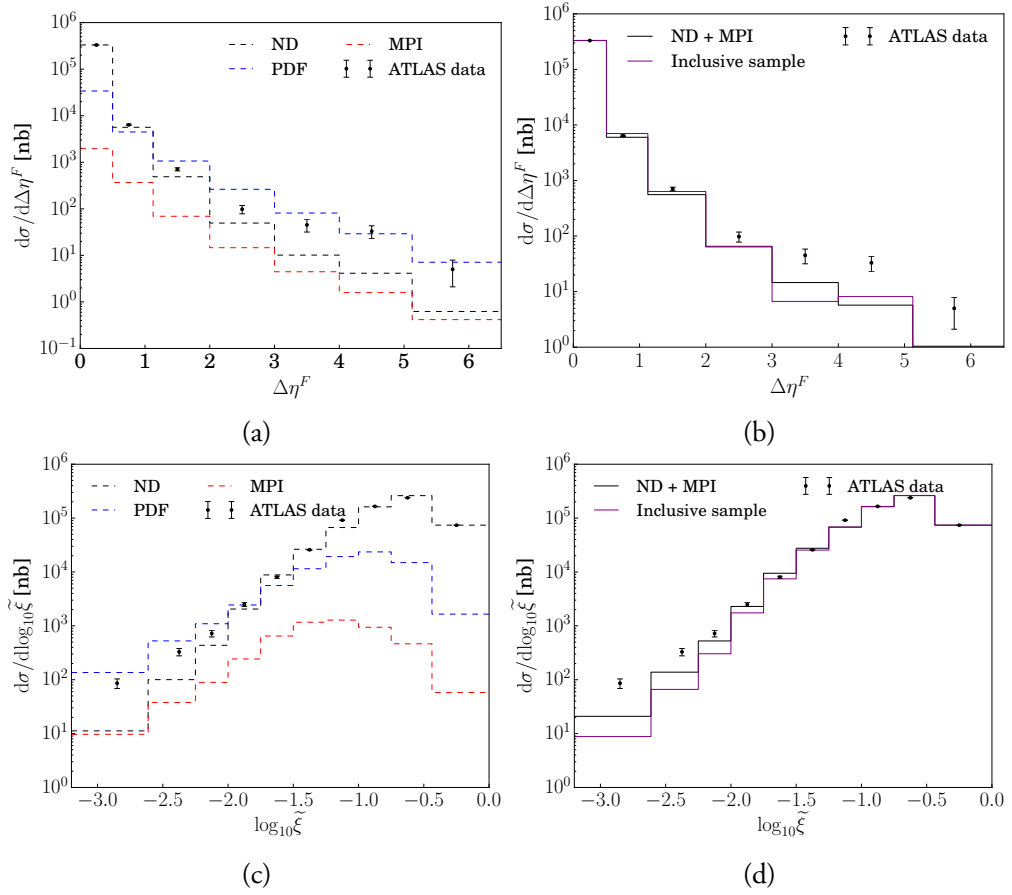


Figure I.15: The dijet cross sections as a function of the size of the rapidity gap (a), (b) and the fractional momentum loss of the proton (c), (d). Compared to the hard diffraction model of Pythia 8 using the SaS flux and H1 Fit B LO PDF. In (b) and (d) the ND + MPI sample is a sum of the black and red dotted lines from (a) and (c), whereas the inclusive sample are generated directly with Pythia 8. Only statistical errors are included in the ATLAS errorbars.

certainty. Another part concerns the MPI framework, which enters twice. When used the first time, to determine the diffractive MPI survival, it involves parameters already tuned to nondiffractive data, so narrowly constrained in principle. There could still be leeway, e.g. if we were to use other parton showers that give less/more activity at small p_{\perp} scales, the average number of MPIs would have to rise/drop to compensate. Thus our studies focus on the sensitivity of some key parameters of the framework. When the MPIs are used the second time, inside the diffractive subsystem itself, the level of uncertainty is considerably higher. A key example is the impact-parameter picture of the $\mathbb{P}\mathbb{P}$ subcollision, notably how impact parameters are related between the $p\mathbb{P}$ and $\mathbb{P}\mathbb{P}$ steps of an event.

Our studies puts the finger on our still limited understanding of diffraction, also when restricted to the Pomeron framework, which is only one model class for diffraction. Fur-

ther, we provide computer code that can be used to compare with data for hard diffractive processes at the LHC. It thus can be used as a “straw man” model, where differences between predictions and data can help pave the way for a deeper understanding and more accurate models. Specifically, with a generator it is possible both to emulate the experimental diffractive trigger and to compare the resulting event properties, both of which are considerably more complicated for analytical models.

Comparisons with data have shown qualitative agreements in many respects, but maybe less so than one could have hoped for. For the Tevatron we face the problem of trying to understand 15 years old analyses, with uncertain results. The main message probably is that the overall Tevatron suppression factor of $\sim 10 - 20$, relative to HERA-based extrapolations, agrees well with what our model gives from the MPI selection step. For the future it will therefore be more interesting to compare with LHC studies, in particular those available in Rivet.

It is well known that the existing PYTHIA model for soft diffraction is not fully describing the existing LHC data; at places the difference can be up to a factor of two. Similarly we have seen less-than-perfect agreement for the hard diffractive processes studied in this article. There is therefore room for improvements in both areas, and also for work to bring the two approaches in closer contact. As one simple example, the soft model currently does not involve a MPI survival step, and therefore the Pomeron flux does not have to be normalized in the same way in the two cases. The intention is to study such issues closer, and to provide an improved description of diffractive cross sections, both integrated and differential ones.

6 Acknowledgments

We thank Marek Tasevsky for detailed descriptions of the ATLAS analysis and providing the data used in figure I.15. Work supported in part by the Swedish Research Council, contract number 621-2013-4287, and in part by the MCnetITN FP7 Marie Curie Initial Training Network, contract PITN-GA-2012-315877. This project has also received funding from the European Research Council (ERC) under the European Union’s Horizon 2020 research and innovation programme (grant agreement No 668679).

References

- [1] M. L. Good and W. D. Walker, Phys. Rev. **120** (1960) 1857.
- [2] M. L. Perl, “High Energy Hadronic Physics” (Wiley-Interscience, 1974, ISBN 0-471-68049-4).
- [3] J. R. Forshaw and D. A. Ross, “Quantum Chromodynamics and the Pomeron,” (Cambridge University Press, 1997, ISBN 0 521 56880 3).
- [4] H. Jung, hep-ph/9809374.
- [5] V. Barone and E. Predazzi, “High-Energy Particle Diffraction” (Springer, 2002, ISBN 3-540-42107-6).
- [6] S. Donnachie, H. G. Dosch, O. Nachtmann and P. Landshoff, “Pomeron Physics and QCD” (Cambridge University Press, 2002, ISBN 0 521 78039 X).
- [7] H. Jung, R. B. Peschanski and C. Royon, Acta Phys. Polon. B **33** (2002) 3645 [hep-ph/0209143].
- [8] M. G. Albrow, T. D. Coughlin and J. R. Forshaw, Prog. Part. Nucl. Phys. **65** (2010) 149 [arXiv:1006.1289 [hep-ph]].
- [9] G. Ingelman and P. E. Schlein, Phys. Lett. B **152** (1985) 256.
- [10] R. Bonino *et al.* [UA8 Collaboration], Phys. Lett. B **211** (1988) 239.
- [11] P. Bruni and G. Ingelman, Conf. Proc. C **930722** (1993) 595.
- [12] T. Sjöstrand, Comput. Phys. Commun. **82** (1994) 74.

- [13] B. E. Cox and J. R. Forshaw, *Comput. Phys. Commun.* **144** (2002) 104 [[hep-ph/0010303](#)].
- [14] G. Corcella, I. G. Knowles, G. Marchesini, S. Moretti, K. Odagiri, P. Richardson, M. H. Seymour and B. R. Webber, *JHEP* **0101** (2001) 010 [[hep-ph/0011363](#)].
- [15] T. Sjöstrand and M. van Zijl, *Phys. Rev. D* **36** (1987) 2019.
- [16] B. Andersson, G. Gustafson, G. Ingelman and T. Sjöstrand, *Phys. Rept.* **97** (1983) 31.
- [17] W. Buchmuller and A. Hebecker, *Phys. Lett. B* **355** (1995) 573 doi:10.1016/0370-2693(95)00721-V [[hep-ph/9504374](#)].
- [18] A. Edin, G. Ingelman and J. Rathsman, *Phys. Lett. B* **366** (1996) 371 doi:10.1016/0370-2693(95)01391-1 [[hep-ph/9508386](#)].
- [19] Y. L. Dokshitzer, V. A. Khoze and T. Sjöstrand, *Phys. Lett. B* **274** (1992) 116.
- [20] J. D. Bjorken, *Phys. Rev. D* **47** (1993) 101.
- [21] T. Affolder *et al.* [CDF Collaboration], *Phys. Rev. Lett.* **84** (2000) 5043.
- [22] T. Sjöstrand, S. Ask, J. R. Christiansen, R. Corke, N. Desai, P. Ilten, S. Mrenna and S. Prestel *et al.*, *Comput. Phys. Commun.* **191** (2015) 159 [[arXiv:1410.3012](#) [[hep-ph](#)]].
- [23] F. D. Aaron *et al.* [H1 and ZEUS Collaborations], *Eur. Phys. J. C* **72** (2012) 2175 [[arXiv:1207.4864](#) [[hep-ex](#)]].
- [24] G. A. Schuler and T. Sjöstrand, *Phys. Rev. D* **49** (1994) 2257.
- [25] P. Bruni and G. Ingelman, *Phys. Lett. B* **311** (1993) 317.
- [26] H. Jung, *Comput. Phys. Commun.* **86** (1995) 147.
- [27] A. Donnachie and P. V. Landshoff, *Nucl. Phys. B* **244** (1984) 322.
- [28] R. Ciesielski and K. Goulianos, *PoS ICHEP 2012* (2013) 301 [[arXiv:1205.1446](#) [[hep-ph](#)]].
- [29] A. Aktas *et al.* [H1 Collaboration], *Eur. Phys. J. C* **48** (2006) 715 [[hep-ex/0606004](#)].
- [30] A. Aktas *et al.* [H1 Collaboration], *Eur. Phys. J. C* **48** (2006) 749 [[hep-ex/0606003](#)].
- [31] A. Aktas *et al.* [H1 Collaboration], *JHEP* **0710** (2007) 042 [[arXiv:0708.3217](#) [[hep-ex](#)]].
- [32] L. Alvero, J. C. Collins, J. Terron and J. J. Whitmore, *Phys. Rev. D* **59** (1999) 074022 doi:10.1103/PhysRevD.59.074022 [[hep-ph/9805268](#)].

- [33] A. Donnachie and P. V. Landshoff, Drell-Yan Pairs,” Nucl. Phys. B **303** (1988) 634.
doi:10.1016/0550-3213(88)90423-3
- [34] A. D. Martin, M. G. Ryskin and G. Watt, Phys. Lett. B **644** (2007) 131
doi:10.1016/j.physletb.2006.11.032 [hep-ph/0609273].
- [35] S. Chekanov *et al.* [ZEUS Collaboration], Nucl. Phys. B **831** (2010) 1
doi:10.1016/j.nuclphysb.2010.01.014 [arXiv:0911.4119 [hep-ex]].
- [36] M. R. Whalley, D. Bourilkov and R. C. Group, hep-ph/0508110.
- [37] A. Buckley, J. Ferrando, S. Lloyd, K. Nordstöm, B. Page, M. Rüfenacht, M. Schönherr
and G. Watt, Eur. Phys. J. C **75** (2015) 3, 132 [arXiv:1412.7420 [hep-ph]].
- [38] R. D. Ball *et al.*, Nucl. Phys. B **867** (2013) 244 [arXiv:1207.1303 [hep-ph]].
- [39] G. Aad *et al.* [ATLAS Collaboration], Nature Commun. **2** (2011) 463
doi:10.1038/ncomms1472 [arXiv:1104.0326 [hep-ex]].
- [40] G. Aad *et al.* [ATLAS Collaboration], Eur. Phys. J. C **72** (2012) 1926
doi:10.1140/epjc/s10052-012-1926-0 [arXiv:1201.2808 [hep-ex]].
- [41] G. Aad *et al.* [ATLAS Collaboration], arXiv:1511.00502 [hep-ex].
- [42] S. Chatrchyan *et al.* [CMS Collaboration], Eur. Phys. J. C **72** (2012) 1839
doi:10.1140/epjc/s10052-011-1839-3 [arXiv:1110.0181 [hep-ex]].
- [43] S. Chatrchyan *et al.* [CMS Collaboration], Phys. Rev. D **87** (2013) 1, 012006
doi:10.1103/PhysRevD.87.012006 [arXiv:1209.1805 [hep-ex]].
- [44] V. Khachatryan *et al.* [CMS Collaboration], Phys. Rev. D **92** (2015) 1, 012003
doi:10.1103/PhysRevD.92.012003 [arXiv:1503.08689 [hep-ex]].
- [45] A. Buckley, J. Butterworth, L. Lönnblad, D. Grellscheid, H. Hoeth, J. Monk,
H. Schulz and F. Siegert, Comput. Phys. Commun. **184** (2013) 2803 [arXiv:1003.0694
[hep-ph]].
- [46] T. Aaltonen *et al.* [CDF Collaboration], Phys. Rev. D **82** (2010) 112004
[arXiv:1007.5048 [hep-ex]].
- [47] D. Acosta *et al.* [CDF Collaboration], Phys. Rev. Lett. **88** (2002) 151802
doi:10.1103/PhysRevLett.88.151802 [hep-ex/0109025].
- [48] T. Aaltonen *et al.* [CDF Collaboration], Phys. Rev. D **86** (2012) 032009
doi:10.1103/PhysRevD.86.032009 [arXiv:1206.3955 [hep-ex]].

- [49] M. Cacciari, G. P. Salam and G. Soyez, JHEP **0804** (2008) 063 doi:10.1088/1126-6708/2008/04/063 [arXiv:0802.1189 [hep-ph]].
- [50] S. Alioli, K. Hamilton, P. Nason, C. Oleari and E. Re, JHEP **1104** (2011) 081 doi:10.1007/JHEP04(2011)081 [arXiv:1012.3380 [hep-ph]].

II

Models of Total, Elastic and Diffractive Cross Sections

Christine O. Rasmussen¹ and Torbjörn Sjöstrand¹.

EPJC, 78 (2018) no.6, 461

doi: 10.1140/epjc/s10052-018-5940-8

e-Print: arXiv:1804.10373[hep-ph]

MCnet-18-08 LU-TP 18-06

¹ Dept. of Astronomy and Theoretical Physics, Lund University, Sölvegatan 14A, SE-223 62 Lund, Sweden.

ABSTRACT:

The LHC has brought much new information on total, elastic and diffractive cross sections, which is not always in agreement with extrapolations from lower energies. The default framework in the PYTHIA event generator is one case in point. In this article we study and implement two recent models, as more realistic alternatives. Both describe total and elastic cross sections, whereas one also includes single diffraction. Noting some issues at high energies, a variant of the latter is proposed, and extended also to double and central diffraction. Further, the experimental definition of diffraction is based on the presence of rapidity gaps, which however also could be caused by color reconnection in nondiffractive events, a phenomenon that is studied in the context of a specific model. Throughout comparisons with LHC and other data are presented.

I Introduction

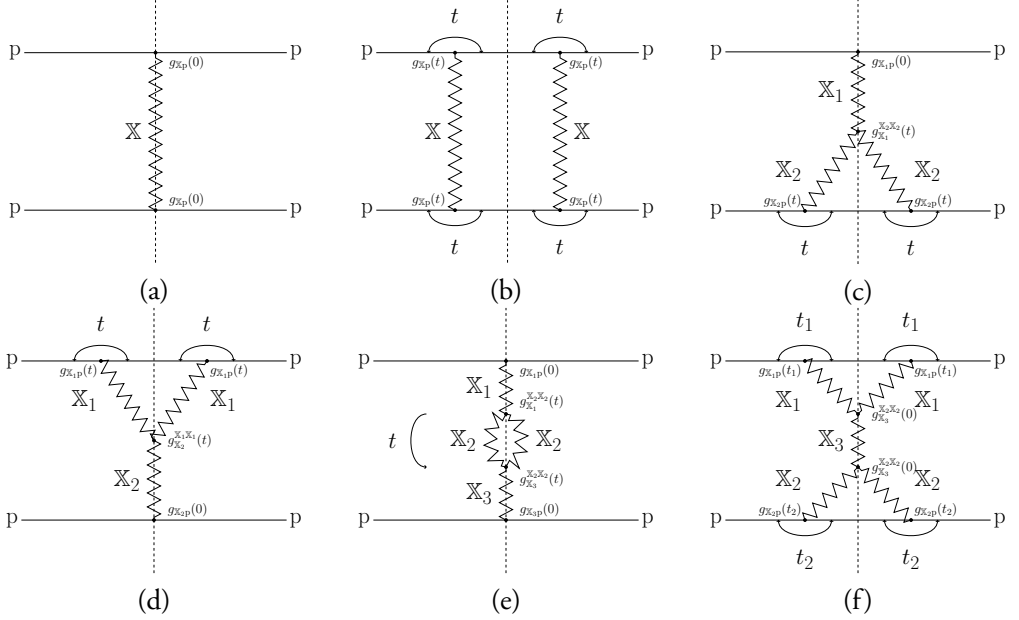


Figure II.1: The squared matrix element for the total (a), elastic (b), single (c,d), double (e) and central (f) diffractive cross sections.

The LHC has provided new information on any number of topics, including total, (differential) elastic and (differential) diffractive cross sections, or σ_{TED} for short. The σ_{TED} kind of quantities cannot be predicted from the QCD Lagrangian, although this is where they have their origin. Therefore σ_{TED} results are often overshadowed by results from the perturbative domain, where comparisons with the Standard Model, and searches for physics beyond it, are more directly related to the underlying theory. Nevertheless, there are good reasons to study the old and new σ_{TED} data now available. One is to assess how well different effective models can describe the data, and implicitly or explicitly pave the way for better models and better understanding, ultimately to form a stronger connection with the underlying QCD theory. Another is that diffractive events form part of the “underlying event” and pileup backgrounds that have a direct impact e.g. on jet energy scales and jet profiles, and thereby on many experimental studies. In this latter aspect they combine with the inelastic nondiffractive events into the overall inelastic event class, with a separation that is far from unambiguous, as we will see. In this article we consider the three simplest diffractive event classes: single, double and central diffraction, corresponding to the dissociation of one, two or zero of the incoming protons, respectively.

Historically there are two main approaches to σ_{TED} in hadron–hadron collisions, the diagrammatical and the geometrical, although both aspects may well be represented in a spe-

cific model [1–4]. In the diagrammatical approach new effective particles are introduced, specifically the Pomeron(s) \mathbb{P} and Reggeon(s) \mathbb{R} , with associated propagators and vertex coupling strengths. A Feynman-diagram-like expansion may be performed into different event classes, with higher-order corrections. A subset of these are shown in fig. II.1, with $\mathbb{X} = \mathbb{P}, \mathbb{R}$ and each of the couplings denoted with a g . In the diagrammatical approach, the dashed line (the cut) represents the diagram at amplitude level. A cut through a \mathbb{P} or \mathbb{R} thus represent particle formation at amplitude level, while an uncut Pomeron or Reggeon represents an area void of particle production. In a geometrical approach the impact-parameter aspects are emphasized, where diffraction largely is related to peripheral collisions. The analogy with wave scattering theory here is natural, and has given the diffractive event class its name. Diffraction can also be viewed as a consequence of the interaction eigenstates being different from the mass ones [5, 6].

Neither of these approaches address the detailed structure of diffractive events. In olden days, at low energies, a diffractive system was simply viewed as an excited proton state that could decay more-or-less isotropically, a “fireball” [1, 7]. This is clearly not a valid picture for higher-mass diffractive states, where the same kind of longitudinal structure is observed as for nondiffractive ones. The simplest partonic approach would then be for a \mathbb{P}/\mathbb{R} to kick out a single quark or gluon from a proton, giving rise to one or two fragmenting color strings. The Ingelman–Schlein picture [8] takes it one step further and introduces an internal structure for the \mathbb{P} , such that a $\mathbb{P}p$ collision may be viewed as an inelastic nondiffractive pp (or better $\pi^0 p$) one in miniature. Thereby also hard jet activity and multiparton interactions (MPIs) become possible within a diffractive system, as supported by data.

A key aspect of MPI modeling is the relation to color reconnection (CR), whereby partons in the final state may be related in color so as to reduce the total string length relative to naive expectations. This opens for another view on diffraction, where CR can generate rapidity gaps dynamically [9, 10]. Then the diffractive and inelastic nondiffractive event classes have a common partonic origin, and only differ by the event-by-event fluctuations in color topologies. Even in models that do not go quite as far, the dividing line between the two kinds of events may be fuzzy. This is even more so since the experimental classification in terms of a rapidity gap allows for misidentification in both directions, relative to the classification in a specific model. High-mass diffraction need not give a gap in the central detector, while nondiffractive events by chance (CR or not) can have a large rapidity gap. The classification of each event type in PYTHIA 8, however, is independent of CR model, such that no double counting occurs on a theoretical level. Each event type has its own specific cross section and, in a combined sample, the mix of event types is based on that. The experimental signature of the events, however, does differ depending on CR model. Thus it is likely that CR models that can give large gaps in nondiffractive events will need a suppression of the diffractive cross sections in order to describe data.

What should now be clear is that description of the σ_{TED} physics, and especially the diffractive part, is too multifaceted to be based purely on analytical calculations. The implementation into Monte Carlo Event Generators is crucial to test different approaches. One of the most commonly used generators is PYTHIA [11, 12], which by default is based on a rather old diagrammatical “tune” for the σ_{TED} issues [13], combined with an Ingelman–Schlein-style approach to the diffractive event structure [14]. In particular the first part does not agree well with LHC data, and so needs an overhaul.

For the total and elastic cross sections we have chosen to implement two different parametrizations, the parametrization from the COMPAS group as found in the Review of Particle Physics 2016 [15] and a model developed by Appleby and collaborators (ABMST) [16]. In addition to a better fit to the integrated cross sections, these also include a more detailed description of the differential elastic cross sections.

The ABMST model also addresses single diffraction. It is in an ambitious diagrammatical approach, supplemented with a careful description of the resonance shape in the low-mass region, based on comparisons with low-energy data. Unfortunately, as is common in such ansätze, the diffractive cross section asymptotically grows faster with energy than the total one, making it marginally acceptable already at LHC energies and definitely unacceptable for FCC ones. We therefore study possible modifications that would give a more reasonable energy behavior. Further, while ABMST does not address double or central diffraction, we use the framework of the model to extend it also to these event classes, and in the process need to make further adjustments. Results for the ABMST-based modeling implemented in PYTHIA are compared with the already existing default framework of Schuler–Sjöstrand (SaS) and Donnachie–Landshoff (DL) [13, 17], and confronted with LHC data.

Furthermore we study the sensitivity to CR by comparing with the Christiansen–Skands QCD-based CR model (CSCR) [18]. This model has no protection against “accidental” rapidity gaps in nondiffractive events, unlike the default CR framework. But it is also not intended to describe (the bulk of) diffraction, and therefore it requires a retuning to provide a sensible combined description. It therefore offers an interesting case study for a tuning task that is likely to become more common in the future.

The plan of the article is as follows: In section 2 we begin by summarizing the current status of PYTHIA 8, the default cross section parametrizations along with the hadronic event properties of diffractive events. In section 3 we describe the new models for total and elastic (differential) cross sections. In section 4, 5, 6 we extend these to single-, double- and central diffractive (differential) cross sections, respectively. In section 7 we provide some comparisons to LHC data and provide new tunes of the default PYTHIA 8 model. We end with section 8, where we summarize and provide an outlook to further studies.

2 The current status of PYTHIA 8

PYTHIA 8 is a multi-purpose event generator aimed at the generation of high-energy events. This includes collisions both of a perturbative and a non-perturbative character, each of which gives contributions to the total collision cross section. In perturbative collisions, the description begins with the matrix element of the hard scattering process in combination with parton distribution functions. This core is dressed up with several other elements such as multiparton interactions, parton showers and hadronization. In non-perturbative scattering collisions, on the other hand, no standard formulation exists for the core process, and phenomenological models are needed. After the model-dependent choices of the key kinematical variables have been made, the event generation may be continued in a similar manner as for perturbative events, where relevant.

In this paper we focus on the non-perturbative scattering processes, and the generation of these. To set the stage for further improvements, the purpose of this section is to describe the current status of the event generator. This we have split into two parts, beginning with the description of the default cross section models, the SaS/DL one, and then go on to describe the event property aspects that are the same regardless of the choice of model.

2.1 Differential cross sections

In the current version of PYTHIA 8, the predictions for the total, elastic and diffractive cross sections do not agree so well with measurements performed at the LHC. The current implementation is the parametrization of DL [17] for the total cross section,

$$\sigma_{\text{tot}}(s) = X^{AB}s^\epsilon + Y^{AB}s^{-\eta}, \quad (\text{II.1})$$

with $s = E_{\text{CM}}^2$, $\epsilon = 0.0808$, $\eta = 0.4525$. A and B denote the initial-state particles, and X^{AB} , Y^{AB} are specific to each such state. The elastic and diffractive cross sections are described using the parametrization of SaS [13],

$$\frac{d\sigma_{\text{el}}}{dt} = (1 + \rho^2) \frac{\sigma_{\text{tot}}^2(s)}{16\pi} \exp(B_{\text{el}}(s) t), \quad (\text{II.2})$$

$$\frac{d\sigma_{XB}(s)}{dt dM_X^2} = \frac{g_{3\mathbb{P}}}{16\pi} \frac{\beta_{A\mathbb{P}}(s) \beta_{B\mathbb{P}}^2(s)}{M_X^2} \exp(B_{XB}(s) t) F_{\text{SD}}(M_X^2, s), \quad (\text{II.3})$$

$$\frac{d\sigma_{AX}(s)}{dt dM_X^2} = \frac{g_{3\mathbb{P}}}{16\pi} \frac{\beta_{A\mathbb{P}}^2(s) \beta_{B\mathbb{P}}(s)}{M_X^2} \exp(B_{AX}(s) t) F_{\text{SD}}(M_X^2, s), \quad (\text{II.4})$$

$$\frac{d\sigma_{XY}(s)}{dt dM_X^2 dM_Y^2} = \frac{g_{3\mathbb{P}}^2}{16\pi} \frac{\beta_{A\mathbb{P}}(s) \beta_{B\mathbb{P}}(s)}{M_X^2 M_Y^2} \exp(B_{XY}(s) t) F_{\text{DD}}(M_X^2, M_Y^2, s), \quad (\text{II.5})$$

where indices X and Y here represent diffractive systems (not to be confused with the coefficients of eq. (II.1)), ρ is the ratio of real to imaginary parts of the elastic scattering amplitude at $t = 0$, $\beta_{A\mathbb{P}}$ and $\beta_{B\mathbb{P}}$ are hadron couplings strengths to the Pomeron, and $g_{3\mathbb{P}}$ the triple-Pomeron vertex strength. The slope parameters are defined as

$$\begin{aligned} B_{\text{el}}(s) &= 2b_A + 2b_B + 4s^\epsilon - 4.2, \\ B_{XB}(s) &= 2b_B + 2\alpha'_{\mathbb{P}} \ln \left(\frac{s}{M_X^2} \right) \\ B_{AX}(s) &= 2b_A + 2\alpha'_{\mathbb{P}} \ln \left(\frac{s}{M_X^2} \right) \\ B_{XY}(s) &= 2\alpha'_{\mathbb{P}} \ln \left(e^4 + \frac{s s_0}{M_X^2 M_Y^2} \right), \end{aligned} \quad (\text{II.6})$$

where $b_i = 2.3$ for $i = p, \bar{p}$, $\alpha'_{\mathbb{P}} = 0.25 \text{ GeV}^{-2}$, $s_0 = 1/\alpha'_{\mathbb{P}}$, and the term e^4 is added by hand in order to avoid $B_{\text{DD}}(s)$ to break down for large values of $M_X^2 M_Y^2$. Special care was taken to avoid unphysical high-energy behaviors; e.g. a logarithmic s dependence of B_{el} would have lead to $\sigma_{\text{el}}(s) > \sigma_{\text{tot}}(s)$ for large s .

Fudge factors are introduced to dampen large (overlapping) mass systems as well as increasing the low-mass “resonance” region, without describing the resonances individually,

$$\begin{aligned} F_{\text{SD}}(M_X^2, s) &= \left(1 - \frac{M_X^2}{s} \right) \left(1 + \frac{c_{\text{res}} M_{\text{res}}^2}{M_{\text{res}}^2 + M_X^2} \right) \\ F_{\text{DD}}(M_X^2, M_Y^2, s) &= \left(1 - \frac{(M_X + M_Y)^2}{s} \right) \left(\frac{s m_{\text{p}}^2}{s m_{\text{p}}^2 + M_X^2 M_Y^2} \right) \\ &\times \left(1 + \frac{c_{\text{res}} M_{\text{res}}^2}{M_{\text{res}}^2 + M_X^2} \right) \left(1 + \frac{c_{\text{res}} M_{\text{res}}^2}{M_{\text{res}}^2 + M_Y^2} \right) \end{aligned} \quad (\text{II.7})$$

where $c_{\text{res}} = 2$ and $M_{\text{res}} = 2 \text{ GeV}$ for pp and $p\bar{p}$.

Central diffraction has been added to PYTHIA 8, but is not widely used in the experimental communities, hence have not been maintained properly after its inclusion. It is off by default, and is not included in any of the tunes performed by the PYTHIA 8 collaboration or the experimental communities. Thus the results obtained with it included should not be trusted too far. The cross section is

$$\sigma_{\text{CD}}(s) = \sigma_{\text{CD}}^{\text{ref}} \frac{\ln^{1.5} \left(\frac{0.06s}{s_{\text{min}}} \right)}{\ln^{1.5} \left(\frac{0.06s_{\text{ref}}}{s_{\text{min}}} \right)}, \quad (\text{II.8})$$

with $\sigma_{\text{CD}}^{\text{ref}} = 1.5 \text{ mb}$, $s_{\text{ref}} = 4 \text{ TeV}^2$ and $s_{\text{min}} = 1 \text{ GeV}^2$. The diffractive mass is chosen from a $(1 - \xi_1)(d\xi_1/\xi_1)(1 - \xi_2)(d\xi_2/\xi_2)$ distribution, with $\xi_{1,2}$ being the momentum

fraction taken from the respective incoming hadron, such that $M_X^2 = \xi_1 \xi_2 s$. The two t values are selected according to exponentials with slope $2b_A + \alpha'_{\mathbb{P}} \ln(1/\xi_1)$ and $2b_B + \alpha'_{\mathbb{P}} \ln(1/\xi_2)$, respectively.

The expressions in eqs. (II.3) – (II.5) can be integrated to give the total elastic and diffractive cross sections. This worked reasonably well up to Tevatron energies, but it overshoot diffractive cross sections observed at the LHC [19]. Simple overall modification factors were therefore introduced [20] to dampen the growth of the diffractive cross sections (including the CD one in eq. (II.8)),

$$\sigma_i^{\text{mod}}(s) = \frac{\sigma_i^{\text{old}}(s) \sigma_i^{\text{max}}}{\sigma_i^{\text{old}}(s) + \sigma_i^{\text{max}}} , \quad (\text{II.9})$$

where the σ_i^{max} are free parameters. The ansatz allows phenomenology at lower energies to be preserved while giving some reasonable freedom for LHC tunes. It gives asymptotically constant diffractive cross sections, but typically with asymptotia so far away that it is not an issue for current studies.

The kinematical limits for t are determined by all the masses in the system. We define the scaled variables $\mu_1 = m_A^2/s$, $\mu_2 = m_B^2/s$, $\mu_3 = M_X^2/s$, $\mu_4 = M_Y^2/s$ where $M_X = m_A$ if A scatters elastically and $M_Y = m_B$ if B scatters elastically. Thus the combinations

$$\begin{aligned} C_1 &= 1 - (\mu_1 + \mu_2 + \mu_3 + \mu_4) + (\mu_1 - \mu_2)(\mu_3 - \mu_4) \\ C_2 &= \sqrt{(1 - \mu_1 - \mu_2)^2 - 4\mu_1\mu_2} \\ &\quad \times \sqrt{(1 - \mu_3 - \mu_4)^2 - 4\mu_3\mu_4} \\ C_3 &= (\mu_3 - \mu_1)(\mu_4 - \mu_2) \\ &\quad + (\mu_1 + \mu_4 - \mu_2 - \mu_3)(\mu_1\mu_4 - \mu_2\mu_3), \end{aligned} \quad (\text{II.10})$$

will lead to the kinematical limits $t_{\min} < t < t_{\max}$.

$$\begin{aligned} t_{\min} &= -\frac{s}{2}(C_1 + C_2) \\ t_{\max} &= \frac{s^2 C_3}{t_{\min}}. \end{aligned} \quad (\text{II.11})$$

These expressions are directly applicable for elastic scattering and for single and double diffraction. For central diffraction $AB \rightarrow AXB$ they can be applied twice, with $\mu_4 = M_{XB}^2/s$ for t_1 and $\mu_3 = M_{AX}^2/s$ for t_2 .

An electromagnetic Coulomb term can be added to describe low- $|t|$ elastic scattering. The implementation is here based on the formalism as outlined e.g. in [21, 22]. Introducing an electromagnetic low- $|t|$ form factor as

$$G(t) \approx \frac{\lambda^2}{(\lambda - t)^2}, \quad \lambda \approx 0.71 \text{ GeV}^2, \quad (\text{II.12})$$

and a Coulomb term phase factor approximation [23, 24]

$$\phi(t) \approx \pm \alpha_{\text{em}} \left(-\gamma_E - \log \left(-\frac{B_{\text{el}}(s) t}{2} \right) \right), \quad (\text{II.13})$$

with $\gamma_E \approx 0.577$, $+$ for pp and $-$ for $p\bar{p}$, Coulomb and interference terms are added to the hadronic $d\sigma_{\text{el}}/dt$ above

$$\begin{aligned} \frac{d\sigma_{\text{el}}^{\text{C+int}}}{dt} &= \frac{4\pi\alpha_{\text{em}}^2 G^4(t)}{t^2} \pm \frac{\alpha_{\text{em}} G^2(t)}{t} \\ &\times (\rho \cos \phi(t) + \sin \phi(t)) \sigma_{\text{tot}}(s) \\ &\times \exp \left(\frac{B_{\text{el}}(s) t}{2} \right). \end{aligned} \quad (\text{II.14})$$

The same expression can also be added to the Minimum Bias Rockefeller (MBR) model [25] (and a flexible “set your own” one), while the ABMST and RPP formalisms each introduce the Coulomb corrections as one extra amplitude term, with the full phase expressions of [24]. Numerically the three implementations give very similar results.

2.2 Hadronic event properties

To model a diffractive system, it is convenient to view its internal structure as a consequence of the interaction between two hadronlike objects, e.g. as a $\mathbb{P}B$ subcollision for the $AB \rightarrow AX$ process, in the same spirit as a high-energy nondiffractive pp event, where perturbative processes largely shape its structure. Such an approach is not viable for low-mass diffractive systems, however. Therefore the diffractive event generation is split into two regimes, a high-mass and a low-mass one, with a smooth transition between the two. The probability for applying the high-mass description is given by [14]

$$P_{\text{pert}} = 1 - \exp \left(-\frac{\max(0, M_X - m_{\text{min}})}{m_{\text{width}}} \right), \quad (\text{II.15})$$

with m_{min} and m_{width} free parameters, both by default 10 GeV. Note how P_{pert} vanishes when below m_{min} .

For very low masses, $M_X \leq m_B + 1$ GeV for a $\mathbb{P}B$ subcollision, the diffractive system is allowed to decay isotropically into a two-hadron state. Above this limit, but still in the nonperturbative regime, the collision process is viewed as the \mathbb{P} kicking out either a valence quark or a gluon from the incoming hadron B . The relative rate of the two is mass-dependent,

$$\frac{P(q)}{P(g)} = \frac{N}{M_X^p}, \quad (\text{II.16})$$

with N and p as free parameters, and M_X in GeV. In the former case a single string will be stretched between the kicked-out quark and the left-behind diquark, whereas the latter gives a “hairpin” string topology, going from one remnant valence quark via the struck gluon and back to the remnant diquark. These strings are then allowed to fragment using the Lund fragmentation model [26]. The default values $N = 5$ and $p = 1$ ensures that the double-string topology wins out at higher masses, consistent with what the exchange of a single gluon (a.k.a. a cut Pomeron) is expected to give in pp collisions.

In the high-mass regime it is assumed that the diffractive cross section factorizes into a Pomeron flux, a

Pomeron–proton cross section, and a proton form factor. Together these determine the mass M_X of the diffractive system and the squared momentum transfer t in the process. Neither the \mathbb{P} flux nor the $\mathbb{P}p$ cross section are known from first principles; therefore seven similar but somewhat different \mathbb{P} flux options are available in PYTHIA 8.

The internal structure of the $\mathbb{P}p$ system is then considered in an Ingelman–Schlein-inspired picture. Thus perturbative processes are allowed, and \mathbb{P} parton distribution functions (PDFs) are introduced like for a hadron. Standard factorization can be assumed, i.e. cross sections are given by hard-scattering matrix elements convoluted with the PDFs of two incoming partons. Furthermore, the full interleaved shower machinery of PYTHIA 8 is enabled, giving rise both to initial- and final-state showers and to multiparton interactions in the $\mathbb{P}p$ system. This results in a more complex color string structure than in the low-mass regime, which can also be subjected to additional color reconnection, owing to overlap and crosstalk between the multiple subsystems.

The activity in the $\mathbb{P}p$ system, as represented e.g. by the average charged multiplicity, can be tuned to roughly reproduce that of a non-diffractive pp collision of the same mass. This activity is closely related to the average number of MPIs per event, the calculation of which differs between the two systems by a \mathbb{P} vs. a p PDF in the numerator, and by $\sigma_{\mathbb{P}p}^{\text{eff}}$ vs. $\sigma_{pp}^{\text{nondiffractive}}$ in the denominator. Given a \mathbb{P} PDF, and assuming the same MPI-framework parameters as in pp, the $\sigma_{\mathbb{P}p}^{\text{eff}}$ thus becomes the main (mass-dependent) tuning parameter. In reality the two systems can be different, however, so experimental information on diffractive mass and multiplicity distributions can be used to refine the tune. Be aware that a different choice of PDFs is likely to require a different $\sigma_{\mathbb{P}p}^{\text{eff}}$ value. Ten different \mathbb{P} PDF sets are implemented [27–30], plus a few toy ones for special purposes. Many of these have been fixed by some convention for the \mathbb{P} flux normalization, that in PYTHIA could be set differently. In principle most of the \mathbb{P} PDFs should only be used with the associated \mathbb{P} flux, as some of the experimentally provided PDFs do not assume a factorization of the \mathbb{P} flux and PDF. In practice the two can be chosen independently, as this opens up for comparative studies. Similarly, the convention used for the \mathbb{P} flux normalization is often dependent on the experimental limits and often normalized to unity at seemingly arbitrary phase space points. Other important aspects, such as the momentum sum rule,

are also usually neglected in the PDFs provided by experiments, but often needed in phenomenological studies. Hence all \mathbb{P} PDFs are implemented with the option to be rescaled, e.g. in order to approximately impose the momentum sum rule.

In the MPI framework [31] the joint probability distribution for extracting several partons from a Pomeron needs to be defined. This is done in the same spirit as for protons [32]. MPIs are ordered in a sequence of decreasing p_\perp scales, and for the hardest interaction the normal PDFs are used. For subsequent ones the x value is interpreted as a fraction of the then remaining \mathbb{P} momentum, thereby ensuring that the momentum sum is not violated. Pomerons are assumed to have no valence quarks; thus the \mathbb{P} PDFs initially only contain gluons and a quark–antiquark-symmetric sea. If a quark is kicked out of the beam, however, flavor conservation requires that an explicit “companion” sea antiquark must also be present in the leftover \mathbb{P} , and vice versa. Such a companion is introduced as an extra component of the \mathbb{P} PDF, similar to a valence (anti)quark, with normalization to unity (just like the d valence in a proton). Overall momentum is preserved by scaling down the gluon and ordinary sea quark distributions to compensate. If the companion is selected for a subsequent MPI, then that “valence” component is removed, and the gluon and sea components of the \mathbb{P} PDF are scaled back up.

Also initial-state radiation (ISR) requires special attention in the MPI framework. ISR is generated starting from the hard interaction and then evolving backwards, to lower scales and larger x values [33]. Such ISR branchings are combined with the MPI generation into one interleaved sequence of falling p_\perp scales. As above special consideration has to be given to branchings that change the flavor of the incoming parton, and that can either induce or remove a companion (anti)quark.

Similar to a proton [32], the Pomeron will leave behind a remnant after the MPIs and showers have removed momentum and removed or added partonic content. To begin, assume that only one gluon is kicked out of the incoming \mathbb{P} . The remnant will then be in a net color octet state, which means that two color strings eventually are stretched to the outgoing partons of the hard collision (or to the other beam remnant). The remnant could only consist of gluons and sea $q\bar{q}$ pairs, since the \mathbb{P} has no valence flavor content, so the simplest representation is as a single gluon or a single $q\bar{q}$ pair. From a physical point of view the two options would give very closely the same end result, since the hairpin string via a gluon remnant eventually would break by the production of $q\bar{q}$ pairs. For convenience, the choice is therefore made to represent the remnant as an octet $u\bar{u}$ or $d\bar{d}$ pair with equal probability. In the general case, further unmatched companion quarks are added to represent the full flavor content needed in the remnant. Most MPI initiators are gluons, however, which carry color that should be compensated in the remnant. This is addressed by attaching the gluon color lines to the already defined remnants, which implicitly introduces color correlations between the initiator partons. Such initial-state correlations can be further enhanced by color reconnections in the final state. The final

color topology decides how strings connect the outgoing partons after the collision, and thereby sets the stage for the hadron production by string fragmentation.

2.3 Hard diffraction

Recently a framework for truly hard diffractive processes have been implemented into PYTHIA [34]. This allows for diffractive subprocesses to generate e.g. hard jets, electroweak particles and other internal PYTHIA processes, unlike the soft-to-medium QCD-only processes that were allowed in the framework described above. This framework decides on whether or not a process is diffractive by evaluating the diffractive part of the proton PDF,

$$\begin{aligned} f_{i/p}^D(x, Q^2) &= \int_0^1 dx_{\mathbb{P}} \int_0^1 dx' f_{\mathbb{P}/p}(x_{\mathbb{P}}) f_{i/\mathbb{P}}(x', Q^2) \delta(x - x_{\mathbb{P}}x') \\ &= \int_x^1 \frac{dx_{\mathbb{P}}}{x_{\mathbb{P}}} f_{\mathbb{P}/p}(x_{\mathbb{P}}) f_{i/\mathbb{P}}\left(\frac{x}{x_{\mathbb{P}}}, Q^2\right), \end{aligned} \quad (\text{II.17})$$

where $f_{\mathbb{P}/p}(x_{\mathbb{P}}) = \int f_{\mathbb{P}/p}(x_{\mathbb{P}}, t) dt$, as t for the most part is not needed. The ratio $f_{i/\mathbb{P}}^D/f_{i/p}$ defines the tentative probability for diffraction. A full evolution of the pp system is then performed and only the fraction of events passing the evolution without any additional MPIs is kept as diffractive. Additional MPIs between the two hadrons give rise to hadronic activity, which could destroy the rapidity gap between the elastically scattered hadron and the interaction subsystem, which is one of the clear experimental signatures of a diffractive event. If the event survives the no-MPI criterion and is classified as diffractive, the partonic sub-collision is assumed to have happened in a $\mathbb{P}p$ sub-system. The $\mathbb{P}p$ system is set up and a full evolution is performed in this subsystem, similar to the method described above.

The no-MPI requirement introduces a gap survival probability determined on an event-by-event basis, unlike other methods used in the literature. As MPIs only occur in hadron-hadron collisions, the framework provides a simple explanation of the differences between the diffractive event rates obtained at HERA and Tevatron. Diffractive fractions and survival probabilities obtained with the new framework show good agreement with experiments, while some distributions show less-than-perfect agreement, see [34] for a discussion. The model is currently only available for single diffraction; future work would be to extend this to both double and central diffraction.

3 Total and elastic cross sections

The parametrizations of the total and elastic cross sections are related through the optical theorem. The elastic cross section has historically been well described in the framework

of Regge theory, with varying complexity based on the number of exchanges included in the model. Up until the LHC era the simple ansatz of DL [17] using only a Pomeron and an effective Reggeon has described the total cross section surprisingly well. With a simple exponential t spectrum, the SaS parametrization [13] extended this to the elastic cross section, and here at least the low- t data was well described. But with the higher energies probed at the LHC it has become obvious that these simple parametrizations fail. More complex trajectories have to be introduced in order to describe both the rise of the total cross section and the t spectrum of the elastic cross section.

We have chosen to implement two additional models in PYTHIA 8. One, the model from the COMPAS group as presented in the Review of Particle Physics 2016 [15], is of great complexity, using six different single exchanges as well as some combinations of double exchanges, along with the exchange of three gluons, the latter becoming important at high $|t|$. The other, the newly developed ABMST model [16], is somewhat simpler, extending the original DL model to four single trajectories and all possible combinations of double exchanges between these, along with the triple-gluon exchange for high $|t|$ values.

Recent TOTEM collaboration data on elastic scattering hint that none of the traditional models describe all aspects of their data. Specifically, TOTEM obtains a decreasing ρ parameter [35], and observes no structure in the high- $|t|$ region (unpublished, but see e.g. [36]). There is an ongoing discussion in both the theoretical and experimental community on how to describe all data simultaneously. None of the models implemented here do that, specifically they do not predict a decreasing ρ value. Further, the ABMST model does not show any sign of structure at high $|t|$, while the COMPAS one does. Models could be extended to include a maximal odderon, similar to the work of Avila et al. [37, 38] (AGN) and Martynov et al. [39] (FMO), which would be able to describe the decrease in ρ . At the time of writing the former has not been fitted to the new TOTEM data and the latter has not been extended to $t \neq 0$. Thus, for now, we have chosen not to implement either in PYTHIA 8, but we show the FMO model in the relevant figures for completeness. Below we will give short descriptions of each of the fully implemented models.

3.1 The COMPAS model

For the Review of Particle Physics 2016 the COMPAS group [15] has fitted a parametrization of the elastic differential cross section to all available pp (upper signs) and $p\bar{p}$ (lower signs) data, using a set of 37 free parameters. The cross sections are functions of the nuclear

amplitude, T_{\pm} , as well as the Coulomb amplitude, T_{\pm}^c ,

$$\begin{aligned}
\sigma_{\text{tot}}(\sqrt{s}) &= \frac{\text{Im}[T_{\pm}(s, 0)]}{\sqrt{s(s - 4m_p^2)}} \\
\frac{d\sigma_{\text{el}}}{dt}(\sqrt{s}, t) &= \frac{|T_{\pm}(s, t) + T_{\pm}^c|^2}{16\pi(\hbar c)^2 s(s - 4m_p^2)} \\
\sigma_{\text{el}}(\sqrt{s}) &= \frac{1}{16\pi(\hbar c)^2 s(s - 4m_p^2)} \int_{t_{\min}}^{t_{\max}} dt |T_{\pm}(s, t)|^2.
\end{aligned} \tag{II.18}$$

The Coulomb term, T_{\pm}^c , and the nuclear term, T_{\pm} , are given as

$$\begin{aligned}
T_{\pm}^c(s, t) &= \pm 8\pi \alpha_{\text{em}} \exp(\mp i \alpha_{\text{em}} \phi_{\pm}^{\text{NC}}(s, t)) \frac{s}{t} \left(1 - \frac{t}{\Lambda^2}\right)^{-4} \\
T_{\pm}(s, t) &= F_{+}(\hat{s}, t) \pm F_{-}(\hat{s}, t) \\
F_{+}(\hat{s}, t) &= F_{+}^H(\hat{s}, t) + F_{+}^P(\hat{s}, t) + F_{+}^{PP}(\hat{s}, t) \\
&\quad + F_{+}^R(\hat{s}, t) + F_{+}^{RP}(\hat{s}, t) + N_{+}(\hat{s}, t) \\
F_{-}(\hat{s}, t) &= F_{-}^{MO}(\hat{s}, t) + F_{-}^O(\hat{s}, t) + F_{-}^{OP}(\hat{s}, t) \\
&\quad + F_{-}^R(\hat{s}, t) + F_{-}^{RP}(\hat{s}, t) + N_{-}(\hat{s}, t).
\end{aligned} \tag{II.19}$$

with the exact definitions of the different terms given as stated in [15]. It should be noted that earlier versions of the PDG contains misprints in the definitions above as well as in the crossing of even and odd functions, and the current still contains sign errors for the Coulomb term, so these should be used with care.

3.2 The ABMST model

A somewhat simpler scattering model was proposed by Appleby et al. describing pp and $p\bar{p}$ data from ISR to Tevatron energies [16]. The model is based on work by Donnachie and Landshoff [40, 41] describing both elastic scattering and single diffractive scattering, but includes new and more sophisticated fits compared to the ones from Donnachie and Landshoff. In this section the details on the elastic scattering will be given, while the single diffractive scatterings are presented in Sec. 4.

The ABMST model includes both the Coulomb and nuclear amplitudes, as well as the

interference between the two. The cross sections are given as

$$\begin{aligned}\frac{d\sigma_{\text{el}}}{dt} &= \pi |f_c(s, t)e^{i\alpha\phi(t)} + f_n(s, t)|^2 \\ \sigma_{\text{el}}(s) &= \pi \int_{t_{\text{min}}}^{t_{\text{max}}} dt |f_n(s, t)|^2 \\ \sigma_{\text{tot}}(s) &= \text{Im}[f_n(s, 0)],\end{aligned}\tag{II.20}$$

where the triple-gluon amplitude is left out of the nuclear amplitude [40] when evaluating the total cross section. The Coulomb amplitude from [42] is used and the nuclear amplitude consists of five terms: A hard Pomeron (\mathbb{P}_h), a soft Pomeron (\mathbb{P}_s), the f_2, a_2 Regge trajectory (\mathbb{R}_1), the ρ, ω Regge trajectory (\mathbb{R}_2) and a triple-gluon exchange amplitude,

$$f_n(s, t) = A_{\text{ggg}}(t) + \sum_{i=\mathbb{P}_h, \mathbb{P}_s, \mathbb{R}_1, \mathbb{R}_2} A_i(s, t).\tag{II.21}$$

Also included is a double exchange term, where e.g. two Pomerons are exchanged. Exact definitions of the various terms are found in [16, 43]. It should be noted that the cross sections are only valid down to $\sqrt{s} = 10$ GeV, and that the fits have only been performed up to UA1 energies. We thus expect good agreement in this energy range, whereas the fit might disagree with data outside of it.

3.3 The FMO model

The FMO model [39] includes the maximal odderon, excluded by hand in the COMPAS model. The odderon has been a controversial subject ever since its introduction, and so far no signs of it has been observed. The main feature of its introduction is that the difference between pp and $\bar{p}p$ total cross sections is not vanishing at high energies. Similarly the ρ values will deviate at high energies. The FMO model only includes the $t = 0$ contribution and can be written as

$$\begin{aligned}\sigma_{\text{tot}}(s) &= \frac{\text{Im} T_{\pm}(s, 0)}{\sqrt{s(s - 4m_p^2)}} \\ T_{\pm} &= F_+^H \pm F_-^{MO} + F_+^R \pm F_-^R,\end{aligned}\tag{II.22}$$

with the exact definitions of the crossing-odd and -even amplitudes found in [39].

3.4 Comparisons with data

In fig. II.2a,b we show the above parametrizations of the total cross section and in fig. II.2c,d the ρ parameter, for pp and $p\bar{p}$ processes respectively. Note how the ABMST $\sigma_{\text{tot}}^{\text{pp}}$ parametrization rises at $\sqrt{s} < 10$ GeV, a consequence of it not being fitted to this range. We do not

aim to describe so low energies in PYTHIA 8, so this is not an issue. Both the ABMST and COMPAS parametrizations well describe the LHC data points in pp, and seem to favor the higher of the Tevatron data points in $p\bar{p}$ processes, unlike the original DL parametrization available in PYTHIA 8. In fig. II.2c the ρ is well described by all three parametrizations, below LHC energies. But at LHC the latest TOTEM value [35] is described only by the FMO model, which explicitly includes the maximal odderon term in order for ρ to decrease here. This term also gives rise to the difference in ρ for pp and $p\bar{p}$ processes, as seen in figs. II.2c,d, a difference not present in the other two models.

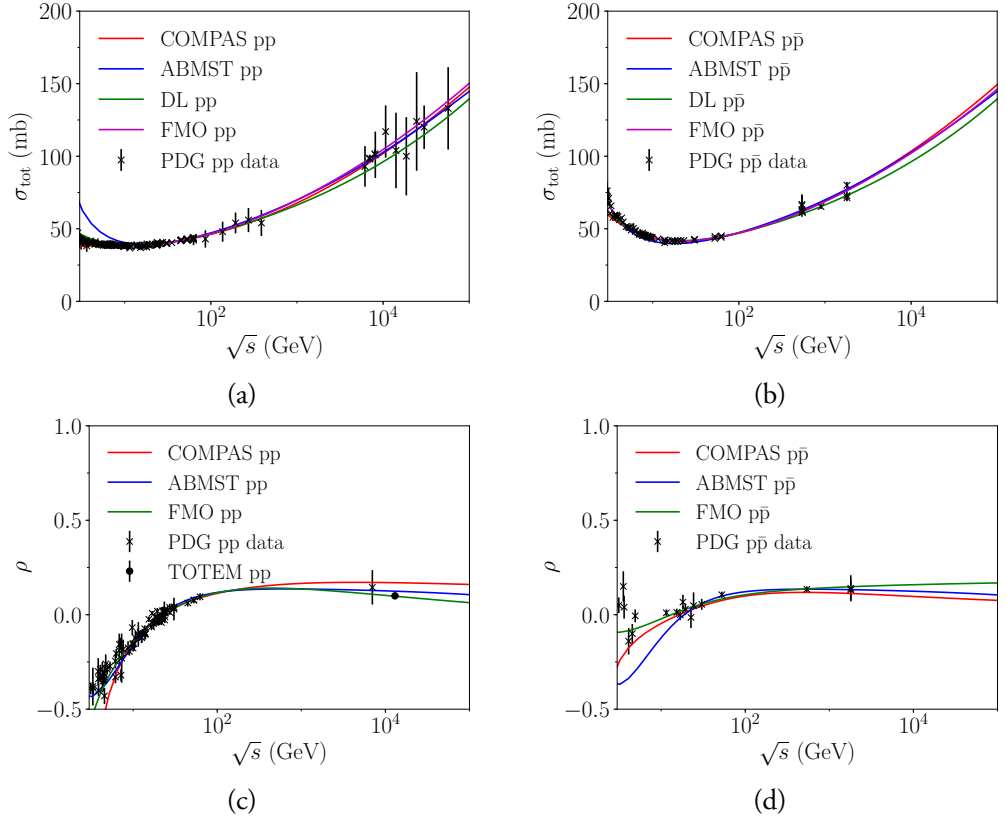


Figure II.2: The total cross section parametrizations in (a) pp and (b) $p\bar{p}$ processes. The ratio of real to imaginary parts of the elastic amplitude at $t = 0$ for pp (c) and $p\bar{p}$ (d). Note that the SaS model has been left out in (c) and (d), as ρ is a constant here, that can be set freely by the user. Data from PDG [15].

In fig. II.3 we show the available parametrizations of the elastic differential (a,b) and integrated (c,d) cross sections for pp and $p\bar{p}$ processes. Here it is evident that the pure exponential description used by SaS only makes sense for small $|t|$. Both the COMPAS and ABMST parametrizations have been fitted to the $\sqrt{s} = 23$ GeV data, but not to the 7 TeV data. Here it seems that the COMPAS parametrization prefers a larger dip than seen in data, while it captures the high- $|t|$ region slightly better than the ABMST parametrization.

It is also evident that SaS underestimates the rise of the total elastic cross section, whereas the other two do quite well.

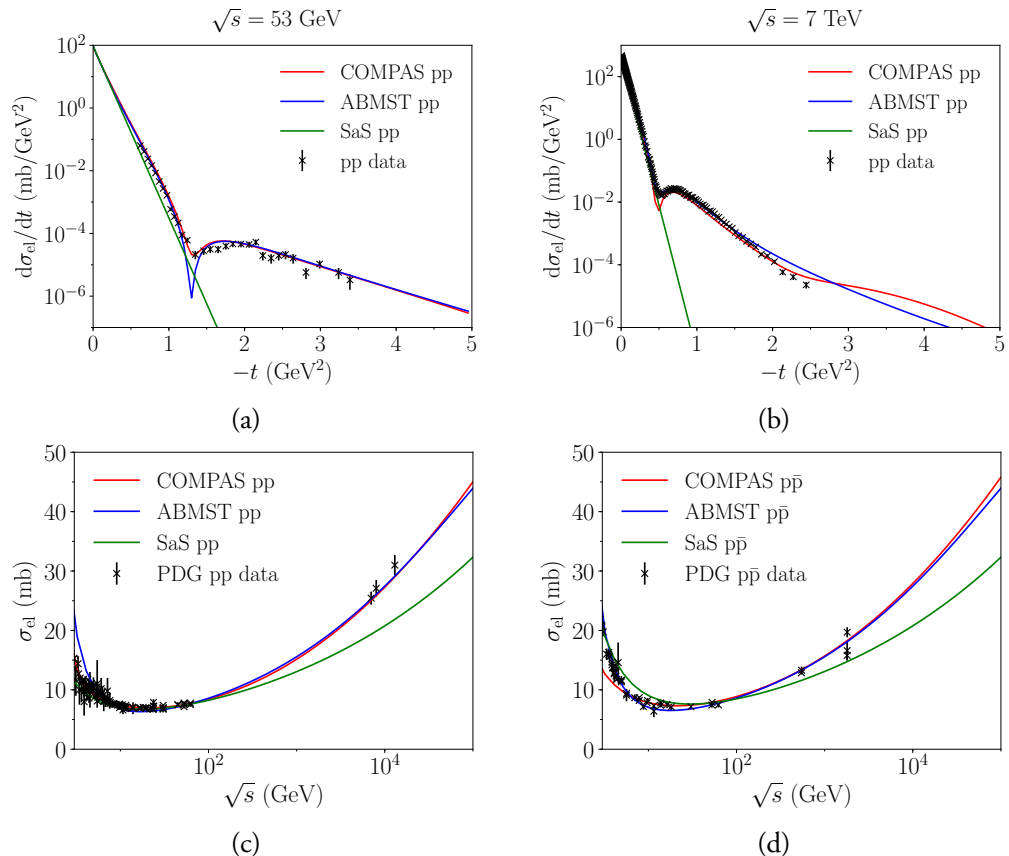


Figure II.3: The elastic differential cross section parametrizations in pp collisions at 53 GeV (a) and 7 TeV (b). The integrated elastic cross section parametrizations in (c) pp and (d) $\bar{p}p$ processes. Data from PDG [15].

4 Single diffractive cross sections

As we proceed to the topologies of diffraction, the situation is more complicated than for total and elastic cross sections. The experimental definition of diffraction is based on the presence of rapidity gaps, but such gaps are subject to random fluctuations in the hadronization process, and therefore cannot be mapped one-to-one to an underlying color-singlet-exchange mechanism. Also the separation between single, double and central diffraction is not always so clearcut. Some single-diffractive data is available at lower energies, but much of it is old and of varied quality. This will of course affect any model trying to describe these topologies, as usually there are model parameters that have to be fitted to data. To

the best of our knowledge, only a few models actually try to fit data fully differentially in both s , M_X^2 and t . The normal ansatz is instead to define an s -independent \mathbb{P} flux, with factorized ξ and t distributions, e.g. of the form $(d\xi/\xi^{1+\delta}) \exp(b t) dt$ [27, 44–46] where δ is a small number. The t -integrated ξ distribution is then directly mapped on to an $M_X^2 = \xi s$ spectrum.

The COMPAS group has not made any attempts to describe other topologies than the elastic, neither has the FMO model. Hence, in addition to the already implemented SaS and MBR models, we are left with the ABMST model as a new alternative, that gives a full description of the single diffractive topologies. This model has been fitted to differential data in the energy range $17.2 < \sqrt{s} < 546$ GeV and in the t range $0.015 < |t| < 4.15$ GeV², and is thus expected to give a reasonable prediction in this range. The model, however, has some unfortunate features, which we will discuss in a later section. But first an introduction to the basics of the model itself.

4.1 The ABMST model

In [16] the authors present a model for single diffractive dissociation inspired by Donnachie and Landshoff. They operate in two regimes, high and low mass diffraction, separated at

$$M_{\text{cut}}(s) = \begin{cases} 3 & s < 4000 \text{ GeV}^2 \\ 3 + 0.6 \ln\left(\frac{s}{4000}\right) & s > 4000 \text{ GeV}^2 \end{cases}. \quad (\text{II.23})$$

In the high mass regime, they use a triple-Regge model with two components; An effective Pomeron and a degenerate Reggeon term. In order for the unknown phases of the propagators to vanish, they require that the two t -dependent propagators in the diagrams contributing to the single diffractive cross section are equal. This results in four diagrams; PPP, PPR, RRP, RRR. The authors also include pion exchange in the differential cross section arriving at

$$\begin{aligned} \frac{d^2\sigma_{\text{HM}}}{dtd\xi}(\xi, s, t) &= f_{\text{PPP}}(t) \xi^{\alpha_{\mathbb{P}}(0)-2\alpha_{\mathbb{P}}(t)} \left(\frac{s}{s_0}\right)^{\alpha_{\mathbb{P}}(0)-1} \\ &+ f_{\text{PPR}}(t) \xi^{\alpha_{\mathbb{R}}(0)-2\alpha_{\mathbb{P}}(t)} \left(\frac{s}{s_0}\right)^{\alpha_{\mathbb{R}}(0)-1} \\ &+ f_{\text{RRP}}(t) \xi^{\alpha_{\mathbb{P}}(0)-2\alpha_{\mathbb{R}}(t)} \left(\frac{s}{s_0}\right)^{\alpha_{\mathbb{P}}(0)-1} \\ &+ f_{\text{RRR}}(t) \xi^{\alpha_{\mathbb{R}}(0)-2\alpha_{\mathbb{R}}(t)} \left(\frac{s}{s_0}\right)^{\alpha_{\mathbb{R}}(0)-1} \\ &+ \frac{g_{\pi\pi\mathbb{P}}^2}{16\pi^2} \frac{|t|}{(t - m_\pi^2)^2} F^2(t) \xi^{1-2\alpha_\pi(t)} \sigma_{\pi^0\mathbb{P}}(s\xi), \end{aligned} \quad (\text{II.24})$$

with trajectories and parameter choices found in [16]. Each of the effective three-Reggeon couplings are given as

$$f_{kki}(t) = A_{kki}e^{B_{kki}t} + C_{kki}, \quad (\text{II.25})$$

except for the triple-Pomeron coupling, which is modified as

$$\begin{aligned} f_{\text{PPP}}(t) &= 0.4 + 0.5t \quad \text{for} \quad -0.25 \leq t < -10^{-4} \\ f_{\text{PPP}}(t) &= (A_{\text{PPP}}e^{B_{\text{PPP}}t} + C_{\text{PPP}}) \left(\frac{t}{t - 0.05} \right) \\ &\quad \text{for} \quad -1.15 \leq t < -0.25 \\ f_{\text{PPP}}(t) &= (A_{\text{PPP}}e^{B_{\text{PPP}}t} + C_{\text{PPP}}) \left(\frac{t}{t - 0.05} \right) \\ &\quad \times [1 + 0.4597(|t| - 1.15) + 5.7575(|t| - 1.15)^2] \\ &\quad \text{for} \quad -4 \leq t < 1.15. \end{aligned} \quad (\text{II.26})$$

Four resonances are modeled in the low-mass regime, along with a background from the high-mass regime and a contact term matching the two regimes smoothly. The resonances are excited states of the proton, each a unit of angular momentum higher than the previous one. The resonances are parametrized by Breit-Wigner shapes with masses m_i , widths Γ_i and couplings c_i ,

$$\frac{d^2\sigma_{\text{res}}}{d\tau d\xi}(\xi, s, t) = \frac{e^{13.5(t+0.05)}}{\xi} \sum_{i=1}^4 \left[\frac{c_i m_i \Gamma_i}{(\xi s - m_i^2)^2 + (m_i \Gamma_i)^2} \right], \quad (\text{II.27})$$

with exact definitions found in the paper. The background is assumed quadratic and vanishes at a threshold, $\xi_{\text{th}} = \frac{(m_p + m_\pi)^2}{s}$,

$$A_{\text{bkg}}(\xi, s, t) = a(s, t)(\xi - \xi_{\text{th}})^2 + b(s, t)(\xi - \xi_{\text{th}}). \quad (\text{II.28})$$

A matching term between the high- and low-mass regions is subtracted from the resonances to avoid any discontinuities at ξ_{cut} , and parametrized such that it is equal to the magnitude of the resonance term at the matching point.

4.2 Comments on the ABMST model

In fig. II.4a,b we show the different components of the ABMST model at an energy of $\sqrt{s} = 7$ TeV along with the integrated cross sections in fig. II.4c,d. We have several comments to these distributions, as they show some unexpected features.

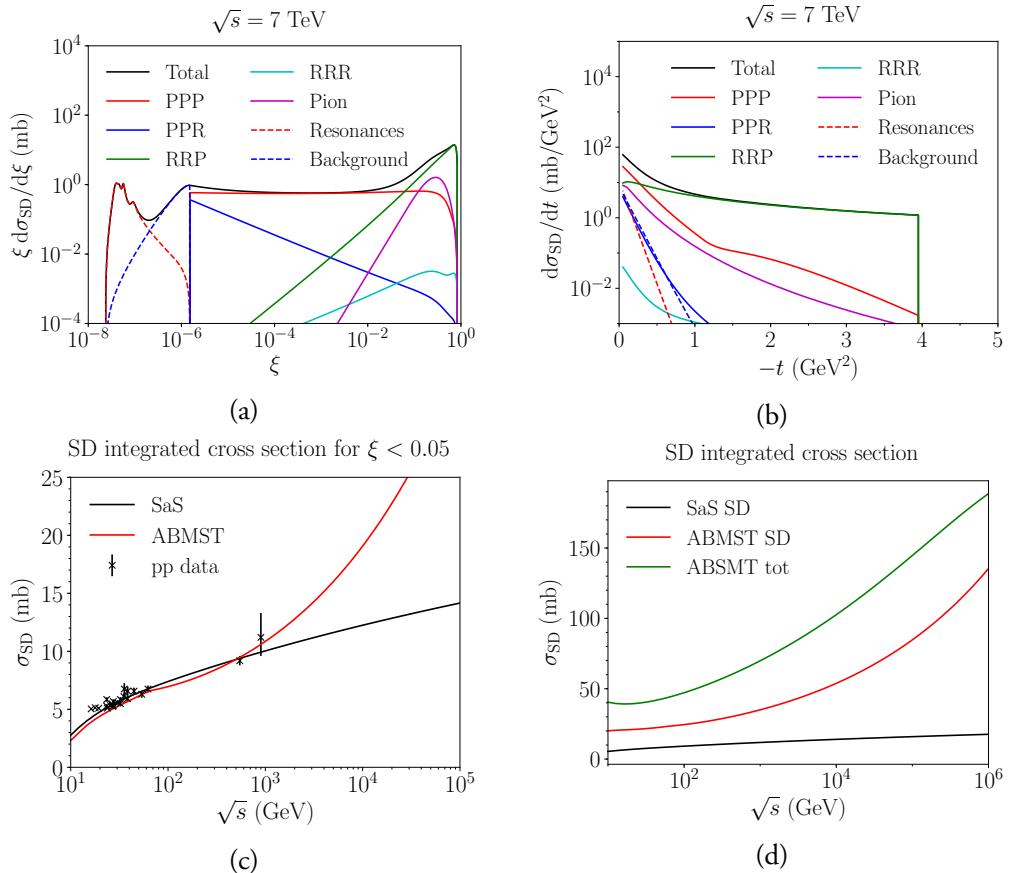


Figure II.4: The different components of the ABMST model for single diffraction as a function of (a) ξ and (b) t at 7 TeV. The integrated single diffractive cross section as a function of \sqrt{s} for $\xi < 0.05$ (c) and in the full single diffractive phase space (d). Data from references in [16].

To begin, consider the differential distribution in fig. II.4a. Here the cross section (multiplied by a factor of ξ for visibility) is shown as a function of ξ , displaying both the low-mass resonances and the high-mass Regge terms. Note, however, the dip between these two regimes, a decrease of a factor of 10. This is a feature of the background modeling, whereas one would expect a more smooth transition between the two regimes. There is no physical motivation as to why the Regge trajectories should have a quadratic behavior at low masses, since none of the terms show this behavior at higher masses. One could imagine a simple continuation of the high-mass background to lower masses, with the resonances added on top. But this would likely cause too high a cross section in the low-mass region, hence requiring a remodeling of the background description to avoid too high a low-mass cross section.

Similarly unexpected is the increase of the cross section at higher masses ($\xi \sim 1$), induced

by the triple-Reggeon and pion terms. The larger the mass of the system the smaller the rapidity gap between the diffractive system and the elastically scattered proton. The rule of thumb is that $\Delta y_{\text{gap}} \approx \ln(\xi)$, so for large ξ there will essentially be no gap at all. The diffractive system will simply look like a non-diffractive one, making it impossible to distinguish between the two experimentally. The rise at $\xi \sim 1$ also introduces a vast increase with energy in the integrated cross section, making the single-diffractive cross section dominate at large energies, which leaves little room for other processes, see fig. II.4d. The authors themselves have tried to dampen the increase of the cross section by allowing the mass cut, separating the low- and high-mass regimes, to vary with s , eq. (II.23). Unfortunately the introduced dampening gives rise to a kink in the integrated cross section where the dampening kicks in, at $\sqrt{s} \sim 60$ GeV, and does not dampen the cross section sufficiently at high energies.

In fig. II.4b we show the ABMST model differential in t . Noteworthy are the t -independent terms C_{kki} and the sharp cutoff at $t = -4 \text{ GeV}^2$, both of which are unphysical on their own. That is, if the sharp cutoff is disregarded, then all but the pion and triple-Pomeron terms become constant at large $|t|$, lacking any form factor suppression for scattering a proton without breaking it up. The choice of t parametrization shape was based on the goodness-of-fit, and not on any physical grounds. The authors note that the parametrization as such gives too large a cross section at high energies, hence the modification of the Pomeron coupling, as this dominates at high energies. The t ansatz may also cause problems if used in other diagrams, e.g. in the extension to double and central diffraction that we will introduce later.

As PYTHIA 8 aims to describe current and future colliders, the need for a more sensible high-energy behavior of the ABMST model is evident. It is not realistic to have a model where single diffraction and elastic scattering almost saturates the total cross section at FCC energies (at 10^5 GeV $\sigma_{\text{tot}} - \sigma_{\text{el}} - \sigma_{\text{SD}} \approx 145 - 45 - 80 \approx 20 \text{ mb}$). At the same time we want to make use of the effort already put into the careful tuning to low-energy and low-diffractive-mass data. We have thus chosen to provide a modified version of the ABMST model, addressing the problems discussed above, as described in the next section, while retaining the good aspects of the ABMST model. Both the modified and the original version of the ABMST model are made available in the latest PYTHIA 8 release.

4.3 The modified ABMST model

To smoothen the dip between the low-mass and high-mass regions, several background terms have been studied, such as a linear background becoming constant at threshold, a combination of the linear and the quadratic background and, as an extreme, a continuation of the high-mass background. The best results was found with the combination of the linear

and quadratic,

$$A_{\text{bkg}}(s) = \begin{cases} A_{\text{bkg}}^{\text{quadratic}} & M_X < M_4 \\ A_{\text{bkg}}^{\text{linear}} & M_4 < M_X < M_{\text{cut}} \end{cases}, \quad (\text{II.29})$$

where M_4 is the mass of the fourth resonance.

The new parametrization of the high-mass background in the low-mass region does smoothen the decrease between the two regions, but in itself does increase the integrated cross section. We tame the integrated cross section by introducing a multiplicative rescaling of the high-mass region, as well as a different M_{cut} parametrization. Again several possibilities have been tried, and best results were obtained for a $\ln^2(s)$ -dependent M_{cut} and rescaling. That is, $M_{\text{cut}} = 3 + c \ln^2(s/s_0)$ GeV and the rescaling factor is $3/(3 + c \ln^2(s/s_0))$, with c a free parameter and $s_0 = 100 \text{ GeV}^2$, which is also where the rescaling begins, so as to avoid kinks in the distributions.

While this change reduces the cross section at intermediate ξ values, it does not address the strong rise near $\xi = 1$. This is an unobservable behavior, as already argued, and therefore we also introduce a dampening factor $1/(1 + (\xi \exp(y_{\text{min}}))^p)$ for the high-mass region. Here y_{min} is the gap size where the dampening factor is $1/2$ and p regulates how steeply this factor drops around y_{min} ; by default $y_{\text{min}} = 2$ and $p = 5$.

Separately, we wish to remove the artificial cut at $t = -4 \text{ GeV}^2$, in favor of a shape that is valid at all t scales. To this end, couplings are modified as

$$f_{kki}^{\text{ABMST}}(t) \rightarrow f_{kki}^{\text{mod}}(t) = (A_{kki} + C_{kki}^{\text{mod}}) e^{B_{kki}^{\text{mod}} t}, \quad (\text{II.30})$$

where two new parameters C_{kki}^{mod} and B_{kki}^{mod} are introduced. These are fixed by the two requirements that the integral over t and the average t value should remain unchanged relative to the original ABMST values. Note, however, that we do not modify the \mathbb{PPP} part, as this already has the desired decreasing behavior at high $|t|$. Besides these modifications, a minimum diffractive slope $B_{SD} = 2$ is introduced, to avoid any unphysical situations where the slope could become negative.

In fig. II.5 we show the components of the modified ABMST model as a function of ξ (a) and t (b). The improvements of the modifications are clearly seen, as the dip between the low- and high-mass description has decreased, the high- ξ region has been dampened and none of the components become constant at large $|t|$. In figs. II.5c,d the two ABMST models are compared to the SaS model available in PYTHIA 8 as default. We note that the modified ABMST model shows better agreement with the SaS model at intermediate ξ values, where SaS is in rough agreement with data, while retaining some features of the ABMST model, such as the detailed resonance structure.

In fig. II.6 we show the comparison between the implemented models and the low-energy data used in [16]. It is clear that the SaS model does not agree with data, while both the

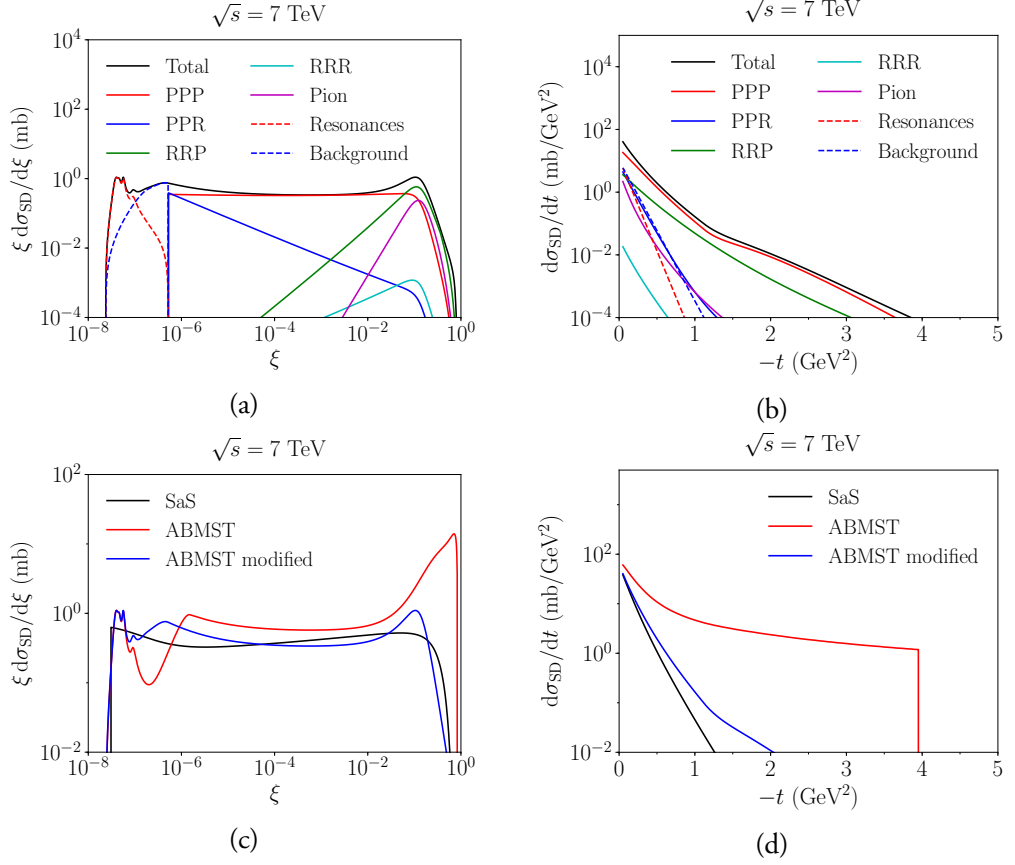


Figure II.5: The different components of the modified ABMST model for single diffraction as a function of (a) ξ and (b) t at 7 TeV. The same distributions are shown in (c) and (d), where we compare the two models ABMST and ABMST modified to the SaS model.

original and the modified ABMST model describe data reasonably well. In figs. II.7a,b the integrated cross sections of all three models are shown in the restricted (a) and full (b) phase space. The growth of the ABMST model has been tamed by our modifications. Insofar as the SaS model seems to be on the high side relative to data, and the modified ABMST is slightly higher, it may become necessary to finetune further for LHC applications. To this end we have introduced an optional overall scaling factor $k(s/m_p^2)^p$, with k, p being tunable parameters.

The bulk of the modifications applied to the ABMST framework are intended to tame the high-energy behavior of the model. One could have used an eikonal approach to the same end, e.g. in the spirit of [47]. This would require a different set of assumptions, however, such as the impact-parameter shape of the different diffractive topologies, and therefore not be any less arbitrary. For now we therefore stay with the current framework and instead

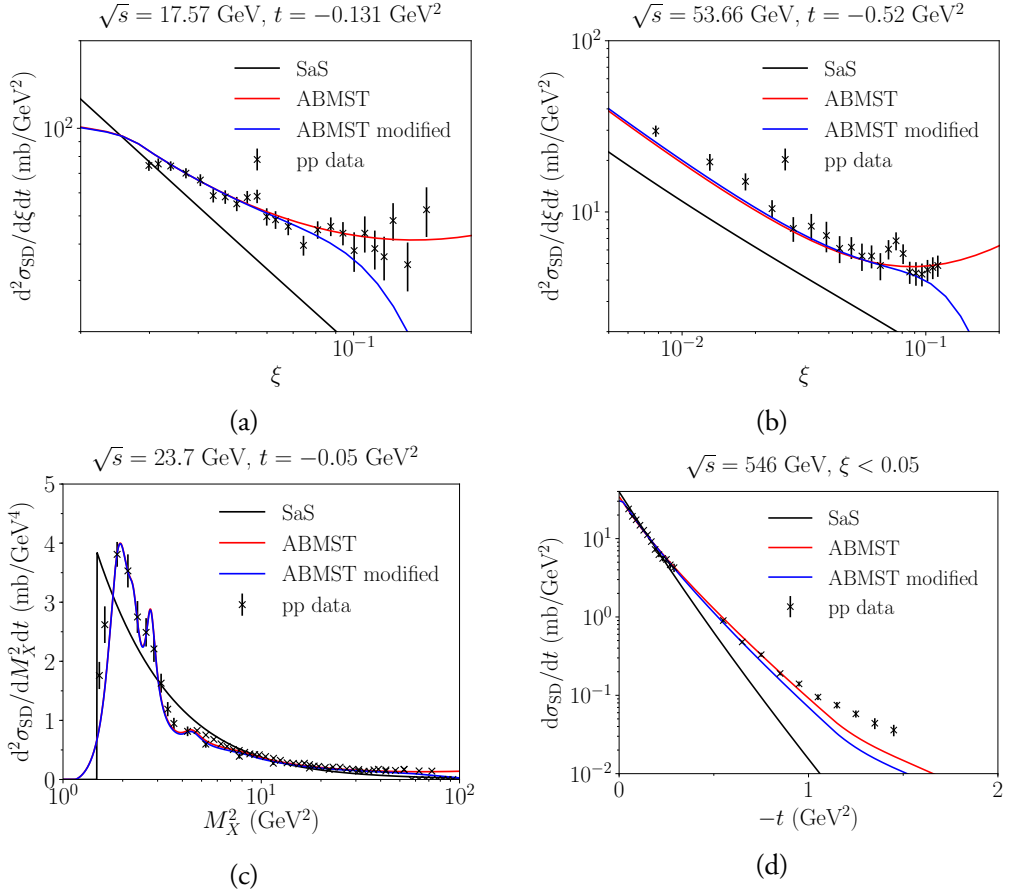


Figure II.6: The single diffractive differential cross section parametrizations in pp collisions at \sqrt{s} 17.57 GeV with $t = -0.131$ GeV² (a) and 53.66 GeV with $t = -0.52$ GeV² (b). The mass-spectrum showing the resonances at $\sqrt{s} = \text{GeV}$ and $t = -\text{GeV}^2$ (c). The integrated t spectrum at $\sqrt{s} = \text{GeV}$ (d). Data from references in [16].

proceed to address other shortcomings of the ABMST model, namely the lack of double and central diffraction.

5 Double diffractive cross sections

The ABMST model only provides a description of the single diffractive differential cross section. We can extend this to double diffractive systems, by extracting the vertices and propagators from the single diffractive framework and using them in double diffractive diagrams. Fig. II.1e shows a double diffractive diagram, where \mathbb{X} is one of the Reggeons used in the single diffractive framework. Thus several diagrams are obtained with Reggeons

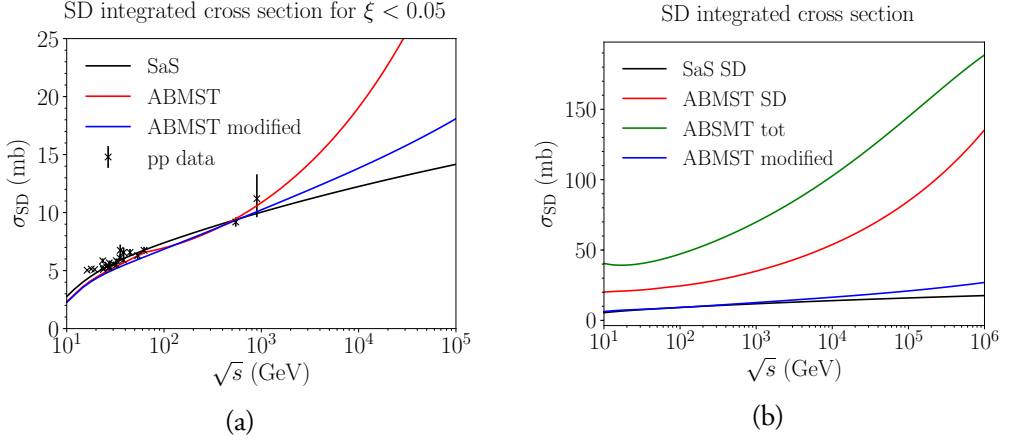


Figure II.7: The integrated single diffractive cross section at different energies for $\xi < 0.05$ (a) and in the full phase space (b). Data from references in [16].

i, j, k (where i, j are connected to the proton and k are in the loop). Similar as for single diffraction, in order for the unknown phases in the propagators to vanish, the requirement of equal Reggeons is enforced in the loop. The fact that there are two different mass regimes (low and high) for the two diffractive systems X and Y gives four different combinations.

If both systems have high mass, $M_{X,Y} > M_{\text{cut}}$, the diagram of fig. II.1e implies a cross section

$$\begin{aligned} \frac{d^3\sigma}{dtdM_X^2dM_Y^2} &= \sum_{ijk} \frac{g_{ip}(0)g_i^{kk}(t)g_{jp}(0)g_j^{kk}(t)}{16\pi M_X^2 M_Y^2} \left(\frac{M_X^2}{s_0}\right)^{\alpha_i(0)-1} \left(\frac{M_Y^2}{s_0}\right)^{\alpha_j(0)-1} \\ &\times \left(\frac{ss_0}{M_X^2 M_Y^2}\right)^{2\alpha_k(t)-2}. \end{aligned} \quad (\text{II.31})$$

Changing variables to $\xi = M^2/s$ and collecting the terms one obtains

$$\begin{aligned} \frac{d^3\sigma}{dtd\xi_X d\xi_Y} &= \frac{1}{16\pi} \sum_{ijk} \left(\frac{s}{s_0}\right)^{2-2\alpha_k(t)} g_{ip}(0)g_i^{kk}(t)\xi_X^{\alpha_i(0)-2\alpha_k(t)} \left(\frac{s}{s_0}\right)^{\alpha_j(0)-1} \\ &\times g_{jp}(0)g_j^{kk}(t)\xi_Y^{\alpha_j(0)-2\alpha_k(t)} \left(\frac{s}{s_0}\right)^{\alpha_j(0)-1}. \end{aligned} \quad (\text{II.32})$$

From the single diffractive framework one has that

$$\frac{d^2\sigma_{\text{HM}}}{dtd\xi} = \frac{1}{16\pi} \sum_{ik} g_{kp}^2(t)g_{ip}(0)g_i^{kk}(t)\xi^{\alpha_i(0)-2\alpha_k(t)} \left(\frac{s}{s_0}\right)^{\alpha_i(0)-1}, \quad (\text{II.33})$$

where we can recognize a part of the single diffractive cross section in the double diffractive cross section,

$$\begin{aligned} \frac{d^3\sigma}{dtd\xi_X d\xi_Y} &= \frac{1}{16\pi} \sum_k \left(\frac{s}{s_0}\right)^{2-2\alpha_k(t)} \left[\frac{16\pi}{g_{kp}^2(t)} \frac{d\sigma_{\text{HM}}}{dtd\xi_X} \right] \left[\frac{16\pi}{g_{kp}^2(t)} \frac{d\sigma_{\text{HM}}}{dtd\xi_Y} \right] \\ &= \frac{d\sigma_{\text{HM}}}{dtd\xi_X} \frac{d\sigma_{\text{HM}}}{dtd\xi_Y} \sum_k \frac{16\pi}{g_{kp}^4(t)} \left(\frac{s}{s_0}\right)^{2-2\alpha_k(t)}. \end{aligned} \quad (\text{II.34})$$

A similar diagrammatic method can be used for the low-mass region, so all four (M_X, M_Y) regions can generically be described as

$$\begin{aligned} \frac{d^3\sigma}{dtd\xi_X d\xi_Y} &= \frac{d\sigma_{\text{SD}}}{dtd\xi_X} \frac{d\sigma_{\text{SD}}}{dtd\xi_Y} \sum_{k=\mathbb{P}, \mathbb{R}} \frac{16\pi}{g_{kp}^4(t)} \left(\frac{s}{s_0}\right)^{2-2\alpha_k(t)} \\ &\rightarrow \frac{d\sigma_{\text{SD}}}{dtd\xi_X} \frac{d\sigma_{\text{SD}}}{dtd\xi_Y} \frac{16\pi}{g_{\mathbb{P}\mathbb{P}}^4(t)} \left(\frac{s}{s_0}\right)^{2-2\alpha_{\mathbb{P}}(t)}. \end{aligned} \quad (\text{II.35})$$

In the last step we have taken the high-energy limit, where the Pomeron term dominates. The last term can then be recognized as the inverse of the elastic cross section in the same limit, and hence [4]

$$\frac{d^3\sigma_{\text{DD}}}{dtd\xi_X d\xi_Y} \approx \frac{d^2\sigma_{\text{SD}}}{dtd\xi_X} \frac{d^2\sigma_{\text{SD}}}{dtd\xi_Y} / \frac{d\sigma_{\text{el}}^{\mathbb{P}}}{dt}. \quad (\text{II.36})$$

In principle this formulation holds only at high energies, and only when using the Pomeron as exchanged particle in all parts of the diagram in fig. II.1c. Nevertheless it offers the best way to introduce double diffraction as a natural extension of the ABMST single diffractive machinery, and is the one we will choose.

One of the drawbacks of this approach is that accidental dips in the elastic cross section denominator can come to blow up the double diffractive cross section beyond what reasonably should be expected. Therefore a slightly modified elastic cross section is called for in this context. In fig. II.8a,b the different Pomeron contributions to the elastic differential cross section are shown at two energies, along with the full description and an interference-free description of the form

$$\frac{d\sigma_{\text{el}}}{dt} = \frac{|\sum_i A_i(s, t)|^2}{16\pi} \simeq \frac{\sum_i |A_i(s, t)|^2}{16\pi} \quad (\text{II.37})$$

where i runs over all four terms. Notice that the hard and soft Pomeron contributions dominate in two different regions. Hence a reasonable approximation would be to use the soft Pomeron term in the low- $|t|$ range and the hard Pomeron term in the high- $|t|$ range.

In practice we use the combination of the hard and soft Pomerons, so as to avoid splitting eq. (II.36) into two different t ranges.

Figs. II.8c,d show the effect of the various elastic parametrizations on the double diffractive distributions. Note the normalization difference between the hard-Pomeron-only description and the others, a difference that arises since the hard Pomeron term is not the dominant one in the low- $|t|$ region, where most of the cross section is. On the other hand, the soft-Pomeron-only t spectrum is much wider than the other distributions shown, since the soft Pomeron contribution to elastic scattering falls off much steeper with t . The “Pure ABMST”, interference-free ABMST and “ABMST both Poms” appear to have the same shapes in figs. II.8c,d. They differ somewhat in normalization, as is expected given that the two latter correspond to somewhat larger elastic cross sections.

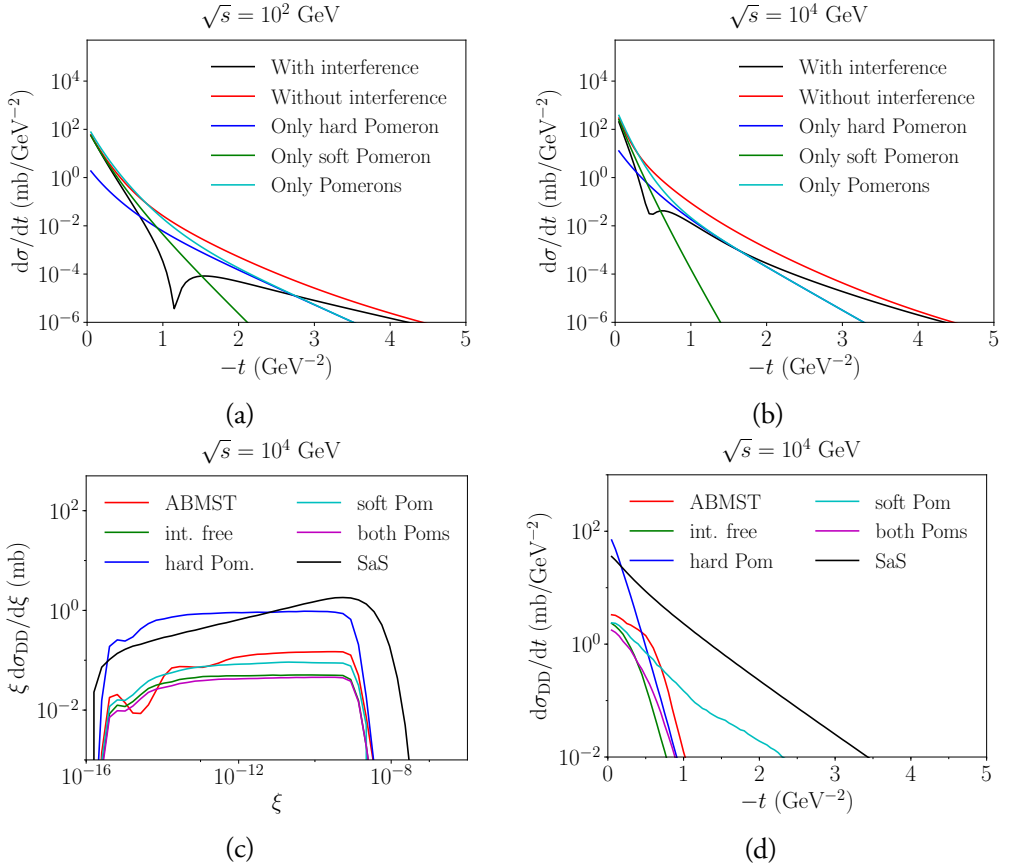


Figure II.8: The effect of using only a subset of the available Pomerons in the elastic parametrization, as used in the expression for the double diffractive cross section, eq. (II.36). In (a) and (b) the elastic differential cross section is shown as a function of t at two energies. In (c) and (d) the effect of these on the double diffractive distributions are shown as a function of $\xi = \xi_1 \xi_2$ and t , respectively. Note that the “Pure ABMST” has a minimal slope of $B_{DD} = 2$ such as to avoid the dip structure of the elastic description.

To correct for the possible suppressions arising from the chosen approximation of the elastic cross section, and from the underestimation implied by the step taken in eq. (II.35), we introduce a scaling factor similar to the one introduced in the single diffractive framework. A minimal double diffractive slope can also be enforced, such as to avoid any unphysical situations. As a final modification, an option to reduce topologies without a rapidity gap is applied in the region where both of the systems are of very large masses. Again, this is to be able to distinguish the double-diffractive system from the non-diffractive ones.

As two different parametrizations are available in the ABMST framework for single diffraction, several choices for the double diffractive framework exists. Presented here are results with three choices:

- Pure ABMST: the original ABMST single diffractive model together with the elastic cross sections using only Pomerons, with the minimal double diffractive slope and with reduced vanishing-gap topologies.
- Model 1: The modified ABMST model for the single diffractive cross section, with the only-Pomerons elastic cross section. A minimal slope is used and the vanishing-gap topologies are also reduced here.
- Model 2: Model 1 scaled with the tuneable factor $k(s/m_p^2)^p$, where by default $k = 2$ and $p = 0.1$.

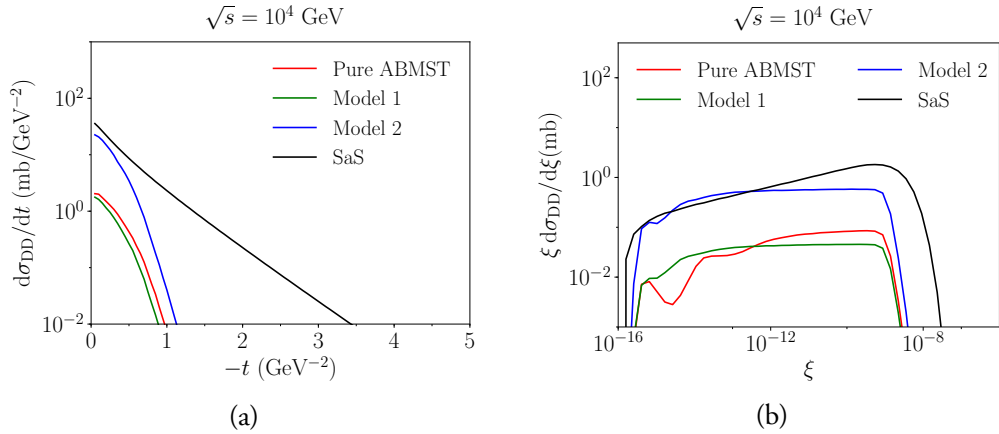


Figure II.9: Some of the DD models available in Pythia 8. In (a) and (b) we show the differential cross section as a function of t and $\xi = \xi_1 \xi_2$, respectively.

Fig. II.9a shows the t spectrum of the different models compared to the SaS model. It is evident that three models vanish faster than the SaS model. This is a result of the modest falloff of the elastic t -spectrum in ABMST, as this affects the double diffractive slope less than a sharply falling elastic t -spectrum in SaS, through the relation $B_{XY} = B_{AY} + B_{XB} - B_{el}$.

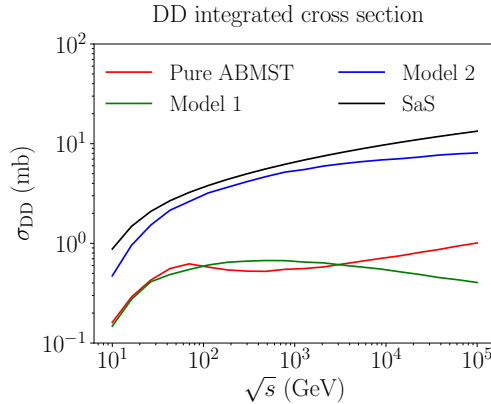


Figure II.10: The integrated double diffractive cross section as a function of energy of some of the models available in Pythia 8.

Fig. II.9b shows the differential cross section as a function of $\xi = \xi_1 \xi_2$. Here, the ABMST models show an approximate $1/\xi$ -behavior, while the SaS model indicates a $1/\xi^{(1+p)}$ behavior with $p > 0$, favoring high-mass diffractive systems. The results of these effects are visible in the integrated cross section, fig. II.10, where both “Pure ABMST” and “Model 1” are significantly suppressed compared to the SaS model. The scaled version, “Model 2”, gives more reasonable estimates of the cross sections, around 10 mb at LHC energies, but because of the choice of the power, $p = 0.1$, in the scaling, it does not rise as steeply as the SaS prediction. Similarly to the single-diffractive case, the SaS model predicts slightly larger cross sections than measured, so one might expect that the scaling chosen in Model 2 could be more in agreement with measurements.

6 Central diffractive cross sections

The central diffractive framework has long been neglected in general-purpose event generators. Dedicated event-generators exist for exclusive central diffractive processes, such as SuperChic [48] and ExHume [49], but these only work with a limited set of final states. PYTHIA 8 provides a description for inclusive high-mass central diffraction, but does not provide any such description for the exclusive processes. As stated earlier, we stress that the framework has not been tuned and thus is not to be trusted too far.

In this work we wish to extend the present description of central diffraction to include the high-mass description of the ABMST model. We have not made any attempt to include any low-mass resonances of central diffraction, as some of these are still not well established. The low-mass resonances used in ABMST are baryonic resonances, hence they cannot be extended to the central diffractive framework, as one expects scalar mesons, possibly scalar

glueballs, to be produced in the collision of two Reggeons. Future work would be to extend the model to such low-mass resonances, e.g. by including a low-mass resonance description similar to what has been developed in [50]. There the central exclusive production of a pion pair is considered and data is used to fit a model of the scalar resonances using complex Breit–Wigner shapes. Lacking a model for all such exclusive states, and since some of the resonances and their decays still are not experimentally under control, we have decided not to include any of the low-mass states in this framework.

The new central diffractive cross section presented here is again mainly based on the ABMST single-diffractive model. By examining the rapidity of the different components in the central diffractive system, one obtains the following relations,

$$\begin{aligned}\Delta y_{\text{tot}} &= \ln \frac{s}{s_0}, & \Delta y_X &= \ln \frac{\xi_1 \xi_2 s}{s_0}, \\ \Delta y_1 &= \ln \frac{1}{\xi_1}, & \Delta y_2 &= \ln \frac{1}{\xi_2},\end{aligned}\tag{II.38}$$

where $M_X^2 = \xi_1 \xi_2 s$, Δy_X is the rapidity span of the diffractive system X , and $\Delta y_{1,2}$ are the sizes of the two rapidity gaps. Thus, after some algebra, we obtain a central diffractive cross section of the form

$$\begin{aligned}\frac{d^4 \sigma_{\text{CD}}}{d\xi_1 d\xi_2 dt_1 dt_2} &= \frac{1}{256\pi^3} \sum_{ijk} \left(\frac{s}{s_0} \right)^{\alpha_k(0)-1} g_{ip}^2(t_1) g_k^{jj}(t_1) (\xi_1)^{\alpha_k(0)-2\alpha_i(t_1)} \\ &\times g_{jp}^2(t_2) g_k^{jj}(t_2) (\xi_2)^{\alpha_k(0)-2\alpha_j(t_2)} \\ &= \frac{1}{\pi} \sum_k \frac{1}{g_{kp}^2(0)} \left(\frac{s}{s_0} \right)^{1-\alpha_k(0)} \frac{d^2 \sigma_{\text{HM}}}{dt_1 d\xi_1} \frac{d^2 \sigma_{\text{HM}}}{dt_2 d\xi_2} \\ &\rightarrow \frac{1}{\pi} \frac{1}{g_{\mathbb{P}\mathbb{P}}^2(0)} \left(\frac{s}{s_0} \right)^{1-\alpha_{\mathbb{P}}(0)} \frac{d^2 \sigma_{\text{HM}}}{dt_1 d\xi_1} \frac{d^2 \sigma_{\text{HM}}}{dt_2 d\xi_2} \\ &= \frac{1}{\pi} \frac{d^2 \sigma_{\text{HM}}}{dt_1 d\xi_1} \frac{d^2 \sigma_{\text{HM}}}{dt_2 d\xi_2} / \sigma_{\text{tot}},\end{aligned}\tag{II.39}$$

where the high-energy limit is taken in the second step and recognized as the total cross section [3]. Similar arguments on the validity of eq. (II.39) applies as for the validity of eq. (II.36), i.e. eq. (II.39) is only valid in the high-energy limit, where the Pomeron term dominates. In practice, however, the expression is used over the entire energy range, using the sum of both the soft and the hard Pomeron term from the total cross section. A scaling factor similar to the scaling for single and double diffraction can be applied, to compensate for the approximations, and the same non-vanishing gap suppression can be applied as in the single-diffractive framework. Finally, a minimal central diffractive slope can also be applied.

Similar to the double diffractive framework, the central diffractive framework will depend on the choice of single diffractive framework, thus several options exist. Fig. II.11 shows three choices of models with the same name conventions as used in the double diffractive framework. Note, however, that the t spectrum is not shown, as this is exactly that of the single diffractive model. The mass of the diffractive system is shown in fig. II.11a, where the sharp cut at $M_X = M_{\text{cut}}$ is present for all ABMST variants. The SaS model has a similar sharp cutoff, but at $M_X = 1$ GeV. Lacking both model and data in the low-mass region, the cut allows for a clear distinction between what is included and not, albeit being unphysical.

Fig. II.11b shows the integrated cross section as a function of energy. Here all ABMST models lie below the SaS prediction, although “Model 2” exceeds it at around LHC energies. The lack of a low-mass model is evident at low energies ($\sqrt{s} < 30$ GeV), where all three models decrease rapidly. In this energy-range the low-mass states make up a large part of the cross section, hence should not be neglected.

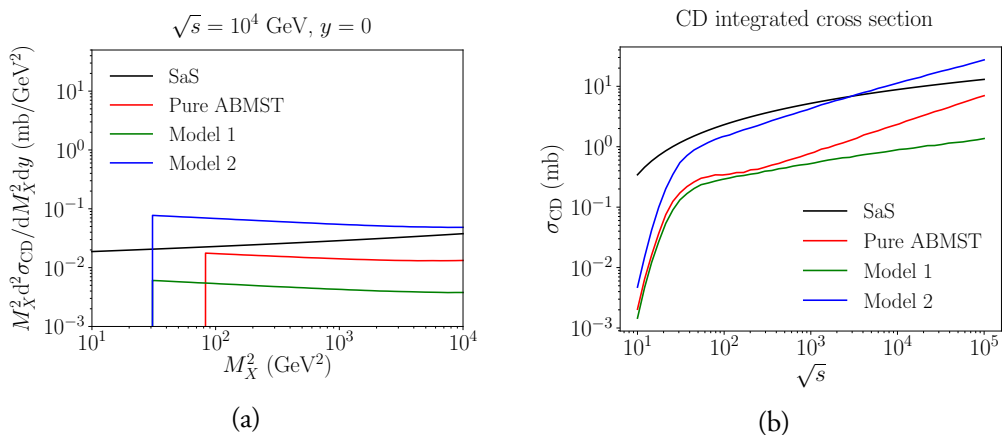


Figure II.11: Some of the CD models available in Pythia 8. In (a) we show the mass of the diffractive system produced at central rapidity and in (b) the integrated cross section as a function of energy.

7 Results

In this section the models are confronted with more recent LHC data. Several experiments have performed measurements on integrated cross sections and diffractive fractions, but not many provide results on differential distributions. We focus on the analyses available in Rivet [51], where only two analyses provide differential results. First we provide a discussion of the available data and the tuning prospects, and end with results obtained with the SaS model, the CSCR model and the ABMST models.

7.1 The 7 TeV LHC data and tuning prospects

In 2012 and 2015 ATLAS [52] and CMS [53] presented results on 7 TeV events with rapidity gaps. Both experiments measure all particles with transverse momenta larger than 200 MeV in pseudo-rapidity ranges of $|\eta| < 4.9$ (4.7) for ATLAS (CMS), and define the measured gap $\Delta\eta_F$ as the largest distance between either detector edge and the particle nearest to it. The two experiments, however, obtain different results for the shape of the distribution.

In fig. II.12a, we show the results obtained with default PYTHIA 8 using the SaS model and the MBR model when comparing to either the ATLAS or CMS Rivet analyses. Both models are shown, since ATLAS uses the SaS model for unfolding, while CMS uses the MBR one, but model agreement is sufficiently close that unfolding differences should not be an issue. Further, from fig. II.12a it is evident that the different experimental η cuts gives at most a 5% effect on either model. This does not account for the approximately 25% difference seen in data, see fig. II.12b. A tune to both datasets will not be able to describe either perfectly, as they so clearly disagree. Experiment-specific tunes would likely improve the description of that particular dataset, hence worsening the description of the other. As we cannot decide which of the two is the preferred one, we instead aim for the middle ground.

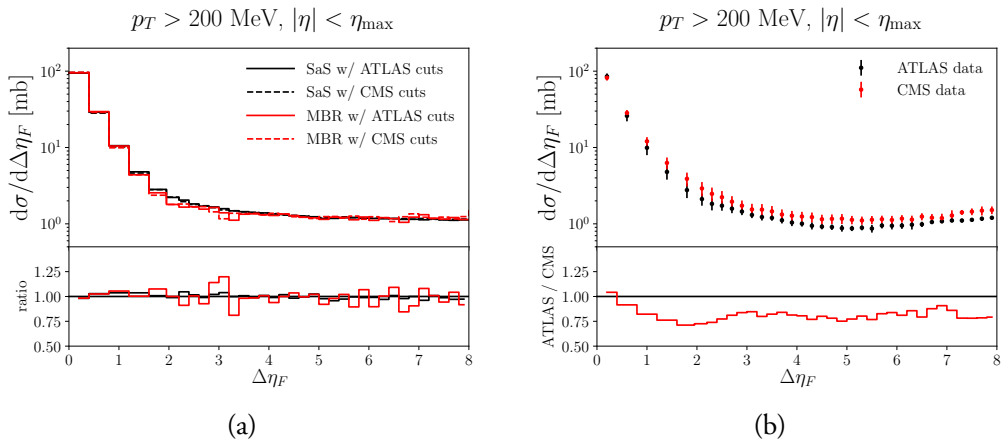


Figure II.12: (a) The SaS and MBR models using either ATLAS or CMS cuts along with the ratio of ATLAS to CMS cuts for both models. (b) The ATLAS [52] and CMS [53] data along with the ratio of ATLAS to CMS data, showing significant differences in the entire range.

Besides the above mentioned datasets measurements of the inelastic and diffractive cross sections have been performed by both ATLAS, CMS and ALICE. We include the following measurements: the inelastic cross section from ATLAS 2011 [54], the inelastic cross section from CMS 2012 [55] and the inelastic and diffractive cross sections from ALICE 2012 [56].

None of the datasets available in the Rivet framework are able to constrain the parameters

related to the hadronic event properties. This includes both the low-to-high-mass transition probability parameters as well as the parameters of the non-perturbative and perturbative description of the evolution of the diffractive system. In particular, the non-perturbative description is left as is in this study, while the effects of changing the $\mathbb{P}p$ cross section is shown in figs. II.13 and II.14. This cross section determines the amount of multiparton interactions activity in a high-mass diffractive event, and thereby e.g. the charged multiplicity distribution. It is interesting because of discrepancies between uncorrected ATLAS data and the Pythia 4C tune (figs. 3a-d in [52]). A direct comparison cannot be made, since the ATLAS distributions show the number of electromagnetic clusters rather than that of charged particles, but the two clearly are related.

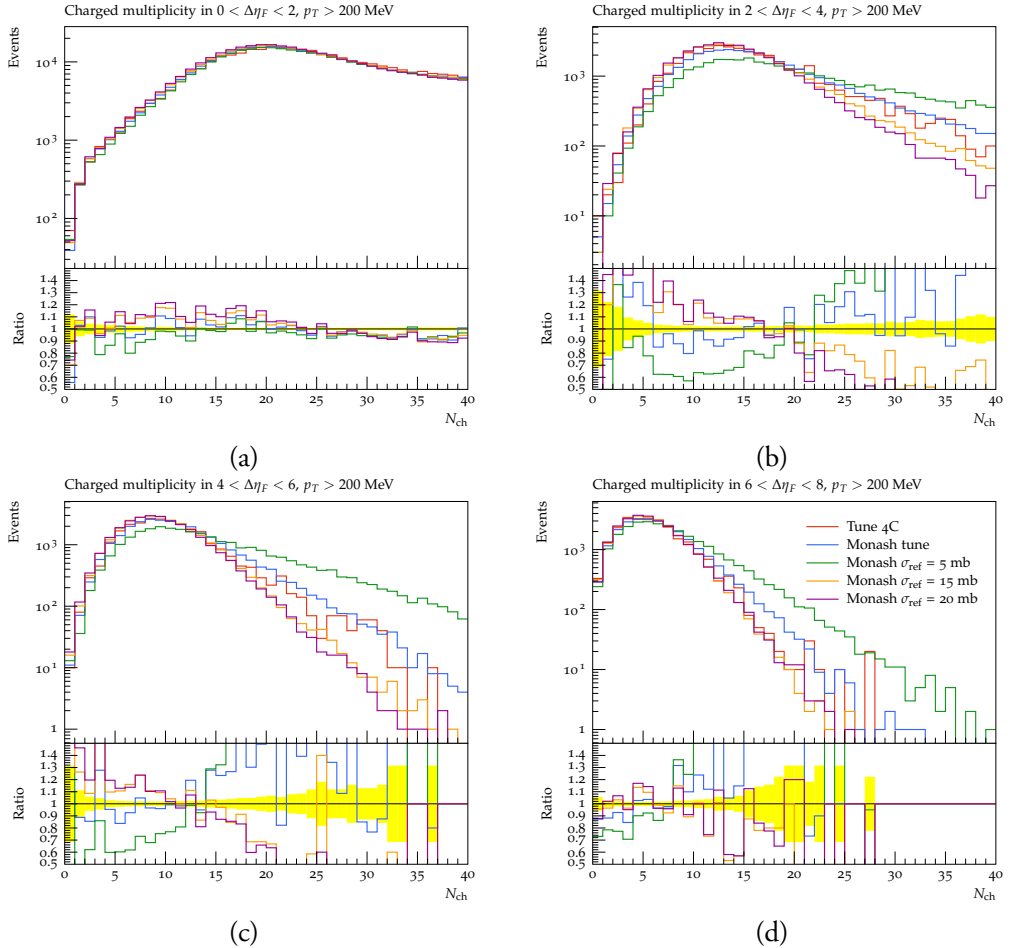


Figure II.13: The effects of changing the reference $\mathbb{P}p$ cross section on the charged multiplicity distribution using the SaS model at 7 TeV in the four gap ranges: 0 to 2 (a), 2 to 4 (b), 4 to 6 (c) and 6 to 8 (d).

Figs. II.13 and II.14 show the effects of changing the $\mathbb{P}p$ cross section on the charged particle

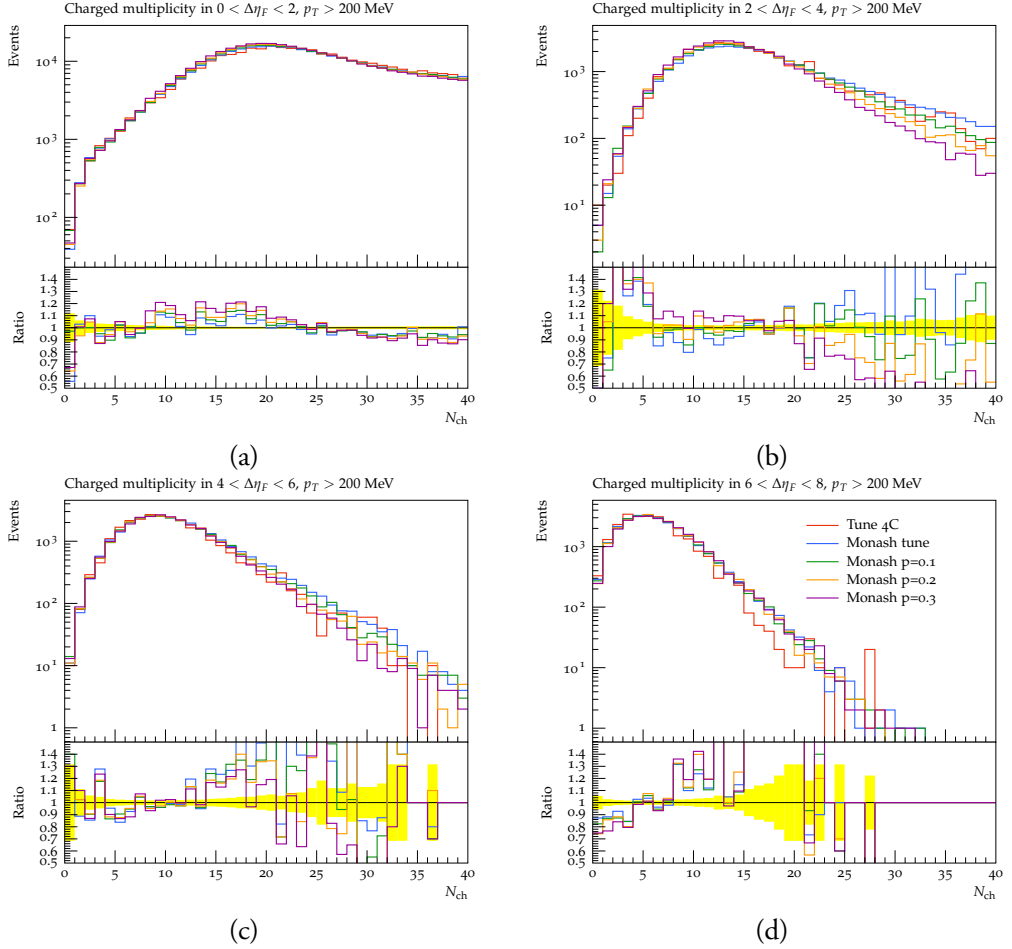


Figure II.14: The effects of changing the power of the mass dependence in the \mathbb{P}_p cross section on the charged multiplicity distribution using the SaS model at 7 TeV in the four gap ranges: 0 to 2 (a), 2 to 4 (b), 4 to 6 (c) and 6 to 8 (d).

distributions in the different $\Delta\eta_F$ bins compared to the 4C tune. In [52] the 4C tune generally was seen to undershoot the low cluster-multiplicities, while overshooting the mid to high cluster multiplicities. In the highest $\Delta\eta_F$ bin, dominated by the diffractive events, Tune 4C undershoots both the low- and high-multiplicity activity. Reducing the \mathbb{P}_p cross section increases the multiplicity, and vice versa. Thus, to describe the high-multiplicity events, a smaller \mathbb{P}_p cross section would be preferred. This could be compensated by allowing the perturbative description to go below $M_X = m_{\min} = 10$ GeV, thus allowing slightly more activity in low-mass systems, possibly increasing the number of low-multiplicity events. The effects of including a mass dependence in the \mathbb{P}_p cross section is seen in fig. II.14. A parametrization has been chosen as $\sigma_{\mathbb{P}_p}^{\text{eff}}(M_X) = \sigma_{\mathbb{P}_p}^{\text{ref}} (M_X/M_{\text{ref}})^p$, with $M_{\text{ref}} = 100$ GeV. Here, an increase of p slightly decreases the high-multiplicity region, albeit more subtly

than with an increase of the $\mathbb{P}p$ cross section. Recall that the mass of the diffractive system is related to the collision energy, such that a value of $p \sim 0.2 - 0.3$ is not unreasonable, corresponding to a rise of the cross section with energy of $s^{0.1} - s^{0.15}$.

A full study of particle production in diffractive events with PYTHIA 8, HERWIG 7 [57, 58], SHERPA [59, 60] and PHOJET [61] could provide further valuable information on the hadronic event properties of diffractive systems, as the generators differ in how they describe such production. The effects of color reconnection in a diffractive system is also of interest, as the amount of “accidental” gaps could be constrained in these systems, if one assumes that the CR scheme is the same in both diffractive and non-diffractive systems. At present we leave the $\mathbb{P}p$ cross section as is at 10 mb, and show the results with the models presented so far in fig. II.15.

The bulk of the cross section arises from nondiffractive events. These tend to only give rise to small rapidity gaps, as the phase space is more or less evenly filled by multiparton interactions. Gaps of intermediate or large size can occur, however, e.g. by color reconnection between the partons [9, 62]. The default PYTHIA CR framework has been designed to avoid accidental gaps, so as to keep a clean separation between diffractive and non-diffractive topologies. In other models, e.g. the CSCR one [18], the color reshuffling tends to give somewhat larger probability for intermediate gaps. A combination of the CSCR model and the default SaS diffractive setup then results in too large a cross section in the intermediate-gap range, cf. figs. II.15a,b.

Diffractive events are more likely to give rise to intermediate to large gaps. Hence, depending on color-reconnection model used, they will dominate from gap sizes of approximately two and larger. The size of the gap is closely connected to the mass of the diffractive system. Thus a model with a dM_X^2/M_X^2 ansatz, like the SaS one (modulo some corrections), will give an approximately flat distribution of measured gap sizes. This can be modified by the recent inclusion of the mass-correction factor ϵ_{SaS} , which introduces an additional $1/M_X^{2\epsilon_{\text{SaS}}}$ factor to the differential model. Depending on the sign of ϵ_{SaS} , it will either increase or decrease the high-mass cross section. In both the ATLAS and CMS datasets an increase of the large-gap cross section is seen. Thus we expect a positive sign for ϵ_{SaS} , as this will enhance the activity at low masses. For simplicity, adding the mass correction will not affect the integrated diffractive cross section.

The ABMST models show slightly better agreement with the shape of the rapidity gap distributions, although the original ABMST model overshoots both datasets. This was to be expected, as the model had trouble with the increase of the single diffractive cross section at LHC energies. The modified version of the ABMST model shows very nice agreement with both datasets, except for an undershoot of the high-mass region of the double-diffractive-dominated region in fig. II.15d. This behavior closely correlates with the flatness of the $\xi d\sigma/d\xi$ -spectrum, fig. II.9b. Both the ABMST models have a mass

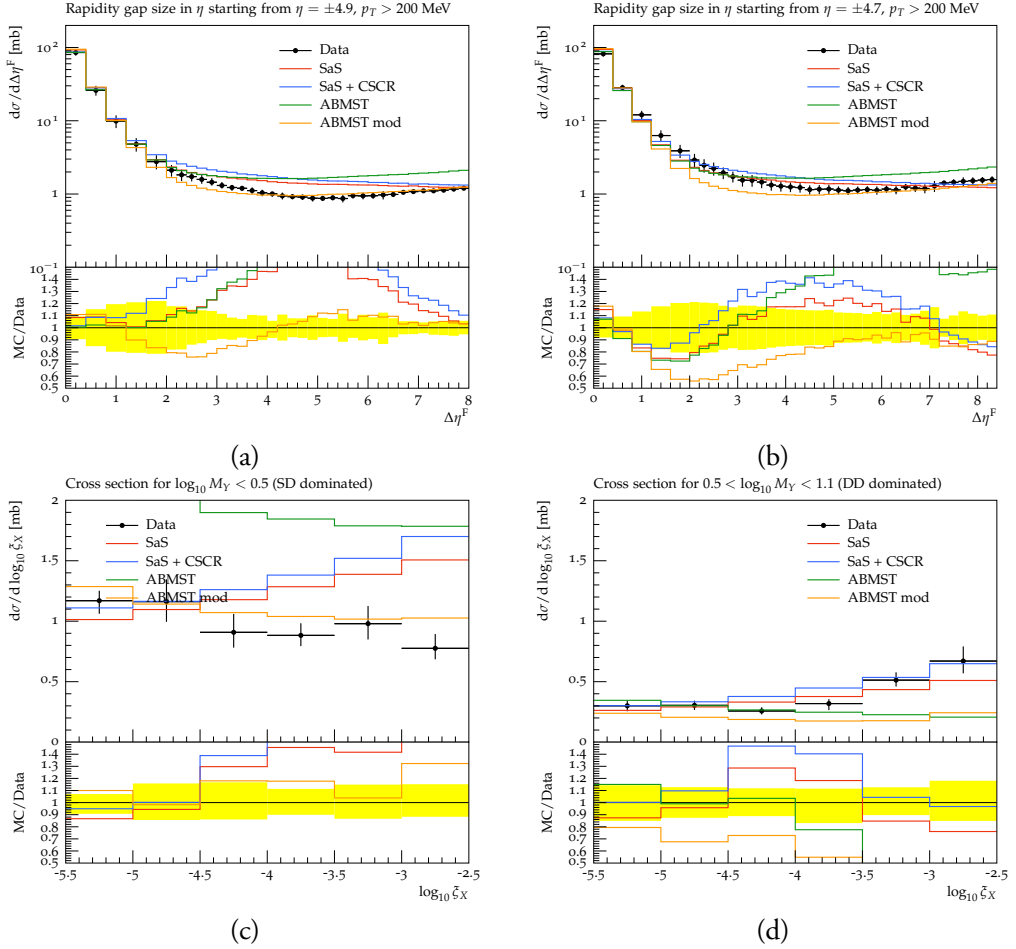


Figure II.15: The cross section as a function of gap size for the default SaS model, the SaS+CSCR model and the untuned ABMST models compared to ATLAS [52] (a) and CMS [53] (b) data. The cross section as a function of $\log_{10} \xi_X$ in a single-diffraction dominated region (c) and double diffraction dominated region (d) compared to CMS [53] data.

spectrum shape comparable to data in the single-diffraction-dominated region, unlike the SaS model, which overshoots the high-mass systems.

7.2 The tuned models

The tunes provided here are performed with the Professor framework [63], varying the high-mass diffractive parameters given in table II.1. All non-diffractive parameters are left at their default values, as given by the Monash tune [64], except for the CSCR-specific changes in that setup. The H1 leading order Pomeron PDF [27] is used in all the tunes.

Table II.1: The parameters used in the tunes for the different models.

	ϵ	α'	σ_{SD}^{\max}	σ_{DD}^{\max}	σ_{CD}^{\max}	ϵ_{SaS}
SaS	0.06	0.4	22.31	39.83	0.	0.
SaS+CSCR	0.15	0.26	20.81	13.13	0.	0.
SaS+ ϵ_{SaS}	0.04	0.30	24.78	52.49	0.	0.08
	k_{SD}	k_{DD}	k_{CD}	p_{SD}	p_{DD}	p_{CD}
ABMST	0.58	2.45	1.0	0.	0.05	0.03
ABMST modified	0.92	1.72	1.38	0.	0.1	0.04

Fig. II.16 shows the three SaS-based models tuned to the above-mentioned data. Neither of the three models are able to describe the shape of the gap data perfectly, figs. II.16a,b. The tune has decreased the amount of activity in the mid- to large-gap region by a decrease of the σ_i^{\max} values used in eq. (II.9). The inclusion of ϵ_{SaS} has shifted some of the activity from intermediate-gaps to larger ones, while keeping the integrated cross section fixed. Unfortunately this is at the expense of an undershoot in the transition region $\Delta\eta^F \sim 2$ between diffractive and nondiffractive topologies. This is the region where CSCR does better, so a combination of CSCR with an $\epsilon_{SaS} > 0$ could provide a flatter MC/data distribution in fig. II.16a,b.

For the mass spectra measured by CMS, fig. II.16c,d, evidently only the SaS+ ϵ_{SaS} model is able to describe the single-diffraction-dominated mass spectrum, whereas it undershoots the high-mass double diffraction region since, relative to the original SaS model, it has shifted some of the high-mass activity to lower masses.

Fig. II.17 shows the tuned ABMST models. The tune has a hard time improving the modified ABMST model, as this gave a good agreement with data already to begin with. The original ABMST model, however, is significantly improved by rescaling, and is now very similar to the modified ABMST model developed in this paper. Note that the mass spectrum of the single-diffraction-dominated region, fig. II.17c, shows the proper shape, while the double-diffraction-dominated one, fig. II.17d, seems to overestimate the low-mass region and underestimate the high-mass one. This is a result of the reduction of the vanishing-gap topologies of double-diffractive systems, that has been kept unchanged in this tune. Combining the ABMST models with the CSCR model has potential also here, as the ABMST models underestimate data in the intermediate gap range, cf. figs. II.17a,b.

Fig. II.18 shows the CMS inelastic cross section obtained with two different approaches. One uses forward calorimetry ($3 < |\eta| < 5$), to measure protons with fractional momentum loss greater than $\xi > 5 \cdot 10^{-6}$, corresponding to everything but low-mass diffractive systems ($M_X > 16$ GeV). The other uses the central tracker, requiring either one, two or three tracks. The SaS+ ϵ_{SaS} and the modified ABMST models perform better than the oth-

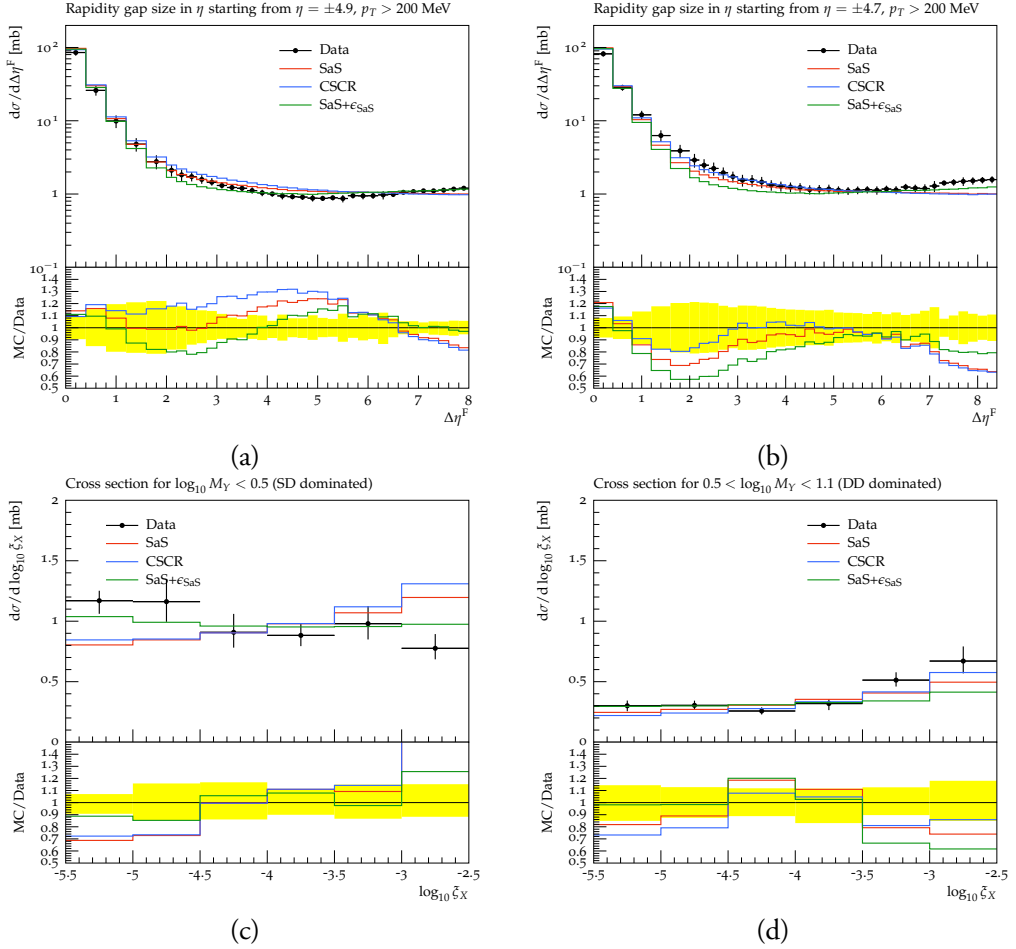


Figure II.16: The cross section as a function of gap size for the three SaS-based models compared to ATLAS [52] (a) and CMS [53] (b) data. The cross section as a function of $\log_{10} \xi_X$ in a single-diffractive dominated region (c) and double diffractive dominated region (d) compared to CMS [53] data.

ers, with a maximum 5% deviation from CMS data. The SaS and the CSCR models has the same model for diffractive systems, and hence it is not expected that these differ in the measured inelastic cross section. With the SaS+ ϵ_{SaS} model, however, some of the activity has been shifted to lower diffractive masses, resulting in a lower inelastic cross section. For ABMST, the reduction of the high-mass systems in the modified model results in a reduction of the inelastic cross section relative to the original one.

Table II.2 shows the integrated cross sections obtained with the ALICE and ATLAS 2011 analyses mentioned above. The ALICE results have been obtained for $M_X < 200$ GeV ($\xi < 0.0008$) for single diffraction, for gap sizes larger than $\Delta\eta > 3$ for double diffraction, and with a van der Meer scan using diffractive events adjusted to data for the inelastic

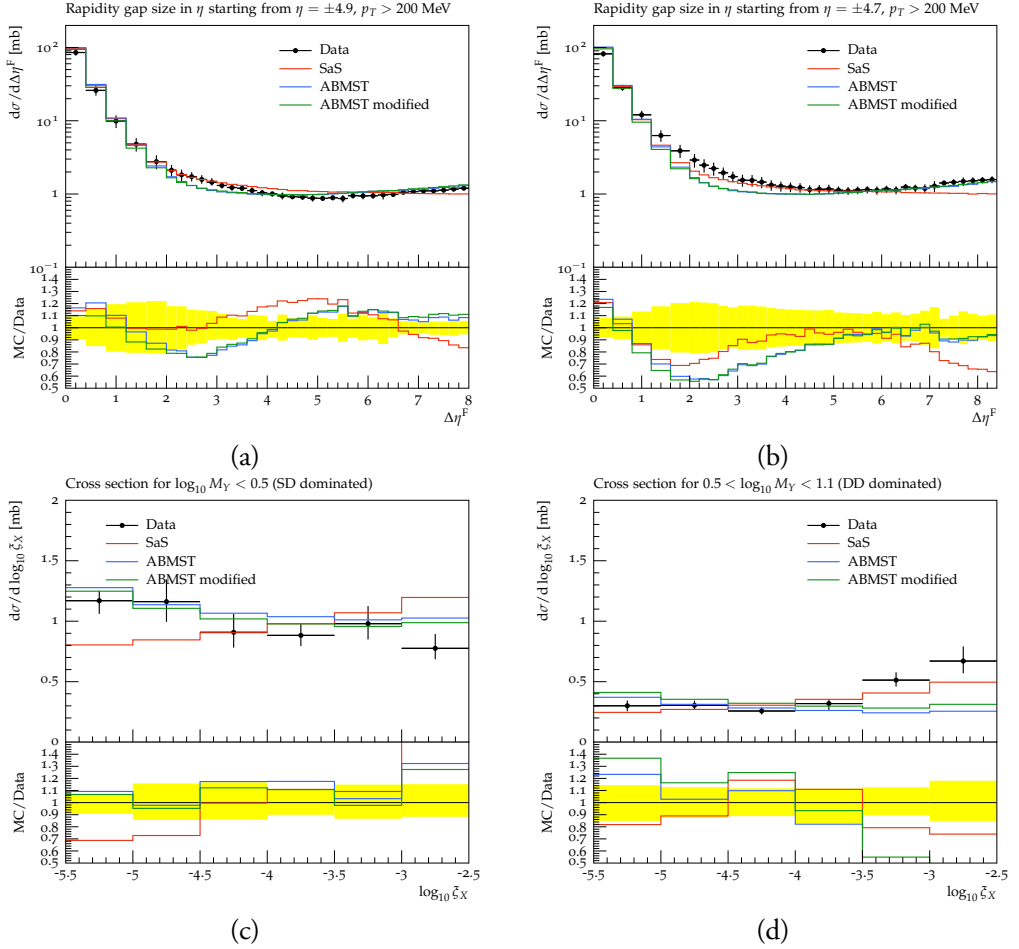


Figure II.17: The cross section as a function of gap size for the two ABMST-based models compared to ATLAS [52] (a) and CMS [53] (b) data. The cross section as a function of $\log_{10} \xi_X$ in a single-diffractive dominated region (c) and double diffractive dominated region (d) compared to CMS [53] data. For reference the tuned SaS model is also shown.

cross section. In the Rivet analysis, this corresponds to at least two tracks in the final state, i.e. effectively without any experimental cuts and hence returning the generator-level cross section. The SaS+ ϵ_{SaS} model gives a better prediction for the single diffractive data, because of the increased low-mass cross section. The CSCR model predicts a larger double diffractive cross section, because of the larger probability for “accidental” gaps. The inelastic cross section, however, is the same for all three SaS-based models when compared with the ALICE data, as all have the same generator-level integrated cross section. In the ATLAS measurement of the inelastic cross section (for $\xi > 5 \cdot 10^{-6}$) the SaS+ ϵ_{SaS} model predicts a lower inelastic cross section, again because of the larger low-mass cross section.

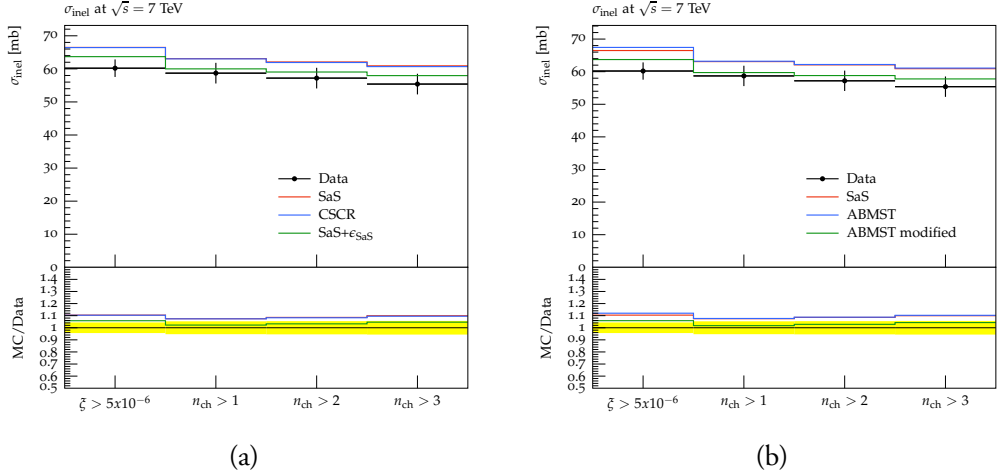


Figure II.18: The inelastic cross section as a function of method described in the text compared to CMS [55] data.

Both the ABMST models give larger single-diffractive cross sections than SaS, having improved in the low-mass region. But both underestimate the double-diffractive cross section as they both underestimate the medium-sized gaps, compared with SaS and data. An addition of the CSCR model would be likely to improve this prediction. The ABMST models predict the same inelastic cross section for ALICE, since the generator-level inelastic cross section is the same for the two models. They differ for the ATLAS analysis, again because of the reduced high-mass systems of the modified ABMST model.

In general, however, all models fail to describe the measured integrated cross sections, although some of the more sophisticated models do improve in some respects. Similarly, it seems that neither of the models describe well the transition from a non-diffractive-dominated region to a diffraction-dominated one. Including a color-reconnection model that allows for larger gaps in the non-diffractive events, like CSCR, is likely to improve the description in the mid-sized-gap range, if combined with a model that predicts a lower diffractive cross section there, like the ABMST models and SaS+ ϵ_{SaS} . The overall question of how to combine the descriptions of non-diffractive and diffractive topologies, however, will still exist even if the CR model “accidentally” (i.e. by “accidental” gaps) improves the description of data. All this highlights our still limited understanding of nonperturbative QCD, which forces us to work with models e.g. rooted in Regge theory. This may be good enough for an overall understanding, but still not for a precise reproduction of all relevant data.

Table II.2: The integrated cross section obtained with the three aforementioned Rivet analyses for the tuned models. For ALICE [56], the SD cross section is for $M_X < 200$ GeV, the double diffractive for gaps larger than 3, the inelastic using a van der Meer scan using diffractive events adjusted to data. The ATLAS [54] inelastic cross section is for $\xi > 5 \cdot 10^{-6}$.

	σ_{SD} (mb) (ALICE)	σ_{DD} (mb) (ALICE)	σ_{inel} (mb) (ALICE)	σ_{inel} (mb) (ATLAS)
data	14.9 ± 5.90	9.00 ± 2.60	73.20 ± 5.28	60.33 ± 2.10
SaS	6.13 ± 0.01	5.72 ± 0.01	71.06 ± 0.02	66.48 ± 0.02
SaS + CSCR	6.15 ± 0.01	6.19 ± 0.01	71.06 ± 0.02	66.43 ± 0.02
SaS + ϵ_{SaS}	7.98 ± 0.01	5.62 ± 0.01	71.06 ± 0.02	63.69 ± 0.02
ABMST	7.24 ± 0.01	4.69 ± 0.01	71.62 ± 0.02	67.44 ± 0.02
ABMST mod	9.41 ± 0.01	5.09 ± 0.01	71.62 ± 0.02	63.72 ± 0.02

8 Conclusions

In this paper we provide an updated description of the cross sections and hadronic event shapes in the event generator PYTHIA 8. The update has been required since the first results appeared from the LHC experiments, showing significant discrepancies between the models provided by Donnachie and Landshoff for the total cross section, as well as the elastic and diffractive cross sections by Schuler and Sjöstrand. By chance the DL undershooting of the total cross section and the SaS undershooting of the elastic cross section partly cancel in the inelastic cross section. Further to that, the SaS overshooting of the diffractive cross sections gave rise to a reasonable agreement between PYTHIA 8 and LHC measurements on the observable non-diffractive cross section, which is the relevant one for many of the measurements performed at the LHC. Thus, in spite of these shortfalls, the default PYTHIA 8 cross sections usually were good enough, notably when diffractive cross sections had been reduced somewhat (eq. II.9).

The discrepancies became largely evident with the precision measurements of the elastic and total cross sections performed by both TOTEM and ATLAS+ALFA. Here the exponential shape of the t spectrum in PYTHIA 8 is too simplistic, and other models have to be used for comparisons. Some of these models have now been implemented into PYTHIA 8, thereby providing a more sophisticated framework for elastic scattering and total cross sections.

For diffractive topologies the precision is less. The studies are marred by non-diffractive events mimicking diffractive ones, and vice versa, making the explicit distinction between the various diffractive and non-diffractive event topologies hard. The possibility of tagging the elastically scattered protons would greatly improve the separation of the samples, but so far no analyses on diffraction with tagged protons have appeared from CMS+TOTEM or ATLAS+ALFA. Thus we are left with measurements only using the central general-purpose detectors. Unfortunately these do not give fully consistent answers. Notably the CMS and ATLAS rapidity-gap measurements disagree in the diffraction-dominated region, making

it hard to compare models with data. Lacking any further guidance, we have here aimed for a middle ground between the two data sets.

The situation is even worse for hadronic event shapes. Single diffractive data is available for very low energies, most of which goes into the ABMST model, but rather little for higher energies. This means that, even if integrated cross sections were provided for diffractive topologies from the LHC experiments, no constraints are put on the internal structure of diffractive systems. The ansatz of PYTHIA 8, that the diffractive system properties are similar to those of non-diffractive events, could be wrong. A future study of these event shapes, and of the different strategies underlying commonly used event generators, would help provide a guideline what would be interesting distributions to see measured at the LHC.

In conclusion, we provide an updated and extended framework for elastic and diffractive topologies, as well as an update for all parts of the total cross section. We rely on previous work provided by several other authors, but have corrected and extended the models where need be. Each of the models has been tuned to available data, thus providing an upgrade of the already present models in PYTHIA 8. We have discussed some of the consequences of different approaches for creating rapidity gaps, such as the CSCR model, and how this affects the predictions for LHC. Still, the lack of data or the discrepancies of present data, leaves us with imperfect descriptions and predictions, in particular for diffraction. The situation may be “good enough” for current needs, but will hopefully improve with new data in the future. At present we are not able to decide which model is “the better one” for diffraction, but in the case of total and elastic cross section the new models, COMPAS and ABMST, offer an improved description as compared to the SaS model. As the COMPAS model offers no description of diffraction, we propose to use the ABMST model for total and elastic cross section and the modified ABMST model for diffraction, with the tuned parameters as provided in this paper. We expect to change the default behavior in the next PYTHIA release.

Foreseeable further work could include a low-mass description for central diffractive topologies, possibly modeling the resonances present there. Other work would be an extensive study of the diffractive event shapes as discussed above. A study on eikonalization aspects, e.g. of events with both diffractive and nondiffractive Pomeron exchanges, could also provide more insight on both cross sections and event topologies. Finally, the diffractive framework could be extended also to other processes, such as γp and $\gamma\gamma$ collisions.

9 Acknowledgments

We would like to thank Vladimir Ezhela from the COMPAS group for assistance with their model. Similarly we would like to thank Rob Appleby, James Molson and Sandy Donnachie for their huge effort in explaining various aspects of their model, as well as providing all of their data used in their fit.

Work supported in part by the Swedish Research Council, contracts number 621-2013-4287 and 2016-05996, and in part by Marie Curie Initial Training Networks, FP7 MCnetITN (grant agreement PITN-GA-2012-315877) and H2020 MCnetITN₃ (grant agreement 722104). This project has also received funding from the European Research Council (ERC) under the European Union's Horizon 2020 research and innovation programme (grant agreement No 668679).

References

- [1] P. D. B. Collins, “An Introduction to Regge Theory and High-Energy Physics,” Cambridge University Press (1977).
- [2] J. R. Forshaw and D. A. Ross, “Quantum chromodynamics and the pomeron,” Cambridge Lect. Notes Phys. **9** (1997) 1.
- [3] S. Donnachie, H. G. Dosch, O. Nachtmann and P. Landshoff, “Pomeron physics and QCD,” Camb. Monogr. Part. Phys. Nucl. Phys. Cosmol. **19** (2002) 1.
- [4] V. Barone and E. Predazzi, “High-Energy Particle Diffraction,” Springer (2002).
- [5] M. L. Good and W. D. Walker, Phys. Rev. **120** (1960) 1857. doi:10.1103/PhysRev.120.1857
- [6] C. Flensburg and G. Gustafson, JHEP **1010** (2010) 014 doi:10.1007/JHEP10(2010)014 [arXiv:1004.5502 [hep-ph]].
- [7] R. Hagedorn, Nuovo Cim. Suppl. **3** (1965) 147.
- [8] G. Ingelman and P. E. Schlein, Phys. Lett. **152B** (1985) 256. doi:10.1016/0370-2693(85)91181-5
- [9] A. Edin, G. Ingelman and J. Rathsman, Phys. Lett. B **366** (1996) 371 doi:10.1016/0370-2693(95)01391-1 [hep-ph/9508386].
- [10] W. Buchmuller and A. Hebecker, Phys. Lett. B **355** (1995) 573 doi:10.1016/0370-2693(95)00721-V [hep-ph/9504374].
- [11] T. Sjöstrand, S. Mrenna and P. Z. Skands, JHEP **0605** (2006) 026 doi:10.1088/1126-6708/2006/05/026 [hep-ph/0603175].

- [12] T. Sjöstrand, S. Ask, J. R. Christiansen, R. Corke, N. Desai, P. Ilten, S. Mrenna and S. Prestel *et al.*, Comput. Phys. Commun. **191** (2015) 159 [arXiv:1410.3012 [hep-ph]].
- [13] G. A. Schuler and T. Sjöstrand, Phys. Rev. D **49** (1994) 2257.
- [14] S. Navin, arXiv:1005.3894 [hep-ph].
- [15] C. Patrignani *et al.* [Particle Data Group], Chin. Phys. C **40** (2016) no.10, 100001. doi:10.1088/1674-1137/40/10/100001
- [16] R. B. Appleby, R. J. Barlow, J. G. Molson, M. Serluca and A. Toader, Eur. Phys. J. C **76** (2016) no.10, 520 doi:10.1140/epjc/s10052-016-4363-7 [arXiv:1604.07327 [hep-ph]].
- [17] A. Donnachie and P. V. Landshoff, Phys. Lett. B **296** (1992) 227 doi:10.1016/0370-2693(92)90832-O [hep-ph/9209205].
- [18] J. R. Christiansen and P. Z. Skands, JHEP **1508** (2015) 003 doi:10.1007/JHEP08(2015)003 [arXiv:1505.01681 [hep-ph]].
- [19] [ATLAS Collaboration], ATLAS-CONF-2010-048.
- [20] R. Corke and T. Sjöstrand, JHEP **1103** (2011) 032 doi:10.1007/JHEP03(2011)032 [arXiv:1011.1759 [hep-ph]].
- [21] D. Bernard *et al.* [UA4 Collaboration], Phys. Lett. B **198** (1987) 583. doi:10.1016/0370-2693(87)90922-1
- [22] G. Antchev *et al.* [TOTEM Collaboration], Eur. Phys. J. C **76** (2016) no.12, 661 doi:10.1140/epjc/s10052-016-4399-8 [arXiv:1610.00603 [nucl-ex]].
- [23] G. B. West and D. R. Yennie, Phys. Rev. **172** (1968) 1413. doi:10.1103/PhysRev.172.1413
- [24] R. Cahn, Z. Phys. C **15** (1982) 253. doi:10.1007/BF01475009
- [25] R. Ciesielski and K. Goulianos, PoS ICHEP **2012** (2013) 301 [arXiv:1205.1446 [hep-ph]].
- [26] B. Andersson, G. Gustafson, G. Ingelman and T. Sjöstrand, Phys. Rept. **97** (1983) 31.
- [27] A. Aktas *et al.* [H1 Collaboration], Eur. Phys. J. C **48** (2006) 715 doi:10.1140/epjc/s10052-006-0035-3 [hep-ex/0606004].
- [28] A. Aktas *et al.* [H1 Collaboration], JHEP **0710** (2007) 042 doi:10.1088/1126-6708/2007/10/042 [arXiv:0708.3217 [hep-ex]].
- [29] L. Alvero, J. C. Collins, J. Terron and J. J. Whitmore, Phys. Rev. D **59** (1999) 074022 doi:10.1103/PhysRevD.59.074022 [hep-ph/9805268].

- [30] M. Goharipour, H. Khanpour and V. Guzey, arXiv:1802.01363 [hep-ph].
- [31] T. Sjöstrand, arXiv:1706.02166 [hep-ph].
- [32] T. Sjöstrand and P. Z. Skands, JHEP **0403** (2004) 053 doi:10.1088/1126-6708/2004/03/053 [hep-ph/0402078].
- [33] T. Sjöstrand, Phys. Lett. **157B** (1985) 321. doi:10.1016/0370-2693(85)90674-4
- [34] C. O. Rasmussen and T. Sjöstrand, JHEP **1602** (2016) 142 doi:10.1007/JHEP02(2016)142 [arXiv:1512.05525 [hep-ph]].
- [35] G. Antchev *et al.* [TOTEM Collaboration],
- [36] TOTEM Collaboration, 132nd LHCC open session and 21st TOTEM RRB. CERN-2017
- [37] R. Avila, P. Gauron and B. Nicolescu, Eur. Phys. J. C **49** (2007) 581 doi:10.1140/epjc/s10052-006-0074-9 [hep-ph/0607089].
- [38] E. Martynov and B. Nicolescu, Eur. Phys. J. C **56** (2008) 57 doi:10.1140/epjc/s10052-008-0629-z [arXiv:0712.1685 [hep-ph]].
- [39] E. Martynov and B. Nicolescu, arXiv:1711.03288 [hep-ph].
- [40] A. Donnachie and P. V. Landshoff, Phys. Lett. B **727** (2013) 500 Erratum: [Phys. Lett. B **750** (2015) 669] doi:10.1016/j.physletb.2015.09.017, 10.1016/j.physletb.2013.10.068 [arXiv:1309.1292 [hep-ph]].
- [41] A. Donnachie and P. V. Landshoff, arXiv:1112.2485 [hep-ph].
- [42] N. A. Amos *et al.*, Nucl. Phys. B **262** (1985) 689. doi:10.1016/0550-3213(85)90511-5
- [43] J. Molson. Proton scattering and collimation for the LHC and LHC luminosity upgrade - 2014. PhD thesis, University of Manchester Press, UK.
- [44] A. Donnachie and P. V. Landshoff, Nucl. Phys. B **244** (1984) 322. doi:10.1016/0550-3213(84)90315-8
- [45] E. L. Berger, J. C. Collins, D. E. Soper and G. F. Sterman, Nucl. Phys. B **286** (1987) 704. doi:10.1016/0550-3213(87)90460-3
- [46] H. Jung, Comput. Phys. Commun. **86** (1995) 147. doi:10.1016/0010-4655(94)00150-Z
- [47] P. Aurenche, F. W. Bopp, A. Capella, J. Kwiecinski, M. Maire, J. Ranft and J. Tran Thanh Van, Phys. Rev. D **45** (1992) 92. doi:10.1103/PhysRevD.45.92

- [48] L. A. Harland-Lang, V. A. Khoze and M. G. Ryskin, *Eur. Phys. J. C* **76** (2016) no.1, 9 doi:10.1140/epjc/s10052-015-3832-8 [arXiv:1508.02718 [hep-ph]].
- [49] J. Monk and A. Pilkington, *Comput. Phys. Commun.* **175** (2006) 232 doi:10.1016/j.cpc.2006.04.005 [hep-ph/0502077].
- [50] E. S. Bols, Proton-proton central exclusive pion production at $\sqrt{s} = 13$ TeV with the ALFA and ATLAS detectors NBI, University of Copenhagen, 2017
- [51] A. Buckley, J. Butterworth, L. Lonnblad, D. Grellscheid, H. Hoeth, J. Monk, H. Schulz and F. Siegert, *Comput. Phys. Commun.* **184** (2013) 2803 doi:10.1016/j.cpc.2013.05.021 [arXiv:1003.0694 [hep-ph]].
- [52] G. Aad *et al.* [ATLAS Collaboration], *Eur. Phys. J. C* **72** (2012) 1926 doi:10.1140/epjc/s10052-012-1926-0 [arXiv:1201.2808 [hep-ex]].
- [53] V. Khachatryan *et al.* [CMS Collaboration], *Phys. Rev. D* **92** (2015) no.1, 012003 doi:10.1103/PhysRevD.92.012003 [arXiv:1503.08689 [hep-ex]].
- [54] G. Aad *et al.* [ATLAS Collaboration], *Nature Commun.* **2** (2011) 463 doi:10.1038/ncomms1472 [arXiv:1104.0326 [hep-ex]].
- [55] S. Chatrchyan *et al.* [CMS Collaboration], *Phys. Lett. B* **722** (2013) 5 doi:10.1016/j.physletb.2013.03.024 [arXiv:1210.6718 [hep-ex]].
- [56] B. Abelev *et al.* [ALICE Collaboration], *Eur. Phys. J. C* **73** (2013) no.6, 2456 doi:10.1140/epjc/s10052-013-2456-0 [arXiv:1208.4968 [hep-ex]].
- [57] M. Bahr *et al.*, *Eur. Phys. J. C* **58** (2008) 639 doi:10.1140/epjc/s10052-008-0798-9 [arXiv:0803.0883 [hep-ph]].
- [58] J. Bellm *et al.*, *Eur. Phys. J. C* **76** (2016) no.4, 196 doi:10.1140/epjc/s10052-016-4018-8 [arXiv:1512.01178 [hep-ph]].
- [59] T. Gleisberg, S. Hoeche, F. Krauss, M. Schonherr, S. Schumann, F. Siegert and J. Winter, *JHEP* **0902** (2009) 007 doi:10.1088/1126-6708/2009/02/007 [arXiv:0811.4622 [hep-ph]].
- [60] A. D. Martin, H. Hoeth, V. A. Khoze, F. Krauss, M. G. Ryskin and K. Zapp, *PoS QNP 2012* (2012) 017 [arXiv:1206.2124 [hep-ph]].
- [61] F. W. Bopp, R. Engel and J. Ranft, hep-ph/9803437.
- [62] A. Edin, G. Ingelman and J. Rathsman, *Z. Phys. C* **75** (1997) 57 doi:10.1007/s002880050447 [hep-ph/9605281].

- [63] A. Buckley, H. Hoeth, H. Lacker, H. Schulz and J. E. von Seggern, Eur. Phys. J. C **65** (2010) 331 doi:10.1140/epjc/s10052-009-1196-7 [arXiv:0907.2973 [hep-ph]].
- [64] P. Skands, S. Carrazza and J. Rojo, Eur. Phys. J. C **74** (2014) no.8, 3024 doi:10.1140/epjc/s10052-014-3024-y [arXiv:1404.5630 [hep-ph]].
- [65] G. Antchev *et al.*, EPL **96** (2011) no.2, 21002 doi:10.1209/0295-5075/96/21002 [arXiv:1110.1395 [hep-ex]].
- [66] G. Antchev *et al.* [TOTEM Collaboration], EPL **101** (2013) no.2, 21002. doi:10.1209/0295-5075/101/21002

III

Hard Diffraction in Photoproduction

Ilkka Helenius¹² and Christine O. Rasmussen³.

EPJC, 79 (2019) no. 5, 413

doi: 10.1140/epjc/s10052-019-6914-1

e-Print: arXiv:1901.05261[hep-ph]

MCnet-19-01 LU-TP 19-06

¹ Institute for Theoretical Physics, Tübingen University, Auf der Morgenstelle 14, 72076 Tübingen, Germany.

² University of Jyväskylä, Department of Physics, P.O. Box 35, FI-40014 University of Jyväskylä, Finland.

³ Dept. of Astronomy and Theoretical Physics, Lund University, Sölvegatan 14A, SE-223 62 Lund, Sweden.

ABSTRACT: We present a new framework for modeling hard diffractive events in photoproduction, implemented in the general purpose event generator PYTHIA 8. The model is an extension of the model for hard diffraction with dynamical gap survival in pp and p \bar{p} collisions proposed in 2015, now also allowing for other beam types. It thus relies on several existing ideas: the Ingelman-Schlein approach, the framework for multiparton interactions and the recently developed framework for photoproduction in γp , $\gamma\gamma$, ep and e^+e^- collisions. The model proposes an explanation for the observed factorization breaking in photoproduced diffractive dijet events at HERA, showing an overall good agreement with data. The model is also applicable to ultraperipheral collisions with pp and pPb beams, and predictions are made for such events at the LHC.

I Introduction

Diffractive excitations represent large fractions of the total cross section in a wide range of collisions. A part of these has been seen to have a hard scale, as in e.g. the case of diffractive dijet production. These *hard diffractive* events allow for a perturbative calculation of the scattering subprocess, but still require some phenomenological modeling. This includes modeling of the Pomeron, expected to be responsible for the color-neutral momentum transfer between the beam and the diffractive system X . In the framework of collinear factorization, a diffractive parton distribution function (dPDF) may be defined. This can further be factorized into a Pomeron flux and a PDF, describing the flux of Pomerons from the beam and the parton density within the Pomeron, respectively.

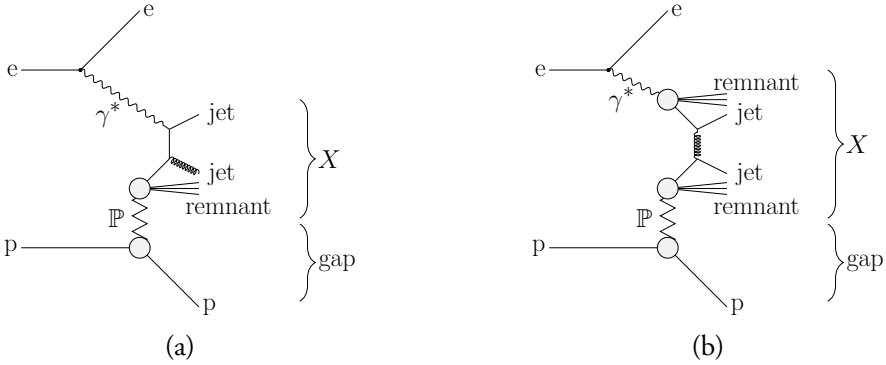


Figure III.1: Leading order Feynman diagrams for diffractive dijet production with photons in ep collisions. Either the photon participates directly in the hard scattering matrix element (a) or a parton from the resolved photon participates (b).

Here we focus mainly on photoproduced diffractive dijets in ep collisions. This scattering process can be separated into different subsystems, visualized in Fig. III.1. The initial state consists of an electron and a proton, with the former radiating off a (virtual) photon. If the photon is highly virtual, we are in the range of deep inelastic scattering (DIS), while a photon with low enough virtuality can be considered (quasi-)real. This is the photoproduction regime. No clear distinction between the two regimes exists, however, and photons of intermediate virtuality require careful consideration to avoid double-counting. A special feature in the photoproduction regime is that there is a non-negligible probability for the photon to fluctuate into a hadronic state. These resolved photons open up for all possible hadron-hadron processes, including diffractive ones.

The next subsystem shown in Fig. III.1 is the photon-proton scattering system. Here, diffraction could in principle occur on both sides if the photon is resolved. In direct photoproduction (and in DIS) the diffractive system can only be present on the photon side, as no Pomeron flux can be defined for point-like photons. In this article the emphasis will be on Pomeron emission from the proton.

The final subsystem is the hard scattering generated inside the diffractive system X . For direct photoproduction (and DIS) this includes the photon as an incoming parton, see Fig. III.1 (a). In the resolved case, Fig. III.1 (b), a parton is extracted from the hadronic photon, which then proceeds to initiate the hard scattering along with a parton extracted from the Pomeron. In both cases a beam remnant is left behind from the Pomeron, while resolved photoproduction also gives rise to a beam remnant from the hadronic photon. Multiple scatterings or multiparton interactions (MPIs) are expected between the remnants, but also in the larger photon-proton system. The particles produced by the latter type of MPIs may destroy the diffractive signature, the *rapidity gap* between the diffractive system and the elastically scattered proton (or meson, depending on the side of the diffractive system).

The model for photoproduced diffractive dijets presented here is based on the general-purpose event generator PYTHIA 8 [1]. It combines the existing frameworks for photoproduction and hard diffraction, the latter originally introduced for purely hadronic collisions. The new model thus allows for event generation of photon-induced hard diffraction with different beam configurations. The model is highly dependent on the components of PYTHIA 8. The relevant ones – the model for MPIs, photoproduction and hard diffraction – are described in the following sections.

The first measurements of diffractive dijets were done by the UA8 experiment at the Sp \bar{p} S collider at CERN [2]. Later on, similar events have been observed in ep collisions at HERA [3], in p \bar{p} collisions at the Tevatron [4], and nowadays also in pp collisions at the LHC [5]. Similarly, diffractively produced W^\pm and Z^0 bosons have been observed at the Tevatron [6]. All of these processes are expected to be calculable within a perturbative framework, such as the Ingelman-Schlein picture [7]. A model for such *hard diffractive* events was included in PYTHIA 8 [8], based on the Ingelman-Schlein approach and the rapidity gap survival idea of Bjorken [9]. The model proposed an explanation of the observed *factorization breaking* in hard diffractive p \bar{p} collisions – the observation that with the Pomeron PDFs and fluxes derived from HERA DIS data, the factorization-based calculation was an order of magnitude above the measurement. The suppression factor required on top of the dPDF-based calculation, was dynamically generated by requiring no additional MPIs in the pp (or p \bar{p}) system. The model predicted production rates in agreement with pp and p \bar{p} measurements, albeit some differential distributions did show room for improvement when comparing to Tevatron data. The latest preliminary analysis on diffractive dijets by CMS [10] finds a very good agreement between the model and data in all differential distributions.

First evidence of factorization breaking for diffractive dijets in ep collisions was observed by an H1 measurement [11], where a suppression factor of 0.6 was required to describe the dijet data in the photoproduction region, whereas the analysis for the DIS region was, by construction, well described by the factorization-based model without a corresponding

suppression factor. Advances in the formulation of the dPDFs improved the description of data in the DIS regime, but the discrepancies remained in the photoproduction limit. Several analyses have been performed by H1 and ZEUS for diffractive dijet production [12–16], all requiring a suppression factor between 0.5 – 0.9 in order for the factorization-based calculations to describe data.

The extension of the hard diffraction model in this article, to collisions with (intermediate) photons, makes it possible to explain the factorization-breaking in the photoproduction regime. The model is also applicable to the DIS regime, but here no further suppression is added since the highly virtual photons do not have any partonic structure that would give rise to the MPIs. Furthermore, the framework can also be applied to diffractive photoproduction in purely hadronic collisions, usually referred to as ultra-peripheral collisions (UPCs) [17]. The model predicts a substantial suppression for diffractive dijets in UPCs at the LHC.

The article is structured as follows: After the introduction in sec. 1, we briefly describe in sec. 2 the event generation procedure in PYTHIA 8. We then proceed in sec. 3 to the photoproduction framework available in PYTHIA 8 and continue to a short description of the hard diffraction model in sec. 4. We present results with our model compared to data from HERA on diffractive dijets in photoproduction in sec. 5, and show some predictions for photoproduction in UPCs at the LHC in sec. 6. We end with sec. 7 where we summarize our work and provide an outlook for further studies.

2 Event generation with PYTHIA 8

Recently, PYTHIA 8 has undergone a drastic expansion. Where the earlier version, PYTHIA 6 [18], was designed to accommodate several types of collisions (lepton-lepton, hadron-hadron and lepton-hadron, excluding nuclei), the rewrite to C++ focused mainly on the hadronic physics at the Tevatron and the LHC. While the LHC will run for years to come, there are several future collider projects under consideration. A common feature between the projected colliders is that they will be using lepton beams either primarily (linear e^+e^- colliders: CLIC and ILC [19,20] or Electron-Ion Collider (EIC) [21]), or as a first phase towards a hadronic collider (FCC [22,23]). To enable studies related to these future colliders, PYTHIA 8 has been extended to handle many processes involving lepton beams. Another major facility has been the extension from pp to pA and AA collisions with the inclusion of the ANGANTYR model for heavy ion collisions [24]. Combining the heavy-ion machinery with the recent developments related to lepton beams will also allow simulations of eA collisions and ultra-peripheral AA collisions. Work in this direction has been started within the PYTHIA collaboration.

The PYTHIA 6 description of lepton-lepton and lepton-hadron collisions included a sophisticated model for merging of the DIS regime (high-virtuality photons) and the photoproduction regime (low-virtuality photons) [25]. This, however, created upwards of 25 different event classes, each of which had to be set up differently. The model for the transition from photoproduction to DIS turned out not to agree so well with data, and the division of the different event classes was somewhat artificial. The aim for the PYTHIA 8 implementation of these processes has been to reduce the number of hard-coded event classes and increase robustness. The present framework, however, does not yet include a smooth merging of the high- and low-virtuality events and therefore the events with intermediate virtualities are not addressed. Work towards such a combined framework is currently ongoing. In addition, there is progress towards improving the parton showers for DIS events (see e.g. [26] and [27]). In this paper we focus on the photoproduction regime, which is mature and well tested for hard-process events with virtuality $\lesssim 1$ GeV against LEP and HERA data [28–30].

The generation of *non-diffractive* (ND) pp or p \bar{p} events proceeds with the following steps. First, the incoming beams are set up with (possible) PDFs at a given (user-defined) energy. Then the hard scattering of interest is generated based on the matrix element (ME) of the process and the PDFs. The generated partonic system is then evolved with a parton shower (PS), in PYTHIA 8 using the interleaved evolution of both initial and final state showers (ISR, FSR) [31] and MPIs [32]. The splitting probabilities for the FSR and ISR are obtained from the standard collinear DGLAP evolution equations. The ISR probabilities also depend on the PDFs of the incoming beams, as the evolution is backwards from a high scale, set by the hard process, to a lower scale. Similarly, the MPI probabilities depend on the PDFs of the incoming beams, and these have to be adjusted whenever an MPI has removed a parton from the beam. Color reconnection (CR) is allowed after the evolution to mimic the finite-color effects that are not taken into account in the infinite-color PS. After the partonic evolution, a minimal number of partons are added as beam remnants in order to conserve color, flavor and the total momentum of the event. Lastly, the generated partons are hadronized using the Lund string model [33] along with decays of unstable particles.

In ep events, PYTHIA 8 operates with two regimes: the DIS regime, where the electron emits a highly virtual photon ($Q^2 \gg 1$ GeV²), and the photoproduction regime, where the photon is (quasi-)real ($Q^2 \lesssim 1$ GeV²). Currently no description is available for intermediate-virtuality photons. In DIS events, the hard scattering occurs between the incoming lepton and a parton from the hadron beam by an exchange of a virtual photon (or another EW boson). The photon can thus be considered devoid of any internal structure. In the photoproduction regime, the photon flux can be factorized from the hard scattering, such that the intermediate photon can be regarded as a particle initiating the hard scattering. In this regime, both point-like and hadron-like states of the photon occur. This significantly increases the complexity of the event generation, thus the photoproduction regime

is thoroughly described in the next section.

3 The photoproduction framework

The (quasi-)real photon contains a point-like, direct part without substructure as well as a hadron-like part with internal structure. The latter part, the resolved photon, dominates the total cross section of the physical photon. The total cross section is expected to contain all types of hadronic collisions, including elastic (el), single- and double diffractive (SD, DD) and inelastic ND collisions. The ND collisions contain both hard and soft events, where the former can be calculated perturbatively, while the latter are modeled using the MPI framework in PYTHIA 8 [34]. Elastic and diffractive collisions require a phenomenological model for the hadronic photon.

The ND processes were first introduced in PYTHIA 8.215 [30], with a cross section given as a fraction of the total cross section, $\sigma_{\text{ND}} = f\sigma_{\text{tot}}$, $f < 1$. The framework for photoproduction has since been expanded to include all soft QCD processes using the Schuler-Sjöstrand model [35] in PYTHIA 8.235, and with this the cross sections for each of the event classes is calculated separately. The full description of these event classes is postponed to a forthcoming paper [30], as we here concentrate on diffractive processes with a hard scale. Between the two versions, the γp and $\gamma\gamma$ frameworks were extended to $e p$ and e^+e^- by the introduction of a photon flux within a lepton, now giving a complete description of all photoproduction events in γp , $\gamma\gamma$, $e p$ and e^+e^- collisions in the latest release, 8.240. Furthermore, an option to provide an external photon flux has been included, allowing the user to study photoproduction also in UPCs, where the virtuality of the intermediate photon is always small and thus the photoproduction framework directly applicable. An internal setup for these cases is under way.

The resolved photon is usually split into two: one describing a fluctuation of the photon into a low-mass meson and the other describing a fluctuation into a $q\bar{q}$ pair of higher virtuality. The former is usually treated according to a vector-meson dominance (VMD) model [36,37], where the photon is a superposition of the lightest vector mesons (usually ρ , ω and ϕ), whereas the latter, the anomalous part of the photon, is treated as “the remainder”, $\sigma_{\text{anom}} = \sigma_{\text{tot}} - \sigma_{\text{direct}} - \sigma_{\text{VMD}}$. A generalization of the VMD exists (the GVMD model) which takes into account also higher-mass mesons with the same quantum numbers as photons [38]. Note, however, that if the resonances are broad and closely spaced, they would look like a smooth continuum.

The event generation for the direct photons begins by sampling the hard scattering between the incoming photon and a parton (or another direct photon in case of $\gamma\gamma$), e.g. $q\gamma \rightarrow qg$. The subsequent parton-shower generation always include FSR and in γp case also ISR for

the hadronic beam. The whole photon momentum goes into the hard process, $x_\gamma \sim 1$, as direct photons do not have any internal structure. Hence there is no energy left for MPIs and no photon remnant is left behind. The hadronization is then performed with the Lund string model as usual.

For resolved photons, a model for the partonic content of the hadronic photon, the photon PDF, needs to be taken into account. This PDF includes both the VMD and the anomalous contributions, the latter being calculable within perturbative QCD, the former requiring a non-perturbative input. As in the case of protons, the non-perturbative input is fixed in a global QCD analysis using experimental data. There are several PDF analyses available for photons [39–42] using mainly data from LEP, but some also exploiting HERA data to constrain the gluonic part of the PDF [43]. Ideally one would have a PDF for each of the VMD states, in practice one uses the same parametrization for all – or approximates these with pion PDFs.

After the setup of the photon PDFs, the hard collision kinematics has to be chosen. Here, a parton from the photon PDF initiates the hard process, carrying a fraction of the photon momentum, $x_i < 1$, with parton i being extracted from the photon. Thus energy is still available in the fluctuation after the initial hard process, opening up for additional MPIs along with ISR and FSR in the subsequent evolution. As with other hadronic processes, a remnant is left behind, with its structure being derived from the flavor content of the original meson or $q\bar{q}$ state and the kicked-out partons.

As in pp collisions, the PS splitting probabilities with resolved photons are based on the DGLAP equations. The DGLAP equation governing the scale evolution of resolved photon PDFs can be written as [44]

$$\frac{\partial f_{i/\gamma}(x_i, Q^2)}{\partial \log(Q^2)} = \frac{\alpha_{\text{em}}(Q^2)}{2\pi} e_i^2 P_{i\gamma}(x_i) + \frac{\alpha_s(Q^2)}{2\pi} \sum_j \int_{x_i}^1 \frac{dz}{z} P_{ij}(z) f_{j/\gamma}\left(\frac{x_i}{z}, Q^2\right), \quad (\text{III.1})$$

where $f_{i(j)/\gamma}$ corresponds to the PDF of the photon, x_i the fractional momenta of the photon carried by the parton i , α_{em} , α_s the electromagnetic and strong couplings, e_i the charge of parton i and P_{ij} , $P_{i\gamma}$ the DGLAP and $\gamma \rightarrow q\bar{q}$ splitting kernels, respectively. The term proportional to $P_{i\gamma}$ gives rise to the anomalous part of the photon PDF. In PYTHIA 8 the separation into VMD and anomalous contributions is not explicitly performed. By the backwards evolution of ISR, however, a resolved parton can be traced back to the original photon by a $\gamma \rightarrow q\bar{q}$ branching at some scale Q^2 . Post facto, an event where this happens for $Q^2 > Q_0^2$ can then be associated with an anomalous photon state, and where not with a VMD state. The dividing scale Q_0 is arbitrary to some extent, but would be of the order of the ρ^0 -meson mass. In the interleaved evolution of the parton showers and MPIs, additional MPIs and ISR splittings on the photon side become impossible below the scale where the photon became unresolved. This reduces the average number of MPIs

for resolved photons compared to hadrons, and therefore has an impact also for the hard diffraction model as discussed in sec. 3.1.

3.1 MPIs with photons

When the photon becomes resolved it is possible to have several partonic interactions in the same event. MPIs in PYTHIA 8 are generated according to the leading-order (LO) QCD cross sections, albeit being regularized by introducing a screening parameter $p_{\perp 0}$ [32],

$$\frac{d\sigma}{dp_{\perp}^2} \sim \frac{\alpha_s^2(p_{\perp}^2)}{p_{\perp}^4} \rightarrow \frac{\alpha_s^2(p_{\perp 0}^2 + p_{\perp}^2)}{(p_{\perp 0}^2 + p_{\perp}^2)^2}. \quad (\text{III.2})$$

Note here that $p_{\perp 0}$ can be related to the size d of the colliding objects, $p_{\perp 0} \sim 1/d$, thus a different value of the screening parameter could be motivated if the photon has a different size than the proton. Further, one could imagine working with different matter profiles for both the proton and the photon, and possibly also for each of the components of the photon. For now the shape is kept common for all systems, but possibly with different scale factors, i.e. average radii.

The screening parameter is allowed to vary with center-of-mass energy \sqrt{s} ,

$$p_{\perp 0}(\sqrt{s}) = p_{\perp 0}^{\text{ref}} \left(\frac{\sqrt{s}}{\sqrt{s_{\text{ref}}}} \right)^p, \quad (\text{III.3})$$

with $p_{\perp 0}^{\text{ref}}$, p tunable parameters and $\sqrt{s_{\text{ref}}}$ a reference scale. Thus both the parameters from the matter profile and the parameters related to $p_{\perp 0}$ require input from data. These parameters can be fixed by a global tune, with the MONASH tune [45] being the current default. The MPI parameters in this tune, however, are derived using only data from pp and p \bar{p} collisions. As the partonic structure and matter profile of resolved photons can be very different from that of protons, the values for the MPI parameters should be revisited for $\gamma\gamma$ and γp collisions. The limitation is that there are only a few data sets sensitive to the MPIs available for these processes, and therefore it is not possible to perform a global retune for all the relevant parameters. Thus we have chosen to use the same form of the impact-parameter profile as for protons and study only the $p_{\perp 0}$ parameters (which allow for different scale factors).

For $\gamma\gamma$ collisions, LEP data is available for charged-hadron p_{\perp} spectra in different $W_{\gamma\gamma}$ bins, allowing studies of the energy dependence of $p_{\perp 0}$ as shown in [28]. In the γp case the HERA data for charged-hadron production is averaged over a rather narrow $W_{\gamma p}$ bin. Hence a similar study of the energy dependence is not possible for γp , and it becomes necessary to assume the same energy dependence for $p_{\perp 0}$ in γp as for pp collisions. The value of the $p_{\perp 0}$ -parameter, however, can be retuned with the available data. As discussed in [29] a

good description of the H1 data from HERA can be obtained with a slightly larger $p_{\perp 0}^{\text{ref}}$ in γp than what is used in the pp tune, $p_{\perp 0}^{\text{ref}}(\gamma p) = 3.00$ GeV versus $p_{\perp 0}^{\text{ref}}(pp) = 2.28$ GeV. Thus the photon-tune is consistent with a smaller size of the photon, i.e. that the photon does not quite reach a typical hadron size during its fluctuation.

The rule of thumb is that a larger screening parameter gives less MPI activity in an event, thus a smaller probability for MPIs with resolved photons is expected compared to proton-proton collisions. As the model for hard diffraction is highly dependent on the MPI framework, we expect that the increased screening parameter gives less gap-suppression in photoproduction than what was found in the proton-proton study. This is simply because there is a larger probability for the event to have no additional MPIs when the $p_{\perp 0}^{\text{ref}}$ -value is larger. Furthermore, since the ISR splittings may collapse the resolved photon into an unresolved state and, by construction, the direct-photon induced processes do not give rise to additional interactions, the role of MPIs is suppressed for photoproduction compared to purely hadronic collisions. Also, the invariant mass of the photon-proton system in the photoproduction data from HERA is typically an order of magnitude smaller than that in previously considered (anti-)proton-proton data, which further reduces the probability for MPIs. Anticipating results to be shown below, this is in accordance with what is seen in diffractive dijet production at HERA, where the suppression factor is much smaller than that at the Tevatron.

3.2 Photon flux in different beam configurations

In the photoproduction regime one can factorize the flux of photons from the hard-process cross section. For lepton beams a virtuality-dependent flux is used,

$$f_{\gamma/e}(x, Q^2) = \frac{\alpha_{\text{em}}}{2\pi} \frac{1 + (1-x)^2}{x} \frac{1}{Q^2}, \quad (\text{III.4})$$

where x is the momentum fraction of the photon w.r.t. the lepton. Integration from the kinematically allowed minimum virtuality up to the maximum Q_{max}^2 allowed by the photoproduction framework, yields the well-known Weizsäcker–Williams flux [46, 47]

$$f_{\gamma/e}(x) = \frac{\alpha_{\text{em}}}{2\pi} \frac{1 + (1-x)^2}{x} \log \left[\frac{Q_{\text{max}}^2(1-x)}{m_e^2 x^2} \right], \quad (\text{III.5})$$

where m_e is the mass of the lepton.

In pp collisions the electric form factor arising from the finite size of the proton, or equivalently that the proton should not break up by the photon emission recoil, needs to be taken into account. A good approximation of a Q^2 -differential flux is given by

$$f_{\gamma/p}(x, Q^2) = \frac{\alpha_{\text{em}}}{2\pi} \frac{1 + (1-x)^2}{x} \frac{1}{Q^2} \frac{1}{(1 + Q^2/Q_0^2)^4}, \quad (\text{III.6})$$

where $Q_0^2 = 0.71 \text{ GeV}^2$. Integration over the virtuality provides the flux derived by Drees and Zeppenfeld [48],

$$f_{\gamma/p}(x) = \frac{\alpha_{\text{em}}}{2\pi} \frac{1 + (1-x)^2}{x} \left[\log(A) - \frac{11}{6} + \frac{3}{A} - \frac{3}{2A^2} + \frac{1}{3A^3} \right], \quad (\text{III.7})$$

where $A = 1 + Q_0^2/Q_{\text{min}}^2$ and Q_{min}^2 is the minimum scale limited by the kinematics of a photon emission. Due to the form factor the photon flux drops rapidly with increasing virtuality and becomes negligible already at $Q^2 \sim 2 \text{ GeV}^2$. This ensures that the photons from protons are well within the photoproduction regime and there is no need to introduce any cut on maximal photon virtuality.

In case of heavy ions it is more convenient to work in impact-parameter space. The size of a heavy nucleus is a better defined quantity than it is for protons, so the impact parameter b of the collision can be used to reject the events where additional hadronic interactions would overwhelm the electromagnetic interaction. Simply rejecting the events for which the minimal impact parameter, b_{min} , is smaller than the sum of the radii of the colliding nuclei (or colliding hadron and nucleus for pA) provides a b -integrated flux,

$$f_{\gamma/A}(x) = \frac{\alpha_{\text{em}} Z^2}{\pi x} \left[2\xi K_1(\xi) K_0(\xi) - \xi^2 (K_1^2(\xi) - K_0^2(\xi)) \right], \quad (\text{III.8})$$

where Z is the charge of the emitting nucleus, K_i are the modified Bessel functions of the second kind and $\xi = b_{\text{min}} x m_N$, where x is a per-nucleon energy fraction and m_N a per-nucleon mass. The downside of working in the impact-parameter space is that the virtuality cannot be sampled according to the flux, as virtuality and impact parameter are conjugate variables. For heavy-ions, however, the maximal virtuality is very small (of the order of 60 MeV [17]), and can be safely neglected for the considered applications. The different photon fluxes are shown in Fig. III.2.

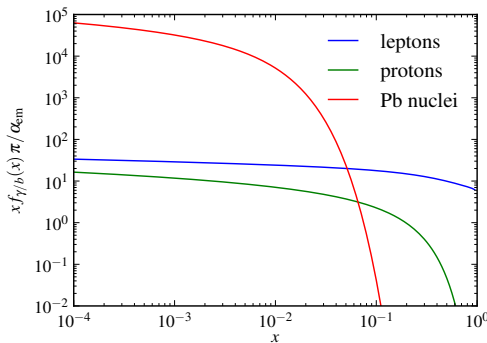


Figure III.2: The photon fluxes used for different beam types. Here $f_{\gamma/b}$ is the photon flux obtained from the beam b .

When extending the photoproduction regime from pure photon-induced processes to collisions where the photon is emitted by a beam particle, some additions are needed. In

direct photoproduction, the partonic processes can be generated by using the photon flux directly in the factorized cross-section formula, similar to what is done with the PDFs in a usual hadronic collision. In resolved photoproduction, a PDF for the partons from the photons emitted from the beam particle is needed. This can be found by convoluting the photon flux from the beam particle $b, f_{\gamma/b}(x)$, with the photon PDFs, $f_{i/\gamma}(x_\gamma, Q^2)$, where Q^2 refers to the scale at which the resolved photon is probed. This scale can be linked to the scale of the hard(est) process, e.g. the p_\perp of the leading jet in jet-production processes. The convolution yields

$$x_i f_{i/b}(x_i, Q^2) = \int_{x_i}^1 \frac{dx}{x} x f_{\gamma/b}(x) \frac{x_i}{x} f_{i/\gamma}\left(\frac{x_i}{x}, Q^2\right), \quad (\text{III.9})$$

with x_i the energy fraction of beam particle momentum carried by parton i and x the energy fraction of the photon w.r.t. the beam. In practice the intermediate photon kinematics is sampled according to the appropriate flux during the event generation, thus taking care of the convolution on the fly.

4 Hard diffraction in PYTHIA 8

The PYTHIA model for hard diffractive events in pp collisions was introduced as an explanation for the factorization breaking between diffractive DIS at HERA and the Tevatron [8]. The model can be applied to any process with sufficiently hard scales, including production of dijets, Z^0 , W^\pm , H etc. It begins with the Ingelman-Schlein picture, where the diffractive cross section factorizes into a Pomeron-particle cross section and a Pomeron flux. Based on this ansatz a tentative probability for diffraction is defined as the ratio of diffractive PDF (dPDF) to inclusive PDF, as it is assumed that the proton PDF can be split into a diffractive and a non-diffractive part,

$$\begin{aligned} f_{i/p}(x_i, Q^2) &= f_{i/p}^{\text{ND}}(x_i, Q^2) + f_{i/p}^{\text{D}}(x_i, Q^2), \\ f_{i/p}^{\text{D}}(x_i, Q^2) &= \int_{x_i}^1 \frac{dx_{\mathbb{P}}}{x_{\mathbb{P}}} f_{\mathbb{P}/p}(x_{\mathbb{P}}) f_{i/\mathbb{P}}\left(\frac{x_i}{x_{\mathbb{P}}}, Q^2\right), \\ p_A^{\text{D}} &= \frac{f_{i/B}^{\text{D}}(x_i, Q^2)}{f_{i/B}(x_i, Q^2)}, \\ p_B^{\text{D}} &= \frac{f_{i/A}^{\text{D}}(x_i, Q^2)}{f_{i/A}(x_i, Q^2)}, \end{aligned} \quad (\text{III.10})$$

with $f_{i/p}$ describing the PDF of the proton, $f_{i/p}^{\text{D}}$ being the diffractive part of the proton PDF defined as a convolution of the Pomeron flux in a proton ($f_{\mathbb{P}/p}$) and the Pomeron

PDFs ($f_{i/\mathbb{P}}$). The probabilities for side A, B to be the diffractive system are given as $P_{A,B}^D$ and each relies on the variables of the opposite side.

This tentative probability is then used to classify an event as preliminary diffractive or non-diffractive. If non-diffractive, the events are handled as usual non-diffractive ones. If diffractive, the interleaved evolution of ISR, FSR and MPIs is applied, but only events surviving without additional MPIs are considered as fully diffractive events. The reasoning behind this is that additional MPIs in the pp system would destroy the rapidity gap between the diffractive system and the elastically scattered proton. The gap survives if no further MPIs occur, and the event can be experimentally quantified as being diffractive, with e.g. the large rapidity gap method. This no-MPI requirement suppresses the probability for diffraction with respect to the tentative dPDF-based probability, and can thus be seen as a gap-survival factor. Unlike other methods of gap survival (e.g. [9, 49–51]) this method is performed on an event-by-event basis, thus inherently is a dynamical effect. Furthermore, it does not include any new parameters, but relies solely on the existing and well tested (for pp/p \bar{p}) MPI framework. Once the system is classified as diffractive, the full interleaved evolution is performed in the $\mathbb{P}p$ subsystem. Here the model does not restrict the number of MPIs, as these will not destroy the rapidity gap between the scattered proton and the Pomeron remnant.

4.1 Hard diffraction with photons

In this article we extend the hard diffraction model to collisions involving one or two (intermediate) photons. The extension is straightforward. Changing the proton PDF in eqs. (III.10) to a photon PDF on one side, it is possible to describe hard diffraction in γp interactions. Changing on both sides, the model is extended to $\gamma\gamma$ collisions. Thus eq. (III.10) is valid in events with (intermediate) photons with the change $p \rightarrow \gamma$. Connecting the event generation with an appropriate photon flux allows to study hard diffraction in both ep and e^+e^- collisions as well as in ultra-peripheral collisions of protons and nuclei. The differential cross section of the *hard scattering* (X_h) in a diffractive system X , e.g. the dijet system within the diffractive system, for direct (dir) and resolved (res) photoproduction can then schematically be written as,

$$\begin{aligned} d\sigma_{\text{dir}}^{AB \rightarrow X_h B} &= f_{\gamma/A}(x) \otimes f_{\mathbb{P}/p}(x_{\mathbb{P}}, t) \otimes f_{j/\mathbb{P}}(x_j, Q^2) \otimes d\sigma^{\gamma j \rightarrow X_h}, \\ d\sigma_{\text{res}}^{AB \rightarrow X_h B} &= f_{\gamma/A}(x) \otimes f_{i/\gamma}(x_\gamma, Q^2) \otimes f_{\mathbb{P}/B}(x_{\mathbb{P}}, t) \otimes f_{j/\mathbb{P}}(x_j, Q^2) \otimes d\sigma^{ij \rightarrow X_h}, \end{aligned} \quad (\text{III.11})$$

with beam A emitting a photon, beam B emitting a Pomeron, and $AB \rightarrow X_h B$ denoting that the diffractive system is present on side A . Changing $A \rightarrow B$ in eqs. (III.11) thus results in a diffractive system on side B . In the above, $f_{\gamma/A}$ denotes the photon flux from beam A , $f_{i/\gamma}$ the photon PDF, while $f_{\mathbb{P}/B}$ and $f_{j/\mathbb{P}}$ are the Pomeron flux and PDF, respectively. $d\sigma^{\gamma(i)j \rightarrow X_h}$ are the partonic cross sections calculated from the hard scattering MEs. The

full diffractive system X also contains partons from MPIs and beam remnants that also have to be taken into account, thus eqs. (III.11) only represent the hard subprocess part of the diffractive system. Presently, neither the double diffractive process $AB \rightarrow X_h^A X_h^B$ nor the central diffractive process $AB \rightarrow AX_h B$ are modeled, and the Pomeron can only be extracted from protons and resolved photons. As the model is based on dPDFs and the dynamical gap survival derived from the MPI framework inside PYTHIA 8, the extension does not require any further modeling or parameters.

The dynamical gap survival is present only in the cases where the photon fluctuates into a hadronic state. Hence the tentative probability, eqs. (III.10), equates the final probability for diffraction in direct photoproduction and in the DIS regime, where no MPIs occur. In resolved photoproduction, the dynamical gap survival suppresses the tentative probability for diffraction, offering an explanation for the discrepancies between next-to-leading order (NLO) predictions for dijets in photoproduction compared to measured quantities at HERA, see e.g. [11, 13, 16]. The observed factorization breaking is not as striking as in pp collisions, but the factorization-based calculation still overshoots the latest H1 analysis by roughly a factor of two [16].

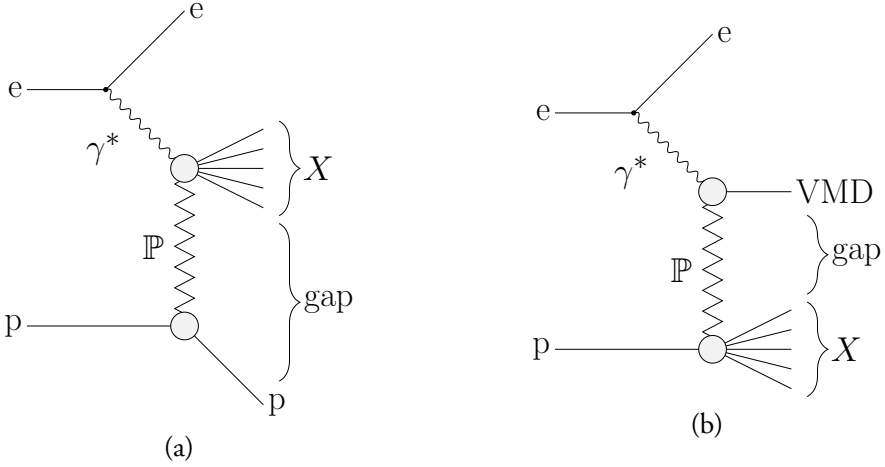


Figure III.3: The two diffractive systems available for resolved photoproduction: either the proton is elastically scattered and the photon side contains the diffractive system (a), or the vector meson is elastically scattered and the proton side contains the diffractive system (b).

It should be noted that this extension allows for diffraction on both sides, i.e. the Pomeron can be extracted from the hadronic photon and/or the proton, see Fig. III.3. Typically, the experiments only considered diffractive events where the diffractive system consists of a photon and a Pomeron, with a rapidity gap on the proton side (and a surviving proton, whether observed or not). The option to generate diffractive events on only one of the sides exist in PYTHIA 8, such as to avoid needless event generation.

4.2 Recent improvements in dPDFs

Since the publication of the hard diffraction model for $pp/p\bar{p}$, several improvements have been made for dPDFs. Work has been put into the inclusion of NLO corrections to the splitting kernels describing the evolution of the partons inside the Pomeron. Other work includes more recent fits to combined HERA data, or includes additional data samples into experiment-specific fits, so as to constrain some of the distributions in the dPDFs. A subset of these new dPDFs have been added to PYTHIA 8 recently and are briefly introduced below.

Specifically two new sets of dPDFs have been introduced, along with the Pomeron fluxes used in these fits. The first set, the GKG18 dPDFs by Goharipour et al. [52], consists of two LO and two NLO dPDFs fitted to two different combined HERA data sets available, using the xFITTER tool [53] recently extended to dPDFs. In addition, we consider an analysis released by the ZEUS collaboration offering three NLO dPDFs fitted to a larger sample of data. One of these, denoted ZEUS SJ, includes also diffractive DIS dijets from [54] in order to have better constraints for the gluon dPDF [14]. Using PDFs derived at NLO is not perfectly consistent with the LO matrix elements available in PYTHIA 8, but since the ZEUS SJ dPDF analysis is the only of the considered dPDF analyses including dijet data¹, it is interesting to compare the results to other dPDFs.

Both the GKG18 and the ZEUS SJ fits uses the following parametrization for the Pomeron flux,

$$f_{\mathbb{P}}(x_{\mathbb{P}}, t) = A_{\mathbb{P}} \frac{\exp(B_{\mathbb{P}} t)}{x_{\mathbb{P}}^{2\alpha_{\mathbb{P}}-1}}, \quad (\text{III.12})$$

with $\alpha_{\mathbb{P}} = \alpha_{\mathbb{P}}(0) + \alpha'_{\mathbb{P}} t$ and A, B being parameters to be included in the fits. The dPDFs are typically parametrized as

$$zf_i(z, Q_0^2) = A_i z^{B_i} (1 - z)^{C_i}, \quad (\text{III.13})$$

again with A_i, B_i, C_i being parameters to be determined in the fits. The dPDFs are then evolved using standard DGLAP evolution [56–59] to higher Q^2 . Different schemes for the inclusion of heavy quarks were invoked in the two fits; see the original papers for details. In both dPDFs the light quarks (u, d, s) have been assumed equal at the starting scale, while heavy quarks (c, b) are generated dynamically above their mass thresholds. We show the new Pomeron PDFs and fluxes in figs. III.4 and III.5, along with the H1 Fit B LO PDF [60] used as a default in PYTHIA 8. The GKG18 dPDFs are available with PYTHIA 8.240, while the ZEUS SJ set is expected in a forthcoming release.

¹H1 has also performed a dPDF analysis with DIS dijets at NLO [55] with very similar results as ZEUS SJ.

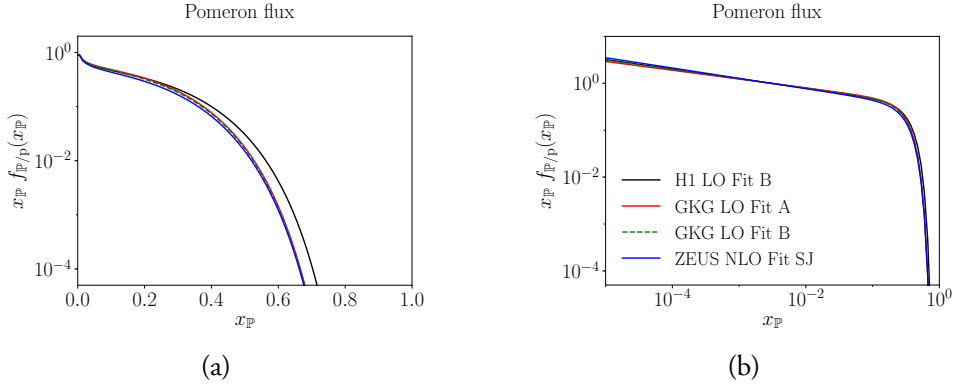


Figure III.4: The GKG18 LO Fit A, B and ZEUS SJ fluxes on a linear (a) and logarithmic (b) scale in $x_{\mathbb{P}}$. Note that t has been integrated over its kinematical range, $f(x_{\mathbb{P}}) = \int dt f(x_{\mathbb{P}}, t)$.

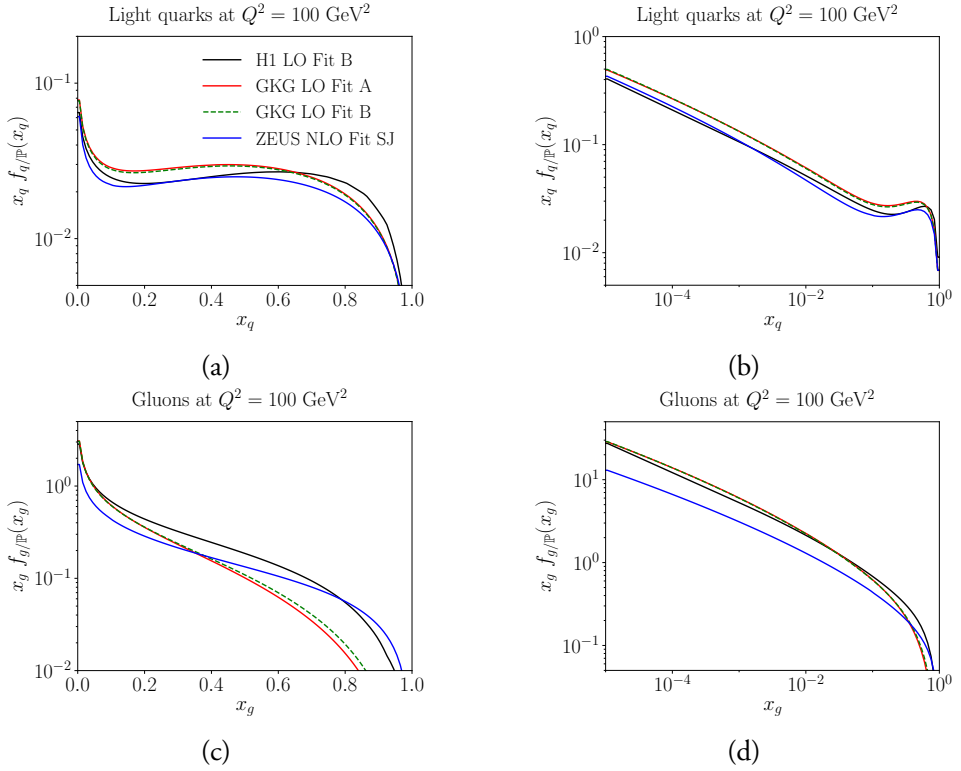


Figure III.5: The GKG18 LO Fit A, B and ZEUS SJ dPDFs on a linear (a,c) and logarithmic (b,d) scale. The upper figures shows the light quark content, the lower the gluonic content.

5 Diffractive dijets in the photoproduction range

The production of dijets in a diffractive system is particularly interesting, as it provides valuable information on the validity of factorization theorems widely used in particle physics.

These factorization theorems are not expected to hold in the case of diffractive dijets arising from resolved photoproduction, as this process essentially is a hadron-hadron collision, where the hard scattering factorization fails.

Both H1 and ZEUS have measured the production of diffractive dijets in both the photoproduction and DIS range. We here limit ourselves to showing results from two analyses, the H1 2007 and ZEUS 2008 analyses on diffractive dijets [12,13]. Other analyses have been presented, including several ones examining only the DIS regime, but as the analysis codes or even the data itself have not always been preserved, we limit ourselves to reconstructing only a subset of these analyses. We aim to validate and provide the analyses used in this article within the Rivet framework [61].

Both experiments have data on ep collisions at $\sqrt{s} = 318$ GeV using 27.5 GeV electrons and 920 GeV protons, with the proton moving in the $+z$ direction. Both use the large rapidity gap method for selecting diffractive systems. The experimental cuts in the two analyses are shown in table III.1. In the H1 analysis we concentrate on the differential cross sections as a function of four variables: invariant mass of the photon-proton system (W), transverse energy of the leading jet ($E_{\perp}^{\text{jet},1}$) and momentum fractions $z_{\mathbb{P}}^{\text{obs}}$ and x_{γ}^{obs} , both constructed from the measured jets as

$$\begin{aligned} x_{\gamma}^{\text{obs}} &= \frac{\sum_{i=1}^2 (E_{\perp}^{\text{jet},i} - p_z^{\text{jet},i})}{2yE_e}, \\ z_{\mathbb{P}}^{\text{obs}} &= \frac{\sum_{i=1}^2 (E_{\perp}^{\text{jet},i} + p_z^{\text{jet},i})}{2x_{\mathbb{P}}E_p}, \end{aligned} \quad (\text{III.14})$$

where E_e (E_p) is the energy of the beam electron (proton) and the summation includes the two leading jets, i.e. the two with highest E_{\perp} . The inelasticity y and Pomeron momentum fraction w.r.t. the proton $x_{\mathbb{P}}$ are determined from the hadronic final state. In the ZEUS analysis the momentum fractions $z_{\mathbb{P}}^{\text{obs}}$ and x_{γ}^{obs} are defined in terms of transverse energy and pseudorapidity of the jets,

$$\begin{aligned} x_{\gamma}^{\text{obs}} &= \frac{\sum_{i=1}^2 E_{\perp}^{\text{jet},i} \exp(-\eta^{\text{jet},i})}{2yE_e}, \\ z_{\mathbb{P}}^{\text{obs}} &= \frac{\sum_{i=1}^2 E_{\perp}^{\text{jet},i} \exp(\eta^{\text{jet},i})}{2x_{\mathbb{P}}E_p}, \end{aligned} \quad (\text{III.15})$$

equivalent to the definitions in eq. (III.14), if the jets are massless. In a LO parton-level calculation these definitions would exactly correspond to the momentum fraction of partons inside a photon (x_{γ}) and Pomeron ($z_{\mathbb{P}}$). Due to the underlying event, parton-shower emissions and hadronization effects, however, the connection between the measured $z_{\mathbb{P}}^{\text{obs}}$ and x_{γ}^{obs} and the actual x_{γ} and $z_{\mathbb{P}}$ is slightly smeared, but still eqs. (III.14) and (III.15) serve as decent hadron-level estimates for the quantities. In place of W the ZEUS analysis provides the differential cross section in terms of invariant mass of the photon-Pomeron system, M_X .

Table III.1: Kinematical cuts used in the experimental analyses by H1 [12] and ZEUS [13]. An asterisk (*) indicates that the observable is evaluated in the photon-proton rest frame. $x_{\mathbb{P}}$, M_Y , t are found in the rest frame of the hadronic system X , while the remaining are found in the laboratory frame.

H1 2007	ZEUS 2008
$Q^2 < 0.01 \text{ GeV}^2$	$Q^2 < 1 \text{ GeV}^2$
-	$0.2 < y < 0.85$
$165 \text{ GeV} < W < 242 \text{ GeV}$	-
$N_{\text{jet}} \geq 2$	$N_{\text{jet}} \geq 2$
$E_{\perp}^{*\text{jet } 1} > 5.0 \text{ GeV}$	$E_{\perp}^{\text{jet } 1} > 7.5 \text{ GeV}$
$E_{\perp}^{*\text{jet } 2} > 4.0 \text{ GeV}$	$E_{\perp}^{\text{jet } 2} > 6.5 \text{ GeV}$
$-1 < \eta^{\text{jet } 1,2} < 2.0$	$-1.5 < \eta^{\text{jet } 1,2} < 1.5$
$x_{\mathbb{P}} < 0.03$	$x_{\mathbb{P}} < 0.025$
$M_Y \leq 1.6 \text{ GeV}$	-
$ t < 1.0 \text{ GeV}^2$	-

There are several theoretical uncertainties affecting the distributions of the diffractive events. Here we focus on the most important ones:

- Renormalization- and factorization-scale variations, estimating the uncertainties of the LO descriptions in PYTHIA 8.
- dPDF variations affecting especially the $z_{\mathbb{P}}^{\text{obs}}$ distribution and indirectly the number of events through the cuts on the squared momentum transfer, t , the momentum fraction of the beam carried by the Pomeron, $x_{\mathbb{P}}$ and the mass of the scattered (and possibly excited) proton, M_Y .
- $p_{\perp 0}^{\text{ref}}$ -variations, affecting the gap survival factor.

Other relevant parameters and distributions have also been varied, showing little or no effect on the end distributions. Remarkably, one of these was the choice of photon PDF. PYTHIA 8 uses the CJKL parametrization [42] as a default both in the hard process and in the shower and remnant description. As the MPI and ISR generation in the current photoproduction framework require some further approximations for the PDFs, that are not universal and thus cannot be determined for an arbitrary PDF set, only the hard-process generation is affected by a change of photon PDF. Thus the effect of a different photon PDF on the various observables is not fully addressed with the present framework. The hard-process generation should, however, provide the leading photon PDF dependence. We find only a minimal change to the final distributions when changing to either the SaS [41], GRV [39] or GS-G [62] provided with LHAPDF5 [63]. There are two reasons for the weak dependence on photon PDFs. Firstly, the cuts applied by the experimental analyses presented here forces x_{γ} to be rather large, where the photon PDFs are relatively well constrained by the

LEP data. Secondly, the no-MPI requirement rejects mainly events from the low- x_γ region, where the differences between the mentioned photon PDFs are more pronounced.

Two other analyses from HERA [11, 16] have also been used to check the current framework, giving results similar to the analyses presented here. For our baseline setup we show comparisons to both the H1 and ZEUS analyses, while for the more detailed variations we focus on comparisons to ZEUS.

5.1 Baseline results

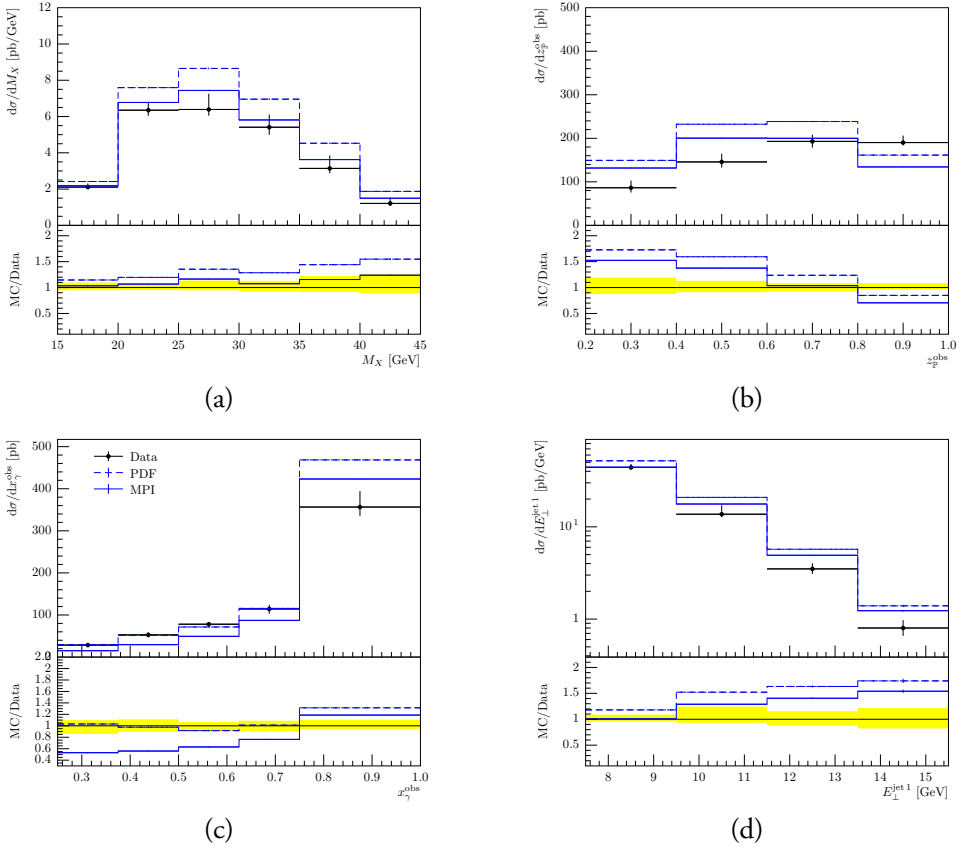


Figure III.6: The model with (solid lines) and without (dashed lines) gap survival compared to ZEUS data on M_X (a), z_γ^{obs} (b), x_γ^{obs} (c) and $E_\perp^{\text{jet},1}$ (d).

In figs. III.6 and III.7 we show the results obtained with PYTHIA 8 along with the experimental measurements. We show two simulated samples, one based on dPDFs solely without the dynamic gap survival (the “PDF” sample, dashed lines), and one including the

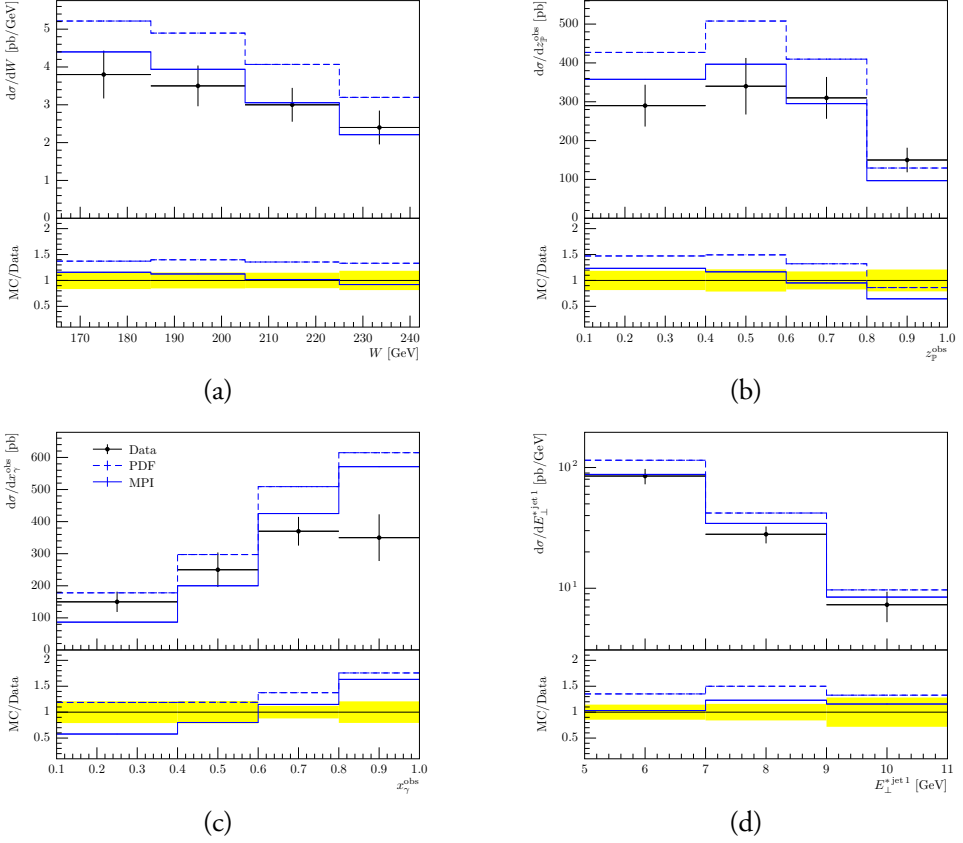


Figure III.7: The model with (solid lines) and without (dashed lines) gap survival compared to H1 data on W (a), z_p^{obs} (b), x_γ^{obs} (c) and $E_\perp^{*, \text{jet } 1}$ (d).

dynamic gap survival (the “MPI” sample, solid lines). The results show that the “PDF” sample is too large compared to data in all distributions except for x_γ , thus showing evidence of factorization breaking. The “MPI” sample, however, seems to give a reasonably good description of data as the ratio of MC/data is smaller for the “MPI” sample than the “PDF” sample, thus hinting that it is the additional probability for multiparton interactions between the photon remnant and the proton that causes the factorization breaking.

A χ^2 -test have been performed in order to quantify which of the models do better. Here, we have performed three different tests; using only either of the H1 or ZEUS datasets, or using both, table III.2. It is evident that the “MPI” model including the gap survival effect does a better job than the “PDF” model without it, within our baseline setup. The calculation of the χ^2 values include all differential cross sections provided by the experimental analyses, excluding the additional x_γ^{obs} -binned distributions in ZEUS analysis to avoid counting the same data twice. Error correlations are not provided and so not considered.

Table III.2: χ^2 tests using three different datasets.

χ^2/n_{DOF}	H1	ZEUS	Combined
PDF	5.20	9.64	7.6
MPI	1.42	5.10	3.44

In general, most distributions are well described by the model including dynamical gap survival. The invariant mass distributions for the photon-Pomeron system (M_X) and for the photon-proton system (W) in figs. III.6 and III.7 (a) are both sensitive to the form of the photon flux from leptons. Both data sets are well compatible with the MPI samples, indicating that the standard Weizsäcker-Williams formula provide a good description of the flux.

It is, however, evident that in some observables the shape of the data is poorly described. Examples are $z_{\mathbb{P}}^{\text{obs}}$ and x_{γ}^{obs} , figs. III.6, III.7 (b, c). The former is sensitive to the dPDFs used in the event generation. The baseline samples use the LO H1 Fit B flux and dPDF, fitted to data that is mainly sensitive to quarks. As the Pomeron is assumed to be primarily of gluonic content, it is expected that the vast majority of the dijets arise from gluon-induced processes. Thus a poorly-constrained gluon dPDF is expected to give discrepancies with distributions sensitive to this parameter, such as $z_{\mathbb{P}}$. In both the H1 and ZEUS analyses $z_{\mathbb{P}}^{\text{obs}}$ is overestimated in the low end, while being underestimated in the high- $z_{\mathbb{P}}^{\text{obs}}$ end. If the measured jets are dominantly gluon-induced, then it is expected that changing from the H1 LO Fit B dPDF to the ZEUS SJ fit should improve on the $z_{\mathbb{P}}^{\text{obs}}$ -distribution, as the low- $z_{\mathbb{P}}^{\text{obs}}$ gluons are suppressed in this dPDF.

The latter observable, x_{γ}^{obs} , is similarly underestimated in the low end and overestimated in the high end. The tight cut on $x_{\mathbb{P}}$ together with the requirement of high- E_{\perp} jets reduces the contribution from lower values of x_{γ}^{obs} . This suppresses the resolved contribution and therefore increases the relative contribution from direct processes, which typically are close to $x_{\gamma}^{\text{obs}} = 1$. The additional no-MPI requirement further suppresses the already low resolved contribution, and we end up with not being able to describe the shape of x_{γ}^{obs} . As already discussed, the discrepancy cannot be explained with the uncertainties in the photon PDFs, as the sensitivity to different PDF analyses was found to be very low. The issue seems to be a problem with the relative normalizations of the direct and resolved contributions. This is evident from Fig. III.8, where the ZEUS analysis conveniently splits the data into two regions, a direct- and a resolved-enhanced region with the division at $x_{\gamma}^{\text{obs}} = 0.75$. Here, the model underestimates the resolved-enriched part of the cross section and overestimates the direct-enriched part, confirming what we already observed in figs. III.6, III.7 (c).

Future measurements could shed more light on this issue, especially experimental setups in

which the events passing the kinematical cuts would not be dominated by the direct contribution. In the experimental analyses considered here, a similar observation was made when comparing to a NLO calculation: the shape of x_γ^{obs} was well described by the NLO calculation (corresponding to our PDF selection) in the direct-enhanced region, but applying a constant suppression factor for the resolved contribution undershot the data at $x_\gamma^{\text{obs}} < 0.75$, similar to what we observe. It is worth pointing out that both poorly-described distributions, x_γ^{obs} and $z_{\mathbb{P}}^{\text{obs}}$, are constructed from the jet kinematics. Therefore further studies on jet reconstruction and their η distributions could offer some insights for the observed discrepancies.

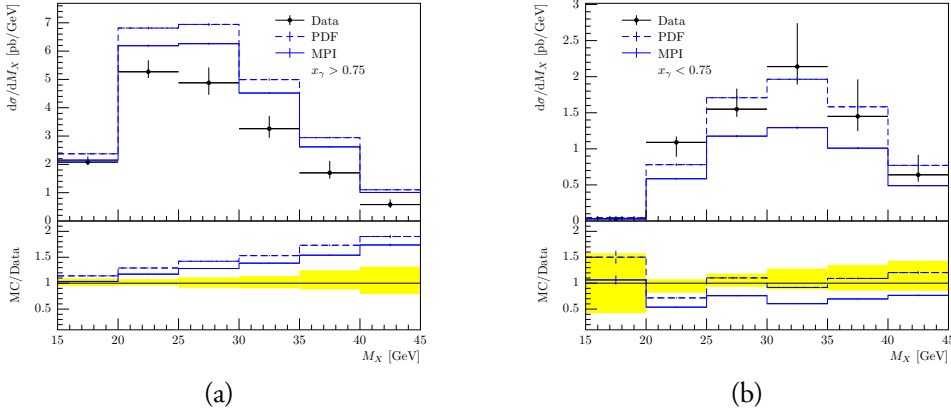


Figure III.8: The model with (solid lines) and without (dashed lines) gap survival compared to ZEUS data on M_X in the direct-enhanced (a) and resolved-enhanced (b) regions.

The jet variable E_\perp can be used to check if the amount of activity within the diffractive system is properly described. As this system contains a Pomeron, it might very well be that the MPI parameters here could be different from the MPI parameters in the γp -system. It seems that using the same parameters for the $\gamma\mathbb{P}$ system as for γp slightly overestimates the high- E_\perp tail. This indicates that there might be too much MPI activity in the events, thus requiring a slightly larger $p_{\perp 0}^{\text{ref}}$ value in the diffractive system than in the γp system. The argument for a different $p_{\perp 0}^{\text{ref}}$ -value for γp as compared to pp can also be applied here: if the Pomeron has a smaller size than the proton, then the $p_{\perp 0}^{\text{ref}}$ -value can be increased. Having too much MPI activity in the $\gamma\mathbb{P}$ -system may also push the x_γ^{obs} distribution towards higher values, as the E_\perp of the jets may increase due to the underlying event. A full discussion of the MPI parameters in the diffractive system in pp collisions has been provided in [8], but have not been pursued further here.

5.2 Scale variations

To probe the uncertainties in the choice of renormalization and factorization scales, μ_R and μ_F , we employ the usual method of varying the scales up and down with a factor of two. Each is probed individually, such that one scale is kept fixed while the other is varied. Only the scales at matrix-element level are varied; thus the shower and MPI scales have been excluded from these variations. Each variation gives rise to an uncertainty band, and in Fig. III.9 we show the envelope using the maximal value obtained from either of the two uncertainty bands. The envelope is dominated by the renormalization scale, giving the largest uncertainty in most of the figures shown – not unusual in a LO calculation. Note, however, that the scale uncertainty in the high- x_γ^{obs} bin actually reaches the upper error of the data point, essentially hinting that the model is able to describe the direct-enhanced region within theoretical uncertainties. The resolved region, however, cannot be fully accounted for within these theoretical uncertainties.

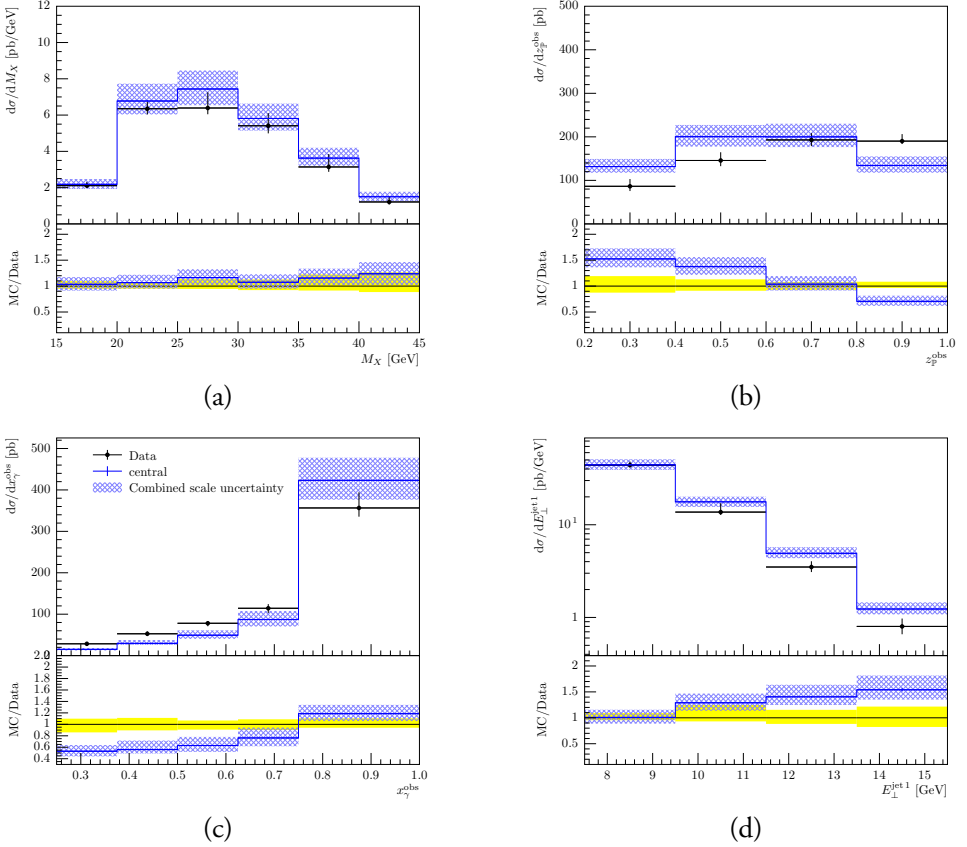


Figure III.9: The model along with the uncertainty bands arising from varying the renormalization- and factorization scales compared to ZEUS data on M_X (a), z_γ^{obs} (b), x_γ^{obs} (c) and $E_\perp^{\text{jet } 1}$ (d).

5.3 Variations of the dPDFs

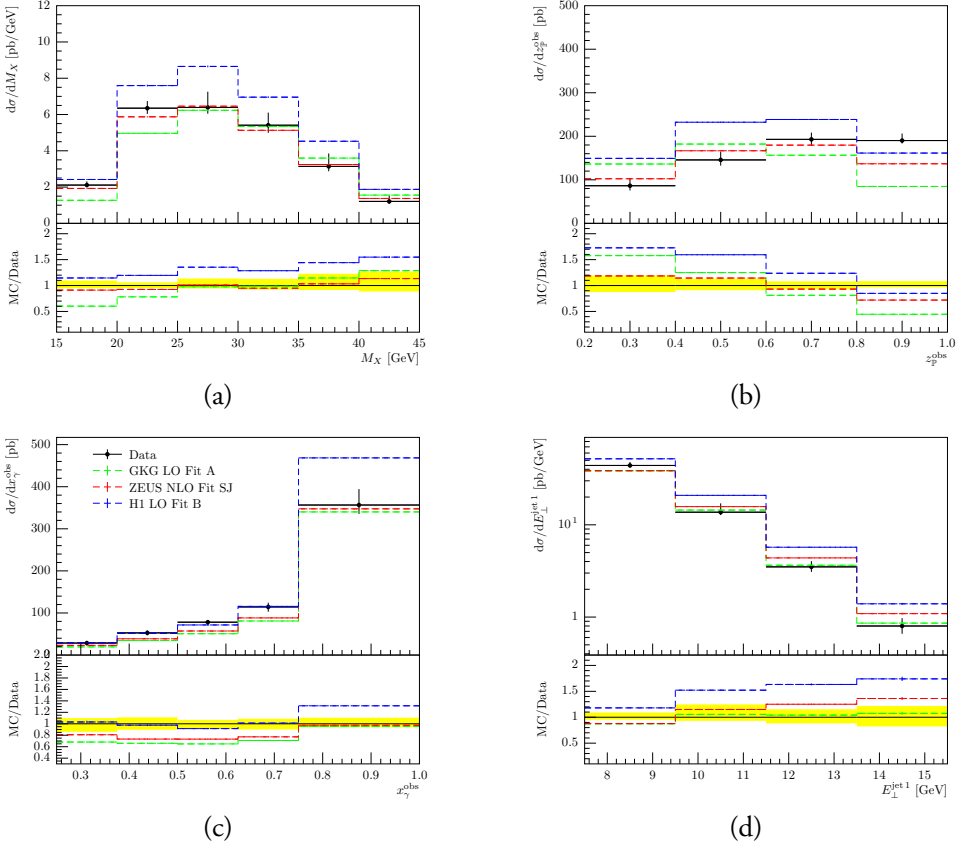


Figure III.10: The model without gap suppression using three different dPDFs: H1 LO Fit B (blue lines), GKG LO Fit A (green lines) and ZEUS NLO SJ (red lines) compared to ZEUS data on M_X (a), z_p^{obs} (b), x_γ^{obs} (c) and $E_{\perp}^{\text{jet } 1}$ (d).

As explained above, the considered observables are sensitive to the dPDFs, especially the fractional momentum carried by the parton from the Pomeron, $z_{\text{P}}^{\text{obs}}$. We here investigate if the increased amount of diffractive DIS data in the GKG LO dPDFs will provide a better description of the data than the less constrained H1 LO Fit B dPDF. We also show results obtained when using the NLO dPDF and flux from ZEUS SJ, as this dPDF includes data on diffractive dijets that is directly sensitive to the gluon distributions. Note, however, that a combination of NLO PDFs and LO matrix elements is still only accurate to LO and mixing different orders may result in different results compared to a situation where the matrix elements and PDF determination are consistently at the same perturbative order.

In Fig. III.10 we show results using two of the new dPDFs, ZEUS NLO SJ [14] and GKG LO Fit A [52] *without* the gap suppression factor. At first glance, the new dPDFs improve

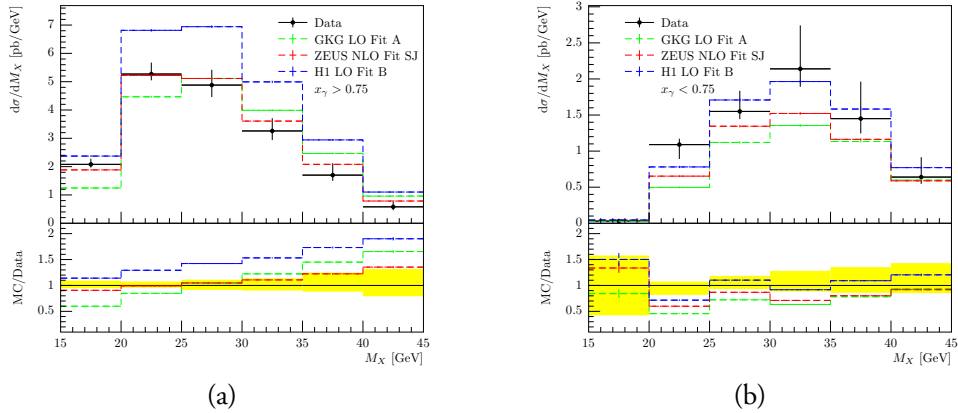


Figure III.11: The model without gap suppression using the three dPDFs: H1 Fit B LO (blue lines), GKG LO Fit A (green lines) and ZEUS SJ (red lines) compared to ZEUS data on M_X in the direct-enhanced (a) and resolved-enhanced (b) regions.

the overall description of data without a further need for suppression. Overall the new dPDFs seem to suppress the distributions as compared to H1 Fit B LO dPDF, with the ZEUS SJ dPDF performing slightly better than GKG LO Fit A as seen e.g. in the $z_{\mathbb{P}}^{\text{obs}}$ distribution. Here, the ZEUS SJ dPDF flattens out at high $z_{\mathbb{P}}^{\text{obs}}$ as compared to the GKG and H1 dPDFs, having a slightly larger x_g -distribution in this regime.

The distributions that the baseline study did not fully describe, also the new dPDFs fail to describe. Especially the x_{γ}^{obs} distribution is still underestimated at $x_{\gamma}^{\text{obs}} < 0.75$, which underlines the discrepancies with the relative normalization between the direct and resolved contributions. The $E_{\perp}^{\text{jet } 1}$ distribution is now well described with the GKG set. With the ZEUS SJ set the normalization is improved compared to the H1 Fit B but the shape of the distribution is similarly off.

A separation of M_X into the two regimes, Fig. III.11, shows that the direct-enhanced region is well described with the ZEUS SJ dPDFs. The GKG set improves the normalization but the shape of the distribution is still not compatible. The resolved region, however, is too suppressed with both of these, so the relative normalizations of the two contributions remain as an unresolved issue. Adding the gap suppression factor on top of this, Fig. III.12, further suppresses the already suppressed resolved-enhanced region, worsening the agreement with the data in this regime. Little effect is seen in the direct-enhanced region, as expected.

These results thus puts forth the question whether the gap suppression is necessary if the dPDFs are refined and improved with additional diffractive data. The improvements seen especially with the ZEUS SJ dPDF in both the x_{γ}^{obs} and $z_{\mathbb{P}}^{\text{obs}}$ distributions might hint towards this. As discussed earlier, this might partly follow from the tight cuts applied in the ZEUS analysis which does not leave much room for MPIs in the γp system. Also,

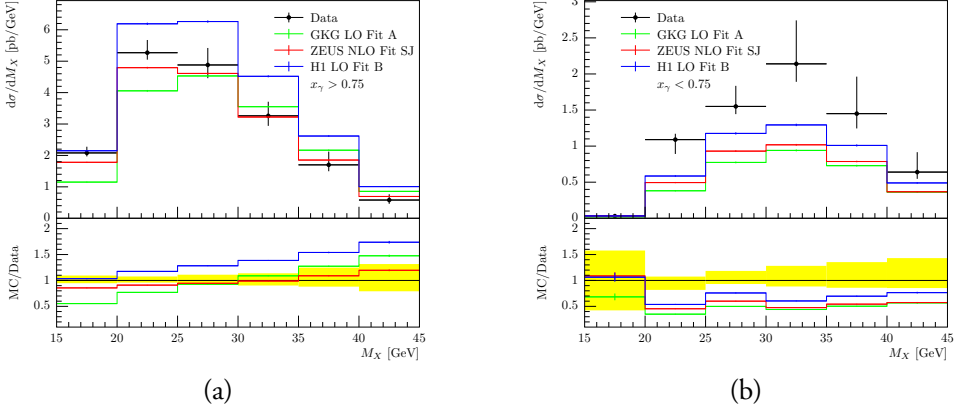


Figure III.12: The model with gap suppression using the three dPDFs: H1 Fit B LO (blue lines), GKGL LO Fit A (green lines) and ZEUS SJ (red lines) compared to ZEUS data on M_X in the direct-enhanced (a) and resolved-enhanced (b) regions.

one should keep in mind that using NLO dPDFs with LO matrix elements might lead to different results compared to a full NLO calculation.

5.4 Variations of the screening parameter

The gap suppression method used here is highly sensitive to the model parameters of the MPI framework. Here we especially look at the screening parameter, $p_{\perp 0}^{\text{ref}}$, as the value of this parameter differs between tunes to ep and to pp collisions. Changing the value of $p_{\perp 0}^{\text{ref}}$ have only a small effect on the “PDF” samples. The “MPI” samples, however, are affected by the value of the screening parameter. A smaller value of $p_{\perp 0}^{\text{ref}}$ results in more MPIs, thus we expect that the gap suppression will be larger if we decrease $p_{\perp 0}^{\text{ref}}$ to its pp value, as a smaller fraction of the events will survive the MPI-selection.

This effect is exactly what is seen in Fig. III.13. The “PDF” samples are not affected, but the pp-tuned $p_{\perp 0}^{\text{ref}}$ value in red causes a stronger suppression, best seen in the ratio plots where the solid red curves, the “MPI” sample with $p_{\perp 0}^{\text{ref}} = 2.28$ GeV, is lower than the solid blue curves with $p_{\perp 0}^{\text{ref}} = 3.00$ GeV. The value of $p_{\perp 0}^{\text{ref}}$ has some effect on the shape of the distributions, mainly because a higher M_X allows for more MPI activity, and thus a smaller fraction of events survive the no-MPI requirement. This means that the gap suppression increases with increasing energy available in the system, i.e. with increasing M_X , seen in Fig. III.13 (a), where ratio-plot shows a suppression factor of approximately 0.9 in the low M_X bin and 0.6 in the high M_X bin.

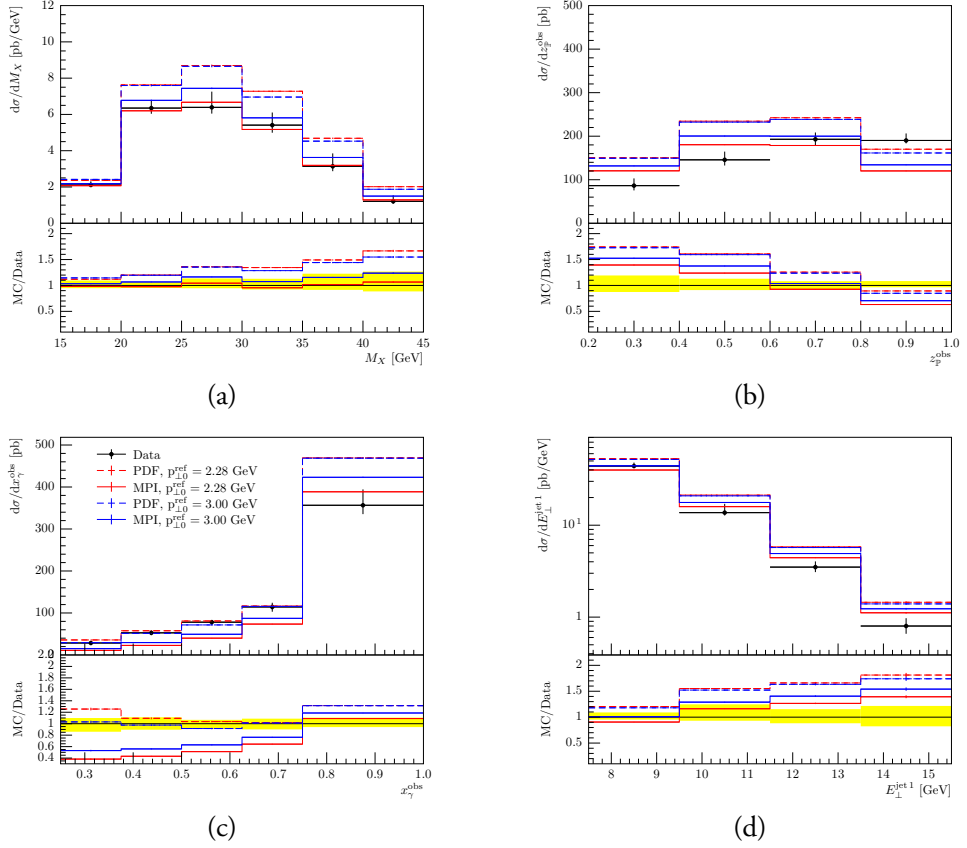


Figure III.13: The model with (solid lines) and without (dashed lines) gap suppression using two values of p_{\perp}^{ref} : The pp-tune, $p_{\perp}^{\text{ref}} = 2.28$ GeV (red lines) and the ep-tune, $p_{\perp}^{\text{ref}} = 3.0$ GeV (blue lines). Again we show the samples in the observables M_X (a), z_2^{obs} (b), x_{γ}^{obs} (c) and E_{\perp}^{jet1} (d).

5.5 Gap suppression factors

Several models have been proposed to explain the factorization breaking in diffractive hadronic collisions. Many of these employ an overall suppression factor, often relying primarily on the impact-parameter of the collision, see e.g. [49–51]. Some also include a suppression w.r.t. a kinematical variable, such as the p_{\perp} of the diffractive dijets. But to our knowledge, the model of dynamical gap survival is the first of its kind to evaluate the gap survival on an event-by-event basis. This means it takes into account the kinematics of the entire event, and is thus also able to provide a gap suppression factor differential in any observable. In the model presented here, the ratio of “PDF” to “MPI” samples equates the gap survival factor, as the two samples only differ by the no-MPI requirement that determines the models definition of a fully diffractive event.

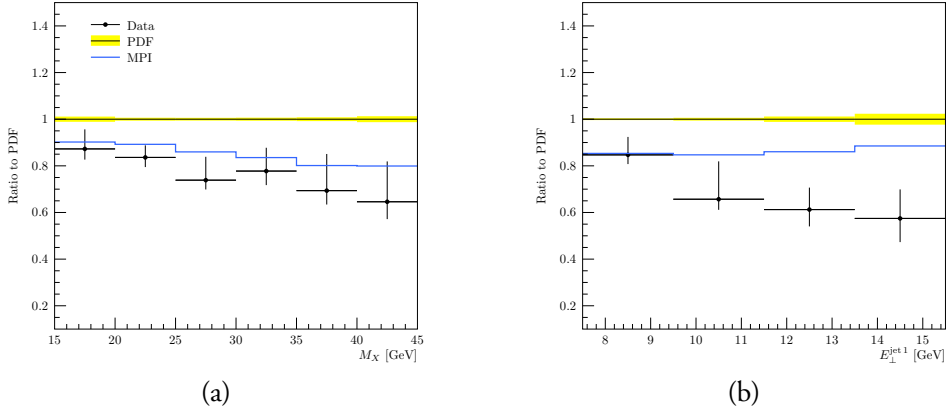


Figure III.14: The predicted gap suppression factors as a function of M_X (a) and $E_{\perp}^{\text{jet } 1}$ (b) compared to the ZEUS analysis.

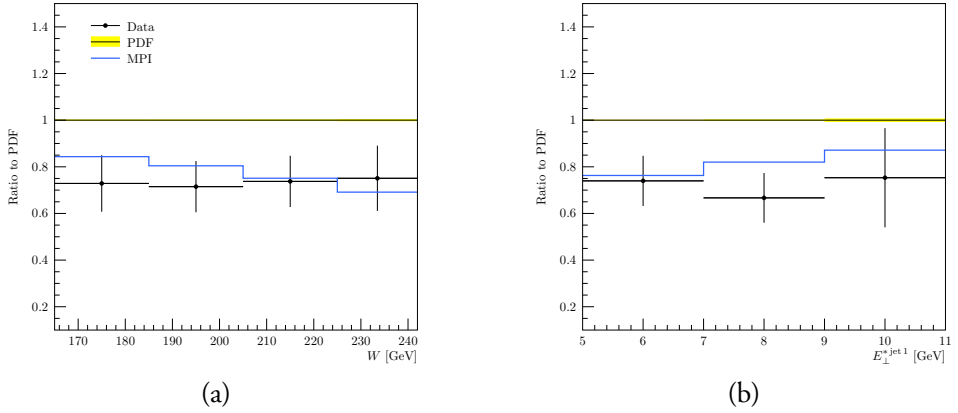


Figure III.15: The predicted gap suppression factors as a function of W (a) and $E_{\perp}^{\text{jet } 1}$ (b) compared to the H1 analysis.

The theoretical uncertainties not directly related to MPI probability (e.g. scale variations) are expected to cancel in such a ratio. Even though many experimental analysis present similar ratios by using a NLO calculation as a baseline, such a ratio is not a measurable quantity, as it always require a theory-based estimation for the unsuppressed result. These ratios, however, are useful for demonstrating the effects arising from different models such as our dynamical rapidity gap survival. In order to estimate the factorization-breaking effect in data w.r.t. our model, we show also the ratio between the data and the “PDF” sample.

In Fig. III.14 we show the gap suppression differential in the observables M_X and $E_{\perp}^{\text{jet } 1}$ from the ZEUS analysis and in Fig. III.15 we show the gap suppression differential in the observables W and $E_{\perp}^{\text{jet } 1}$ from the H1 analysis. These distributions demonstrate some of the main features of our dynamical rapidity gap survival model. We show the ratio of data

to “PDF” sample (black dots) and the ratio of “MPI” to “PDF” sample (solid blue curve). This latter ratio is exactly the gap suppression factor predicted by the model. The shapes of the gap suppression factors agree reasonably well with the suppression factors derived from the data (the black dots), albeit the shape of Fig. III.14 (b) is off in the high- E_{\perp} end, as already mentioned in the baseline results.

The model predicts a slowly decreasing suppression in $E_{\perp}^{(*)\text{jet } 1}$, while the suppression increases towards larger M_X and W . This increase follows as the larger diffractive masses are correlated with larger invariant masses of the γp -system, where there is more room for MPIs at fixed jet E_{\perp} . This results in a larger fraction of the events having additional MPIs, thus a smaller fraction of the events survive as diffractive. Similarly, high- E_{\perp} jets takes away more momentum than low- E_{\perp} jets, again leaving less room for MPIs to take place. Thus we do not predict a flat overall suppression, as has often been applied in the experimental analyses.

Suppression factors in the range 0.7 – 0.9 are predicted in the shown observables. Given the uncertainty on the “PDF” sample, this is in agreement with the suppression factors of approximately 0.5 – 0.9, as observed by H1 [11, 12, 15, 16] and ZEUS [13]. A somewhat contradictory result was observed in ref. [14], in which the ZEUS dijet data from ref. [13] was found consistent with the purely factorization-based NLO calculation when using the ZEUS SJ dPDFs.

The experimental cuts applied in the ZEUS analysis, as compared to the analysis from H1, forces x_{γ}^{obs} to very large values, where the suppression from the MPIs does not have a large effect. Thus the ZEUS measurement requires less suppression than what is needed in the H1 measurement. The shown distributions, however, are still marred by the large theoretical uncertainties. One way to reduce these theoretical uncertainties would be to consider the ratio of photoproduced dijets to ones from DIS, as done e.g. in the recent H1 analysis [16]. The kinematic domain is slightly different due to different virtualities, but this would still greatly reduce dependency on dPDFs and scale variations, leaving only the mild photon PDF dependence in addition to the factorization breaking effects, that would be pronounced in this ratio. Unfortunately the current PYTHIA 8 description of DIS events at intermediate virtualities is not adequate to describe the inclusive DIS dijet data, so such a comparison is a project for the future.

6 Photoproduction in ultra-peripheral collisions

Because of the more than an order of magnitude larger \sqrt{s} at the LHC, the accessible invariant masses of the γp system are much larger than what could be studied at HERA. This allows us to study the factorization-breaking effects in hard-diffractive photoproduc-

Table III.3: Kinematics for the UPC analyses.

	pPb	pp
$\sqrt{s_{\text{NN}}}$	5.0 TeV	13.0 TeV
$E_{\perp,\text{min}}^1$		8.0 GeV
$E_{\perp,\text{min}}^2$		6.0 GeV
$M_{\text{jets,min}}$		14.0 GeV
$x_{\text{p}}^{\text{max}}$		0.025
$ \eta^{\text{max}} $		4.4

tion in a previously unexplored kinematical region. Such measurements would fill the gap between the rather mild suppression observed at HERA and the striking effect observed in $p\bar{p}$ and pp collisions at Tevatron and the LHC. This would provide important constraints for different models and thus valuable information about the underlying physics. Besides the results we present here, predictions for these processes have been computed in a framework based on a factorized NLO perturbative QCD calculation with two methods of gap survival probabilities, one with an overall suppression and one where the suppression is only present for resolved photons [64]. The authors here expect that the two scenarios can be distinguished at LHC, especially in the x_{γ}^{obs} -distribution. The model presented in this work should thus be comparable to the latter suppression scheme from [64]. Another work considering similar processes is presented in Ref. [65].

In principle these measurements could be done in all kinds of hadronic and nuclear collisions, since all fast-moving charged particles generate a flux of photons. There are, however, some differences worth covering. In pp collisions, the photons can be provided by either of the beam particles with an equal probability. The flux of photons is a bit softer for protons than with leptons, but still clearly harder than with nuclei. Experimentally it might be difficult to distinguish the photon-induced diffraction and “regular” double diffraction in pp , since both processes would leave a similar signature with rapidity gaps on both sides. In $p\text{Pb}$ collisions the heavy nucleus is the dominant source of photons, as the flux is amplified by the squared charge of the emitting nucleus, Z^2 . Thus the photon-induced diffraction should overwhelm the QCD-originating colorless exchanges (Pomerons and Reggeons). Similarly, in PbPb collisions the photon fluxes are large and thus would overwhelm the Regge exchanges. The latter type is currently not possible to model with PYTHIA 8, however, as in addition to regular MPIs, one should also take into account the further interactions between the resolved photon and the other nucleons, that could destroy the rapidity gap. Since these are currently not implemented in the photoproduction framework, we leave the PbPb case for a future study.

6.1 pPb collisions

The setup for the photoproduction in pPb collisions is the same as our default setup for ep, albeit the photon flux is now provided by eq. (III.8). We here neglect the contribution where the proton would provide the photon flux, such that all photons arise from the nucleus. The jets are reconstructed with an anti- k_T algorithm using $R = 1.0$ as implemented in FASTJET package [66]. The applied cuts are presented in table III.3 and are very similar to the ones used by HERA analyses. The experimentally reachable lower cut on E_\perp is not set in stone, however. This depends on how well the jets can be reconstructed in this process. On one hand, the underlying event activity is greatly reduced in UPCs as compared to pp collisions, thus possibly allowing for a decrease of the reachable jet E_\perp . On the other hand, the increased W might require an increase of the minimum E_\perp w.r.t. the HERA analyses. Feasibility of such a measurement has been recently demonstrated in a preliminary ATLAS study [67] which measured inclusive dijets in ultra-peripheral PbPb collisions at the LHC.

The resulting differential cross sections for diffractive dijets from UPCs in pPb collisions are presented in Fig. III.16. Similar to sec. 4 we show the results differential in W , M_X , x_γ^{obs} and $z_{\text{IP}}^{\text{obs}}$. The “PDF” samples (dashed lines) are without the gap suppression and “MPI” samples (solid lines) are with the gap suppression. The lower panels show the ratio of the two, corresponding to the rapidity gap suppression factor predicted by the model. As discussed earlier, the energy dependence of the $p_{\perp 0}$ screening parameter in γp collisions was constrained by HERA data in a narrow W bin around 200 GeV. As the UPC events at the LHC will extend to much higher values of W , the poorly-constrained energy dependence of $p_{\perp 0}$ will generate some theoretical uncertainty for the predictions. To get a handle on this uncertainty we show samples with both the pp-tuned (red lines) and ep-tuned (blue lines) values for $p_{\perp 0}$.

The predicted gap suppression factor is rather flat as a function of $z_{\text{IP}}^{\text{obs}}$ at around ~ 0.7 . The suppression factor is, however, strongly dependent on W and M_X , also observed in the HERA comparisons. It is more pronounced at the LHC thanks to the extended range in W , with an average suppression being roughly two times larger than at HERA. A similar strong dependence is also seen in x_γ^{obs} . As concluded earlier, the increasing suppression with W follows from the fact that the probability for MPIs is increased with a higher W , due to the increased cross sections for the QCD processes. Thus a larger number of tentatively diffractive events are rejected due to the additional MPIs. Similarly, decreasing x_γ^{obs} will leave more room for the MPIs to take place, since the momentum extracted from the photon to the primary jet production is decreased.

A reduction of the $p_{\perp 0}^{\text{ref}}$ -value from 3.00 GeV to 2.28 GeV increases the MPI probability, thus having a twofold effect. Firstly, it increases the jet cross section in the “PDF”-sample, as the additional MPIs allowed with the lower reference value increase the energy inside the jet cone. Secondly, the enhanced MPI probability rejects a larger number of tentatively

diffractive events, thus giving a larger gap suppression effect. Collectively, these effects lead to 20 – 30 % larger gap-suppression factors as compared to the γp value for $p_{\perp 0}^{\text{ref}}$.

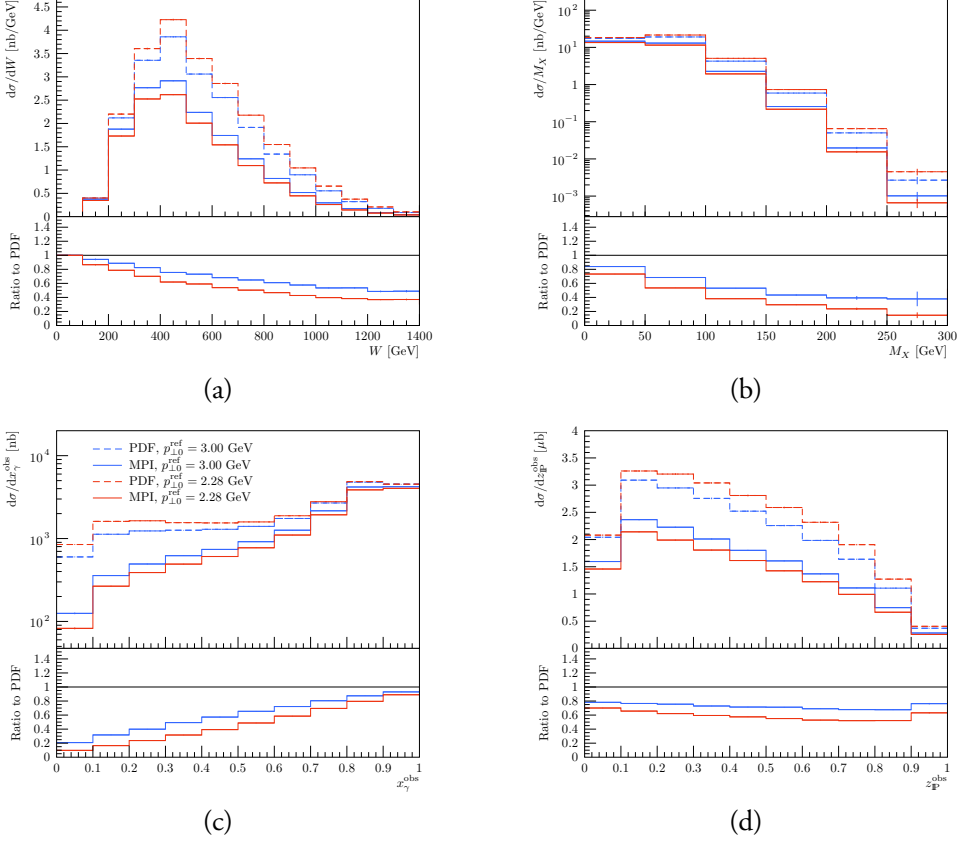


Figure III.16: Cross section for diffractive dijets in ultra-peripheral pPb collisions for observables W (a), M_X (b), x_γ^{obs} (c) and z_p^{obs} (d). Vertical bars denote the statistical uncertainty in the MC generation.

6.2 pp collisions

The kinematical cuts applied in pp equals those from pPb. Due to the increased \sqrt{s} and the harder photon spectrum from protons compared to heavy ions, the W range probed is extended to even larger values. When keeping jet kinematics fixed this leaves more room for MPIs in the γp -system, while also increasing the relative contribution from resolved photons. Thus the predicted gap-suppression factors are further increased here, as compared to pPb and ep case, cf. Fig. III.17. At extreme kinematics – high- M_X , low- x_γ^{obs} – the gap-suppression factors are almost as large as what have been found in hadronic diffractive pp events. The pp suppression factors should provide an estimate of the upper limit for

photoproduction, as the latter includes the (unsuppressed) direct contribution. The suppression factors show a similar sensitivity to the value of $p_{\perp 0}^{\text{ref}}$ as in pPb collisions, such that the lower value gives more suppression. Notice that the cross sections are calculated assuming that the photon is emitted from the beam with positive p_z .

A particularly interesting observable is the x_γ^{obs} distribution. Due to the extended W reach, the dijet production starts to be sensitive also to the low- x part of the photon PDFs. Here, the photon PDF analyses find that gluon distributions rise rapidly with decreasing x , the same tendency as seen in proton PDFs. This generates the observed rise of the cross section towards low values of x_γ^{obs} when the MPI rejection is not applied. However, the contribution from the low- x_γ^{obs} region is significantly reduced when the rejection is applied, as these events have a high probability for MPIs. Note, however, that there are large differences in the gluon distributions between different photon PDF analyses in this region. Thus here a variation of the photon PDF in the hard scattering could have some effect on the predicted gap-suppression factor, even though only very mild impact was seen in the HERA comparisons. But as most of these events with a soft gluon in the hard scattering will be rejected due to the presence of additional MPIs, the predicted cross-sections shown in Fig. III.17 is expected to be rather stable against such variations. Further uncertainty again arises from the dPDFs. But as the purpose of the shown UPC results is to demonstrate the gap survival effects, we do not discuss the sensitivity to dPDF variation here explicitly.

7 Conclusions

In this paper we present a model for explaining the factorization-breaking effects seen in photoproduction events at HERA. The model, implemented in the general purpose event generator PYTHIA 8, is an extension of the hard diffraction model to photoproduction. It is a novel combination of several existing ideas, and it is the first model of its kind with a dynamical gap suppression based on the kinematics of the entire event.

The starting point is the Ingelman-Schlein approach, where the cross section is factorized into a Pomeron flux and a PDF, convoluted with the hard scattering cross section. The Pomeron flux and PDF are extracted from HERA data, but if used out-of-the-box these give an order-of-magnitude larger cross sections in pure hadron-hadron collisions, while the differences in photoproduction are around a factor of two at most. Thus, factorization was observed to be broken in diffractive events with a hard scale. The dynamical model extended here, explain this factorization breaking with additional MPI activity filling the rapidity gap used for experimental detection of the diffractive events. Thus the MPI framework of PYTHIA 8 is used as an additional suppression factor on an event-by-event basis, giving cross sections very similar to what is seen in data, both in pp and p \bar{p} events. As low virtuality photons are allowed to fluctuate into a hadronic state, MPIs are also possible in

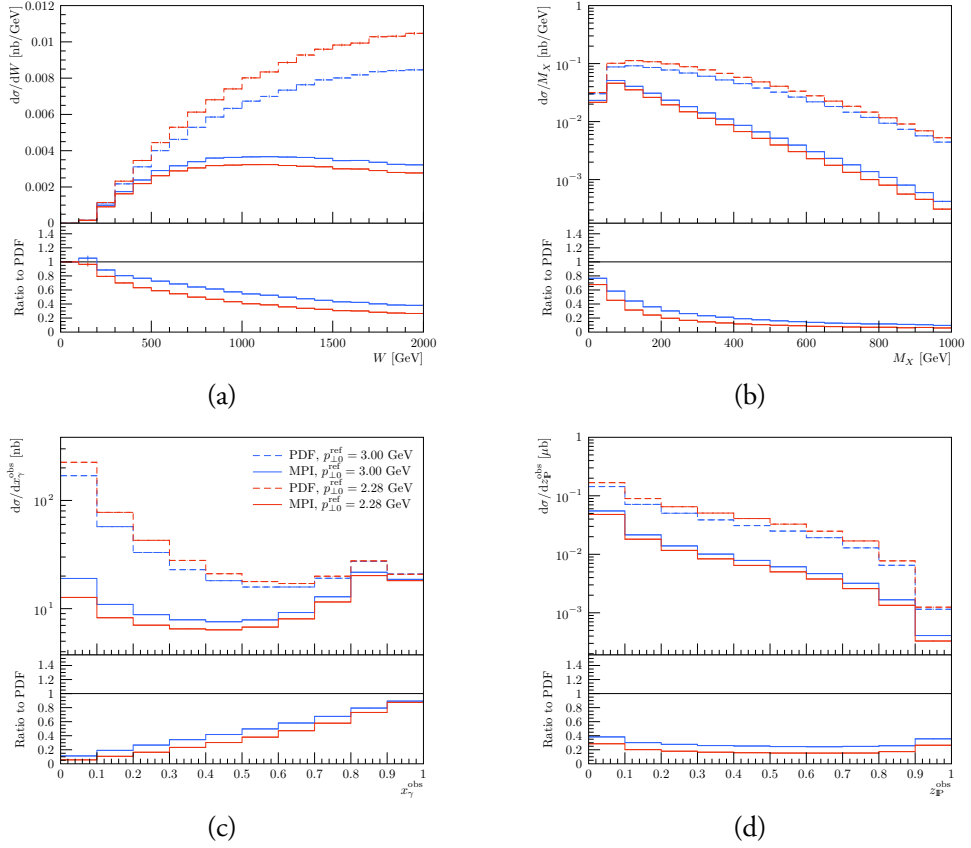


Figure III.17: Cross section for diffractive dijets in ultra-peripheral pp collisions for observables W (a), M_X (b), x_γ^{obs} (c) and z_p^{obs} (d). Vertical bars denote the statistical uncertainty in the MC generation.

these systems. Thus the same mechanism is responsible for the factorization breaking in photoproduction events in ep collisions, and also here the model predicts cross sections similar to what is seen in ep data.

We present results obtained with the model compared to experimental data from H1 and ZEUS for diffractive dijet photoproduction. The agreement with the data is improved when the MPI rejection is applied, supporting the idea behind the factorization-breaking mechanism. However, the kinematical cuts applied by the experiments reduce the contribution from resolved photons, so the observed suppression is rather mild with the HERA kinematics, especially for the ZEUS data. The improvements in the dPDFs raises the question if such a suppression is actually needed, as the new dPDFs seem to describe data fairly well without, especially in the direct-enhanced region of phase space. Furthermore, there are several theoretical uncertainties that hamper the interpretation of the data, and the description is far from perfect for all considered distributions. Many of these theoretical

uncertainties could be reduced by considering ratios of diffractive dijets in DIS and photoproduction regimes, but have not been pursued here as the description for DIS in PYTHIA 8 is not yet complete.

As an additional example for the range of the model, we present predictions for diffractive dijets in ultra-peripheral pp and pPb collisions at the LHC. In these processes a quasi-real photon emitted from a proton or nucleus interacts with a proton from the other beam. Due to the larger invariant masses of the γp system in these processes, the contribution from resolved photons is significantly increased. Thus UPCs is an excellent place to study the gap suppression in photoproduction. The results demonstrate that a measurement of photoproduced diffractive dijet cross sections in pp collisions would provide very strong constraints on our dynamical rapidity gap survival model, as the effects are much more pronounced than with HERA kinematics. The distinct features of the model are well accessible within the kinematical limits for UPCs at LHC. If such a measurement is not feasible due to the pure QCD background, a measurement in pPb collisions would be sufficient to confirm the factorization breaking in diffractive photoproduction and provide constraints on the underlying mechanism.

Future work consists of opening up for different photon PDFs in the photoproduction framework, improving the DIS description in PYTHIA 8 and merging the two regimes in a consistent manner. The first allows for probing additional theoretical uncertainties of the photoproduction framework, the second allows for probing the double ratios of photoproduction to DIS cross sections for diffractive dijets. The merging of the two regimes would allow for full event generation of all photon virtualities needed for future collider studies. Similarly a combination of the current model and the ANGANTYR model for heavy ions is planned, such that eA and ultraperipheral UPCs in AA collisions could be probed as well.

8 Acknowledgments

We thank Torbjörn Sjöstrand for reading through and commenting on the manuscript and Stefan Prestel for providing plotting tools. We also thank Hannes Jung for support with the HERA analyses, and Radek Zlebcik for providing the ZEUS SJ dPDFs.

This project has received funding from the European Research Council (ERC) under the European Union’s Horizon 2020 research and innovation program (grant agreement No 668679), and in part by the Swedish Research Council, contract number 2016-05996 and the Marie Skłodowska-Curie Innovative Training Network MCnetITN₃ (grant agreement 722104). Further support is provided by the Carl Zeiss Foundation and the Academy of Finland, Project 308301.

References

- [1] T. Sjöstrand, S. Ask, J. R. Christiansen, R. Corke, N. Desai, P. Ilten, S. Mrenna and S. Prestel *et al.*, Comput. Phys. Commun. **191** (2015) 159 [arXiv:1410.3012 [hep-ph]].
- [2] R. Bonino *et al.* [UA8 Collaboration], Phys. Lett. B **211** (1988) 239. doi:10.1016/0370-2693(88)90840-4
- [3] M. Derrick *et al.* [ZEUS Collaboration], Phys. Lett. B **332** (1994) 228. doi:10.1016/0370-2693(94)90883-4
- [4] T. Affolder *et al.* [CDF Collaboration], Phys. Rev. Lett. **84** (2000) 5043. doi:10.1103/PhysRevLett.84.5043
- [5] G. Aad *et al.* [ATLAS Collaboration], Phys. Lett. B **754** (2016) 214 doi:10.1016/j.physletb.2016.01.028 [arXiv:1511.00502 [hep-ex]].
- [6] T. Aaltonen *et al.* [CDF Collaboration], Phys. Rev. D **82** (2010) 112004 doi:10.1103/PhysRevD.82.112004 [arXiv:1007.5048 [hep-ex]].
- [7] G. Ingelman and P. E. Schlein, Phys. Lett. **152B** (1985) 256. doi:10.1016/0370-2693(85)91181-5
- [8] C. O. Rasmussen and T. Sjöstrand, JHEP **1602** (2016) 142 doi:10.1007/JHEP02(2016)142 [arXiv:1512.05525 [hep-ph]].
- [9] J. D. Bjorken, Phys. Rev. D **47** (1993) 101.
- [10] CMS Collaboration [CMS Collaboration], CMS-PAS-FSQ-12-033.
- [11] C. Adloff *et al.* [H1 Collaboration], Eur. Phys. J. C **6** (1999) 421 doi:10.1007/s100529801046 [hep-ex/9808013].

- [12] A. Aktas *et al.* [H1 Collaboration], Eur. Phys. J. C **51** (2007) 549 doi:10.1140/epjc/s10052-007-0325-4 [hep-ex/0703022].
- [13] S. Chekanov *et al.* [ZEUS Collaboration], Eur. Phys. J. C **55** (2008) 177 doi:10.1140/epjc/s10052-008-0598-2 [arXiv:0710.1498 [hep-ex]].
- [14] S. Chekanov *et al.* [ZEUS Collaboration], Nucl. Phys. B **831** (2010) 1 doi:10.1016/j.nuclphysb.2010.01.014 [arXiv:0911.4119 [hep-ex]].
- [15] F. D. Aaron *et al.* [H1 Collaboration], Eur. Phys. J. C **70** (2010) 15 doi:10.1140/epjc/s10052-010-1448-6 [arXiv:1006.0946 [hep-ex]].
- [16] V. Andreev *et al.* [H1 Collaboration], JHEP **1505** (2015) 056 doi:10.1007/JHEP05(2015)056 [arXiv:1502.01683 [hep-ex]].
- [17] A. J. Baltz *et al.*, Phys. Rept. **458** (2008) 1 doi:10.1016/j.physrep.2007.12.001 [arXiv:0706.3356 [nucl-ex]].
- [18] T. Sjöstrand, S. Mrenna and P. Z. Skands, JHEP **0605** (2006) 026 doi:10.1088/1126-6708/2006/05/026 [hep-ph/0603175].
- [19] L. Linssen, A. Miyamoto, M. Stanitzki and H. Weerts, doi:10.5170/CERN-2012-003 arXiv:1202.5940 [physics.ins-det].
- [20] H. Baer *et al.*, arXiv:1306.6352 [hep-ph].
- [21] A. Accardi *et al.*, Eur. Phys. J. A **52** (2016) no.9, 268 doi:10.1140/epja/i2016-16268-9 [arXiv:1212.1701 [nucl-ex]].
- [22] M. Bicer *et al.* [TLEP Design Study Working Group], JHEP **1401** (2014) 164 doi:10.1007/JHEP01(2014)164 [arXiv:1308.6176 [hep-ex]].
- [23] M. L. Mangano *et al.*, CERN Yellow Report (2017) no.3, 1 doi:10.23731/CYRM-2017-003.1 [arXiv:1607.01831 [hep-ph]].
- [24] C. Bierlich, G. Gustafson, L. Lönnblad and H. Shah, JHEP **1810** (2018) 134 [JHEP **2018** (2020) 134] doi:10.1007/JHEP10(2018)134 [arXiv:1806.10820 [hep-ph]].
- [25] C. Friberg and T. Sjöstrand, JHEP **0009** (2000) 010 doi:10.1088/1126-6708/2000/09/010 [hep-ph/0007314].
- [26] B. Cabouat and T. Sjöstrand, Eur. Phys. J. C **78** (2018) no.3, 226 doi:10.1140/epjc/s10052-018-5645-z, 10.1140/s10052-018-5645-z [arXiv:1710.00391 [hep-ph]].
- [27] S. Höche and S. Prestel, Eur. Phys. J. C **75** (2015) no.9, 461 doi:10.1140/epjc/s10052-015-3684-2 [arXiv:1506.05057 [hep-ph]].

- [28] I. Helenius, arXiv:1708.09759 [hep-ph].
- [29] I. Helenius, arXiv:1806.07326 [hep-ph].
- [30] I. Helenius, T. Sjöstrand, In preparation.
- [31] T. Sjostrand and P. Z. Skands, Eur. Phys. J. C **39** (2005) 129 doi:10.1140/epjc/s2004-02084-y [hep-ph/0408302].
- [32] T. Sjöstrand and P. Z. Skands, JHEP **0403** (2004) 053 doi:10.1088/1126-6708/2004/03/053 [hep-ph/0402078].
- [33] B. Andersson, G. Gustafson, G. Ingelman and T. Sjostrand, Phys. Rept. **97** (1983) 31. doi:10.1016/0370-1573(83)90080-7
- [34] T. Sjöstrand and M. van Zijl, Phys. Rev. D **36** (1987) 2019. doi:10.1103/PhysRevD.36.2019
- [35] G. A. Schuler and T. Sjöstrand, Phys. Rev. D **49** (1994) 2257. doi:10.1103/PhysRevD.49.2257
- [36] L. Stodolsky, Phys. Rev. Lett. **18** (1967) 135. doi:10.1103/PhysRevLett.18.135
- [37] H. Joos, Phys. Lett. **24B** (1967) 103. doi:10.1016/0370-2693(67)90359-0
- [38] J. J. Sakurai and D. Schildknecht, Phys. Lett. **40B** (1972) 121. doi:10.1016/0370-2693(72)90300-0
- [39] M. Glück, E. Reya and A. Vogt, Phys. Rev. D **46** (1992) 1973. doi:10.1103/PhysRevD.46.1973
- [40] P. Aurenche, J. P. Guillet and M. Fontannaz, Z. Phys. C **64** (1994) 621 doi:10.1007/BF01957771 [hep-ph/9406382].
- [41] G. A. Schuler and T. Sjöstrand, Z. Phys. C **68** (1995) 607 doi:10.1007/BF01565260 [hep-ph/9503384].
- [42] F. Cornet, P. Jankowski, M. Krawczyk and A. Lorca, Phys. Rev. D **68** (2003) 014010 doi:10.1103/PhysRevD.68.014010 [hep-ph/0212160].
- [43] W. Slominski, H. Abramowicz and A. Levy, Eur. Phys. J. C **45** (2006) 633 doi:10.1140/epjc/s2005-02458-7 [hep-ph/0504003].
- [44] R. J. DeWitt, L. M. Jones, J. D. Sullivan, D. E. Willen and H. W. Wyld, Jr., Phys. Rev. D **19** (1979) 2046 Erratum: [Phys. Rev. D **20** (1979) 1751]. doi:10.1103/PhysRevD.19.2046, 10.1103/PhysRevD.20.1751

- [45] P. Skands, S. Carrazza and J. Rojo, Eur. Phys. J. C **74** (2014) no.8, 3024 doi:10.1140/epjc/s10052-014-3024-y [arXiv:1404.5630 [hep-ph]].
- [46] C. F. von Weizsäcker, Z. Phys. **88** (1934) 612. doi:10.1007/BF01333110
- [47] E. J. Williams, Phys. Rev. **45** (1934) 729. doi:10.1103/PhysRev.45.729
- [48] M. Drees and D. Zeppenfeld, Phys. Rev. D **39** (1989) 2536. doi:10.1103/PhysRevD.39.2536
- [49] V. A. Khoze, A. D. Martin and M. G. Ryskin, Eur. Phys. J. C **18** (2000) 167 doi:10.1007/s100520000494 [hep-ph/0007359].
- [50] E. Gotsman, E. Levin, U. Maor, E. Naftali and A. Prygarin, hep-ph/0511060.
- [51] S. P. Jones, A. D. Martin, M. G. Ryskin and T. Teubner, JHEP **1311** (2013) 085 doi:10.1007/JHEP11(2013)085 [arXiv:1307.7099 [hep-ph]].
- [52] M. Goharipour, H. Khanpour and V. Guzey, Eur. Phys. J. C **78** (2018) no.4, 309 doi:10.1140/epjc/s10052-018-5787-z [arXiv:1802.01363 [hep-ph]].
- [53] S. Alekhin *et al.*, Eur. Phys. J. C **75** (2015) no.7, 304 doi:10.1140/epjc/s10052-015-3480-z [arXiv:1410.4412 [hep-ph]].
- [54] S. Chekanov *et al.* [ZEUS Collaboration], Eur. Phys. J. C **52** (2007) 813 doi:10.1140/epjc/s10052-007-0426-0, 10.3204/proco7-01/112 [arXiv:0708.1415 [hep-ex]].
- [55] A. Aktas *et al.* [H1 Collaboration], JHEP **0710** (2007) 042 doi:10.1088/1126-6708/2007/10/042 [arXiv:0708.3217 [hep-ex]].
- [56] L. N. Lipatov, Sov. J. Nucl. Phys. **20** (1975) 94 [Yad. Fiz. **20** (1974) 181].
- [57] V. N. Gribov and L. N. Lipatov, Sov. J. Nucl. Phys. **15** (1972) 438 [Yad. Fiz. **15** (1972) 781].
- [58] G. Altarelli and G. Parisi, Nucl. Phys. B **126** (1977) 298. doi:10.1016/0550-3213(77)90384-4
- [59] Y. L. Dokshitzer, Sov. Phys. JETP **46** (1977) 641 [Zh. Eksp. Teor. Fiz. **73** (1977) 1216].
- [60] A. Aktas *et al.* [H1 Collaboration], Eur. Phys. J. C **48** (2006) 715 doi:10.1140/epjc/s10052-006-0035-3 [hep-ex/0606004].
- [61] A. Buckley, J. Butterworth, L. Lönnblad, D. Grellscheid, H. Hoeth, J. Monk, H. Schulz and F. Siegert, Comput. Phys. Commun. **184** (2013) 2803 doi:10.1016/j.cpc.2013.05.021 [arXiv:1003.0694 [hep-ph]].

- [62] L. E. Gordon and J. K. Storrow, Nucl. Phys. B **489** (1997) 405 doi:10.1016/S0550-3213(97)00048-5 [hep-ph/9607370].
- [63] M. R. Whalley, D. Bourilkov and R. C. Group, hep-ph/0508110.
- [64] V. Guzey and M. Klasen, JHEP **1604** (2016) 158 doi:10.1007/JHEP04(2016)158 [arXiv:1603.06055 [hep-ph]].
- [65] E. Basso, V. P. Goncalves, A. K. Kohara and M. S. Rangel, Eur. Phys. J. C **77** (2017) no.9, 600 doi:10.1140/epjc/s10052-017-5173-2 [arXiv:1705.08834 [hep-ph]].
- [66] M. Cacciari, G. P. Salam and G. Soyez, Eur. Phys. J. C **72** (2012) 1896 doi:10.1140/epjc/s10052-012-1896-2 [arXiv:1111.6097 [hep-ph]].
- [67] The ATLAS collaboration, ATLAS-CONF-2017-011.

IV

Dipole evolution: perspectives for collectivity and γ^* A collisions

Christian Bierlich¹² and Christine O. Rasmussen².

Submitted to *JHEP*

e-Print: arXiv:1907.12871 [hep-ph]

MCnet-19-17 LU TP 19-32

¹ Niels Bohr Institute, Blegdamsvej 17, 2100 København Ø, Denmark

² Dept. of Astronomy and Theoretical Physics, Lund University, Sölvegatan 14A, SE-223 62 Lund, Sweden.

ABSTRACT: The transverse, spatial structure of protons is an area revealing fundamental properties of matter, and provides key input for deeper understanding of emerging collective phenomena in high energy collisions of protons, as well as collisions of heavy ions. In this paper eccentricities and eccentricity fluctuations are predicted using the dipole formulation of BFKL evolution. Furthermore, first steps are taken towards generation of fully exclusive final states of γ^* A collisions, by assessing the importance of color fluctuations in the initial state. Such steps are crucial for the preparation of event generators for a future electron-ion collider. Due to the connection between an impact parameter picture of the proton structure, and cross sections of ep and pp collisions, the model parameters can be fully determined by fits to such quantities, leaving results as real predictions of the model.

I Introduction

In the research program at the Large Hadron Collider (LHC) and the Relativistic Heavy Ion Collider (RHIC), collisions of ultra relativistic heavy ions are hypothesized to result in the creation of a quark-gluon plasma (QGP) with partonic degrees of freedom. One of the main avenues for investigating and characterizing this plasma consists of measurements of azimuthal correlations between particle pairs separated in rapidity, connecting particle emission angles to the initial geometry of the collision. Non-trivial correlations reflecting collective properties were first observed in gold–gold and copper–copper collisions at RHIC [1], but has since been investigated also in lead–lead (PbPb) collisions at the LHC [2–4]. Such non-trivial azimuthal correlations had at that point already been hypothesized to be a signal for hydrodynamic behavior [5], or, even earlier, to involve microscopic dynamics of overlapping “quark tubes” or strings [6].

Similar results have been obtained in smaller collision systems such as proton–lead (pPb) [7], deuteron–gold [8], and, perhaps most surprisingly, in proton–proton (pp) [9]. Attempts to observe similar behavior in even smaller collision systems, e.g. e^+e^- , has, while carrying interesting prospects, so far not produced positive results [10]. Even though the discovery of collectivity in pp is almost ten years old, the origin of such correlations in small collision systems is still highly debated (see ref. [11] for a recent review), and its resolution is among the top priorities for the future heavy ion program at LHC [12]. One possibility is that the correlations in these small collision systems are due to coherence effects [13] or initial state correlations [14]. Another is a repetition of the argument from heavy ion collisions, where the observed collective behavior is a hydrodynamic response to the initial partonic spatial configuration [15]. A picture where a hydrodynamic “core” coexists with a non-hydrodynamic “corona” has been shown by the EPOS model [16, 17] to provide good descriptions of collectivity even in small collision systems.

The possibility of a hydrodynamic (or in fact any other) response to an initial geometric configuration of partons, poses a challenge to the traditional strategies for pp event generators, such as PYTHIA 8 [18] or HERWIG 7 [19], both based on perturbative QCD (pQCD) with no obvious way to extract a spatial configuration for which to calculate a response. Attempts to calculate such a structure [20–22] generally involve assuming a certain spatial distribution of partons in the proton and, using the eikonal approximation, then transferring this structure to a spatio-temporal structure of the multiple partonic interactions (MPIs). The immediate drawbacks of such an approach are that (a) such models will in general contain parameters which need to be fitted to the same type of particle correlations as they wish to predict, and (b) assuming a spatial distribution of partons in a proton will generally contain many *ad hoc* elements.

Even though the spatial distribution of partons in a proton cannot be assessed *ab initio*, the

evolution of said distribution can be calculated perturbatively in the formalism of Mueller [23, 24]. At high energies, average properties will retain little dependence on the initial configuration, i.e. be mostly dependent on the evolution. Since the transverse substructure of the colliding protons (or virtual photons) can be linked to total or semi-inclusive cross sections, any model parameters can be tuned to such quantities, and leave any further estimation of collective effects as real predictions of the model. Attempts to predict the elliptic flow in pp collisions using an implementation of Mueller’s model was provided in 2011 [25], showing $v_{2,3}$ comparable to values found from PbPb at RHIC and LHC energies.

This paper is concerned with presenting a new Monte Carlo implementation of Mueller’s model, study its description of cross sections in pp and γ^* p collisions, in order to provide estimates on parton level geometries in pp, proton–ion (pA) and ion–ion (AA) collisions, linked to collective phenomena. Mueller’s model has been implemented as a Monte Carlo several times before, as it is not only useful for calculating spatial distributions of partons, but in fact has much wider applications due to the equivalence of the Mueller formalism with B-JIMWLK (Balitsky, Jalilian-Marian, Iancu, McLerran, Weigert, Leonidov and Kovner) [26–33] evolution (see section 2). Such an implementation makes direct introduction of effects beyond the leading logarithmic approximation possible, e.g. conservation of energy and momentum without imposing kinematical constraints on the splitting kernel [34]. This makes the implementation attractive for estimation of basic quantities dominated by small x processes (e.g. cross sections) in cases where little guidance from data exists. In this paper (see section 7) we will also apply the formalism to extract Glauber–Gribov (GG) color fluctuations in γ^* p collisions, in order to take the initial steps towards a generation of electron–ion (eA) collisions within the ANGANTYR framework [35, 36] – a possibility which is foreseen to aid the preparation of an eA program currently being planned [37].

Earlier implementations of the Mueller dipole model include the public OEDIPUS [38] and DIPSY [39, 40] codes, as well as a private implementation by Kovalenko *et. al.* [41]. All implementations treat only gluons in the evolution, as will this work. The implementation in this paper is similar to the implementation in DIPSY in some respects, but differs in other, while bearing less resemblance to the other two. The key differences between most of the used approaches, lies in the treatment of effects beyond leading order. In section 2 a more detailed overview is given, but worth mentioning already here, is the treatment of sub-leading N_c (number of colors) effects in the evolution, leading to saturation in the cascade. In DIPSY, this is addressed through so-called swing mechanisms [42, 43], which suppresses the contribution from large dipoles in dense environments by replacing them with small dipoles. In this paper we consider only sub-leading N_c effects in the collision frame, by including multiple interactions in a way consistent with unitarity. Thus we make no attempt at treating saturation effects sub-leading in N_c in the cascade, as the focus is rather to

study how well one can do with an approach that includes only a minimal set of sub-leading corrections. Effects included in this paper is energy-momentum conservation and recoil effects (which are beyond leading log) and confinement (which is a non-perturbative effect). This also separates our approach from the IP-GLASMA approach [44], which includes N_c suppressed gluon saturation effects in the initial configuration explicitly, and evolve using B-JIMWLK.

On a more technical note, the approach presented in this paper is implemented within the larger framework of the PYTHIA 8 Monte Carlo event generator. This first of all means that the implementation will become publicly available,¹ and to aid reproducibility and transparency, a large part of the manuscript, as well as appendix 10, are devoted to the details of the implemented model. Our approach is simplistic in the sense that only a minimal amount of corrections to Mueller’s original model has been added, and where ambiguities have arisen, the simplest possible choice has been taken.

The structure of the paper is as follows: After this introduction, the pQCD model of Mueller is introduced. Then follows a description on how observables are calculated within the Good-Walker framework as well as a definition of the observables related to the substructure of protons. The next section describes the overall features of the Monte Carlo implementation, before we proceed to the results on cross sections, eccentricities and color fluctuations in processes with incoming virtual photons. Lastly, a section is devoted to conclusions and forthcoming work.

2 Proton substructure evolution

In this section we will outline the theoretical basis of the initial state evolution approach used in subsequent sections, and briefly review its relation to other approaches. The theoretical basis is the well known dipole QCD model by Mueller *et. al.* [23, 24].

2.1 Dipole evolution in impact parameter space

We consider in general a picture with a projectile with a dipole structure incident on a target. In the simplest case, the projectile is just a single dipole r_{12} , spanned between the coordinates \vec{r}_1 and \vec{r}_2 , in impact parameter space. The probability at leading order for this dipole to branch when evolved in rapidity (y), is

$$\frac{d\mathcal{P}}{dy} = d^2\vec{r}_3 \frac{N_c\alpha_s}{2\pi^2} \frac{r_{12}^2}{r_{13}^2 r_{23}^2} \equiv d^2\vec{r}_3 \kappa_3. \quad (\text{IV.1})$$

¹From a future version of Pythia, larger than version 8.300, yet to be determined. See <https://home.thep.lu.se/Pythia> for up-to-date information.

Here \vec{r}_3 is the transverse coordinate of the emitted gluon and κ_3 is used as a short-hand for the splitting kernel. An observable O known initially, will after an infinitesimal interval dy have the expectation value (denoted by a bar), assuming unitarity:

$$\bar{O}(y + dy) = dy \int d^2\vec{r}_3 \kappa_3 [O(r_{13}) \otimes O(r_{23})] + O(r_{12}) \left[1 - dy \int d^2\vec{r}_3 \kappa_3 \right], \quad (\text{IV.2})$$

where \otimes denotes the evaluation of the observable O in the two dipole system r_{13}, r_{23} . In the limit $dy \rightarrow 0$ this becomes:

$$\frac{\partial \bar{O}}{\partial y} = \int d^2\vec{r}_3 \kappa_3 [O(r_{13}) \otimes O(r_{23}) - O(r_{12})]. \quad (\text{IV.3})$$

Remarkably, eq. (IV.3) allows for the evolution of any observable calculable in impact parameter space. In the case of S -matrices in impact parameter space, the evaluation in the two dipole system reduces to a normal product in the eikonal approximation. Thus $O(r_{13}) \otimes O(r_{23}) \rightarrow S(r_{13})S(r_{23})$. Changing to scattering amplitudes, T , by substituting $T \equiv 1 - S$, one obtains:

$$\frac{\partial \langle \bar{T} \rangle}{\partial y} = \int d^2\vec{r}_3 \kappa_3 [\langle T_{13} \rangle + \langle T_{23} \rangle - \langle T_{12} \rangle - \langle T_{13} T_{23} \rangle]. \quad (\text{IV.4})$$

This is the B-JIMWLK equation hierarchy [26–33] in impact parameter space, which, as shown already by Mueller [45], can be generated directly from eq. (IV.1).

2.2 Non-linear evolution, the color glass condensate and saturation

Equation (IV.4) includes a non-linear term, $\langle T_{13} T_{23} \rangle$, and the treatment of this term is defining for many of the various approaches dealing with initial state evolution at low x .

Removal of the non-linear term yields the BFKL (Balitsky, Fadin, Kuraev and Lipatov) equation [46, 47], which correctly sums all of the leading logarithms in energy (or, more precisely in rapidity $(\alpha_s \cdot y)^n$) to all orders. Other than simply neglecting it, the simplest treatment of the non-linear term is by a mean-field approach, where it factorizes as: $\langle T_{13} T_{23} \rangle \rightarrow \langle T_{13} \rangle \langle T_{23} \rangle$. This approximation yields the BK (Balitsky and Kovchegov) equation [26, 48].

The non-linear term is connected to saturation of the cross section. This is particularly evident from the BK equation, which is briefly discussed in the following. The dipole-proton scattering cross section is $\sigma_{12} \equiv \int d^2\vec{b} \, 2\langle T \rangle$ (see section 3.1), and directly from eq. (IV.4):

$$\frac{\partial \bar{\sigma}_{12}}{\partial y} = \int d^2\vec{r}_3 \kappa_3 \left[\sigma_{13} + \sigma_{23} - \sigma_{12} - \frac{1}{2} \sigma_{13} \sigma_{23} \right]. \quad (\text{IV.5})$$

Here, the first two terms corresponds to a branching of dipole r_{12} to two dipoles, r_{13}, r_{23} and the scattering of each of the new dipoles with the proton. The third subtracts the contribution from the initial r_{12} dipole, as it is destroyed in the creation of the two new dipoles. The last term has a negative sign, thus the non-linear term can be seen as a reduction, or saturation, of the dipole-proton cross section, in particular for large y . The saturation of the cross section corresponds directly to a double scattering contribution, making the result consistent with unitarity, and we note that the term formally carries an extra factor of α_s/N_c w.r.t. BFKL, and is thus color suppressed.

Color suppressed saturation effects beyond the mean field approximation of the BK equation are often treated in the Color Glass Condensate (CGC) framework [49, 50], an effective theory for QCD at high gluon densities. High energy nucleons or nuclei are here treated as classical gluon fields. This allows expressing the dipole-target scattering matrix in terms of Wilson lines [51]:

$$S_{12} = \frac{1}{N_c} \langle V_1^\dagger V_2 \rangle, \quad (\text{IV.6})$$

where subscripts (1, 2) denote the transverse coordinates of the quark and anti-quark in the projectile dipole, keeping in line with the notation introduced above. The Wilson lines describe the multiple scattering of the quark and antiquark in the dipole, off a classical color field in the target. The key ingredient is to note that the field can be evolved according to B-JIMWLK. This is not a trivial statement, but shall here simply be taken as fact, and the evolution of S_{12} can be obtained directly from eq. (IV.4):

$$\frac{\partial S_{12}}{\partial y} = \int d^2\vec{r}_3 \kappa_3 \left[\frac{1}{N_c^2} \langle V_1^\dagger V_3 V_3^\dagger V_2 \rangle - \frac{1}{N_c} \langle V_1^\dagger V_2 \rangle \right]. \quad (\text{IV.7})$$

From this treatment, where no assumption of individual emissions is made, it is directly seen that the non-linear term is suppressed by a factor $1/N_c^2$, and the CGC formalism thus handles saturation effects in the cascade correctly. The reason not to use the CGC formalism in this paper, is due to the approximation of the target by a classical field. Since all small- x gluons in the CGC approach are radiated directly from the classical source, some fluctuations from successive emissions are omitted. As the goal of this paper is to study fluctuations in the initial geometry associated with flow fluctuations, we want to go beyond this approximation.

It is, however, possible to perform a more phenomenological assessment of the effect of gluon saturation in the cascade, which we will use in section 4.4 to introduce a toy model for saturation. Equating proton form factors calculated in the DGLAP formalism and the dipole formalism, indicates that the dipole-proton cross section is proportional to the squared dipole radius [52], $\sigma_{\text{dip}} \sim r^2 G(x, Q^2 \sim 1/r^2)$, with G the gluon momentum density of the proton. This means that while small dipoles are unaffected by the non-linear term, it becomes highly important for large dipoles. This introduces a new length scale, the

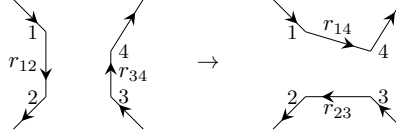


Figure IV.1: Schematic view of two colliding gluon dipoles. The initial dipoles denoted r_{12} and r_{34} are allowed to interact via two-gluon exchange. This results in the creation of two new dipoles, r_{14} and r_{23} and a connection of the two dipole chains. The lines r_{13} and r_{24} are not drawn, but enters in eq. (IV.9).

saturation length (or equivalently a saturation scale) $r_s(x) \sim 1/Q_s$, which must depend on x to reflect the increase in the dipole-proton cross section with decreasing x . Thus the dipole-proton cross section should depend on the scaling variable $r/r_s(x)$ for large r , a property known as geometric scaling, see e.g. [53].

2.3 The Mueller dipole model

Several approaches have been proposed to utilize the simple, but powerful evolution equation introduced in eq. (IV.4). What they all have in common, is that the saturation behavior introduced by the non-linear term is approximated in some way. Here we will focus on the Mueller dipole model which is particularly suitable for calculation of geometric quantities. Usually, eq. (IV.4) is solved as an initial value problem: given a scattering matrix at small initial rapidity (y_0), it determines the resulting scattering matrix at any $y \geq y_0$. Note however, that eq. (IV.3) is applicable for any type of observable calculable in impact-parameter space, notably observables linked to the geometry of the partonic initial state. As an example, consider the average vertex coordinate position, $\langle z \rangle$, where z is either the x or y coordinate of a dipole. For a single dipole $\langle z \rangle = (z_1 + z_2)/2$, for the two dipole system $\langle z \rangle = (z_1 + z_2 + z_3)/3$, where the two dipoles has a common point z_3 , and directly:

$$\frac{\partial \langle z \rangle}{\partial y} = \int d^2 \vec{r}_3 \kappa_3 \left(\frac{1}{3} z_3 - \frac{1}{6} (z_1 + z_2) \right). \quad (\text{IV.8})$$

For more complicated geometric observables, such as eccentricity (see section 3.2), the analytic expressions become quite involved, and must be handled observable by observable. They are, however, quite easy to handle in a Monte Carlo, where any O can be evaluated event by event, and the expectation value extracted from a large statistics sample.

The starting point for the model, is the evolution of an Onium (or $\gamma^* \rightarrow q\bar{q}$) state in transverse space and rapidity, following eq. (IV.1). Instead of calculating average quantities directly from the evolution equation, Monte Carlo events are generated, by performing a probabilistic evolution of a given initial state, corresponding to a collision event performed by an experiment. The calculational details of performing such an evolution are deferred to section 4 and appendix 10. It is, however, important to note here the approximation of

this evolution, namely that all dipoles in the dipole-chain radiate independently, removing the non-linear effect from the cascade itself.

After a full evolution in rapidity, a single dipole will have evolved to a chain of dipoles, each of which are allowed to interact with dipoles from another evolved system through gluon exchange. The lowest order interaction between two dipoles, at amplitude level, is single gluon exchange, resulting in two gluon exchange at cross section level. This cross section can be related to the elastic amplitude (cf. section 3.1) through the optical theorem. The dipole-dipole cross section depends on the distances between the interacting dipoles (the enumeration of dipoles follows figure IV.1) as [54]:

$$\begin{aligned} \frac{d\sigma_{\text{dip}}}{d^2\vec{b}} &= \frac{\alpha_s^2 C_F}{N_c} \log^2 \left[\frac{r_{13}r_{24}}{r_{14}r_{23}} \right] \\ &\rightarrow \frac{\alpha_s^2}{2} \log^2 \left[\frac{r_{13}r_{24}}{r_{14}r_{23}} \right] \equiv f_{ij}, \end{aligned} \quad (\text{IV.9})$$

where the arrow indicates that the 't Hooft large- N_c limit² is taken to reach line 2 of eq. (IV.9), which then defines f_{ij} . The 't Hooft large- N_c limit is taken in order to ensure consistency with the leading logarithmic approximation in the (BFKL) evolution. The distances r_{ij} are indicated in figure IV.1, except for r_{13} and r_{24} , the distances between (anti-)color-(anti-)color pairs (1,3) and (2,4). Note that the dipole-dipole interaction is formally $1/N_c^2$ suppressed, but that this is not directly visible from f_{ij} as defined in line 2 of eq. (IV.9).

A single collision can contain several dipole-dipole scatterings, equivalent to MPIs in a standard parton language. Assuming that the individual scatterings are uncorrelated, the contribution from each scattering exponentiates, resulting in the unitarized scattering amplitude for a single event (see section 3.1):

$$T(\vec{b}) = 1 - \exp \left(- \sum_{ij} f_{ij} \right). \quad (\text{IV.10})$$

An expansion of the exponent into a power series results in factors of $(\sum_{ij} f_{ij})^n$. In the 't Hooft limit, each part of the expansion of the exponent comes with factors of $(1/N_c^2)^n$. These higher order terms correspond to the non-linear terms from eq. (IV.4) when counting factors of $1/N_c^2$. Formally, one can count two-gluon exchanges and compare to the evolution kernel, which comes with a factor $N_c \alpha_s \sim 1$. Thus in the collision frame, the dipole model with unitarization of the scattering amplitude gives a formalism which correctly resums $1/N_c^2$ suppressed terms. In Regge terminology, each scattering f_{ij} can be viewed as a Pomeron exchange. The first term in the expansion corresponds to single Pomeron exchange, and the latter terms to multi-Pomeron exchanges. The scattering amplitude can

²The 't Hooft large- N_c limit is the limit where factors of $\alpha_s N_c$ are kept fixed while factors of $1/N_c^2$ are suppressed.

thus also be viewed as a resummation of all possible Pomeron exchanges in the collision frame.

2.4 Dipole evolution beyond leading order

Significant formal progress has been made in the pursuit of systematic next-to-leading order (NLO) in α_s corrections to the BK equation [55] and the full B-JIMWLK hierarchy [56–58]. Numerical studies of NLO BK [59] have, however, shown that the equation becomes unstable for some values of the initial conditions, making it yet unsuitable for a full Monte Carlo implementation. Recent work by Ducloué *et. al.* [60] have shown that, for a specific choice of the initial scattering matrix, some problems of unphysical results can be overcome in the dilute-dense limit, by reformulating the NLO evolution equation w.r.t. rapidity of the dense target. This gives hope that a future improvement of the model, implemented as a Monte Carlo in this paper, could include formal improvements beyond leading order, but at this point it is not deemed feasible.

An approach for going beyond leading color in the cascade, which is also suited for Monte Carlo implementation, is the so-called “swing” mechanism, introduced by Avsar *et. al.* [43, 61]. This can be understood as an extension of the identification of multiple interactions in the collision frame with Pomeron loops, as presented in the previous section. Since loops cannot be formed during the BFKL-like evolution, only loops cut in the collision frame are included. The problem is then posed as equivalent to forming $1/N_c^2$ suppressed dipole configurations, by allowing dipoles to reconnect in such a way that the formalism becomes frame independent. This is another viable path for future extensions beyond leading order. Further work on the formalism is needed, however. Currently only a $2 \rightarrow 2$ dipole swing has been thoroughly studied, which is not enough to make the formalism fully frame independent. Going beyond $2 \rightarrow 2$ is a full study by itself, and not considered in the present paper.

In this paper we instead choose to include corrections beyond (formal) leading-log arising from energy–momentum conservation. It is well known that the leading-log BFKL equation, derived in the high-energy limit, will get sizable corrections at collider energies [62]. From studies of the full next-to-leading log BFKL [63, 64], it is shown that contributions beyond leading log are very large, and a sizable amount are related to energy-momentum conservation [65]. In a Monte Carlo such corrections can be implemented directly, see details in appendix 10. Related are non-eikonal corrections. Non-eikonal corrections arise due to the large but finite energy available during the cascade. In the CGC approach this can be understood as sub-leading effects to infinite Lorentz dilation of the projectile, which are troublesome but manageable analytically [66]. In a Monte Carlo implementation of the dipole model, the finite energy can be treated as recoil effects in the dipole splittings.

A non-perturbative effect from confinement is also included in our simulation. This must be done both in the cascade, where large dipoles must be suppressed, and in the interaction, where the range of the interaction must be limited to take confinement into account. Following ref. [42], this is done by replacing $1/p_g^2$ in the Coulomb propagator implicitly entering eq. (IV.9) by $1/(p_g^2 + M_g^2)$, where M_g can be taken as a confinement scale, or a fictitious gluon mass. This changes the expressions for the splitting kernel and the dipole-dipole interaction probability, the full expressions are written in section 4.

3 From substructure to observables

The following section is dedicated to the introduction of the framework used for linking partonic substructure to physical observables, such as cross sections and flow coefficients. First, we describe the Good–Walker formalism for calculating cross sections for particles with an inner structure, from obtained scattering amplitudes, and secondly, the apparent scaling of flow coefficients with initial state eccentricity seen in heavy ion collisions is explained.

3.1 The Good–Walker formalism and cross sections

The Good–Walker formalism is a method of calculating cross sections of particles with a well-defined wave function. It includes a normalized and complete set of eigenstates $\{|\psi_i\rangle\}$ of the imaginary part of the scattering amplitude (neglecting the real part, which is vanishing at high energies), denoted $\hat{T}(\vec{b})$ (related to the \hat{S} -matrix through $\hat{T} \equiv 1 - \hat{S}$), with eigenvalues $\hat{T}(\vec{b})|\psi_i\rangle = T_i(\vec{b})|\psi_i\rangle$. These scattering states have equal quantum numbers, but differ in masses. The wave function of the incoming beams can thus be expressed in terms of the above eigenstates, and written in short-hand notation as

$$|\psi_I\rangle = |\psi_p, \psi_t\rangle = \sum_{p=1}^{N_p} \sum_{t=1}^{N_t} c_p c_t |\psi_p, \psi_t\rangle \quad (\text{IV.11})$$

with $|\psi_{p,t}\rangle$ denoting the projectile and target wave functions, respectively, and $c_{p,t}$ the expansion coefficients. The scattered wave function is found by operating with the transition matrix on the incoming wave function,

$$|\psi_S\rangle = \hat{T}(\vec{b})|\psi_I\rangle = \sum_{p,t} c_p c_t T_{p,t}(\vec{b}) |\psi_p, \psi_t\rangle, \quad (\text{IV.12})$$

and from these definitions, the profile function for elastic scattering (at fixed Mandelstam s) can be defined:

$$\begin{aligned}\Gamma_{\text{el}}(\vec{b}) &= \langle \psi_S | \psi_I \rangle = \sum_{p,t} |c_p|^2 |c_t|^2 T_{p,t}(\vec{b}) \langle \psi_p, \psi_t | \psi_p, \psi_t \rangle \\ &= \sum_{p,t} |c_p|^2 |c_t|^2 T_{p,t}(\vec{b}) \equiv \langle T(\vec{b}) \rangle_{p,t},\end{aligned}\quad (\text{IV.I3})$$

where we have defined an average over projectile and target states in the last equality and suppressed indices on T inside the average (which is done in all the following, unless specifically noted otherwise). Thus we obtain the cross sections and elastic slope in the eikonal approximation (again also at fixed Mandelstam s),

$$\sigma_{\text{tot}} = 2 \int d^2\vec{b} \Gamma(\vec{b}) = 2 \int d^2\vec{b} \langle T(\vec{b}) \rangle_{p,t}, \quad (\text{IV.I4})$$

$$\sigma_{\text{el}} = \int d^2\vec{b} |\Gamma(\vec{b})|^2 = \int d^2\vec{b} \langle T(\vec{b}) \rangle_{p,t}^2, \quad (\text{IV.I5})$$

$$B_{\text{el}} = \frac{\partial}{\partial t} \log \left(\frac{d\sigma_{\text{el}}}{dt} \right) \Big|_{t=0} = \frac{\int d^2\vec{b} b^2 / 2 \langle T(\vec{b}) \rangle_{p,t}}{\int d^2\vec{b} \langle T(\vec{b}) \rangle_{p,t}}. \quad (\text{IV.I6})$$

In eqs. (IV.I4–IV.I6) we have implicitly assumed a particle wave function $\langle \psi | \psi \rangle = 1$. In cases where the wave function is not normalizable, one has to take into account the wave function in the above cross sections. This includes processes with photons, where the wave function is well-defined in pQCD for high virtualities. The total γ^*p cross section would thus require an additional integration over wave function parameters:

$$\sigma^{\gamma^*p}(s) = \int_0^1 dz \int_0^{r_{\text{max}}} r dr \int_0^{2\pi} d\phi (|\psi_L(z, r)|^2 + |\psi_T(z, r)|^2) \sigma_{\text{tot}}(z, \vec{r}), \quad (\text{IV.I7})$$

with z the fractional momentum carried by the quark, r the distance between the quark and anti-quark, $\psi_{L,T}$ the longitudinal and transverse parts of the photon wave function and $\sigma(z, \vec{r})$ the dipole cross section calculated from the elastic profile function, eq. (IV.I4). The photon wave function implemented in our approach is given in eqs. (IV.25–IV.26) and the discussion for γ^*A is continued in section 7.

3.2 Eccentricity scaling of flow observables

Anisotropic flow is measured as momentum space anisotropies and quantified in flow coefficients (v_n), obtained by a Fourier expansion of the azimuthal (ϕ) spectrum:

$$\frac{dN}{d\phi} \propto 1 + 2 \sum_n v_n \cos [n(\phi - \Psi_n)], \quad (\text{IV.I8})$$

with Ψ_n the symmetry plane of the n th harmonic. For a hydrodynamical expansion, it has been shown that v_2 and v_3 are proportional to the initial state eccentricity in the corresponding harmonic, $v_n \propto \epsilon_n$, to a very good approximation [67], with the constant of proportionality depending on the properties of the QGP transporting the initial state anisotropy to the final state. A similar relation may be expected when a pressure gradient is obtained without a thermalized or hydrodynamized plasma [22, 68]. In the following, the eccentricities will therefore be taken as a proxy for flow observables, noting that the model imposed for the response may deviate from this linear scaling behavior. In pp and pA collisions this type of behavior becomes very apparent, due to the dominance of non-flow effects,³ in particular at small event multiplicities. Non-flow mechanisms aside, it is clear that no matter what the actual response is, measurable observables will be affected by large deviations in predicted eccentricities.

We follow the usual definition of the initial anisotropy or participant eccentricity [69, 70]:

$$\epsilon_n = \frac{\sqrt{\langle r^2 \cos(n\phi) \rangle^2 + \langle r^2 \sin(n\phi) \rangle^2}}{\langle r^2 \rangle}. \quad (\text{IV.19})$$

Here r and ϕ are usual polar coordinates, with the origin shifted to the center of the distribution. From eq. (IV.19), higher order cumulants can be calculated:

$$\epsilon_n^2\{2\} = \langle \epsilon_n^2 \rangle, \quad (\text{IV.20})$$

$$\epsilon_n^4\{4\} = 2\langle \epsilon_n^2 \rangle^2 - \langle \epsilon_n^4 \rangle, \quad (\text{IV.21})$$

$$4\epsilon_n^6\{6\} = \langle \epsilon_n^6 \rangle - 9\langle \epsilon_n^4 \rangle \langle \epsilon_n^2 \rangle + 12\langle \epsilon_n^2 \rangle^3, \quad (\text{IV.22})$$

$$33\epsilon_n^8\{8\} = 144\langle \epsilon_n^2 \rangle^4 + 18\langle \epsilon_n^4 \rangle^2 + 16\langle \epsilon_n^6 \rangle \langle \epsilon_n^2 \rangle - 144\langle \epsilon_n^4 \rangle \langle \epsilon_n^2 \rangle^2 - \langle \epsilon_n^8 \rangle. \quad (\text{IV.23})$$

In nuclear collisions, the normal participant nucleon eccentricity is used as a baseline. The notion of “participating” is, however, a model dependent statement. We use the definition from ANGANTYR [35, 36], which defines participating nucleons as either “inelastically” or “absorptively” (inelastic non-diffractively) wounded, see appendix II for a brief review. For pp collisions, and for fluctuations in nuclear collisions, we follow Avsar *et. al.* [25], and define a participant *parton* eccentricity (though somewhat modified from the cited exploratory work). Assuming that the hydrodynamic evolution takes place at the end of the perturbative parton cascade, the participant parton eccentricity should be evaluated at this point in the evolution. In section 6.1 this participant parton eccentricity will be compared to a more purist initial state approach, where the final state parton cascade is not included. This is meant to inform a discussion about what the notion of an “initial state” really ought to entail.

Parton level eccentricities are, however, not infrared safe. Consider the simple example of a soft gluon emission at the same impact parameter point as its mother. Such an emission

³Including correlations from jets and due to particle decays.

will double count this spatial point at parton level, but disappear after hadronization, which will place two such partons inside the same hadron. To improve this, all contributions are weighted by a factor $p_{\perp}/(p_{\perp} + p_{\perp\min})$, where $p_{\perp\min} = 0.1$ GeV ensures that considerably soft gluons will not double count.

Normalized symmetric cumulants will also be studied. Such quantities eliminate the dependence on the magnitude of the flow coefficients, and should thus remove the response factor between flow harmonics and eccentricities, and directly probe the substructure [71]. They are defined as:

$$NSC(n, m) = \frac{\langle v_n^2 v_m^2 \rangle - \langle v_n^2 \rangle \langle v_m^2 \rangle}{\langle v_n^2 \rangle \langle v_m^2 \rangle} \approx \frac{\langle \epsilon_n^2 \epsilon_m^2 \rangle - \langle \epsilon_n^2 \rangle \langle \epsilon_m^2 \rangle}{\langle \epsilon_n^2 \rangle \langle \epsilon_m^2 \rangle}, \quad (\text{IV.24})$$

where the last approximate equality indicates the removal of the response. Especially interesting for this study is $NSC(3, 2)$, it being sensitive to initial-state fluctuations, namely the geometric correlation between ϵ_2 and ϵ_3 , the elliptical and triangular parts of the Fourier expansion.

Finally it is noted that, since the model is implemented in a full event generator able to generate full final states for pp, pA and AA collisions, it is possible to investigate the event geometry as a function of final state multiplicity with the same acceptance as the experiment.

4 Monte Carlo implementation

In this section, the Monte Carlo implementation of Mueller's model is briefly described. The full details are given in appendix 10. First, the details of the various initial states are described, then some assumptions on the cascade and the interaction are described, and lastly, some geometric properties of the evolution are presented.

4.1 The initial states

The new implementation is applicable for both virtual photon and proton beams. A photon state is represented by a single dipole, with a wave function given as,

$$|\psi_L(z, r)|^2 = \frac{6\alpha_{\text{em}}}{\pi^2} \sum_q e_q^2 Q^2 z^2 (1-z)^2 K_0^2 \left(\sqrt{z(1-z)} Qr \right) \quad (\text{IV.25})$$

$$|\psi_T(z, r)|^2 = \frac{3\alpha_{\text{em}}}{2\pi^2} \sum_q e_q^2 Q^2 [z^2 + (1-z)^2] z(1-z) K_1^2 \left(\sqrt{z(1-z)} Qr \right), \quad (\text{IV.26})$$

where we include the three lightest (massless) quarks. Here z is the longitudinal momentum fraction carried by the quark, $(1 - z)$ the longitudinal momentum fraction carried by the anti-quark, r is the distance between them, Q^2 the photon virtuality and K_i the modified Bessel functions. For protons, the wave function is not known. In stead it is represented by three dipoles in an equilateral triangle configuration and normalized to unity. The lengths of the initial dipoles are allowed to fluctuate on an event-by-event basis, chosen from a Gaussian distribution with mean r_0 , and width r_w .

4.2 The dipole evolution

To implement eq. (IV.1) as a parton shower, it is modified by a Sudakov factor:

$$\begin{aligned} \frac{d\mathcal{P}}{dy d^2\vec{r}_3} &= \frac{N_c \alpha_s}{2\pi^2} \frac{r_{12}^2}{r_{13}^2 r_{23}^2} \exp \left(- \int_{y_{\min}}^y dy d^2\vec{r}_3 \frac{N_c \alpha_s}{2\pi^2} \frac{r_{12}^2}{r_{13}^2 r_{23}^2} \right) \\ &\equiv \frac{N_c \alpha_s}{2\pi^2} \frac{r_{12}^2}{r_{13}^2 r_{23}^2} \Delta(y_{\min}, y), \end{aligned} \quad (\text{IV.27})$$

allowing for a trial emission from each dipole in the cascade. The strategy of “the winner takes it all” is then employed, such that only the trial emission with the lowest rapidity is chosen as a true branching. This lowest rapidity then becomes the minimal rapidity in the next (trial) emission. The process is reiterated until none of the trial emissions are below a maximal rapidity, governed by the energy of the collision,

$$\text{pp} : \quad y_{\max}^p = \log \left(\frac{\sqrt{s}}{m_p} \right), \quad (\text{IV.28})$$

$$\gamma^* p : \quad y_{\max}^{p,\gamma^*} = \log \left(\frac{W}{m_0} \right), \quad (\text{IV.29})$$

with m_p the proton mass, m_0 a reference scale set to 1 GeV, and W, \sqrt{s} the γ^*p and pp center-of-mass (CM) energies, respectively. Note that eq. (IV.29) is an approximation to the actual rapidity available for the dipole formed by a virtual photon. The “true” rapidity is not well-defined for virtual photons, as it depends not only on W , but also on Q^2 and momentum fractions carried by the quark and anti-quark ends of the dipole. This introduces different rapidity ranges available for either end of the dipole, complicating the evolution further. Equation (IV.29) was chosen as the simplest possible rapidity range.

If confinement is taken into account (as described in section 2.4), the evolution equation is modified accordingly:

$$\frac{dP}{dy d^2\vec{r}} = \frac{N_c \alpha_s}{2\pi^2} \frac{1}{r_{\max}^2} \left[\frac{\vec{r}_{13}}{|\vec{r}_{13}|} K_1(|r_{13}|/r_{\max}) - \frac{\vec{r}_{23}}{|\vec{r}_{23}|} K_1(|r_{23}|/r_{\max}) \right]^2 \Delta(y_{\min}, y), \quad (\text{IV.30})$$

Table IV.1: The input parameters used in this section.

Parameter	Value	Meaning
r_0 [fm]	1.	Mean of normally distributed initial dipole sizes
r_w [fm]	0.	Width of normally distributed initial dipole sizes
r_{\max} [fm]	1.	Maximally allowed dipole size (confined evolution only)
α_s	0.21	Value of fixed strong coupling

with K_1 the modified Bessel functions of the first kind and r_{\max} a maximal radius of the initial dipole, left as a tunable parameter.

4.3 Geometric properties of the dipole evolution

Given a specific parameter set, table IV.1, the probability distribution in rapidity for the first emission, dP/dy , is shown in figure IV.2. This distribution has a mean at around two units of rapidity. Thus, on average, a new emission is assigned a rapidity of roughly two units larger than the mother (or emitter) dipole. It is worth noting that the inclusion of confinement effects slightly increases the mean as compared to the unconfined distribution. This is caused by the additional suppression of large dipoles, requiring large dipoles to be discarded in the evolution and an emission at a larger rapidity to be tried.

In each step of the dipole evolution a mother dipole is split into two daughters. Figure IV.3 shows the distribution in sizes of the smaller and larger dipole, scaled w.r.t. their mothers' size for three different evolutions ($y_{\max} = 4, 8, 12$). Here, it is evident that on average the larger dipole retains the size of the mother, while the distribution of the smaller is much broader. At lower y_{\max} there is a bump in the distribution at around 30-40% of the mothers size, while this bump is less pronounced at larger maximal rapidity.

Figure IV.4 shows the corresponding average and standard deviation in the lengths of all the daughter dipoles scaled w.r.t. the length of their mothers', as a function of maximal rapidity of the evolution. As stated above, it is clear that while the larger of the two daughter dipoles can be taken to be identical to the mother dipole, the size of the smaller dipole has larger fluctuations. The average size of the smaller dipole is, however, fixed at roughly a third of the mother dipole for all y_{\max} .

After a full evolution, an initial proton consisting of three dipoles will have evolved to a larger set of dipoles of mostly smaller sizes than the initial dipoles, cf. figure IV.5. From these two figures it is evident that the effect of confinement plays a large role in the evolution, effectively reducing the number of large dipoles in the final configuration. Thus, as $\sigma_{\text{dip}} \sim r^2$, confinement is expected to play a large role when evaluating the cross sections. Confinement also introduces more activity – or hot spots – around the endpoints of the dipoles.

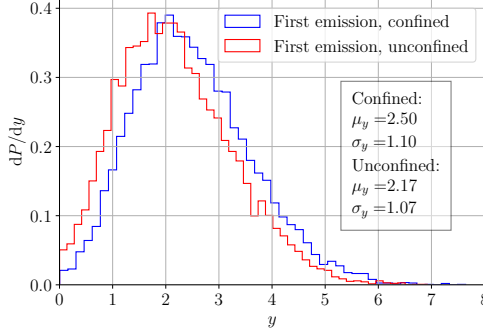


Figure IV.2: The probability distribution in rapidity for unconfined (a) and confined (b) dipole-evolution. The box shows the average and spread of the distributions.

4.4 Pascal approximation for dipole evolution

The full dipole evolution can be approximated based on the geometric observation above. On average one dipole splitting happens per two units of rapidity, and the lengths of the two resulting dipoles after the splitting, are approximately equal to and one third the size of the mother dipole respectively. This behavior is tabulated in table IV.2 for four generations of evolution. Similar results have been observed within the DIPSY framework, although their dipole swing slightly increases the size of the smaller dipole in a branching [72] to half of the size of the mother dipole.

The number of dipoles in table IV.2 follows the coefficients of the binomial theorem, with the number in column n row k being equal to $\binom{n}{k}$, and can thus be arranged to form Pascal's triangle. The total number of dipoles after a given number of generation, as well as the number of dipoles of a certain size, can be quickly approximated this way. Knowing the positions of the initial dipoles and the emitted dipole sizes, positions of all dipoles can also be inferred.

To exploit further these simple relations in the dipole evolution, we have created an alternative toy-model denoted the Pascal approximation. Here, the step size in rapidity (Δy) and the size of the smaller dipole ($r_s = fr_m$) in a branching are implemented as tunable parameters, with r_m the size of the mother dipole and f a tunable fraction. The number of steps taken in total is calculated from the step size, $N_{\text{steps}} = y_{\text{max}}^b / \Delta y$ with $b = p, \gamma^*$ and y_{max} given in eqs. (IV.28–IV.29). To mimic the recoil effects in the full dipole evolution, a Gaussian smearing of the daughter lengths is introduced with mean $\mu = r_m, r_s$ for the larger and smaller daughters, respectively. Knowing the lengths of the mother and daughter dipoles, they are placed in transverse space by calculating the angles of the triangle spanned by the endpoints of the three (connected) dipoles.

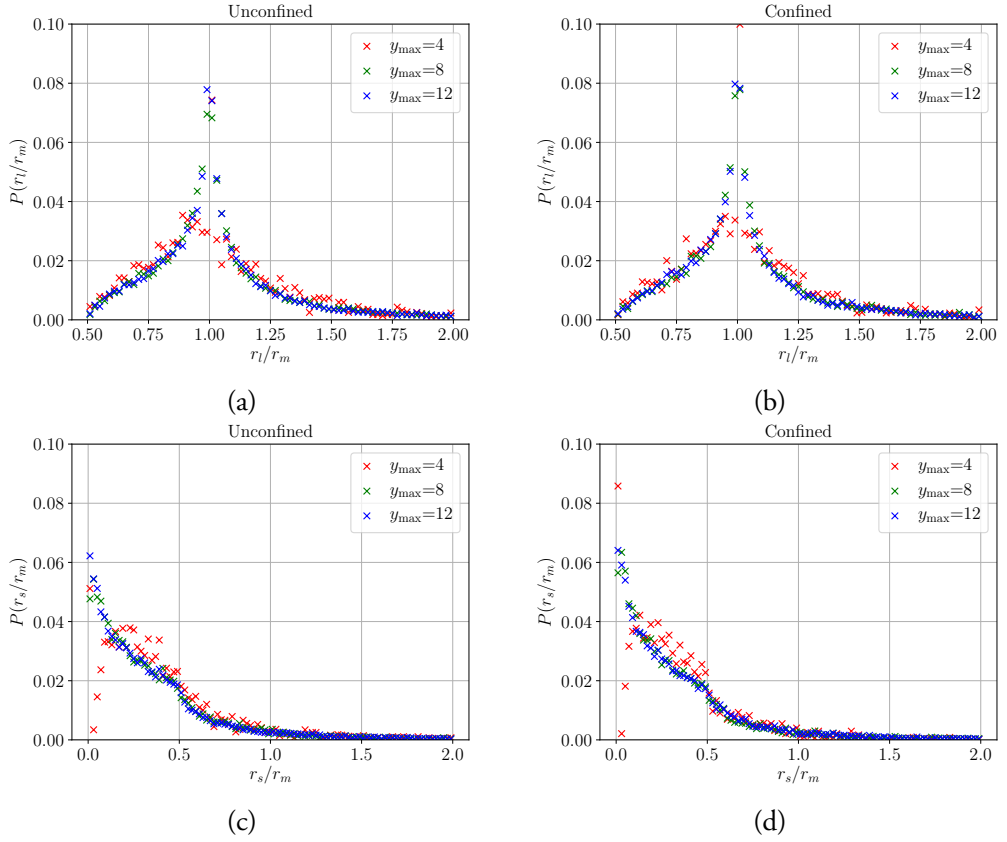


Figure IV.3: The scaled lengths of the daughter dipoles w.r.t. the mother dipole as a function of maximal rapidity for unconfined (a,c) and confined (b,d) dipole-evolution. Figures (a,b) shows the larger of the daughter dipoles, while figures (c,d) shows the smaller of the daughter dipoles. The parameters used in the dipole evolution are the same as presented in table IV.1.

This simple approximation is useful for introducing toy-models for confinement and saturation effects, as basic quantities like total number of dipoles after a given evolution, can be calculated analytically. A crude model for saturation (and to some degree confinement) based on the arguments of a saturation length ($r_s \sim 1/Q_s$) given in section 2.2, is introduced by requiring the length of the emitted dipoles to not exceed a tunable maximally allowed cutoff, r_{\max} . If this occurs, the branching is discarded and the next step in rapidity is tried. Once the full evolution has occurred, each of the dipoles are allowed to interact using the dipole-dipole scattering amplitude given in eq. (IV.9) (or eq. (IV.31) for the confined version).

In fig IV.6(a) the average number of dipoles in a single proton after a full evolution to maximal rapidity y is shown. The same parameters as given in table IV.1 are used, while the parameters $f, \Delta y$ are extracted from figures IV.2 and IV.3. It is evident that the Pascal model

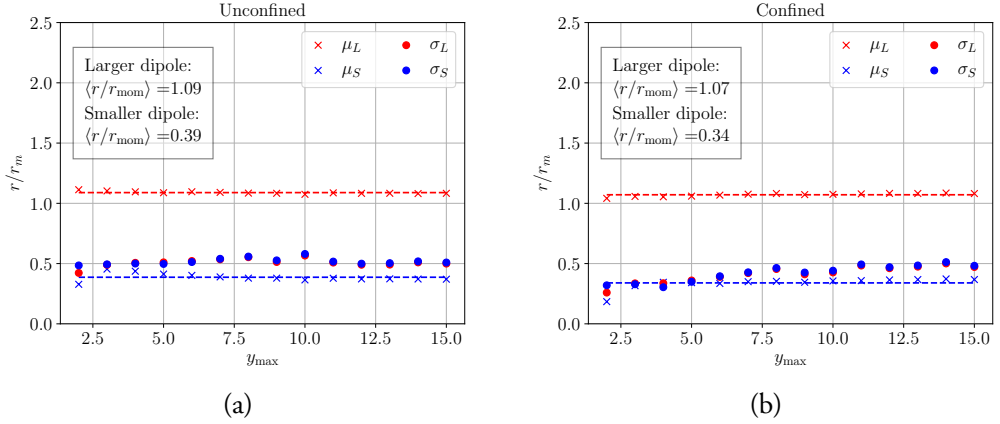


Figure IV.4: The scaled lengths of the daughter dipoles w.r.t. the mother dipole as a function of maximal rapidity for unconfined (a) and confined (b) dipole-evolution. The parameters used in the dipole evolution are the same as presented in table IV.1.

has a different slope than the full dipole model, with the effect of the crude saturation model introduced clearly seen at large y_{\max} . Here, the Pascal model results in a smaller average number of dipoles as compared to the full dipole model. As the most direct effect of sub-leading color effects is removal of soft (low p_{\perp} corresponding to large r) gluons in the high energy limit, this is what is expected. When pp cross sections are studied in section 5.2, we will use this toy model to investigate whether inclusion of saturation effects is necessary.

In figure IV.6 (b) the dipole configuration of an evolved proton for $y_{\max} = 8.86$ is shown. This has more features in common with full, unconfined dipole evolution than full, confined dipole evolution, with dipoles being more randomly distributed, than focused around hot spots.

A practical advantage of the Pascal approximation, besides being a toy model for testing approaches to saturation, is its computational speed. For simple cascade-quantities like numbers of dipoles, results can be calculated analytically. With inclusion of geometry, event-by-event results can be generated approximately a factor of 1000 faster, for large maximal rapidity ($y_{\max} \geq 10$). It thus serves as a decent replacement for the full dipole evolution model for calculation of cascade properties with limited computational resources. For full calculations of amplitudes and cross sections, the efficiency gain is not nearly as large, as in that case the bottleneck is the calculation of all f_{ij} in eq. (IV.9).

4.5 Dipole-dipole interactions

The dipole-dipole interactions are defined to occur at rapidity zero and given by eq. (IV.9). If confinement is introduced in the splitting kernel (eq. (IV.30)), one also has to change

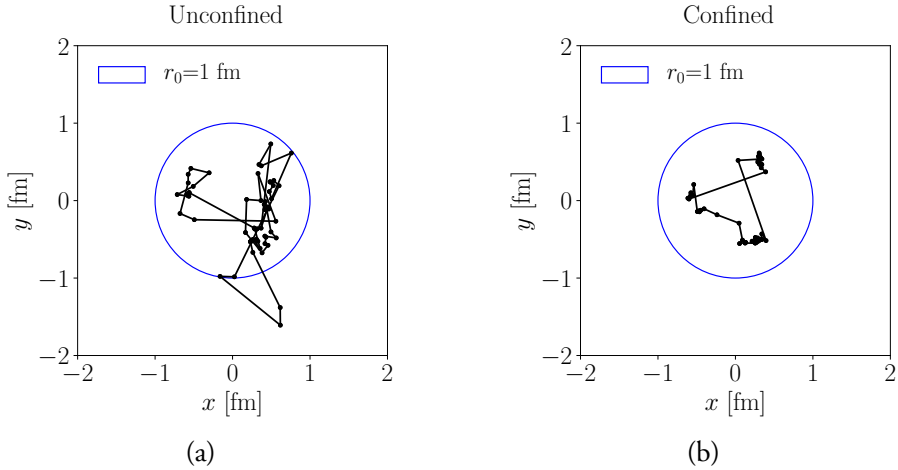


Figure IV.5: An initial state proton consisting of three dipoles in an equilateral triangle configuration after a full evolution at 7 TeV (corresponding to $y_{\text{max}} = 8.86$). (a) has been evolved without confinement, while (b) has been evolved with confinement. The parameters of table IV.1 have also been applied in this evolution.

the interaction probability in order to make the event generation consistent. This modifies eq. (IV.9) to

$$f_{ij} = \frac{\alpha_s^2}{2} \left[K_0 \left(\frac{r_{13}}{r_{\text{max}}} \right) + K_0 \left(\frac{r_{24}}{r_{\text{max}}} \right) - K_0 \left(\frac{r_{14}}{r_{\text{max}}} \right) - K_0 \left(\frac{r_{23}}{r_{\text{max}}} \right) \right]^2, \quad (\text{IV.31})$$

where K_0 is the modified Bessel function and r_{max} the maximally allowed size for a dipole in the evolution.

The choice of collision frame, however, is not trivial. Obviously, no observables should depend on the frame-choice of the collision. In practice, the choice does matter, as no sub-leading color corrections are included in the dipole evolution. Previous studies have shown that for symmetric systems, e.g. pp collisions, the optimal frame choice is the center-of-mass (CM) frame [73]. This is also utilized in our approach, cf. eq. (IV.28), where both beams are evolved the same distance in rapidity. In asymmetric systems, such as γ^*p or pA systems, the CM frame lies more towards the heavier of the two objects, and it has been previously argued that the optimal frame here would be the rest frame of the heavier beams [73]. This, however, is not the choice we have taken. The maximal rapidity chosen in eq. (IV.29) is found in what we call the center-of-rapidity frame. Here, both beams are evolved the same distance in rapidity, similarly to what is chosen in symmetric collision systems. As already stated, this work does not attempt to include sub-leading color effects in the evolution, thus frame-independence is not possible to obtain. Hence the simplest choice has been made to use the same frame for all systems, i.e. the center-of-rapidity frame given in eqs. (IV.28–IV.29).

Table IV.2: Approximate behavior of dipole evolution for four generations of dipoles. The number of dipoles in column n row k is equal to the binomial coefficient $\binom{n}{k}$.

	$y = 0$	$y = 2$	$y = 4$	$y = 6$	$y = 8$
r	1	1	1	1	1
$r/3$	0	1	2	3	4
$r/9$	0	0	1	3	6
$r/27$	0	0	0	1	4
$r/81$	0	0	0	0	1
N_{dip}	1	2	4	8	16

4.6 Assigning spatial vertices to MPIs

In order to utilize the formalism developed so far in real pp, pA and AA events, the dipole cascade is matched to the PYTHIA 8 MPI model [74]. This allows for evaluation of geometric initial state quantities, such as eccentricities (see section 3.2), at fixed number of charged hadrons in the final state, using a similar definition of charged particles as the experiments. The PYTHIA 8 MPI model considers pp collisions, treating all partonic sub-collisions as separate $2 \rightarrow 2$ QCD scatterings, which are uncorrelated up to momentum conservation. Other factors present in the MPI model is a rescaling of the parton density between each scattering, preservation of valence quark content and a sophisticated treatment of beam remnants [75].

In the MPI framework, the sub-collisions and their kinematics are selected using the normal $2 \rightarrow 2$ QCD cross section. But since this cross section diverges at low p_{\perp} , the expression is regulated using a parameter, $p_{\perp 0}$:

$$\frac{d\sigma_{2 \rightarrow 2}}{dp_{\perp}^2} \propto \frac{\alpha_s^2(p_{\perp}^2)}{p_{\perp}^4} \rightarrow \frac{\alpha_s^2(p_{\perp}^2 + p_{\perp 0}^2)}{(p_{\perp}^2 + p_{\perp 0}^2)^2}. \quad (\text{IV.32})$$

For matching of vertices to each individual partonic sub-collision, it is also useful to note that MPIs are generated in decreasing order of p_{\perp} , starting from a (process-dependent) maximal scale. This decreasing order is generated from a Sudakov-like expression of the form:

$$\frac{d\mathcal{P}}{dp_{\perp i}} = \frac{1}{\sigma_{\text{ND}}} \frac{d\sigma}{dp_{\perp i}} \exp \left[- \int_{p_{\perp i}}^{p_{\perp}^{i-1}} \frac{1}{\sigma_{\text{ND}}} \frac{d\sigma}{dp'_{\perp}} dp'_{\perp} \right], \quad (\text{IV.33})$$

with $d\sigma/dp_{\perp i}$ given by eq. (IV.32). The impact-parameter of the collision is also taken into account in the evolution by connecting the average number of MPIs to the overlap $\mathcal{O}(b)$ of the two colliding protons. This introduces additional factors of $\mathcal{O}(b)/\langle \mathcal{O}(b) \rangle$ in eq. (IV.33) along with the need to select the impact parameter consistently.⁴ Furthermore, new partons are generated by initial- and final-state radiation.

⁴Here $\langle \mathcal{O} \rangle \equiv \int d^2\vec{b} \mathcal{O}(b) / \int d^2\vec{b} [1 - \exp(-k\mathcal{O}(b))]$, where k is constrained by the ratio of the dampened $2 \rightarrow 2$ QCD cross section in equation (IV.32) to the total non-diffractive cross section.

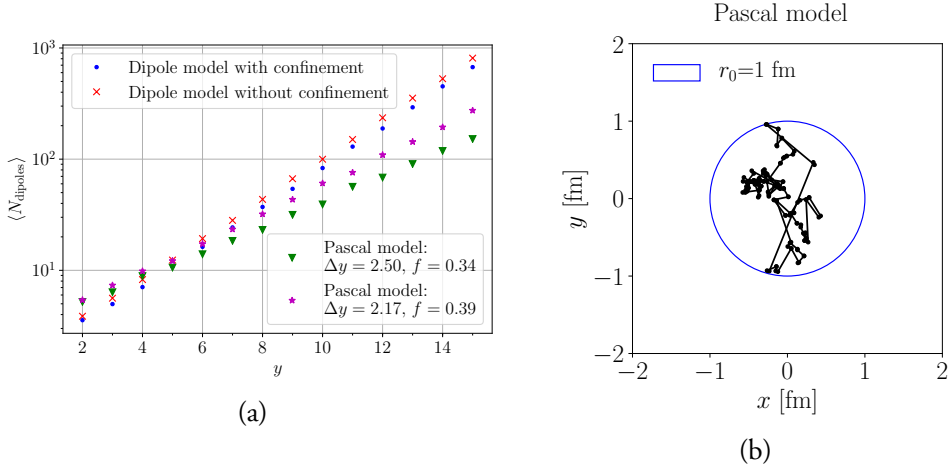


Figure IV.6: (a) The average number of dipoles inside a proton after a full evolution to maximal rapidity y . (b) An initial state proton consisting of three dipoles in an equilateral triangle configuration after a full evolution with the Pascal model at 7 TeV (corresponding to $y_{\text{max}} = 8.86$).

Recently, a method of assigning space-time information to the MPIs in PYTHIA 8 was introduced [22]. Here, the transverse coordinates are sampled from a two-dimensional Gaussian distribution defined by the overlap of the mass distributions of the two colliding protons. The width of the Gaussian is a free parameter (which should not be too far from the proton radius) and a mean equal to the impact parameter chosen in the MPI framework. Initial- and final-state radiation are then treated as small displacements of the selected anchor points of the MPIs. This introduces an additional smearing of an MPI vertex whenever a parton is radiated off from the partons involved in the MPI. The smearing is done using another Gaussian with a width of σ_{\perp}/p_{\perp} , where σ_{\perp} is a parameter with default value 0.1 GeV·fm.

Using the dipole framework to generate space-time vertices requires (as with the Gaussian model) some assumptions, as this matching can not be derived from first principles. In order to obtain a reasonable matching, the following is noted:

- Each branch of the (projectile) dipole cascade can be identified as a virtual emission, which goes on shell if, and only if, it collides with a corresponding virtual emission from the target.
- Each proton–proton collision has many *potential* sub-collisions between all combinations of virtual emissions. We order the sub-collisions in terms of contribution to total cross section, thus the MPI with largest p_{\perp} is identified with the dipole-dipole scattering with the largest f_{ij} .

The concrete matching is done by first generating two dipole cascades, and allowing them to collide with the same impact parameter used in the generation of the MPIs. This produces

a list of possible dipole–dipole collisions, each with an interaction strength f_{ij} . As the MPIs are generated (from hardest to softest), they are each assigned a vertex sampled from this list with a weight equal to f_{ij} , normalized to the summed dipole-dipole interaction strength (and *not* the unitarized interaction). The vertex is simply given as the mean of the transverse coordinates of the dipoles in the interaction. Once a set of dipoles have been assigned to an MPI, they are both flagged as used, and cannot initially be re-used to ensure a reasonable spread. In cases where the list runs out of interactions containing only unused dipoles, the dipoles are allowed to re-interact, though not with the same dipole as initially.

As opposed to the default model, vertices are now selected from a distribution which event-by-event is asymmetric, and contains "hot spots" with large activity, as shown in figure IV.5 (b) for the full evolution including confinement effects.

The matching of largest f_{ij} to hardest MPI requires further discussion, as one could argue the opposite. The dipole-dipole scattering amplitude is driven by the distances between the endpoints of the interacting dipoles, as indicated in figure IV.1. One can argue that small f_{ij} corresponds to small distances, which in turn corresponds to large p_{\perp} of the gluons emitted in the interaction. Hard MPIs would with this reasoning correspond to small f_{ij} . This is indeed the choice made in the DIPSY event generator for exclusive final states [40], but opposite to the choice made above. We do, however, also note that the exclusive final states generated by DIPSY describes p_{\perp} spectra of charged particles poorly, in particular the high- p_{\perp} part of the distributions vastly overshoots data. We therefore refrain from associating the dipole sizes directly to the p_{\perp} of emerging partons, but rather give larger attention to the cross section. We note that large f_{ij} interactions dominate the cross sections. A guiding principle is therefore to ensure that such interactions are *always* identified with an MPI, by assigning it first.

There are several possible future improvements of the matching technique. A small improvement of the existing technique, could include to also identify initial state radiation with emissions going on shell, and assign them vertices from the cascade as such. Going beyond improvement of matching techniques, would be a full re-evaluation of the MPI model, with the dipole cascade and interactions as a starting point. Instead of creating a completely new model like DIPSY, it should be possible to use the dipole model to improve the existing model. A first step would be to replace σ_{ND} in eq. (IV.33) with a dynamically calculated cross section, event-by-event. Secondly, the parameter $p_{\perp 0}$ in eq. (IV.32) could be re-evaluated in terms of the dipole model. The physical interpretation of $p_{\perp 0}$ in the MPI model, is that of a color screening scale. The perturbative treatment of eq. (IV.33) would naively break down at some minimal scale $\sim \hbar/r_p \sim \Lambda_{\text{QCD}}$, where r_p is the (color screening) size of a proton, left as a free parameter. In the dipole model, this color screening length could be identified as either the transverse size of the cascade after the evolution, or the length of the largest color connected dipole chain. In that way the energy dependence of $p_{\perp 0}$ would also come for free, instead of having to assume a power-law dependence, as

is the default assumption in PYTHIA 8.

Heavy ion collisions

The method described above can be directly applied to heavy ion collisions as they are modeled in the ANGANTYR framework for heavy ion collisions in PYTHIA 8 (see appendix 11 for a brief review, and refs. [35, 36] for a full description). In the ANGANTYR model, sub-collisions are chosen using a Glauber-like approach. Sub-collisions are in turn associated with one out of several types of pp events, depending on the properties of the sub-collision. Since all these events are generated using the MPI model described above, the generalization is only a matter of generating vertices for each sub-collision in its local coordinate system, and then moving them to the global coordinate system defined by the Glauber calculation.

5 Results I – comparing cross sections

In this section we present results on integrated cross sections for pp and γ^*p collisions. For pp we present results for both the dipole evolution model and for the Pascal model, while for γ^*p we focus our attention on the dipole model. The main purpose of this section is tuning: the model parameters have to be estimated by comparisons with data, preferably data that we do not aim to make predictions for in later sections.

It is thus not the aim of this section to be able to describe the cross sections perfectly – but more generally, to get an overall agreement between model and data, especially at LHC energies, where we aim to make predictions for the substructure observables.

More dedicated models are available to describe the cross sections at all energies, from the GeV range to the TeV range, results of which are shown alongside results from the dipole model in the pp section. The most widespread model is based on the 1992 total cross section fit by Donnachie and Landshoff (DL) [76] and the models for elastic and diffractive cross sections by Schuler and Sjöstrand (SaS) [77]. Another, more recent model by Appleby *et. al.* (ABMST) [78] is more complex than SaS, and able to describe latest LHC data better. The models are both implemented in PYTHIA 8, with some additions to the original models [79]. In this paper we compare to the original models, and not those adapted to PYTHIA 8.

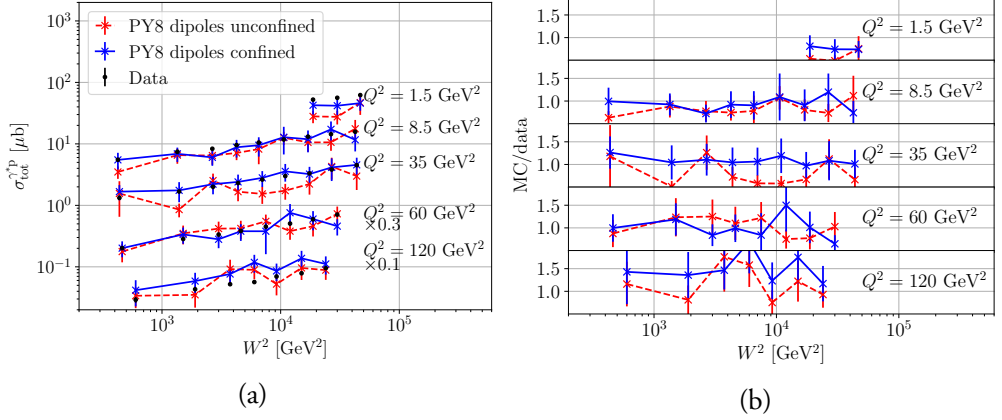


Figure IV.7: The total photon-proton cross section, $\sigma_{\text{tot}}^{\gamma^*p}$, as a function of squared photon-proton center-of-mass energy, W^2 , for several virtualities (a). Note that the distributions for the two highest virtualities ($Q^2 = 60, 120 \text{ GeV}^2$) have been scaled with a factor of 0.3, 0.1, respectively, for better visibility. (b) shows the ratio MC/data as a function of squared center-of-mass energy, W^2 , for the five different virtualities.

5.1 Results for γ^*p

We begin with the results on photon-proton total cross sections. Here, we compare the dipole evolution model to data obtained from H1 [80] at different energies and virtualities. We note that the photon wave function implemented only includes the three lightest quarks, and none of the vector meson states present at low Q^2 . Thus we expect the results to be less precise at low virtualities, where the probability for the photon to fluctuate into a hadronic state becomes non-negligible. Similarly, the masses of the quarks should be taken into account if the argument of the Bessel functions become close to the squared quark masses, i.e. if

$$z(1-z)Q^2 \simeq m_q^2 \quad (\text{IV.34})$$

occurring in the limits $z \rightarrow 0, 1$ or if Q^2 small. The contribution from c -quarks are neglected for simplicity, the uncertainty arising from this approximation is discussed at the end of the section.

The H1 data presents results on the proton structure function $F_2(x, Q^2)$ at a large range of virtualities and energies. This is translated into a photon-proton total cross section as follows:

$$\sigma_{\text{tot}}^{\gamma^*p} = \frac{4\pi^2\alpha_{\text{em}}\hbar^2 c^2}{Q^2} F_2(x, Q^2) \quad (\text{IV.35})$$

with the CM energy given as $W^2 = Q^2(1-x)/x$ and $\hbar c$ a unit conversion factor.

Table IV.3: The parameter values obtained when tuning to the $\sigma_{\text{tot}}^{\gamma^*p}$ data set and the χ^2 obtained for the two models.

Parameter	γ^*p	
	unconfined	confined
r_0 [fm]	1.08	1.15
r_{max} [fm]	-	3.50
r_w [fm]	0.10	0.10
r_{max}^* [fm]	2.07	2.56
α_s	0.21	0.22
χ^2/N_{dof} (shown Q^2 values)	2.41	0.57
χ^2/N_{dof} (full H1 data set)	2.99	1.98

It is evident from figure IV.7 that we undershoot data at low Q^2 . At intermediate virtualities the model does a fairly good job, while at the highest virtuality probed the prediction overshoots data with roughly 50%. In order to quantify the performance of the models, a χ^2 test has been performed, taking into account the errors of the measurement:

$$\chi^2 = \sum_{i=W^2} \frac{(D[W^2] - M[W^2])^2}{\sigma_{D[W^2]}^2 + \sigma_{M[W^2]}^2} \quad (\text{IV.36})$$

with D denoting the cross section measured in data at a given squared energy W^2 , M the model prediction for that squared energy and $\sigma_{D,M}^2$ the variance of the data and model predictions, respectively.

The model has been tuned with the PROFESSOR2 framework [81], and the parameters are shown along with the χ^2/N_{dof} in table IV.3. The parameters of the tune are reasonable, giving a initial dipole size roughly of order 1 fm with a width of the Gaussian fluctuations at around 0.1 fm. Adding confinement allows for a slightly larger initial dipole size, as the largest dipoles in the evolution will be suppressed as compared to the unconfined model, while also the upper integration limit on the photon is allowed to increase when turning on confinement. The width of the fluctuations and the strong coupling appear not to be affected by the confinement effect. Taking the full H1 data set into account, the confined model gives a reasonable χ^2/N_{dof} , and performs slightly better than the unconfined model.

Since the charm contribution to the γ^*p cross section has been neglected, an assessment of the uncertainty arising from this approximation should be made. Adding massless charm quarks shifts the total γ^*p cross section upwards by 67%, estimated by the ratio:

$$\frac{e_u^2 + e_d^2 + e_s^2 + e_c^2}{e_u^2 + e_d^2 + e_s^2} - 1 = 4/6. \quad (\text{IV.37})$$

This rise in cross section can be tuned away in a way similar to the procedure described above. Adding quark masses (lighter quark masses neglected) reduces the contribution. The reduction is larger for smaller Q^2 . The quantitative effect of adding masses was studied

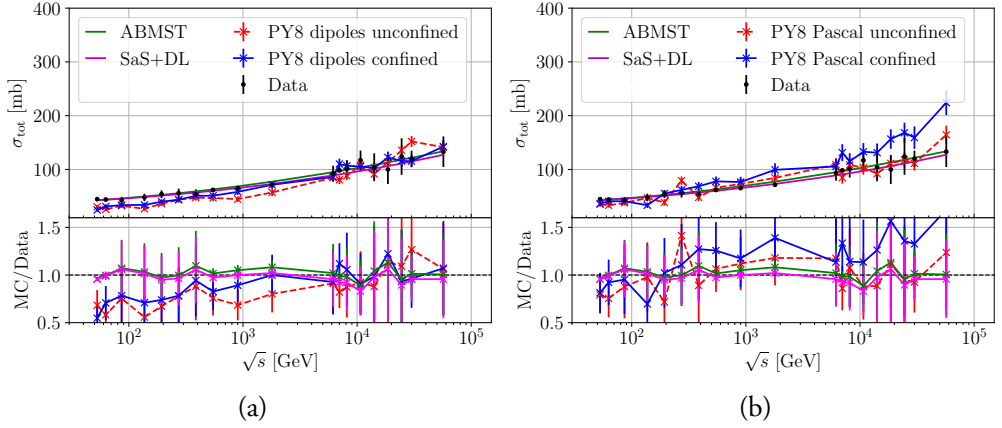


Figure IV.8: The total pp cross section as a function of \sqrt{s} for the dipole (a) and Pascal (b) models. Both show the confined and unconfined versions in solid blue and dashed red lines, respectively. Both figures show the ABMST (solid green lines) and SaS+DL (solid magenta lines) for comparison.

in ref. [72]. For small Q^2 the decrease compared to the massless charm case is $\sim 15\%$ and for large Q^2 the decrease is $\sim 40\%$. Both represent untuned values. A conservative, untuned estimate of the uncertainty in figure IV.7 from neglecting (massive) charm quarks is therefore up to $\sim 25\%$. Retuning will allow for shifting the cross section upwards in the low Q^2 region where the values in figure IV.7 undershoots, improving the overall agreement.

5.2 Results for pp

In figure IV.8 we show the total cross section as a function of CM collision energy for both the full dipole model (a) and the Pascal model (b). Both figures show results using the confined (solid blue lines) and unconfined (dashed red lines) models as well as the ABMST (solid green lines) and SaS+DL model (solid magenta lines). It is evident that the full dipole model undershoots data at low \sqrt{s} , whereas it agrees with data at roughly $\sqrt{s} \geq 10^2$ GeV, with the confined model having a smaller χ^2/N_{dof} (cf. table IV.4) than the unconfined model using only this data set. The Pascal model, figure IV.8 (b), shows an overall shift towards higher cross sections as compared to the full dipole model, thus describing the lower energies well while slightly overshooting the higher energies. With only this data set, both Pascal models have a lower χ^2/N_{dof} than the dipole models. As explained in section 4.4, the key difference between the models, is the introduction of gluon saturation by suppressing dipoles with $r > r_s \sim 1/Q_s$, thus indicating that $1/N_c^2$ suppressed saturation effects in the evolution becomes important for pp. In both figures, it is evident that both the SaS+DL and ABMST models perform better, not surprising as these models have been created to reproduce (a subset of) this data.

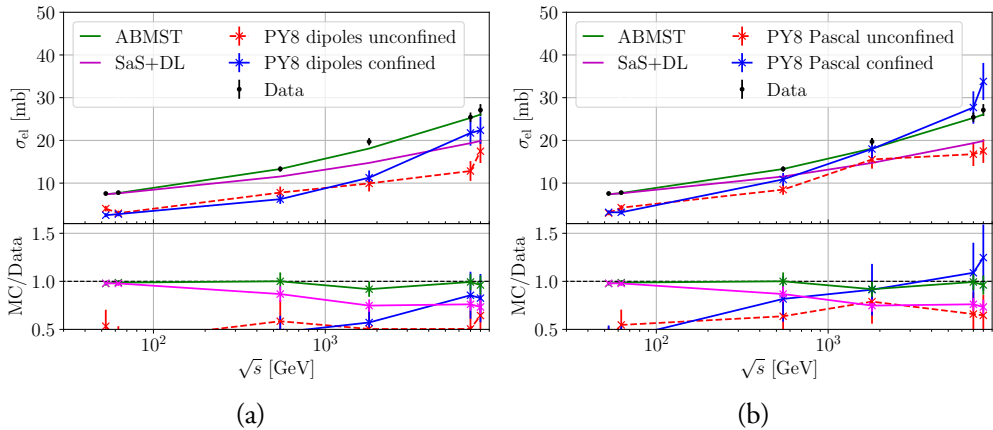


Figure IV.9: The elastic pp cross section as a function of \sqrt{s} for the dipole (a) and Pascal (b) models. Both show the confined and unconfined versions in solid blue and dashed red lines, respectively. Both figures show the ABMST (solid green lines) and SaS+DL (solid magenta lines) for comparison.

In figure IV.9 we show the elastic pp cross section for the full dipole model (a) and the Pascal model (b). Neither of the dipole models are able to describe this cross section, being roughly 50% below data in the entire energy range, except for the very last bins, i.e. at LHC energies. The Pascal model, however, agrees with data at lower energies better than the full model, again an indication towards $1/N_c^2$ suppressed saturation in the cascade being an important effect if both the total and elastic cross sections are to be described simultaneously. Also here, the two dedicated models describe the elastic data better than the dipole and Pascal models, with the SaS+DL model deviating from the data at LHC energies, while ABMST describes data in the entire energy range. This is partly due to a modification of the elastic slope in the SaS model, and partly due to the additional trajectories included in the ABMST model: where SaS+DL only contains a single Pomeron in the description of the elastic cross section, ABMST has two – along with additional terms not dominating at these energies. This of course introduces more freedom to the model, thus a better agreement with data at high energies.

The last result is the elastic slope at $t = 0$, shown in figure IV.10. Second to the total cross section, this is the most important distribution for us to describe, as this is sensitive to the internal structure of the proton, i.e. the actual impact parameter value used in the calculation, while e.g. the elastic cross section is only sensitive to the average impact parameter. Figure IV.10 again shows the results for the full dipole model (a) and the Pascal model (b). Here, both models are undershooting the data by roughly 50% in the entire energy range, except that the dipole model is able to describe data in the very last bin. Also here, the ABMST and SaS+DL models predictions are closer to the data than the dipole and Pascal models.

Also evident from figure IV.10, is that the suppression of dipoles with $r > r_s$ has little effect

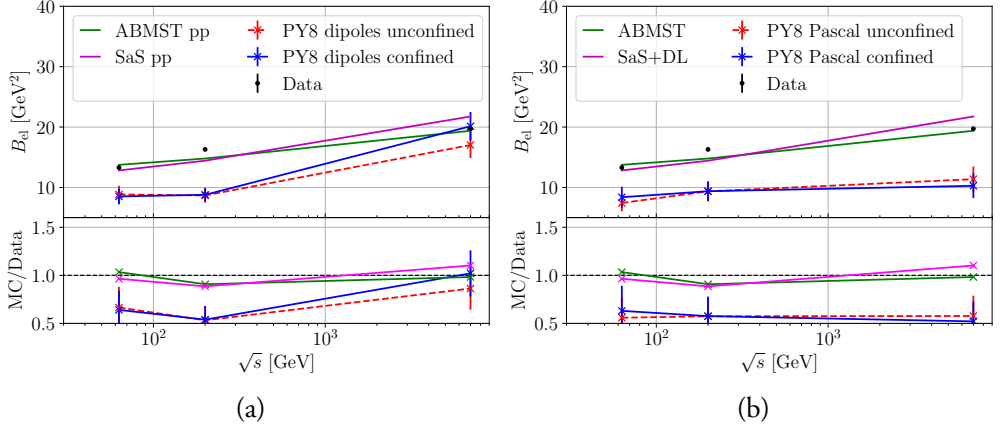


Figure IV.10: The elastic slope for pp collisions as a function of \sqrt{s} for the dipole (a) and Pascal (b) models. Both show the confined and unconfined versions in solid blue and dashed red lines, respectively. Both figures show the ABMST (solid green lines) and SaS+DL (solid magenta lines) for comparison.

for lower energies, with the effect only visible at LHC energies. Instead we expect that the introduction of a running strong coupling would aid in the description of the data. This introduction would have to appear in two places: in the dipole evolution and in the dipole-dipole scattering. A larger strong coupling in the evolution decreases the average step size in rapidity and increases the average size of the emitted dipoles, thus allowing for a larger number of larger dipoles at the end of the evolution. This, along with the increased dipole-dipole scattering cross section with increased strong coupling, would essentially increase all the cross sections, and thus also the elastic slope. The scale choice in such a running coupling would not be obvious, however, and we thus postpone the inclusion of a running coupling to future work.

The combined results on σ_{el} , σ_{tot} and the elastic slope deserves a further comment. From the optical theorem the differential elastic cross section is:

$$\frac{d\sigma_{\text{el}}}{dt} = \frac{\sigma_{\text{tot}}^2}{16\pi} (1 + \rho^2). \quad (\text{IV.38})$$

Neglecting the real part of the amplitude puts $\rho = 0$. The left hand side is often approximated by an exponential: $d\sigma_{\text{el}}/dt = \exp(B_{\text{el}} \cdot t)$, giving $\sigma_{\text{el}} = \sigma_{\text{tot}}^2 / (16\pi B_{\text{el}})$ when integrated over t . The results in figures IV.8, IV.9 and IV.10 are not in agreement with this simple proposition. This can either mean that the exponential approximation is not a good one (which is manifestly true for large $|t|$), or that B_{el} can not be adequately calculated by a Fourier transform of $T(b)$.

Table IV.4 shows the parameters obtained when tuning to all three observables (σ_{tot} , σ_{el} , B_{el}) using PROFESSOR2. We also show the χ^2/N_{dof} for three data sets of various sizes. It is striking that the inclusion of the elastic cross section to the χ^2 -calculation swaps the behavior of

Table IV.4: The parameter values obtained when tuning to the $\sigma_{\text{tot}}, \sigma_{\text{el}}, B_{\text{el}}$ data set and the χ^2 obtained for the different models.

Parameter	Full dipole model		Pascal model		ABMST	SaS+DL
	unconfined	confined	unconfined	confined		
r_0 [fm]	0.53	0.70	1.03	1.41		
r_{max} [fm]	-	3.00	3.64	2.05		
r_w [fm]	0.17	0.27	0.44	0.20		
α_s	0.24	0.22	0.18	0.14		
f_r	-	-	0.27	0.40		
Δy	-	-	2.20	2.45		
$\chi^2/N_{\text{dof}} : \sigma_{\text{tot}}$	5.22	3.34	1.31	1.94	0.28	0.41
$\chi^2/N_{\text{dof}} : \sigma_{\text{tot}}, B_{\text{el}}$	6.89	5.40	3.60	3.81	0.25	0.34
$\chi^2/N_{\text{Dof}} : \sigma_{\text{tot}}, B_{\text{el}}, \sigma_{\text{el}}$	11.21	13.67	8.09	9.08	0.20	0.46

the full dipole model – without the elastic data set, the confined model has a lower χ^2/N_{dof} than the unconfined model, while the opposite is true with the inclusion of the elastic cross section. This swap is caused by the first two data points in the elastic cross section, where the unconfined version of the full dipole describes data slightly better than the confined version. The parameters obtained with the tunes again show the behavior observed in γ^*p : adding confinement allows for an increased initial dipole size and slightly larger fluctuations around this size. The initial dipole size seems reasonable for both the confined dipole model and the unconfined Pascal model, giving sizes of the order $r_0 \sim 0.7 - 1$. fm also confirmed by DIPSY ($r_0 \sim 0.7$ fm) and proton charge radii measurements (giving roughly $r_0 \sim 0.9$ fm). Thus the unconfined dipole model seems to be giving too small initial dipole sizes and the confined Pascal model too large. This behavior is, however, balanced by the increased α_s for the unconfined dipole model and the decreased value for the confined model.

As already stated, the inclusion of a running strong coupling is expected to improve results for both the dipole and Pascal model. Saturation in the dipole cascade is also expected to have an effect, as the Pascal model in general has a lower χ^2 than the dipole model. As we currently are aiming to describe proton substructure at the TeV scale, we can, however, ignore the small deviations from σ_{tot} and B_{el} at lower energies for the moment.

6 Results II – eccentricities in small and large systems

In this section we turn our attention to predictions related to the geometry of an event. The parton-level eccentricities of both small and large systems are examined using the matching between the dipole model and the MPI framework described as in section 4.6. Results from the dipole model⁵ are shown along with the default models of PYTHIA 8: in pp collisions,

⁵We do not show eccentricities calculated using the Pascal approximation, as it is, at this point, mainly intended as a toy model for studying effects of gluon saturation from an imposed saturation scale. If the Pascal

the default scheme of PYTHIA 8 is a transverse placement according to a 2D Gaussian, while for larger systems two default PYTHIA 8 methods are available – the usual Glauber approach and the 2D Gaussian pp model extended to larger systems. In order to compare to data, all events are hadronized with PYTHIA 8 after the parton-level eccentricities are calculated. Results are presented and in a single case compared to data from ALICE [82]. Parton level eccentricities were calculated with a p_{\perp} weighting, cf. section 3.2, and events accepted if they passed the ALICE high-multiplicity trigger. Eccentricities and normalized symmetric cumulants are presented as a function of average central multiplicity ($|\eta| < 0.8$).

Recall from section 4.6 that PYTHIA 8 includes a p_{\perp} -dependent Gaussian smearing of parton vertices in the initial- and final-state shower. It is not clear from first principles whether such effects should be included in the calculation of geometric quantities or not. Consider, on one hand, creation of a QGP at early times, right after the collision. Here a parton shower will not be able to influence the geometry of the event, before a hydrodynamic response should be taken into account. On the other hand, one can imagine a system with large gradients (such as a small collision system) which will take time to hydrodynamize, and will therefore be influenced by geometric fluctuations from the final state shower as well. It is important to note, however, that no QGP is assumed in any results presented below as no QGP is assumed in neither PYTHIA 8 nor ANGANTYR.

Opening up for a discussion, we show results in figure IV.11 with and without shower. It is evident that the eccentricities are vastly affected by the models. First consider the simplest case, i.e. placing all MPIs in the proton center and not introducing any shower smearing. This gives no eccentricity as expected, cf. solid black line in figure IV.11. Symmetric distributions, such as the 2D Gaussian shower smearing and the MPI vertex assignment, should in principle give no eccentricity. But, as we are sampling only a finite number of MPIs from such symmetric distributions, an eccentricity does appear for these models, cf. dashed red and dashed black lines of figure IV.11. The two methods overlap, thus the exact same effect can be introduced with either (a) no MPI vertex assignment with a Gaussian smearing from the shower or (b) a Gaussian MPI vertex assignment and no shower smearing. That the two overlap is not so surprising as both are Gaussian smearings, and applying such a smearing during the shower or assigning it to the MPIs should make no difference: both methods give rise to a more lenticular overlap region of the two colliding protons.

Applying Gaussian smearing twice, i.e. both in the MPI vertex assignment and during the shower smears the lenticular shape from the MPI assignment slightly, thus causing the eccentricity to drop, cf. the solid red line in figure IV.11. The largest effect on the eccentricity is seen when purely considering MPI vertex assignment with the dipole model, cf. the dashed blue line in figure IV.11. The eccentricity with the dipole model is approximately twice as large as with the Gaussian model, thus indicating that event-by-event asymmetries

approximation should be used for studies of eccentricities, we should point out that the large spread in daughter sizes as seen in figure IV.4 must be incorporated, in order to provide reasonable estimates for flow fluctuations.

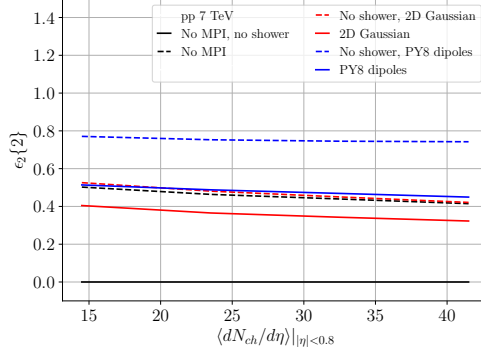


Figure IV.11: The eccentricities in pp collisions obtained with the several different options: No MPI vertex assignment and no shower smearing (solid black lines), no MPI vertex assignment, with shower smearing (dashed black lines), the 2D Gaussian MPI vertex with/without shower smearing (solid/dashed red lines, respectively) and the dipole model MPI vertex assignment with/without shower smearing (solid/dashed blue lines).

in the initial state gives rise to larger fluctuations and thus larger eccentricities. Adding the Gaussian shower smearing on top of the dipole model, solid blue line of figure IV.11, washes out some of these features – i.e. makes the almond shape of the overlap region rounder.

Figure IV.12 shows the eccentricities $\epsilon_{2,3}\{2\}$ in three different systems. Beginning with ϵ_2 we observe in pp that an asymmetric proton state gives rise to a larger eccentricity than the symmetric proton state, also shown in figure IV.11, ranging from 0.5 at low multiplicity to roughly 0.4 at higher. The same decrease is observed in the symmetric proton, albeit with eccentricities roughly 20% less than with the asymmetric state. Proceeding to larger systems, pPb and PbPb, it is evident that the same trend is seen: the dipole model gives rise to larger ϵ_2 than the symmetric model. The Glauber model, however, is consistently larger than the other two models at low multiplicity, while all three models appear to approach the same eccentricity at higher multiplicities. Thus it becomes evident that the proton initial state does have an effect on eccentricities, and that it is especially evident in low-multiplicity events, e.g. peripheral PbPb collisions.

Unfortunately, the low-multiplicity events are often marred by large non-flow effects. Measuring the eccentricities with higher-order cumulants can remove some of the contributions from non-flow, thus making it easier to compare data to models. We present results for ϵ_2 with higher-order cumulants in appendix 12, as the results are similar in shape as figure IV.12, but differ in normalization. Figure IV.12 (b) show $\epsilon_3\{2\}$ for all three systems. Here, it becomes more difficult to distinguish between the models in symmetric systems, while a large discrepancy between the Glauber approach and the other two is seen in pPb.

Another feature seen in figure IV.12 is that the dipole model gives roughly the same results for $\epsilon_{2,3}$ in both pp and pPb collisions. If one assumes that the response functions are the same for the two systems (however one may have obtained these response functions,

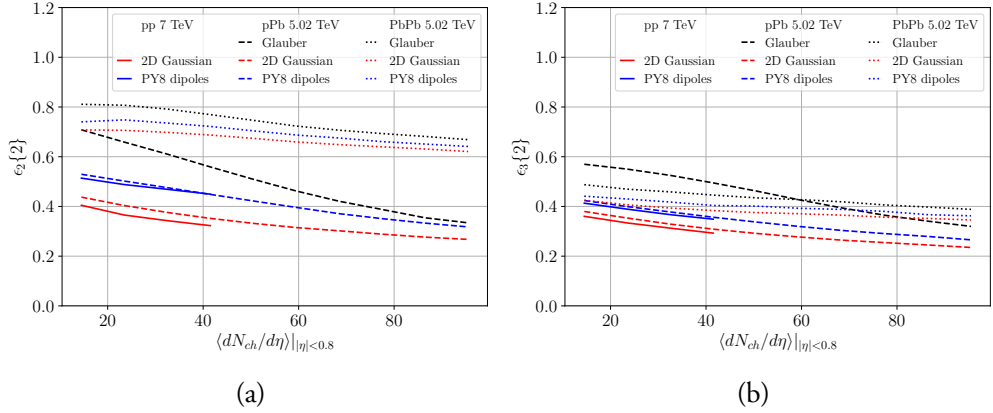


Figure IV.12: The second (b) and third (c) order eccentricities using two-particle cumulants for pp, pPb, PbPb collisions (solid, dashed, dotted, respectively) using the Glauber (black), Gaussian (red) and dipole (blue) models.

QGP or by string-string interactions), the ratio of pPb to pp eccentricities should thus be comparable to the ratio of flow coefficients measured with the ALICE detector. This ratio is shown in figure IV.13 for the second-order eccentricity. Both the Gaussian and dipole models are compatible with the ALICE data, however, so we cannot presently discriminate between the two. Additional measurements of the flow coefficients in low-multiplicity events are thus required in order to discriminate between models in this observable.

Figure IV.13 (b) shows the normalized symmetric cumulant, $NSC(3, 2)$. This has been constructed to study the correlations between the eccentricities and normalized to the uncorrelated eccentricities in order to remove the effects of the response function. ALICE reports that all three systems have the same $NSC(3, 2)$ at the same average multiplicity, indicating that the correlation between the flow coefficients are the same in different collision systems. We observe no such effect. Focusing on the dipole model, the correlations appear equal in magnitude for pp and pPb, but PbPb results are consistently below the smaller systems. Results for the Gaussian model shows no similarities at all between systems, as the pPb $NSC(3, 2)$ is positive, while pp and PbPb are negative. Thus the normalized symmetric cumulants for pPb systems would be an ideal place to discriminate between the symmetric and asymmetric initial state. PbPb results for all three models are in agreement with IP-GLASMA predictions presented in the ALICE paper. The main difference between the dipole model and the IP-GLASMA approach is the inclusion of saturation in the cascade of the latter. As the two approaches give similar results, we do not find that saturation plays a large role in this observable.

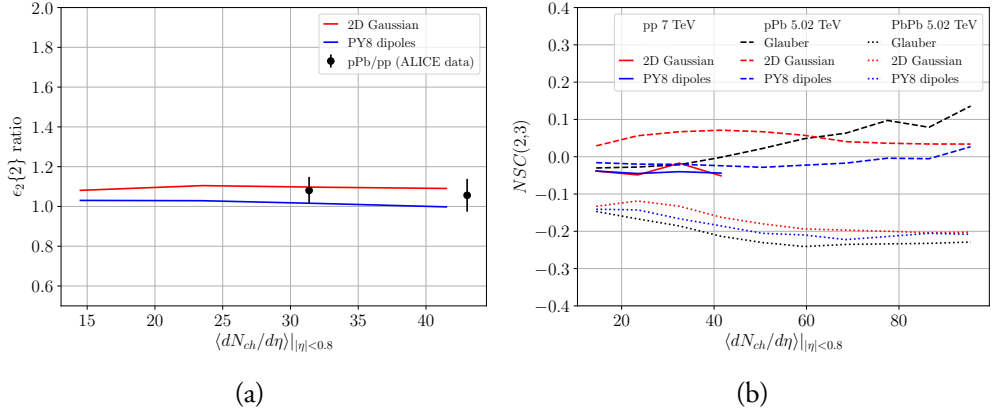


Figure IV.13: (a) The ratio of second order eccentricities obtained in pPb w.r.t. the baseline pp sample using the Gaussian (red) and dipole (blue) models. Data points calculated from ALICE figures [82]. (b) The normalized symmetric cumulants $NSC(3, 2)$ for pp, pPb, PbPb collisions (solid, dashed, dotted, respectively) using the Glauber (black), Gaussian (red) and dipole (blue) models.

6.1 Flow fluctuations in pPb collisions

Recently, CMS presented results on multi-particle correlations using higher-order particle cumulants in pPb collisions [83]. Ratios of the flow-coefficients based on these cumulants were presented, including the first measurements of the ratio of $v_3\{4\}/v_3\{2\}$ in pPb. In figure IV.14 we show the predictions for the ratios with the confined dipole model and the default Gaussian model as a function of multiplicity. Both models reasonably reproduce the shape seen in the elliptical ratio, figure IV.14 (a) showing $v_2\{4\}/v_2\{2\}$, while the normalization of the dipole model is slightly better than with the Gaussian model. For the triangular ratio, figure IV.14 (b), both models appear to undershoot data at high multiplicities, where data is available. As opposed to model predictions presented in the CMS paper [84,85], our predictions have *not* been applied a 10% *ad hoc* increase in normalization. And where the model predictions presented in [84,85] predicts roughly the same ratio for both ϵ_2 and ϵ_3 , neither the dipole nor the Gaussian model predicts the same normalization for the two ratios, cf. the height of figure IV.14 (a) and (b) differs.

Figure IV.15 shows the higher-order cumulant ratios for elliptic flow as a function of the lower-order ratio presented in figure IV.14 (a). For higher order cumulants, the Gaussian model predicts purely imaginary values for even powers of the cumulants, hence it has been left out of the figures. The dipole model, however, is able to describe data reasonably well. The dipole predictions decrease with decreasing $v_2\{4\}/v_2\{2\}$ ratio in figure IV.15 (a), while being roughly constant at unity in figure IV.15 (b). This is in accordance with the model predictions presented by CMS [86], assuming a non-Gaussian model for the initial state. We note that the eccentricities presented with the dipole model here are (a) based on a pQCD model, and (b) related to final state multiplicities calculated in the same acceptance

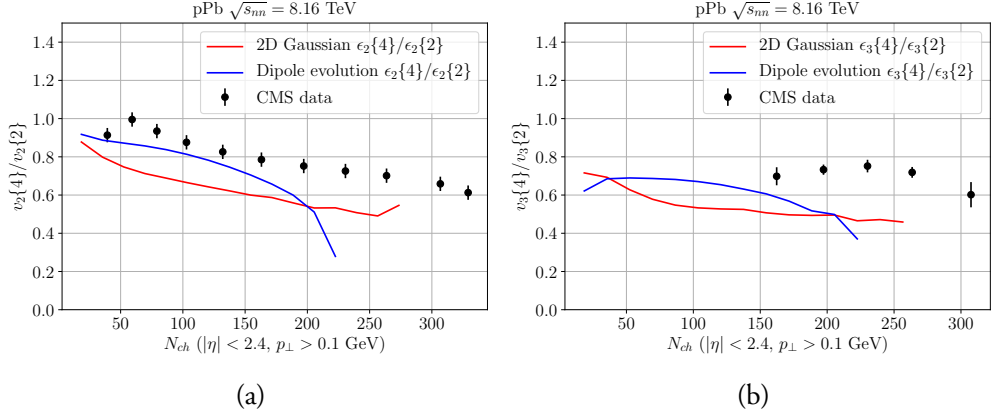


Figure IV.14: Ratios of $v_n\{4\}/v_n\{2\}$ with $n = 2$ (a) and $n = 3$ (b) as measured by CMS as function of multiplicity in pPb collisions, compared to eccentricity ratios calculated with the Gaussian and the dipole models.

as the experiment.

7 Results III – dynamic color fluctuations in Glauber calculations

A general feature of several models describing both collisions of protons and of nuclei, is the notion of interacting nucleons and nuclear sub-collisions, calculated in the formalism of Glauber [87, 88]. The basic formalism is mainly concerned with calculating the full AA scattering matrix or amplitude from knowledge of the nucleon-nucleon amplitude and spatial positions. Multiple interactions between nucleons factorize in transverse coordinates, so in the eikonal limit the S -matrix for scattering between two nuclei A and B becomes:

$$\hat{S}^{(AB)}(\vec{b}) = \prod_{i=1}^A \prod_{j=1}^B \hat{S}^{(N_i N_j)}(\vec{b}_{ij}), \quad (\text{IV.39})$$

where i and j denote the individual nucleons, \vec{b} is the nucleus–nucleus impact parameter and \vec{b}_{ij} is the nucleon–nucleon impact parameter. We will here consider the simplifying case where only one projectile (either p or γ^* , called n below) collides with a nucleus (A), which reduces eq. (IV.39) considerably:

$$\hat{T}^{(nA)}(\vec{b}) = 1 - \prod_{i=1}^A \hat{S}^{(nN_i)}(\vec{b}_{ni}) = 1 - \prod_{i=1}^A (1 - \hat{T}^{(nN_i)}(\vec{b}_{ni})). \quad (\text{IV.40})$$

If no fluctuations in the interaction are included, the projectile-nucleon elastic amplitude can be inserted, and the total and elastic cross sections can be calculated directly from

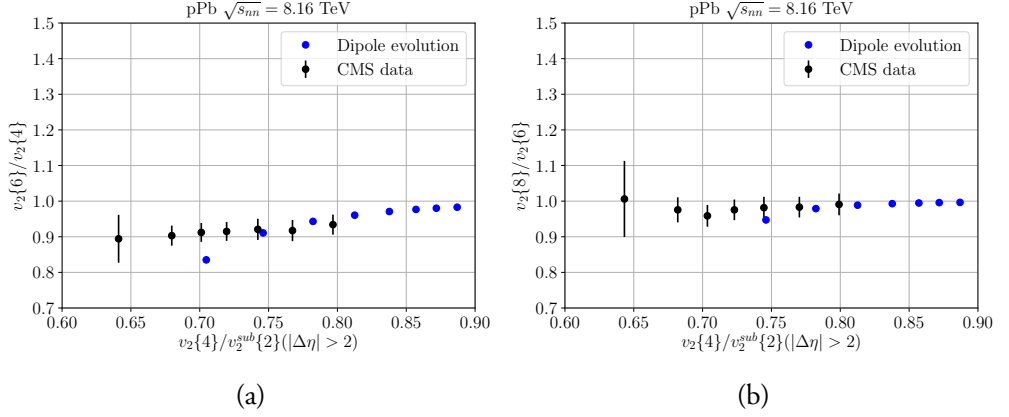


Figure IV.15: Correlations between higher order flow harmonics as measured by the CMS experiment, compared to correlations between higher order eccentricity ratios calculated in the dipole model.

eqs. (IV.14–IV.15). If fluctuations for projectile and target are included, as calculated for example in the dipole model, the amplitude will depend on the states of target (t_i) and projectile (p) respectively. As shown in section 3.1, the elastic amplitude can be calculated as an average over all states. In ref. [89] it was pointed out that in the evaluation of such an average, the projectile must remain frozen in the same state throughout the passage of the target. Similar to eq. (IV.13) the elastic profile function (at fixed Mandelstam s) for a fixed state (k) of the projectile scattered on a single target nucleon (all states) becomes:

$$\begin{aligned}\Gamma_k(\vec{b}) &= \langle \psi_S | \psi_I \rangle = \langle \psi_k, \psi_t | \hat{T}(\vec{b}) | \psi_k, \psi_t \rangle = (c_k)^2 \sum_t |c_t|^2 T_{tk}(\vec{b}) \langle \psi_k, \psi_t | \psi_k, \psi_t \rangle \\ &= (c_k)^2 \sum_t |c_t|^2 T_{tk}(\vec{b}) \equiv \langle T_{tk}(\vec{b}) \rangle_t,\end{aligned}\quad (\text{IV.41})$$

where previously suppressed indices k and t on T are spelled out for clarity. For a projectile-nucleus collision, with the projectile frozen in the state k , the relevant projectile-nucleon (nN_i) amplitude becomes:

$$\langle T_{ti,k}^{(nN_i)}(\vec{b}_{ni}) \rangle_t \equiv T_k^{(nN_i)}(\vec{b}_{ni}). \quad (\text{IV.42})$$

In the short hand notation on the right hand side, the average over the repeated index t is suppressed. This is the amplitude used to determine which nucleons are “wounded” in a collision. If the purpose is to determine which nucleons participate in the collision either elastically or inelastically, the differential wounded cross section can be calculated with the normal differential pp total cross section as an ansatz, $d\sigma_{\text{tot}}/d^2\vec{b} = 2\langle T \rangle_{p,t}$ from eq. (IV.14). Since the projectile should be frozen in the state k , the expression for T from eq. (IV.42) is inserted to the differential pp total cross section. This just recovers the normal

total projectile-nucleon cross section:

$$\frac{d\sigma_{\text{tot}}}{d^2\vec{b}} = 2\langle T_k \rangle_p = 2\langle \langle T_{t,k} \rangle_p \rangle_t = 2\langle T \rangle_{p,t}. \quad (\text{IV.43})$$

In a Monte Carlo, the number of wounded nucleons can then be generated by assigning each projectile or nucleon a radius of $\sqrt{\sigma_{\text{tot}}/2\pi}$, where the expression in eq. (IV.43) has been integrated over $d^2\vec{b}$ to give σ_{tot} . Normally one is not interested in the number of wounded nucleons including elastic interaction, but rather those that contribute to particle production (i.e. where there is a color exchange). A usual approach is to just use the inelastic cross section in place of σ_{tot} in the Monte Carlo recipe. This does, however, not account fully for color fluctuations, as the inelastic cross section is modified when averaging over target states with a frozen projectile. Instead of directly using the inelastic cross section in the Monte Carlo, the modified cross section should be used. This cross section was dubbed the “wounded cross section” in ref. [35], and can be constructed by generalizing the inelastic cross section, using eq. (IV.42). The inelastic cross section can from eqs. (IV.14–IV.15) be directly written down as:

$$\frac{d\sigma_{\text{inel}}}{d^2\vec{b}} = 2\langle T(\vec{b}) \rangle_{p,t} - \langle T(\vec{b}) \rangle_{p,t}^2. \quad (\text{IV.44})$$

When the frozen projectile is taken into account by inserting T from eq. (IV.42), the usual expression is now not recovered, but the average over targets must be made *before* squaring the second term:

$$\frac{d\sigma_w}{d^2\vec{b}} = 2\langle T_k(\vec{b}) \rangle_p - \langle T_k^2(\vec{b}) \rangle_p = 2\langle T(\vec{b}) \rangle_{t,p} - \langle \langle T(\vec{b}) \rangle_t^2 \rangle_p, \quad (\text{IV.45})$$

with internal indices again suppressed in the last equality. In a Monte Carlo this can be generated as above, now only by inserting σ_w in place of σ_{tot} .

Generalizing this procedure to γ^*A collisions requires additional considerations. Starting from the elastic profile function for γ^*p , a contribution from the photon fluctuating to a dipole state must be included. Examining only the hadronic (non–VMD) components of the photon state, gives:

$$|\gamma^*\rangle \sim c_1|q\bar{q}\rangle + c_2|q\bar{q}g\rangle + \text{higher order Fock states} \quad (\text{IV.46})$$

where quark helicities have been neglected. We keep only the first (leading order) term, as the higher order Fock states are included in the dipole evolution. Thus with a photon wave function given in eqs. (IV.25–IV.26), we obtain:

$$|\gamma^*\rangle = \int dz \int d^2\vec{r} (|\psi_L(z, r)|^2 + |\psi_T(z, r)|^2) |\psi_T(r, z)\rangle, \quad (\text{IV.47})$$

with $|\psi_I\rangle$ a dipole state. The elastic profile is now:

$$\begin{aligned}\Gamma_{\text{el}}(\vec{b}) &= \int dz \int d^2\vec{r} \langle \psi_S(z, \vec{r}) | \hat{T}(\vec{b}) | \psi_I(z, \vec{r}) \rangle \langle \psi_I(z, \vec{r}) | \gamma^* \rangle \\ &= \int dz \int d^2\vec{r} (|\psi_L(z, \vec{r})|^2 + |\psi_T(z, \vec{r})|^2) \langle T(\vec{b}) \rangle_{p,t}.\end{aligned}\quad (\text{IV.48})$$

The wounded cross section for γ^*A collisions can now be defined. The first interaction is calculated using the photon wave function in the elastic profile function, leading directly to:

$$\frac{d\sigma_w}{d^2\vec{b}} = \int dz \int d^2\vec{r} (|\psi_L(z, \vec{r})|^2 + |\psi_T(z, \vec{r})|^2) (2\langle T(\vec{b}) \rangle_{t,p} - \langle \langle T(\vec{b}) \rangle_t^2 \rangle_p). \quad (\text{IV.49})$$

This first interaction has now turned to photon from a superposition of all dipole states into a single, specific dipole (or vector meson). *This* is the state that the projectile should be frozen to throughout the passage of the nucleus: the first interaction chooses a specific dipole state $|\psi_I\rangle_{z,\vec{r}}$ with given z and \vec{r} . This reduces the elastic profile function for the secondary interactions to the well known eq. (IV.13), from which a differential wounded cross section has already been calculated (eq. (IV.45)).

Thus, in a Monte Carlo, the number of wounded nucleons can be generated with the following method:

- First by selecting, for each event, a dipole with r and z corresponding to the wave function weight, w_γ in eq. (IV.85)
- Secondly, testing if any nucleons are hit including the photon wave function normalization proportional to α_{em} (i.e. according to eq. (IV.48))
- If any nucleons are hit, then subsequently testing all (other) nucleons, w.r.t. the dipole-target weight (i.e. eq. (IV.13))

In the following section, color fluctuations from the introduced dipole model (where $T(\vec{b})$ can be evaluated directly from eq. (IV.10)) are compared to a parametrized approach for fluctuations in pp collisions and γ^*p collisions, and finally for γ^*A .

7.1 Color fluctuations in pp, γ^*p and γ^*A collisions

Fluctuations in the pp cross sections, to estimate the influence of fluctuations in pA collisions, are often parametrized using [90–92]:

$$P(\sigma) = \rho \frac{\sigma}{\sigma + \sigma_0} \exp\left(-\frac{(\sigma/\sigma_0 - 1)^2}{\Omega^2}\right), \quad (\text{IV.50})$$

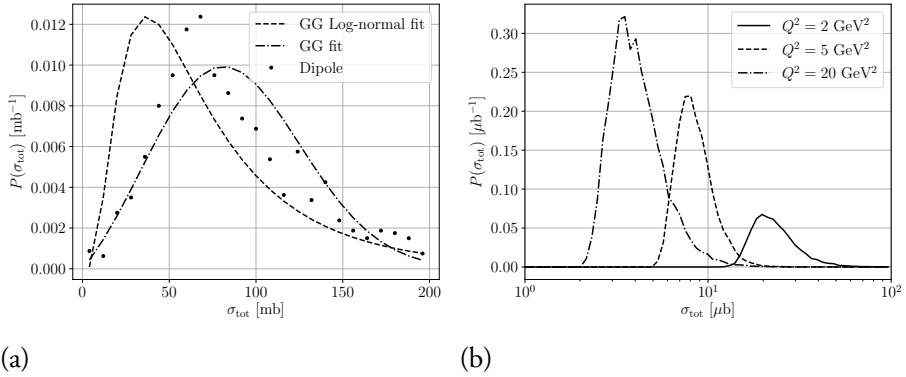


Figure IV.16: (a) Fluctuating cross section in pp at $\sqrt{s} = 5 \text{ TeV}$, compared to a GG fit (eq. (IV.50)) and a log-normal fit (eq. (IV.87)). (b) Fluctuating cross section in γ^*p at $W^2 = 5000 \text{ GeV}^2$ and various Q^2 , calculated with the dipole model (the double peak structure for $Q^2 = 20 \text{ GeV}^2$ is a statistical fluctuation). The cross section is shown on a logarithmic horizontal axis, to assess the log-normal approximation (cf. eq. (IV.87)).

where σ_0 and Ω are parameters, and ρ is a normalization constant. In ref. [35] it was found that a log-normal distribution (see eq. (IV.87) in appendix II) describes fluctuations generated by a dipole approach better. In figure IV.16 (a) both parametrizations are compared to the fluctuating total cross section in pp at $\sqrt{s} = 5 \text{ TeV}$, integrated over $d^2\vec{b}$.

While the log-normal distribution does better in capturing the skewness of the distribution, none of the two parametrizations fully describes the distribution. The problem increases in γ^*p for several reasons. First of all, any parametrization must include the correct dependence on DIS kinematics, which changes the average cross section, cf. figure IV.16 (b). Here is shown the cross section distributions for three values of Q^2 all with $W^2 = 5000 \text{ GeV}^2$ with a logarithmic first axis. This allows for a by-eye assessment of the validity of a log-normal fit, as a log-normal distribution is Gaussian with such choice of axes. It is seen directly that fluctuations in the high- σ tails are too large to be described by such a parametrization.

Instead of the parametrization approach, the wounded cross section can be calculated directly from the dipole evolution. This also allows for simultaneous calculation of both the part including electromagnetic contributions, and the pure dipole part (given z and r), as introduced in the previous section. This allows directly for a calculation of the distribution of wounded nucleons in a γ^*A collision, as shown in figure IV.17. In the figure, the nucleus is taken to be Au-197, colliding with a virtual photon with $W^2 = 5000 \text{ GeV}^2$ for a range of Q^2 values, compatible with projected EIC design [37]. Two methods of calculating wounded nucleons are presented: the full treatment using a frozen wave function, where the photon wave function has collapsed to a dipole state when probed by the first collision, and the naive black disk approach, where the photon re-forms after the full collision and no fluctuations are included. In such a treatment, the cross section for additional collisions

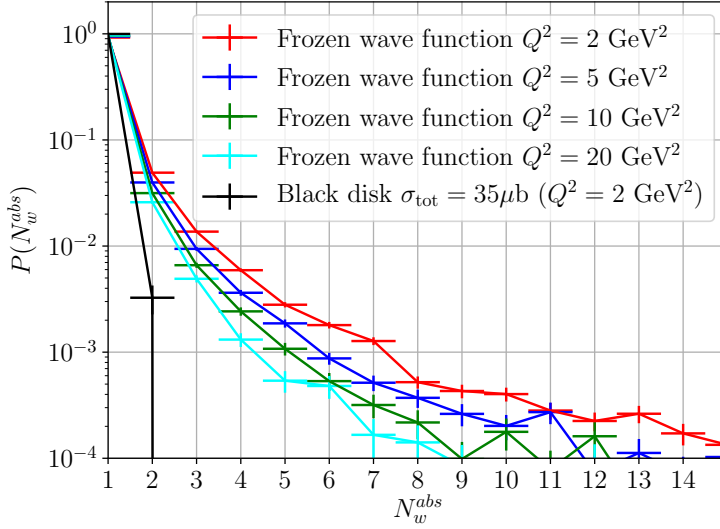


Figure IV.17: Number of wounded nucleons in a γ^* Au collision with $W^2 = 5000 \text{ GeV}^2$ and a range of Q^2 , comparing a treatment with the projectile wave function (denoted wf. in legend) frozen throughout the passage of the nucleus, to a naive black disk approach.

has an additional factor α_{em}^2 compared to the frozen treatment, from the normalization of the wave function. It is directly visible that a full treatment is necessary in order to provide reasonable phenomenological projections for a new collider.

8 Conclusion and outlook

One of the main challenges for the understanding of collective effects, is to grasp how the well-known understanding of flow results from heavy ion collisions can be transferred to collision of protons with protons and heavy nuclei. In this paper we have presented a Monte Carlo implementation of Mueller's dipole model with several sub-leading corrections, and with all parameters of the model fixed to total and semi-inclusive cross sections calculated within the Good-Walker formalism. This model thus allows for the calculation of proton substructure without tuning any model parameters to observables sensitive to said substructure.

The current implementation of the model includes:

- BFKL evolution of projectile and target states, be it protons or photons, in rapidity and impact parameter space.

- Sub-leading corrections in the evolution:
 1. Energy-momentum conservation.
 2. Non-eikonal corrections in terms of dipole recoils.
 3. Confinement effects by the introduction of a fictitious gluon mass.
- Projectile–target interactions using the unitarized amplitude, which in a Regge field theory language corresponds to multi-Pomeron exchange and Pomeron loops.
- Matching to the PYTHIA 8 MPI model, in order to assign spatial vertices to produced partons in pp collisions.
- Generalization to heavy ion collisions through the ANGANTYR framework.

Besides the implementation of the dipole model, a simpler version has been provided, based on the geometric properties of the dipole evolution. This model, denoted the Pascal approximation, allows for easy insertion of saturation toy-models, thus giving a handle on the importance of such effects. From the comparisons to the total and semi-inclusive cross sections we observe that $1/N_c^2$ suppressed gluon saturation in the cascade is important, if both the total and elastic cross sections are to be described simultaneously.

We have shown that given simple, but reasonable, assumptions of a final–state response (from e.g. hydrodynamics or interacting strings), the eccentricities produced with the implementation provides a reasonable description of flow data from the ALICE and CMS experiments. This includes non-trivial observations such as ratios between pA and pp flow coefficients at fixed event multiplicity, normalized symmetric cumulants in different systems, and ratios between different order flow harmonics in pA collisions. All are signatures which cannot be described in a simpler model, where the spatial structure of MPIs are assumed to be distributed according to a rotationally symmetric distribution. We want to stress that even though we have here chosen flow-type observables to illustrate the effect of the space-time structure of the initial state on observations of collective effects, effects linked to enhancement of strangeness and baryon production [93–95] and even modifications of jets in high multiplicity pp collisions [96, 97] are expected to be influenced as well.

Lastly, we have provided the initial steps towards the generation of fully exclusive final states in electron-ion collisions, by determining the importance of color-fluctuations in the collisions with virtual photons. We have shown that previous parametrizations from pp collisions do not fully capture the color-fluctuations predicted by the dipole formulation of BFKL evolution, and thus argue that it is better to calculate the cross sections directly from the dipole model – which has not been possible in the ANGANTYR model before this work. Secondly, we stress that the collapse of the photon wave function at first interaction

provides a larger number of wounded nucleons as compared to the black disk approximation. Each of the wounded nucleons are expected to give rise to final state activity, thus more complicated final states are expected with the proper treatment as opposed to the naive expectations.

The implemented dipole model can be improved in several ways, including:

- Running α_s in the dipole evolution and in the scattering, which will capture some of the NLO corrections in α_s .
- On longer term, an inclusion of full NLO-BK should be the goal, though further theoretical development is needed first.
- Gluon saturation effects in the cascade, which are $1/N_c^2$ suppressed, such as those included in the CGC formalism. To maintain the current treatment of the effect of gluon branchings in the cascade (as opposed to CGC), this could be included by the introduction of a simple swing mechanism, e.g. a mock $2 \rightarrow 1$ dipole recombination.
- Several improvements are expected w.r.t. the initial dipole configuration in protons and photons, as well as in the wave functions of these particles. This includes adding the VMD contribution to the photon wave function, to be able to study lower Q^2 and vector meson production in various processes.
- New ways of treating MPIs in pp collisions by fully merging the dipole approach with more traditional approaches are foreseen. It is our hope that this could provide new tools to improve understanding of particle production mechanisms across collision systems.

Detailed understanding of the interplay between the proton geometry, color suppressed saturation effects and the response of final state interactions in hadronic and heavy ion collisions, is crucial for the understanding of collectivity and particle production mechanisms. Since detailed understanding requires tools which are both accessible and transparent, it is our hope that the detailed treatment presented here, and the accompanying open Monte Carlo implementation, can help facilitate this process.

9 Acknowledgments

We thank Gösta Gustafson, Leif Lönnblad and Torbjörn Sjöstrand for several discussions during the making of this project and Gösta and Torbjörn for reading through and com-

menting on the manuscript. We also thank the ALICE group at the Niels Bohr Institute, University of Copenhagen for hospitality during the writing of this work.

This project has received funding in part from the European Research Council (ERC) under the European Union's Horizon 2020 research and innovation program (grant agreement No 668679), and in part by the Swedish Research Council, contract numbers 2016-05996 and 2017-0034 as well as the Marie Skłodowska-Curie Innovative Training Network MC-netITN3 (grant agreement 722104).

10 Appendix: The dipole model

Below we go through the details of the dipole model not included in sections 2.3 and 4.

We here work with light cone momenta,

$$p_{\pm} = E \pm p_z, \quad (\text{IV.51})$$

and can thus define the rapidity as

$$y = \frac{1}{2} \log \left(\frac{p_+}{p_-} \right) = \log \left(\frac{p_+}{p_{\perp}} \right), \quad (\text{IV.52})$$

with the latter equality valid for massless particles. Hence we can express the lightcone momenta in terms of dipole p_{\perp} and rapidity,

$$p_{\pm} = p_{\perp} \exp(\pm y). \quad (\text{IV.53})$$

The p_{\perp} of a dipole can be related to its size through $p_{\perp} \sim \hbar/r$.

The dipole-dipole scatterings are defined to occur at rapidity zero. Thus the evolution of the beams begin at rapidity $y = \pm y_{\text{max}}$ and evolve to zero, i.e. with negative rapidity steps. For technical reasons, the actual evolution is easier to implement with positive steps in rapidity. Thus the internal rapidity used in the code (and in the next section) is negated w.r.t. the rapidity defined in eq. (IV.52):

$$y_{\text{MC}} = -y = \log \left(\frac{p_{\perp}}{p_+} \right) \Rightarrow \quad (\text{IV.54})$$

$$p_{\pm} = p_{\perp} \exp(\mp y_{\text{MC}}). \quad (\text{IV.55})$$

where in the forthcoming sections we will skip the subscript MC.

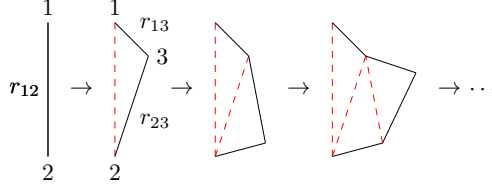


Figure IV.18: Schematic view of a dipole splitting. The initial dipole is spanned by partons 1 and 2, that emits a new parton (3), thus creating two new dipoles: the dipole spanned by partons 1 and 3 and the dipole spanned by partons 2 and 3. This can be succeeded by additional splittings as indicated by the additional figures following the arrows.

10.1 Mueller's dipole branching

We begin by examining the dipole splitting function,

$$\frac{dP}{dy d^2\vec{r}} = \frac{N_c \alpha_s}{2\pi^2} \frac{r_{12}^2}{r_{13}^2 r_{23}^2}, \quad (\text{IV.56})$$

where \vec{r} is the transverse location of the emitted parton 3 from the original dipole spanned by partons 1, 2 and r_{ij} the length of the dipoles, also shown in figure IV.18. In order to turn this into a dipole evolution, a Sudakov factor, $\Delta(y_{\min}, y)$, restricting emission between y_{\min} and y , has to be introduced. The full dipole splitting kernel then reads,

$$\frac{dP}{dy d^2\vec{r}} = \frac{N_c \alpha_s}{2\pi^2} \frac{r_{12}^2}{r_{13}^2 r_{23}^2} \Delta(y_{\min}, y), \quad (\text{IV.57})$$

For event generation to proceed, we need to find an overestimate for the above splitting probability. The Sudakov factor is included via the veto algorithm, and is thus neglected in the expressions below.

First we sample a transverse location of the emitting dipole. Assuming partons 1 and 2 located in the (x, y) -plane at $\vec{r}_1 = (0, 0)$ and $\vec{r}_2 = (1, 0)$ with length $r_{12} = 1$ fm, while the emitted parton is located at $\vec{r}_3 = (r_x, r_y)$, we can write the splitting probability as,

$$\begin{aligned} \frac{dP}{dy dr_x dr_y} &= \frac{N_c \alpha_s}{2\pi^2} \frac{r_{12}^2}{(r_x^2 + r_y^2)((r_{2,x} - r_x)^2 + r_y^2)} \\ &= \frac{N_c \alpha_s}{2\pi^2} \frac{1}{(r_x^2 + r_y^2)((1 - r_x)^2 + r_y^2)}, \end{aligned} \quad (\text{IV.58})$$

where in the second step we have inserted the values for $r_{2,x} = 1$ fm and $r_{12}^2 = 1$ fm², but suppressed dimensions. These dimensions are suppressed throughout the section. This distribution is symmetric around $r_x = 1/2$ fm and $r_y = 0$ fm, so the limits of integration can be changed from $r_{x/y} \in]-\infty, \infty[$ to $r_x \in [-\infty, 1/2]$ and $r_y \in [-\infty, 0]$.

The above splitting probability can be overestimated by the function,

$$\frac{dP_1}{dy dr_x dr_y} = \frac{N_c \alpha_s}{2\pi^2} \frac{2}{(r_x^2 + r_y^2)(r_x^2 + r_y^2 + \frac{1}{4})}. \quad (\text{IV.59})$$

Changing to cylindrical coordinates we obtain,

$$\frac{dP_1}{dy r dr d\phi} = \frac{N_c \alpha_s}{2\pi^2} \frac{2}{r^2(r^2 + \frac{1}{4})}, \quad (\text{IV.60})$$

which can be integrated from a minimal dipole size, ρ . Thus we obtain,

$$\frac{dP_1}{dy} = \frac{4N_c \alpha_s}{\pi} \log \left(1 + \frac{1}{4\rho^2} \right). \quad (\text{IV.61})$$

Without energy ordering, the minimal dipole size ρ has to be fixed to a number larger than zero to avoid the distribution from blowing up. Here, energy the ordering is introduced by ordering of positive lightcone momenta [39]. Again relating the transverse momentum of the dipole to its size, gives an expression for ρ related to the kinematics of the parent dipole (p),

$$p_+^3 \leq p_+^p \Rightarrow p_\perp^3 e^{-y} = \frac{1}{\rho} e^{-y} \leq p_+^p \Rightarrow \rho \geq e^{-y}/p_+^p. \quad (\text{IV.62})$$

This expression is then used in eq. (IV.61),

$$\frac{dP_1}{dy} = \frac{4N_c \alpha_s}{\pi} \log \left(1 + \frac{(p_\perp^p)^2}{4} e^{2y} \right). \quad (\text{IV.63})$$

This overestimate cannot trivially be integrated, so we find yet another,

$$\frac{dP_2}{dy} = \frac{4N_c \alpha_s}{\pi} \log \left[e^{2y} \left(1 + \frac{(p_\perp^p)^2}{4} \right) \right] \equiv \frac{4N_c \alpha_s}{\pi} \log [e^{2y} A] \quad (\text{IV.64})$$

which is both integrable and invertible. We take into account the Sudakov factor by using the Veto algorithm, and thus the rapidity can be sampled from this distribution by

$$y_i = 1/2 \sqrt{[\log(A) + 2y_{i-1}]^2 - \pi \log(R_1)/(N_c \alpha_s) - 1/2 \log(A)}, \quad (\text{IV.65})$$

where R_1 is a uniformly distributed random number.

From eq. (IV.61) we can sample both r and ϕ ,

$$\phi = 2\pi R_2, \quad (\text{IV.66})$$

$$r = \sqrt{\frac{1}{4} \frac{\rho^{2R_3}}{(\rho^2 + 1/4)^{R_3} - \rho^{2R_3}}}, \quad (\text{IV.67})$$

with R_2, R_3 two new random numbers. Here we should note that we've changed the integration limits, such that any $r_x = r \cos(\phi) > 1/2$ must be rejected in the event generation. Half of the remaining events should be mirrored to $r_x \rightarrow 1 - r_x$, and this should be taken into account in the overestimate $dP_1/dy dr_x dr_y$ as well, such that

$$\begin{aligned} \frac{dP_1}{dy dr_x dr_y} &= \frac{N_c \alpha_s}{2\pi^2} \frac{2}{(r_x^2 + r_y^2)(r_x^2 + r_y^2 + \frac{1}{4})} \rightarrow \\ &\frac{N_c \alpha_s}{2\pi^2} \left[\frac{1}{(r_x^2 + r_y^2)(r_x^2 + r_y^2 + \frac{1}{4})} + \frac{1}{((1 - r_x)^2 + r_y^2)((1 - r_x)^2 + r_y^2 + \frac{1}{4})} \right]. \end{aligned} \quad (\text{IV.68})$$

The events are weighted to the correct distributions with,

$$w_r = \frac{(r_x^2 + r_y^2 + 1/4)((1 - r_x)^2 + r_y^2 + 1/4)}{((1 - r_x)^2 + r_y^2)((1 - r_x)^2 + r_y^2 + 1/4) + (r_x^2 + r_y^2)(r_x^2 + r_y^2 + 1/4)}, \quad (\text{IV.69})$$

$$w_y = \frac{\log(1 + \frac{(p_\perp^p)^2}{4} e^{2y})}{2y + \log(A)}, \quad (\text{IV.70})$$

such that if $w_r w_y < R_4$ the event is rejected and the process is reiterated.

The evolution of an initial dipole thus goes as follows. Firstly, a trial emission from the initial dipole is performed according to eq. (IV.56). If the rapidity y_0 of this emission is below the maximally allowed rapidity, then the trial branching is accepted, thus two new dipoles are created. Trial emissions are then allowed from each of these dipoles using $y_{\min} = y_0$ in eq. (IV.56). This creates two new emissions with rapidities $y_{1,2}$. But here *only* the dipole with the smallest rapidity is accepted. Thus after the second iteration we have three dipoles, from each of which trial emissions are created and only the emission with the smallest rapidity is accepted, thus creating an additional dipole. The process is reiterated until no trial emissions are produced below the maximally allowed rapidity. The process is visualized in figure IV.18.

The choice of p_\perp of the emitted parton is not obvious. Here we assign the parton the largest p_\perp of the system,

$$p_\perp^3 = \frac{1}{\min(r_{13}, r_{23})}. \quad (\text{IV.71})$$

Ordering of lightcone momenta

We here rely on approximate energy conservation through ordering of p_+ . This has already been discussed in the above, where we found the cutoff for small dipoles in the event

generation of r , eq. (IV.62). Thus we have implemented energy conservation as

$$p_+^3 \leq p_+^p, \quad (\text{IV.72})$$

which implies a rapidity-dependent cutoff for smaller dipoles.

Momentum conservation is introduced through the ordering of p_- ,

$$p_-^3 \geq \max(p_-^1, p_-^2), \quad (\text{IV.73})$$

where it should be noted that this requirement is applied *after* the recoils have been taken into account. This choice also sets an upper bound for the dipole size through

$$p_-^3 \geq p_-^p \Rightarrow p_\perp e^{y_3} = \frac{1}{r} e^{y_3} \geq p_-^p \Rightarrow r \leq \frac{e^{y_3}}{p_-} \quad (\text{IV.74})$$

Recoil effects

The recoil of the emitted parton is shared equally between the partons spanning the emitting dipole. Energy conservation requires that the energy of the emitter after the emission of a new dipole equals the energy of the emitter before the collision minus the recoil,

$$p_+^{\text{after}} = p_+^{\text{before}} - p_+^{\text{recoil}}. \quad (\text{IV.75})$$

The recoil cannot be determined from first principles thus have to make an ansatz. The choice here is also from [39],

$$\begin{aligned} p_+^{1,\text{recoil}} &= \frac{r_{23}}{r_{13} + r_{23}} p_+^3 \\ p_+^{2,\text{recoil}} &= \frac{r_{13}}{r_{13} + r_{23}} p_+^3 \end{aligned} \quad (\text{IV.76})$$

thus the recoil on parton 1 depends on the length of the dipole spanned by partons 2, 3 and vice versa. Energy conservation is satisfied in the event generation by always requiring that $p_+^{i,\text{recoil}} \leq p_+^{i,\text{before}}$.

The recoil will also affect the p_\perp of the emitter. Here the choice is

$$p_\perp^{i,\text{after}} = \max \left(p_\perp^i, \frac{1}{r_{i3}} \right), \quad (\text{IV.77})$$

where $i = 1, 2$ are the initial partons and 3 is the emitted parton.

Changing both the p_{\perp} and p_{+} of the emitter thus also requires us to change the rapidity of the emitter for consistency,

$$y^{i,\text{after}} = \log \left(\frac{p_{\perp}^{i,\text{after}}}{p_{+}^{i,\text{after}}} \right). \quad (\text{IV.78})$$

Note here that the rapidity of the parent after the recoil will always be larger than the rapidity of the parent dipole *before* the recoil. This is because p_{+} after the recoil is always smaller than p_{+} before the recoil, while the p_{\perp} after the recoil is always larger than or equal to the p_{\perp} before the recoil. Because of this, we must require that the rapidity of the emitters after the recoil is smaller than the rapidity of the emitted gluon, $y^{1,\text{after}}, y^{2,\text{after}} \leq y^3$.

Effects of confinement

Here it should be noted that the modified Bessel functions behave as $K_1(x) \sim 1/x$ for small arguments, while falling off exponentially at large arguments, $K_1(x) \sim \sqrt{\pi/x} \exp(-x)$. Thus the confined distribution is overestimated by the unconfined distribution, and the introduction of confinement only adds an additional weight $f(\text{confined})/f(\text{unconfined})$ that vetoes events with large dipole sizes.

10.2 Initial states

The initial dipole configuration depends on the particle. Here we present two types: a proton sampler and a photon sampler. The difference here lies both in the number of initial dipoles (three for protons, one for photons) and in the wave function of the particle itself.

Protons

The initial state proton is not known from QCD, but instead has to be described by some phenomenological model. At rest, it consists primarily of three valence quarks, which we can view as endpoints of the initial dipoles. The configuration of these dipoles, however, is not known, thus we here work with a single scenario: An equilateral triangle.

We allow the dipole length to be distributed according to a Gaussian of mean r_0 and width σ_r , such that the length of the initial dipoles is given as:

$$r = r_0 + r_w R_g \quad (\text{IV.79})$$

with R_g a Gaussian random number. The center of the triangle is fixed at origo.

Photons

The wave function used in this work is presented in eqs. (IV.25–IV.26). The full cross section for γ^*p is then given as

$$\sigma^{\gamma^*p}(s) = \int_0^1 dz \int_0^{r_{\max}} r dr \int_0^{2\pi} d\phi (|\psi_L(z, r)|^2 + |\psi_T(z, r)|^2) \sigma(z, \vec{r}), \quad (\text{IV.80})$$

with $\sigma(z, \vec{r})$ the dipole-dipole scattering cross sections given in equations (IV.14–IV.16). The dipole-dipole scattering cross section goes roughly as the square of the size of the largest dipole, $\sigma(z, \vec{r}) \sim r^2$, thus an overestimate of the γ^*p cross section can be found by sampling the parameters from the following distributions, we obtain

$$z = R_1, \quad (\text{IV.81})$$

$$\phi = 2\pi R_2 \quad (\text{IV.82})$$

$$r = r_{\max} R_3, \quad (\text{IV.83})$$

$$\sigma_{\gamma^*p}^O = \frac{2\pi r_{\max}}{N} \sum_{i=1}^N r_i^3 (|\psi_L(z_i, r_i)|^2 + |\psi_T(z_i, r_i)|^2) \quad (\text{IV.84})$$

The maximal value obtained in the sum is kept to accept or reject the integrand in the algorithm, where first and z_i, r_i are chosen and then accepted w.r.t.

$$w_\gamma = \frac{r_i^3 (|\psi_L(z_i, r_i)|^2 + |\psi_T(z_i, r_i)|^2)}{(\max. \text{ value})}. \quad (\text{IV.85})$$

If this weight is less than a new random number, $w_\gamma < R_4$, the event is rejected. If kept, the event is given a weight $w = \sigma_{\gamma^*p}^O / r_i^2$ to take into account the overestimation of the dipole-dipole scattering cross section.

II Appendix: The ANGANTYR model for heavy ion collisions

The ANGANTYR model for heavy ion collisions is based on the following four components:

- Firstly, the position of the nucleons inside the nuclei has to be determined.
- Secondly, the number of interacting nucleons and binary NN collisions has to be calculated within the Glauber-Gribov (GG) formalism.
- Thirdly, the contribution to the final state of each interacting nucleon has to be determined. Here ANGANTYR uses the wounded nucleon model by Białaś, Bleszyński and Czyż [98].

- Lastly, any hard partonic subcollision has to be modeled, thus introducing the concepts of primary and secondary absorptive interactions.

Each of the four components will here be shortly reviewed. For the full explanation, see [35, 36].

The nucleon distribution is generated using a Woods-Saxon potential:

$$\rho(r) = \frac{\rho_0 (1 + wr^2/R^2)}{1 + \exp((r - R)/a)} \quad (\text{IV.86})$$

with $\rho(r)$ the radial density of the nucleons, R the radius of the nucleus, a the skin width and w the Fermi parameter, introducing a varying density but set to zero in ANGANTYR. The A nucleons are thus generated randomly according to $P(\vec{r}_i) = \rho(\vec{r}_i)d^3\vec{r}_i$, assuming isospin invariance, such that $p = n$. ANGANTYR uses the hard core assumption, such that a new position for a nucleus is tried if the distance to its neighbors falls below twice the hard-core radius R_b . Once the nuclear distributions are set up, the impact parameter of the collision is sampled using a Gaussian distribution. This information is then passed the GG framework, which determines the fluctuations of the target and projectiles.

The fluctuations arise because of fluctuations in the proton wave function. Because the wave function enters in the cross section calculations and because it is assumed that the projectile state is frozen during its interaction with the target, these fluctuation are then translated into fluctuating cross sections. In the dipole model, the probabilistic nature of the dipole evolution gives rise to different dipole configurations before the collisions, thus giving rise to different dipole-dipole interactions and hence integrated cross sections. ANGANTYR uses a probability distribution for the cross section in pA extracted from DIPSY:

$$P_{\text{tot}}(\log \sigma) = \frac{1}{\Omega\sqrt{2\pi}} \exp\left[-\frac{\log^2(\sigma/\sigma_0)}{2\Omega^2}\right], \quad (\text{IV.87})$$

$$\langle T(\vec{b}, \sigma) \rangle = T_0 \Theta\left(\sqrt{\frac{\sigma}{2\pi T_0}} - b\right), \quad (\text{IV.88})$$

with $\sigma = \int d^2\vec{b} \langle 2T(\vec{b}) \rangle$ and eq. (IV.88) describing a slightly modified version of the elastic scattering amplitude. The parameters σ_0 , Ω , T_0 are tuned to data. For AA the fluctuations

are instead determined by a Gamma function,

$$P(r) = \frac{r^{k-1} e^{-r/r_0}}{\Gamma(k) r_0^k}, \quad (\text{IV.89})$$

$$T(\vec{b}, r_p, r_t) = T_0(r_p + r_t) \Theta \left(\sqrt{\frac{(r_p + r_t)^2}{2T_0}} - b \right), \quad (\text{IV.90})$$

$$T_0(r_p + r_t) = \left(1 - \exp \left[-\frac{\pi(r_p + r_t)^2}{\sigma_t} \right] \right)^\alpha, \quad (\text{IV.91})$$

where $P(r)$ determines fluctuations in the nucleon radius r_p and r_k . $T(\vec{b}, r_p, r_t)$ again describes a slightly modified elastic amplitude with an opacity T_0 depending on the radii of both the target and projectile. Here, the parameters σ_t, α, k, r_0 are tuned to data. The number of wounded target nucleons in pA collisions is then determined by

$$\frac{d\sigma_{\text{wt}}}{d^2\vec{b}} = 1 - \langle \langle S_{pt} \rangle_t^2 \rangle_p, \quad (\text{IV.92})$$

with S_{pt} the S-matrix for a given target (t) and projectile (p) state. Subscript on the brackets determines averages over one side only. In AA collisions ANGANTYR distinguishes between absorptively and diffractively wounded nucleons, with the former dominating given by,

$$\frac{d\sigma_{\text{abs}}}{d^2\vec{b}} = 1 - \langle S_{pt}^2 \rangle_{pt}, \quad (\text{IV.93})$$

and the latter determined by generating the auxiliary states p', t' for both target and projectile, and from these determining the number of wounded target states with either t or t' from eq. (IV.92), i.e. using either $S_{pt'}$ or S_{pt} in the derivation. Non-negative probabilities are ensured by shuffling when to use t, t' .

Once the number of wounded target and projectile states has been determined, the wounded nucleon model is used to create final-state partons,

$$\frac{dN_{\text{ch}}}{d\eta} = w_p F(\eta) + w_t F(-\eta), \quad (\text{IV.94})$$

with the functions $F(\pm\eta)$ determined from the MPI framework of PYTHIA 8. Each nucleon in the target (and projectile) is allowed to interact several times, similar to an ordinary pp collision containing several MPIs. Thus the pairs of projectile-target nucleons are ordered w.r.t. their impact-parameter $b_{\mu\nu}$. The list is iterated over several times in order to determine which pairs give rise to a primary absorptive scattering, and which are secondary. Once a pair has been selected, the MPI framework of PYTHIA 8 is used to generate an event, and the pair is marked as having interacted in a primary interaction. If the pair is again chosen

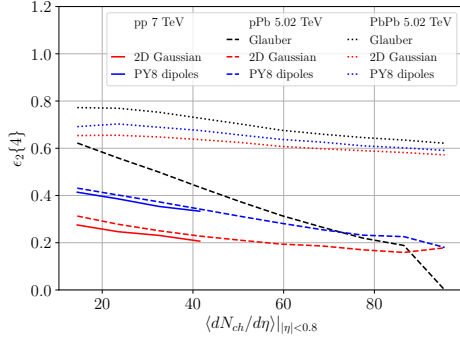
to interact, it will be marked as a secondary interaction. After the determination of the absorptive interactions, the diffractive ones are chosen by iterating the list several times, thus creating primary and secondary diffractive interactions. An already wounded nucleon cannot be further excited, but an unwounded nucleon can participate in several diffractive interactions, until itself becomes wounded.

After the determination of the absorptive and diffractively primary and secondary interactions, each of the events are passed to PYTHIA 8 and the parton-level events are stacked on top of each other. The PYTHIA 8 description of single-diffractive events are modified to look like non-diffractive ones, to describe the secondary absorptive events, while diffractive primary and secondary events remain unmodified. We are thus left with a large set of parton-level events that can be passed to the hadronization framework of PYTHIA 8 and further analyzed.

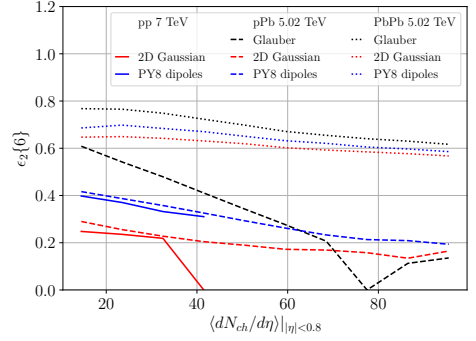
12 Appendix: Additional eccentricity figures

In this section, we show additional eccentricity figures not presented in the main body of the text. Figure IV.19 (a-c) shows ϵ_2 using higher-order cumulants in the evaluation. It is evident that the eccentricities are the same regardless of the number of particles used in the calculation, except for the effects from lack of statistics in the high-multiplicity tail for both the pp and pPb figures. Figure IV.19 (d) shows the normalized symmetric cumulant $NSC(4, 2)$. This cumulant is positive in the entire multiplicity range, consistent with measurements in ALICE. Here, it is evident that discrimination between models would be possible in both pp and pPb collisions, as opposed to $NSC(3, 2)$ where discriminatory power was not evident in pp collisions.

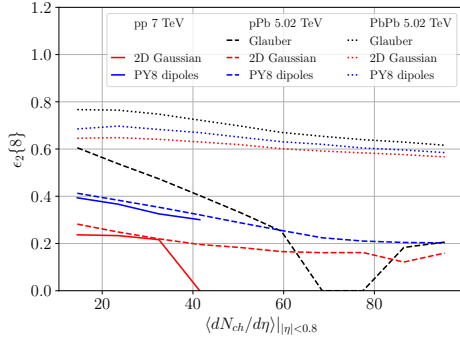
For completeness, we also show the eccentricities $\epsilon_{1,3}$ obtained in pp collisions with and without shower smearing in figure IV.20. Both are shown to give an estimate of the effects on the size of the additional terms in the Fourier expansion of the flow coefficients.



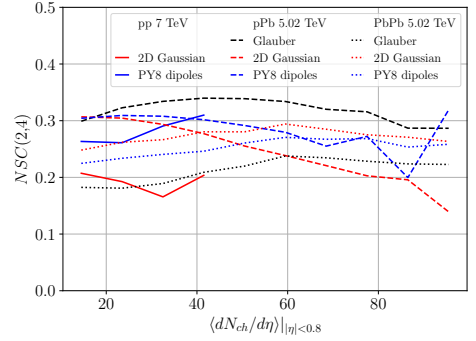
(a)



(b)

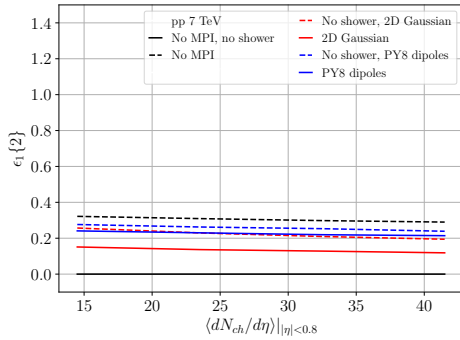


(c)

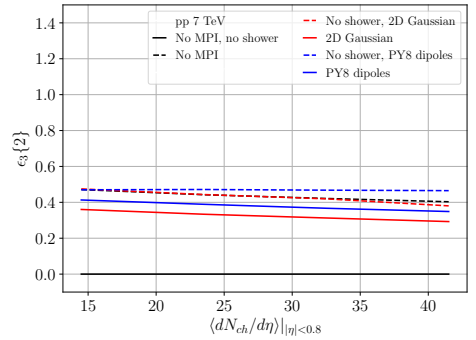


(d)

Figure IV.19: (a-c) The eccentricity ϵ_2 with higher order cumulants $\{4, 6, 8\}$. (d) The normalized symmetric cumulant $N_{SC}(4, 2)$ as a function of average multiplicity for pp, pA, AA systems.



(a)



(b)

Figure IV.20: $\epsilon_{1,3}\{2\}$ shown for different MPI vertex assignments with and without the shower smearing.

References

- [1] K. H. Ackermann *et al.* [STAR Collaboration], Phys. Rev. Lett. **86** (2001) 402 doi:10.1103/PhysRevLett.86.402 [nucl-ex/0009011].
- [2] K. Aamodt *et al.* [ALICE Collaboration], Phys. Rev. Lett. **105** (2010) 252302 doi:10.1103/PhysRevLett.105.252302 [arXiv:1011.3914 [nucl-ex]].
- [3] S. Chatrchyan *et al.* [CMS Collaboration], JHEP **1107** (2011) 076 doi:10.1007/JHEP07(2011)076 [arXiv:1105.2438 [nucl-ex]].
- [4] G. Aad *et al.* [ATLAS Collaboration], Phys. Rev. C **86** (2012) 014907 doi:10.1103/PhysRevC.86.014907 [arXiv:1203.3087 [hep-ex]].
- [5] J. Y. Ollitrault, Phys. Rev. D **46** (1992) 229. doi:10.1103/PhysRevD.46.229
- [6] V. A. Abramovsky, E. V. Gedalin, E. G. Gurvich and O. V. Kancheli, JETP Lett. **47** (1988) 337 [Pisma Zh. Eksp. Teor. Fiz. **47** (1988) 281].
- [7] S. Chatrchyan *et al.* [CMS Collaboration], Phys. Lett. B **718** (2013) 795 doi:10.1016/j.physletb.2012.11.025 [arXiv:1210.5482 [nucl-ex]].
- [8] C. Aidala *et al.* [PHENIX Collaboration], Phys. Rev. Lett. **120** (2018) no.6, 062302 doi:10.1103/PhysRevLett.120.062302 [arXiv:1707.06108 [nucl-ex]].
- [9] V. Khachatryan *et al.* [CMS Collaboration], JHEP **1009** (2010) 091 doi:10.1007/JHEP09(2010)091 [arXiv:1009.4122 [hep-ex]].
- [10] A. Badea *et al.*, arXiv:1906.00489 [hep-ex].
- [11] J. L. Nagle and W. A. Zajc, Ann. Rev. Nucl. Part. Sci. **68** (2018) 211 doi:10.1146/annurev-nucl-101916-123209 [arXiv:1801.03477 [nucl-ex]].

- [12] Z. Citron *et al.*, arXiv:1812.06772 [hep-ph].
- [13] B. Blok, C. D. Jäkel, M. Strikman and U. A. Wiedemann, JHEP **1712** (2017) 074 doi:10.1007/JHEP12(2017)074 [arXiv:1708.08241 [hep-ph]].
- [14] K. Dusling and R. Venugopalan, Phys. Rev. D **87** (2013) no.5, 054014 doi:10.1103/PhysRevD.87.054014 [arXiv:1211.3701 [hep-ph]].
- [15] R. D. Weller and P. Romatschke, Phys. Lett. B **774** (2017) 351 doi:10.1016/j.physletb.2017.09.077 [arXiv:1701.07145 [nucl-th]].
- [16] K. Werner, Phys. Rev. Lett. **98** (2007) 152301 doi:10.1103/PhysRevLett.98.152301 [arXiv:0704.1270 [nucl-th]].
- [17] T. Pierog, I. Karpenko, J. M. Katzy, E. Yatsenko and K. Werner, Phys. Rev. C **92** (2015) no.3, 034906 doi:10.1103/PhysRevC.92.034906 [arXiv:1306.0121 [hep-ph]].
- [18] T. Sjöstrand *et al.*, Comput. Phys. Commun. **191** (2015) 159 doi:10.1016/j.cpc.2015.01.024 [arXiv:1410.3012 [hep-ph]].
- [19] J. Bellm *et al.*, Eur. Phys. J. C **76** (2016) no.4, 196 doi:10.1140/epjc/s10052-016-4018-8 [arXiv:1512.01178 [hep-ph]].
- [20] D. d’Enterria, G. K. Eyyubova, V. L. Korotkikh, I. P. Lokhtin, S. V. Petrushanko, L. I. Sarycheva and A. M. Snigirev, Eur. Phys. J. C **66** (2010) 173 doi:10.1140/epjc/s10052-009-1232-7 [arXiv:0910.3029 [hep-ph]].
- [21] J. L. Albacete and A. Soto-Ontoso, Phys. Lett. B **770** (2017) 149 doi:10.1016/j.physletb.2017.04.055 [arXiv:1605.09176 [hep-ph]].
- [22] C. Bierlich, G. Gustafson and L. Lönnblad, Phys. Lett. B **779** (2018) 58 doi:10.1016/j.physletb.2018.01.069 [arXiv:1710.09725 [hep-ph]].
- [23] A. H. Mueller, Nucl. Phys. B **415** (1994) 373. doi:10.1016/0550-3213(94)90116-3
- [24] A. H. Mueller and B. Patel, Nucl. Phys. B **425** (1994) 471 doi:10.1016/0550-3213(94)90284-4 [hep-ph/9403256].
- [25] E. Avsar, C. Flensburg, Y. Hatta, J. Y. Ollitrault and T. Ueda, Phys. Lett. B **702** (2011) 394 doi:10.1016/j.physletb.2011.07.031 [arXiv:1009.5643 [hep-ph]].
- [26] I. Balitsky, Nucl. Phys. B **463** (1996) 99 doi:10.1016/0550-3213(95)00638-9 [hep-ph/9509348].
- [27] I. Balitsky, Phys. Rev. Lett. **81** (1998) 2024 doi:10.1103/PhysRevLett.81.2024 [hep-ph/9807434].

- [28] I. Balitsky, Phys. Lett. B **518** (2001) 235 doi:10.1016/S0370-2693(01)01041-3 [hep-ph/0105334].
- [29] J. Jalilian-Marian, A. Kovner, A. Leonidov and H. Weigert, Nucl. Phys. B **504** (1997) 415 doi:10.1016/S0550-3213(97)00440-9 [hep-ph/9701284].
- [30] J. Jalilian-Marian, A. Kovner, A. Leonidov and H. Weigert, Phys. Rev. D **59** (1998) 014014 doi:10.1103/PhysRevD.59.014014 [hep-ph/9706377].
- [31] E. Iancu, A. Leonidov and L. D. McLerran, Phys. Lett. B **510** (2001) 133 doi:10.1016/S0370-2693(01)00524-X [hep-ph/0102009].
- [32] E. Iancu, A. Leonidov and L. D. McLerran, Nucl. Phys. A **692** (2001) 583 doi:10.1016/S0375-9474(01)00642-X [hep-ph/0011241].
- [33] H. Weigert, Nucl. Phys. A **703** (2002) 823 doi:10.1016/S0375-9474(01)01668-2 [hep-ph/0004044].
- [34] M. Deak, K. Kutak, W. Li and A. M. Staśto, arXiv:1906.09062 [hep-ph].
- [35] C. Bierlich, G. Gustafson and L. Lönnblad, JHEP **1610** (2016) 139 doi:10.1007/JHEP10(2016)139 [arXiv:1607.04434 [hep-ph]].
- [36] C. Bierlich, G. Gustafson, L. Lönnblad and H. Shah, JHEP **1810** (2018) 134 doi:10.1007/JHEP10(2018)134 [arXiv:1806.10820 [hep-ph]].
- [37] A. Accardi *et al.*, Eur. Phys. J. A **52** (2016) no.9, 268 doi:10.1140/epja/i2016-16268-9 [arXiv:1212.1701 [nucl-ex]].
- [38] G. P. Salam, Comput. Phys. Commun. **105** (1997) 62 doi:10.1016/S0010-4655(97)00066-0 [hep-ph/9601220].
- [39] E. Avsar, G. Gustafson and L. Lönnblad, JHEP **0507** (2005) 062 doi:10.1088/1126-6708/2005/07/062 [hep-ph/0503181].
- [40] C. Flensburg, G. Gustafson and L. Lönnblad, JHEP **1108** (2011) 103 doi:10.1007/JHEP08(2011)103 [arXiv:1103.4321 [hep-ph]].
- [41] V. Kovalenko and V. Vechernin, PoS Baldin -ISHEPP-XXI (2012) 077 doi:10.22323/1.173.0077 [arXiv:1212.2590 [nucl-th]].
- [42] E. Avsar, G. Gustafson and L. Lönnblad, JHEP **0712** (2007) 012 doi:10.1088/1126-6708/2007/12/012 [arXiv:0709.1368 [hep-ph]].
- [43] E. Avsar, JHEP **0711** (2007) 027 doi:10.1088/1126-6708/2007/11/027 [arXiv:0709.1371 [hep-ph]].

- [44] B. Schenke, P. Tribedy and R. Venugopalan, Phys. Rev. Lett. **108** (2012) 252301 doi:10.1103/PhysRevLett.108.252301 [arXiv:1202.6646 [nucl-th]].
- [45] A. H. Mueller, Phys. Lett. B **523** (2001) 243 doi:10.1016/S0370-2693(01)01343-0 [hep-ph/0110169].
- [46] E. A. Kuraev, L. N. Lipatov and V. S. Fadin, Sov. Phys. JETP **45** (1977) 199 [Zh. Eksp. Teor. Fiz. **72** (1977) 377].
- [47] I. I. Balitsky and L. N. Lipatov, Sov. J. Nucl. Phys. **28** (1978) 822 [Yad. Fiz. **28** (1978) 1597].
- [48] Y. V. Kovchegov, Phys. Rev. D **60** (1999) 034008 doi:10.1103/PhysRevD.60.034008 [hep-ph/9901281].
- [49] E. Iancu and R. Venugopalan, In "Hwa, R.C. (ed.) et al.: Quark gluon plasma" 249-3363 doi:10.1142/9789812795533_0005 [hep-ph/0303204].
- [50] F. Gelis, E. Iancu, J. Jalilian-Marian and R. Venugopalan, Ann. Rev. Nucl. Part. Sci. **60** (2010) 463 doi:10.1146/annurev.nucl.010909.083629 [arXiv:1002.0333 [hep-ph]].
- [51] I. Balitsky, In *Shifman, M. (ed.): At the frontier of particle physics, vol. 2* 1237-1342 doi:10.1142/9789812810458_0030 [hep-ph/0101042].
- [52] F. Close, S. Donnachie and G. Shaw, Camb. Monogr. Part. Phys. Nucl. Phys. Cosmol. **25** (2007) 1.
- [53] A. M. Stasto, K. J. Golec-Biernat and J. Kwiecinski, Phys. Rev. Lett. **86** (2001) 596 doi:10.1103/PhysRevLett.86.596 [hep-ph/0007192].
- [54] Y. V. Kovchegov and E. Levin, Camb. Monogr. Part. Phys. Nucl. Phys. Cosmol. **33** (2012) 1. doi:10.1017/CBO9781139022187
- [55] I. Balitsky and G. A. Chirilli, Phys. Rev. D **77** (2008) 014019 doi:10.1103/PhysRevD.77.014019 [arXiv:0710.4330 [hep-ph]].
- [56] A. Kovner, M. Lublinsky and Y. Mulian, Phys. Rev. D **89** (2014) no.6, 061704 doi:10.1103/PhysRevD.89.061704 [arXiv:1310.0378 [hep-ph]].
- [57] A. Kovner, M. Lublinsky and Y. Mulian, JHEP **1408** (2014) 114 doi:10.1007/JHEP08(2014)114 [arXiv:1405.0418 [hep-ph]].
- [58] M. Lublinsky and Y. Mulian, JHEP **1705** (2017) 097 doi:10.1007/JHEP05(2017)097 [arXiv:1610.03453 [hep-ph]].
- [59] T. Lappi and H. Mäntysaari, Phys. Rev. D **91** (2015) no.7, 074016 doi:10.1103/PhysRevD.91.074016 [arXiv:1502.02400 [hep-ph]].

- [60] B. Ducloué, E. Iancu, A. H. Mueller, G. Soyez and D. N. Triantafyllopoulos, JHEP **1904** (2019) 081 doi:10.1007/JHEP04(2019)081 [arXiv:1902.06637 [hep-ph]].
- [61] E. Avsar, G. Gustafson and L. Lönnblad, JHEP **0701** (2007) 012 doi:10.1088/1126-6708/2007/01/012 [hep-ph/0610157].
- [62] G. Beuf, Phys. Rev. D **89** (2014) no.7, 074039 doi:10.1103/PhysRevD.89.074039 [arXiv:1401.0313 [hep-ph]].
- [63] V. S. Fadin and L. N. Lipatov, Phys. Lett. B **429** (1998) 127 doi:10.1016/S0370-2693(98)00473-0 [hep-ph/9802290].
- [64] M. Ciafaloni and G. Camici, Phys. Lett. B **430** (1998) 349 doi:10.1016/S0370-2693(98)00551-6 [hep-ph/9803389].
- [65] G. P. Salam, Acta Phys. Polon. B **30** (1999) 3679 [hep-ph/9910492].
- [66] T. Altinoluk, N. Armesto, G. Beuf, M. Martínez and C. A. Salgado, JHEP **1407** (2014) 068 doi:10.1007/JHEP07(2014)068 [arXiv:1404.2219 [hep-ph]].
- [67] H. Niemi, G. S. Denicol, H. Holopainen and P. Huovinen, Phys. Rev. C **87** (2013) no.5, 054901 doi:10.1103/PhysRevC.87.054901 [arXiv:1212.1008 [nucl-th]].
- [68] C. Bierlich, G. Gustafson and L. Lönnblad, arXiv:1612.05132 [hep-ph].
- [69] Z. Qiu and U. W. Heinz, Phys. Rev. C **84** (2011) 024911 doi:10.1103/PhysRevC.84.024911 [arXiv:1104.0650 [nucl-th]].
- [70] Y. Zhou, CERN-THESIS-2016-005.
- [71] J. L. Albacete, H. Petersen and A. Soto-Ontoso, Phys. Lett. B **778** (2018) 128 doi:10.1016/j.physletb.2018.01.011 [arXiv:1707.05592 [hep-ph]].
- [72] E. Avsar and G. Gustafson, JHEP **0704** (2007) 067 doi:10.1088/1126-6708/2007/04/067 [hep-ph/0702087].
- [73] A. H. Mueller and G. P. Salam, Nucl. Phys. B **475** (1996) 293 doi:10.1016/0550-3213(96)00336-7 [hep-ph/9605302].
- [74] T. Sjöstrand and M. van Zijl, Phys. Rev. D **36** (1987) 2019 doi:10.1103/PhysRevD.36.2019
- [75] T. Sjöstrand and P. Z. Skands, JHEP **0403** (2004) 053 doi:10.1088/1126-6708/2004/03/053 [hep-ph/0402078].
- [76] A. Donnachie and P. V. Landshoff, Phys. Lett. B **296** (1992) 227 doi:10.1016/0370-2693(92)90832-O [hep-ph/9209205].

- [77] G. A. Schuler and T. Sjöstrand, Phys. Rev. D **49** (1994) 2257. doi:10.1103/PhysRevD.49.2257
- [78] R. B. Appleby, R. J. Barlow, J. G. Molson, M. Serluca and A. Toader, Eur. Phys. J. C **76** (2016) no.10, 520 doi:10.1140/epjc/s10052-016-4363-7 [arXiv:1604.07327 [hep-ph]].
- [79] C. O. Rasmussen and T. Sjöstrand, Eur. Phys. J. C **78** (2018) no.6, 461 doi:10.1140/epjc/s10052-018-5940-8 [arXiv:1804.10373 [hep-ph]].
- [80] C. Adloff *et al.* [HI Collaboration], Eur. Phys. J. C **21** (2001) 33 doi:10.1007/s100520100720 [hep-ex/0012053].
- [81] A. Buckley, H. Hoeth, H. Lacker, H. Schulz and J. E. von Seggern, Eur. Phys. J. C **65** (2010) 331 doi:10.1140/epjc/s10052-009-1196-7 [arXiv:0907.2973 [hep-ph]].
- [82] S. Acharya *et al.* [ALICE Collaboration], arXiv:1903.01790 [nucl-ex].
- [83] A. M. Sirunyan *et al.* [CMS Collaboration], arXiv:1904.11519 [hep-ex].
- [84] G. Giacalone, J. Noronha-Hostler and J. Y. Ollitrault, Phys. Rev. C **95** (2017) no.5, 054910 doi:10.1103/PhysRevC.95.054910 [arXiv:1702.01730 [nucl-th]].
- [85] J. E. Bernhard, J. S. Moreland, S. A. Bass, J. Liu and U. Heinz, Phys. Rev. C **94** (2016) no.2, 024907 doi:10.1103/PhysRevC.94.024907 [arXiv:1605.03954 [nucl-th]].
- [86] L. Yan and J. Y. Ollitrault, Phys. Rev. Lett. **112** (2014) 082301 doi:10.1103/PhysRevLett.112.082301 [arXiv:1312.6555 [nucl-th]].
- [87] R. J. Glauber, Phys. Rev. **100** (1955) 242. doi:10.1103/PhysRev.100.242
- [88] M. L. Miller, K. Reygers, S. J. Sanders and P. Steinberg, Ann. Rev. Nucl. Part. Sci. **57** (2007) 205 doi:10.1146/annurev.nucl.57.090506.123020 [nucl-ex/0701025].
- [89] M. Alvioli and M. Strikman, Phys. Lett. B **722** (2013) 347 doi:10.1016/j.physletb.2013.04.042 [arXiv:1301.0728 [hep-ph]].
- [90] H. Heiselberg, G. Baym, B. Blaettel, L. L. Frankfurt and M. Strikman, Phys. Rev. Lett. **67** (1991) 2946. doi:10.1103/PhysRevLett.67.2946
- [91] B. Blaettel, G. Baym, L. L. Frankfurt, H. Heiselberg and M. Strikman, Phys. Rev. D **47** (1993) 2761. doi:10.1103/PhysRevD.47.2761
- [92] V. P. Gonçalves, R. P. da Silva and P. V. R. G. Silva, Phys. Rev. D **100** (2019) no.1, 014019 doi:10.1103/PhysRevD.100.014019 [arXiv:1905.00806 [hep-ph]].
- [93] T. S. Biro, H. B. Nielsen and J. Knoll, Nucl. Phys. B **245** (1984) 449. doi:10.1016/0550-3213(84)90441-3

- [94] C. Bierlich, G. Gustafson, L. Lönnblad and A. Tarasov, JHEP **1503** (2015) 148 doi:10.1007/JHEP03(2015)148 [arXiv:1412.6259 [hep-ph]].
- [95] C. Bierlich and J. R. Christiansen, Phys. Rev. D **92** (2015) no.9, 094010 doi:10.1103/PhysRevD.92.094010 [arXiv:1507.02091 [hep-ph]].
- [96] M. L. Mangano and B. Nachman, Eur. Phys. J. C **78** (2018) no.4, 343 doi:10.1140/epjc/s10052-018-5826-9 [arXiv:1708.08369 [hep-ph]].
- [97] C. Bierlich, Phys. Lett. B **795** (2019) 194 doi:10.1016/j.physletb.2019.06.018 [arXiv:1901.07447 [hep-ph]].
- [98] A. Bialas, M. Bleszynski and W. Czyz, Nucl. Phys. B **111** (1976) 461. doi:10.1016/0550-3213(76)90329-1

List of Figures

1	The running of the strong coupling as a function of Q [2]. Data points show the large variety of experiments, that are able to measure the strong coupling constant, with parantheses indicating the perturbative order at which the calculation is performed.	5
2	The LO diagram for $qq' \rightarrow qq'$	7
3	The impact parameter b of the collision between two contracted protons p_1, p_2 . The open circles represent the center of the two protons, while the arrows indicate their motion.	11
4	(a) The color flow in a $qq' \rightarrow qq'$ process. (b) A schematic view of the particle production as a function of rapidity produced by two strings (red lines) compared to a full event containing MPIs (blue lines).	16
5	A schematic view of elastic (blue lines) and diffractive processes: single diffraction (SD, green lines), double diffraction (DD, purple lines) and central diffraction (CD, red lines). The picture shows how the particles are distributed in rapidity y , and the rapidity gaps present.	17
6	The elastic (a) and single (b), double (c) and central (d) diffractive processes in pp collisions. Here p is a proton and \mathbb{P} a Pomeron, the “particle” responsible for the momentum transfer. X, Y are diffractive systems. . . .	18
7	A visualization of the unitarity equations. Grey blobs represent an unspecified scattering. Solid lines represent physical particles (of which n are intermediate on the right hand side). The vertical dashed line represents a final-state cut (cf. section 5.5).	21
8	(a) A two-body scattering process $a+b \rightarrow c+d$ with momentum indicated as p_i . The arrows with the text “ s -channel” or “ t -channel” indicate the time-direction in the respective channels. (b) The physical regions for equal-mass scatterings.	22
9	The s - (a), t - (b) and u -channels (c) obtained if the scattering of figure 8 (a) contains a single intermediate particle.	22
10	The Regge trajectories for the ρ, ω families along with the observed mesons [32].	27

II	(a) The elastic amplitude (left of the arrow) and its cross section (right of the arrow). (b) The multiplicity as a function of rapidity for elastic scattering.	29
12	Cutting through a Pomeron approximately corresponds to cutting through two gluons (a). This gives rise to two color-strings stretched between the two hadrons, hence giving rise to particle production in the entire phase space (b).	30
13	The latest results from CMS [10] on diffractive dijet production. (a) shows the differential cross section as a function of $-t$, while (b) shows it as a function of $\xi = x/x_{\mathbb{P}}$. The model developed in this thesis is denoted “Pythia8 DG” in the plots and is shown with a light-blue dashed line. . . .	34
14	A schematic evolution in rapidity of a single dipole (solid, black lines) stretched between a quark-antiquark pair denoted 1, 2. The dipole emits a gluon (denoted 3) thus breaking into two new dipoles spanned between partons 1, 3 and 2, 3, respectively. The mother dipole is represented by dashed, red lines. Only one of the new dipoles are allowed to emit in each step of the process. Definitions of the lengths, r_{ij} , have been shown in the first and second step of the evolution.	39
15	A schematic view of a dipole-dipole interaction. Here the dipole spanned between partons 1,2 interact with the dipole spanned between partons 3,4. The scattering probability of these two dipoles depends on the lengths between the endpoints r_{ij} . In this figure the lengths $r_{12}, r_{34}, r_{14}, r_{23}$ are shown, while lengths r_{13}, r_{24} have been omitted for simplicity.	40
16	An initial state proton consisting of three dipoles in an equilateral triangle configuration (a). After a full evolution in rapidity ($y_{\max} = 9$) the three dipoles have evolved into several smaller ones in (b). In both figures $r_0 = 1$ fm is the size of the initial dipoles.	41
I.1	The seven different Pomeron fluxes included in PYTHIA on linear (a) and logarithmic scale (b). Note that the MBR flux has not been renormalized (see [25]).	65
I.2	The QCD charge-weighted sum, eq. (I.8), of the H1 PDFs and the toy PDF PomFix compared to the NNPDF 2.3 proton PDF on linear (a) and logarithmic scale (b). The QCD charge-weighted sum, eq. (I.8), of the ACTW PDFs compared to the NNPDF 2.3 proton PDF on linear (c) and logarithmic scale (d).	66
I.3	The H1 \mathbb{P} gluon distribution on linear (a) and logarithmic (b) scale. The H1 \mathbb{P} quark and antiquark distributions on linear (c) and logarithmic (d) scale. Both compared to the NNPDF 2.3 proton PDF distributions. Note that for the \mathbb{P} we have $d = u = s = \bar{d} = \bar{u} = \bar{s} (= c = \bar{c})$, where the c, \bar{c} are only included in H1Jets.	67

I.4	The ACTW \mathbb{P} gluon distribution on linear (a) and logarithmic (b) scale. The ACTW \mathbb{P} quark and antiquark distributions on linear (c) and logarithmic (d) scale. Both compared to the NNPDF 2.3 proton PDF distributions. Note that for the \mathbb{P} we have $d = u = s = \bar{d} = \bar{u} = \bar{s} (= c = \bar{c})$, where the c, \bar{c} are only included in H1Jets.	68
I.5	The convolution of Pomeron fluxes and H1 PDFs for a few cases, with the range between the extremes marked in yellow; (a) linear and (b) logarithmic x scale. The convolution of DL flux and ACTW PDFs on (c) linear and (d) logarithmic x scale.	69
I.6	Some kinematics distributions obtained with variations of the Pomeron parametrizations: (a) $x_{\mathbb{P}}$, (b) M_X , (c) t and (d) θ	71
I.7	The rapidity of the W-boson produced in $q\bar{q} \rightarrow W^\pm$ at $\sqrt{s} = 8$ TeV. . . .	72
I.8	Impact-parameter distribution of $2 \rightarrow 2$ QCD processes with $p_\perp > 20$ GeV in $\sqrt{s} = 8$ TeV pp collisions. (a) The change during the selection steps. (b) The dependence on $p_{\perp 0}^{\text{ref}}$. (c) The distribution in the $\mathbb{P}p$ subcollision. (d) The dependence on impact-parameter profile.	73
I.9	Charged multiplicity distributions in the (a) $\mathbb{P}p$ subsystem for diffractive events, (b) pp system for nondiffractive events, in $2 \rightarrow 2$ QCD processes with $p_\perp > 20$ GeV as before.	74
I.10	Charged multiplicity distribution distributions for the $\mathbb{P}p$ diffractive subsystem, for events with $2 \rightarrow 2$ QCD processes with $p_\perp > 20$ GeV as before. (a) For three different $b_{\mathbb{P}p}$ impact-parameter profiles. (b) With or without rescaled \mathbb{P} flux and PDFs, see text.	75
I.11	(a) The diffractive fractions obtained in $2 \rightarrow 2$ QCD processes with $p_\perp > 20$ GeV (circles and solid lines) and $q\bar{q} \rightarrow W^\pm$ (squares and dashed lines) in pp collisions at different energies. (b) The diffractive fractions obtained in $q\bar{q} \rightarrow W^\pm$ with the default overlap function (squares and dashed lines) and the exponential overlap function (crosses and dashed-dotted lines). PYTHIA is run with the SaS flux and the H1 Fit B LO PDF.	77
I.12	The p_\perp of the hardest process obtained with (a) the soft (or inclusive) diffraction framework, and (b) both the soft and hard diffraction frameworks for events with $p_\perp > 10$ GeV.	78
I.13	The mean E_T of the leading jets in both SD and ND events using (a) the SaS and (b) the H1 Fit B flux. The mean η of the leading jets in both SD and ND events using (c) the SaS and (d) the H1 Fit B flux. The mean difference in ϕ between the leading jets in both SD and ND events using (e) the SaS and (f) the H1 Fit B flux.	84
I.14	The antiproton momentum fraction carried by the parton entering the hard collision, for PYTHIA 8 compared with CDF data. PYTHIA is run with the H1 Fit B LO PDF and (a) the SaS or (b) H1 Fit B flux. (c) and (d) shows the ratio SD to ND using (a) and (b).	85

I.15	The dijet cross sections as a function of the size of the rapidity gap (a), (b) and the fractional momentum loss of the proton (c), (d). Compared to the hard diffraction model of PYTHIA 8 using the SaS flux and H1 Fit B LO PDF. In (b) and (d) the ND + MPI sample is a sum of the black and red dotted lines from (a) and (c), whereas the inclusive sample are generated directly with PYTHIA 8. Only statistical errors are included in the ATLAS errorbars.	88
II.1	The squared matrix element for the total (a), elastic (b), single (c,d), double (e) and central (f) diffractive cross sections.	96
II.2	The total cross section parametrizations in (a) pp and (b) $p\bar{p}$ processes. The ratio of real to imaginary parts of the elastic amplitude at $t = 0$ for pp (c) and $p\bar{p}$ (d). Note that the SaS model has been left out in (c) and (d), as ρ is a constant here, that can be set freely by the user. Data from PDG [15].	109
II.3	The elastic differential cross section parametrizations in pp collisions at 53 GeV (a) and 7 TeV (b). The integrated elastic cross section parametrizations in (c) pp and (d) $p\bar{p}$ processes. Data from PDG [15].	110
II.4	The different components of the ABMST model for single diffraction as a function of (a) ξ and (b) t at 7 TeV. The integrated single diffractive cross section as a function of \sqrt{s} for $\xi < 0.05$ (c) and in the full single diffractive phase space (d). Data from references in [78].	113
II.5	The different components of the modified ABMST model for single diffraction as a function of (a) ξ and (b) t at 7 TeV. The same distributions are shown in (c) and (d), where we compare the two models ABMST and ABMST modified to the SaS model.	116
II.6	The single diffractive differential cross section parametrizations in pp collisions at \sqrt{s} 17.57 GeV with $t = -0.131 \text{ GeV}^2$ (a) and 53.66 GeV with $t = -0.52 \text{ GeV}^2$ (b). The mass-spectrum showing the resonances at $\sqrt{s} = \text{GeV}$ and $t = -\text{GeV}^2$ (c). The integrated t spectrum at $\sqrt{s} = \text{GeV}$ (d). Data from references in [78].	117
II.7	The integrated single diffractive cross section at different energies for $\xi < 0.05$ (a) and in the full phase space (b). Data from references in [78]. . . .	118
II.8	The effect of using only a subset of the available Pomerons in the elastic parametrization, as used in the expression for the double diffractive cross section, eq. (II.36). In (a) and (b) the elastic differential cross section is shown as a function of t at two energies. In (c) and (d) the effect of these on the double diffractive distributions are shown as a function of $\xi = \xi_1 \xi_2$ and t , respectively. Note that the “Pure ABMST” has a minimal slope of $B_{DD} = 2$ such as to avoid the dip structure of the elastic description. . . .	120

II.9	Some of the DD models available in PYTHIA 8. In (a) and (b) we show the differential cross section as a function of t and $\xi = \xi_1 \xi_2$, respectively. . . .	121
II.10	The integrated double diffractive cross section as a function of energy of some of the models available in PYTHIA 8.	122
II.11	Some of the CD models available in PYTHIA 8. In (a) we show the mass of the diffractive system produced at central rapidity and in (b) the integrated cross section as a function of energy.	124
II.12	(a) The SaS and MBR models using either ATLAS or CMS cuts along with the ratio of ATLAS to CMS cuts for both models. (b) The ATLAS [52] and CMS [53] data along with the ratio of ATLAS to CMS data, showing significant differences in the entire range.	125
II.13	The effects of changing the reference $\mathbb{P}p$ cross section on the charged multiplicity distribution using the SaS model at 7 TeV in the four gap ranges: 0 to 2 (a), 2 to 4 (b), 4 to 6 (c) and 6 to 8 (d).	126
II.14	The effects of changing the power of the mass dependence in the $\mathbb{P}p$ cross section on the charged multiplicity distribution using the SaS model at 7 TeV in the four gap ranges: 0 to 2 (a), 2 to 4 (b), 4 to 6 (c) and 6 to 8 (d).	127
II.15	The cross section as a function of gap size for the default SaS model, the SaS+CSCR model and the untuned ABMST models compared to ATLAS [52] (a) and CMS [53] (b) data. The cross section as a function of $\log_{10}\xi_X$ in a single-diffraction dominated region (c) and double diffraction dominated region (d) compared to CMS [53] data.	129
II.16	The cross section as a function of gap size for the three SaS-based models compared to ATLAS [52] (a) and CMS [53] (b) data. The cross section as a function of $\log_{10}\xi_X$ in a single-diffraction dominated region (c) and double diffractive dominated region (d) compared to CMS [53] data. . . .	131
II.17	The cross section as a function of gap size for the two ABMST-based models compared to ATLAS [52] (a) and CMS [53] (b) data. The cross section as a function of $\log_{10}\xi_X$ in a single-diffraction dominated region (c) and double diffractive dominated region (d) compared to CMS [53] data. For reference the tuned SaS model is also shown.	132
II.18	The inelastic cross section as a function of method described in the text compared to CMS [55] data.	133
III.1	Leading order Feynman diagrams for diffractive dijet production with photons in ep collisions. Either the photon participates directly in the hard scattering matrix element (a) or a parton from the resolved photon participates (b).	144
III.2	The photon fluxes used for different beam types. Here $f_{\gamma/b}$ is the photon flux obtained from the beam b	152

III.3	The two diffractive systems available for resolved photoproduction: either the proton is elastically scattered and the photon side contains the diffractive system (a), or the vector meson is elastically scattered and the proton side contains the diffractive system (b).	155
III.4	The GKG18 LO Fit A, B and ZEUS SJ fluxes on a linear (a) and logarithmic (b) scale in $x_{\mathbb{P}}$. Note that t has been integrated over its kinematical range, $f(x_{\mathbb{P}}) = \int dt f(x_{\mathbb{P}}, t)$	157
III.5	The GKG18 LO Fit A, B and ZEUS SJ dPDFs on a linear (a,c) and logarithmic (b,d) scale. The upper figures shows the light quark content, the lower the gluonic content.	157
III.6	The model with (solid lines) and without (dashed lines) gap survival compared to ZEUS data on M_X (a), $z_{\mathbb{P}}^{\text{obs}}$ (b), x_{γ}^{obs} (c) and $E_{\perp}^{\text{jet } 1}$ (d).	160
III.7	The model with (solid lines) and without (dashed lines) gap survival compared to H1 data on W (a), $z_{\mathbb{P}}^{\text{obs}}$ (b), x_{γ}^{obs} (c) and $E_{\perp}^{*\text{jet } 1}$ (d).	161
III.8	The model with (solid lines) and without (dashed lines) gap survival compared to ZEUS data on M_X in the direct-enhanced (a) and resolved-enhanced (b) regions.	163
III.9	The model along with the uncertainty bands arising from varying the renormalization- and factorization scales compared to ZEUS data on M_X (a), $z_{\mathbb{P}}^{\text{obs}}$ (b), x_{γ}^{obs} (c) and $E_{\perp}^{\text{jet } 1}$ (d).	164
III.10	The model without gap suppression using three different dPDFs: H1 LO Fit B (blue lines), GKG LO Fit A (green lines) and ZEUS NLO SJ (red lines) compared to ZEUS data on M_X (a), $z_{\mathbb{P}}^{\text{obs}}$ (b), x_{γ}^{obs} (c) and $E_{\perp}^{\text{jet } 1}$ (d).	165
III.11	The model without gap suppression using the three dPDFs: H1 Fit B LO (blue lines), GKG LO Fit A (green lines) and ZEUS SJ (red lines) compared to ZEUS data on M_X in the direct-enhanced (a) and resolved-enhanced (b) regions.	166
III.12	The model with gap suppression using the three dPDFs: H1 Fit B LO (blue lines), GKG LO Fit A (green lines) and ZEUS SJ (red lines) compared to ZEUS data on M_X in the direct-enhanced (a) and resolved-enhanced (b) regions.	167
III.13	The model with (solid lines) and without (dashed lines) gap suppression using two values of $p_{\perp 0}^{\text{ref}}$: The pp-tune, $p_{\perp 0}^{\text{ref}} = 2.28$ GeV (red lines) and the ep-tune, $p_{\perp 0}^{\text{ref}} = 3.0$ GeV (blue lines). Again we show the samples in the observables M_X (a), $z_{\mathbb{P}}^{\text{obs}}$ (b), x_{γ}^{obs} (c) and $E_{\perp}^{\text{jet } 1}$ (d).	168
III.14	The predicted gap suppression factors as a function of M_X (a) and $E_{\perp}^{\text{jet } 1}$ (b) compared to the ZEUS analysis.	169
III.15	The predicted gap suppression factors as a function of W (a) and $E_{\perp}^{*\text{jet } 1}$ (b) compared to the H1 analysis.	169

III.16	Cross section for diffractive dijets in ultra-peripheral pPb collisions for observables W (a), M_X (b), x_γ^{obs} (c) and $z_{\mathbb{P}}^{\text{obs}}$ (d). Vertical bars denote the statistical uncertainty in the MC generation.	173
III.17	Cross section for diffractive dijets in ultra-peripheral pp collisions for observables W (a), M_X (b), x_γ^{obs} (c) and $z_{\mathbb{P}}^{\text{obs}}$ (d). Vertical bars denote the statistical uncertainty in the MC generation.	175
IV.1	Schematic view of two colliding gluon dipoles. The initial dipoles denoted r_{12} and r_{34} are allowed to interact via two-gluon exchange. This results in the creation of two new dipoles, r_{14} and r_{23} and a connection of the two dipole chains. The lines r_{13} and r_{24} are not drawn, but enters in eq. (IV.9).	189
IV.2	The probability distribution in rapidity for unconfined (a) and confined (b) dipole-evolution. The box shows the average and spread of the distributions.	198
IV.3	The scaled lengths of the daughter dipoles w.r.t. the mother dipole as a function of maximal rapidity for unconfined (a,c) and confined (b,d) dipole-evolution. Figures (a,b) shows the larger of the daughter dipoles, while figures (c,d) shows the smaller of the daughter dipoles. The parameters used in the dipole evolution are the same as presented in table IV.1.	199
IV.4	The scaled lengths of the daughter dipoles w.r.t. the mother dipole as a function of maximal rapidity for unconfined (a) and confined (b) dipole-evolution. The parameters used in the dipole evolution are the same as presented in table IV.1.	200
IV.5	An initial state proton consisting of three dipoles in an equilateral triangle configuration after a full evolution at 7 TeV (corresponding to $y_{\text{max}} = 8.86$). (a) has been evolved without confinement, while (b) has been evolved with confinement. The parameters of table IV.1 have also been applied in this evolution.	201
IV.6	(a) The average number of dipoles inside a proton after a full evolution to maximal rapidity y . (b) An initial state proton consisting of three dipoles in an equilateral triangle configuration after a full evolution with the Pascal model at 7 TeV (corresponding to $y_{\text{max}} = 8.86$).	203
IV.7	The total photon-proton cross section, $\sigma_{\text{tot}}^{\gamma^* \text{p}}$, as a function of squared photon-proton center-of-mass energy, W^2 , for several virtualities (a). Note that the distributions for the two highest virtualities ($Q^2 = 60, 120 \text{ GeV}^2$) have been scaled with a factor of 0.3, 0.1, respectively, for better visibility. (b) shows the ratio MC/data as a function of squared center-of-mass energy, W^2 , for the five different virtualities.	206

IV.8	The total pp cross section as a function of \sqrt{s} for the dipole (a) and Pascal (b) models. Both show the confined and unconfined versions in solid blue and dashed red lines, respectively. Both figures show the ABMST (solid green lines) and SaS+DL (solid magenta lines) for comparison.	208
IV.9	The elastic pp cross section as a function of \sqrt{s} for the dipole (a) and Pascal (b) models. Both show the confined and unconfined versions in solid blue and dashed red lines, respectively. Both figures show the ABMST (solid green lines) and SaS+DL (solid magenta lines) for comparison.	209
IV.10	The elastic slope for pp collisions as a function of \sqrt{s} for the dipole (a) and Pascal (b) models. Both show the confined and unconfined versions in solid blue and dashed red lines, respectively. Both figures show the ABMST (solid green lines) and SaS+DL (solid magenta lines) for comparison.	210
IV.11	The eccentricities in pp collisions obtained with the several different options: No MPI vertex assignment and no shower smearing (solid black lines), no MPI vertex assignment, with shower smearing (dashed black lines), the 2D Gaussian MPI vertex with/without shower smearing (solid/dashed red lines, respectively) and the dipole model MPI vertex assignment with/without shower smearing (solid/dashed blue lines).	213
IV.12	The second (b) and third (c) order eccentricities using two-particle cumulants for pp, pPb, PbPb collisions (solid, dashed, dotted, respectively) using the Glauber (black), Gaussian (red) and dipole (blue) models. . . .	214
IV.13	(a) The ratio of second order eccentricities obtained in pPb w.r.t. the baseline pp sample using the Gaussian (red) and dipole (blue) models. Data points calculated from ALICE figures [82]. (b) The normalized symmetric cumulants $NSC(3, 2)$ for pp, pPb, PbPb collisions (solid, dashed, dotted, respectively) using the Glauber (black), Gaussian (red) and dipole (blue) models.	215
IV.14	Ratios of $v_n\{4\}/v_n\{2\}$ with $n = 2$ (a) and $n = 3$ (b) as measured by CMS as function of multiplicity in pPb collisions, compared to eccentricity ratios calculated with the Gaussian and the dipole models.	216
IV.15	Correlations between higher order flow harmonics as measured by the CMS experiment, compared to correlations between higher order eccentricity ratios calculated in the dipole model.	217
IV.16	(a) Fluctuating cross section in pp at $\sqrt{s} = 5$ TeV, compared to a GG fit (eq. (IV.50)) and a log-normal fit (eq. (IV.87)). (b) Fluctuating cross section in γ^*p at $W^2 = 5000$ GeV ² and various Q^2 , calculated with the dipole model (the double peak structure for $Q^2 = 20$ GeV ² is a statistical fluctuation). The cross section is shown on a logarithmic horizontal axis, to assess the log-normal approximation (cf. eq. (IV.87)).	220

IV.17	Number of wounded nucleons in a γ^* Au collision with $W^2 = 5000 \text{ GeV}^2$ and a range of Q^2 , comparing a treatment with the projectile wave function (denoted wf. in legend) frozen throughout the passage of the nucleus, to a naive black disk approach.	221
IV.18	Schematic view of a dipole splitting. The initial dipole is spanned by partons 1 and 2, that emits a new parton (3), thus creating two new dipoles: the dipole spanned by partons 1 and 3 and the dipole spanned by partons 2 and 3. This can be succeeded by additional splittings as indicated by the additional figures following the arrows.	225
IV.19	(a-c) The eccentricity ϵ_2 with higher order cumulants $\{4, 6, 8\}$. (d) The normalized symmetric cumulant $NSC(4, 2)$ as a function of average multiplicity for pp, pA, AA systems.	234
IV.20	$\epsilon_{1,3}\{2\}$ shown for different MPI vertex assignments with and without the shower smearing.	234